NAZARBAYEV UNIVERSITY

Mutual Coupling Reduced Innovative Millimeter-Wave MIMO Antenna Designs for IoT and WBAN Applications

by

Jawad Ahmad

Submitted in partial fulfillment of the requirements for the degree of Doctor of Philosophy in Electrical Engineering

Date of Completion
April, 2025

Mutual Coupling Reduced Innovative Millimeter-Wave MIMO Antenna Designs for IoT and WBAN Applications

by
Jawad Ahmad

Submitted in partial fulfillment of the requirements for the degree of
Doctor of Philosophy in Electrical Engineering

School of Engineering and Digital Sciences
Nazarbayev University

April, 2025

Supervised by
Lead Supervisor: Prof. Mohammad Hashmi
Internal Co-Supervisor: Prof. Galymzhan Nauryzbayev
External Co-Supervisor: Prof. Francisco Falcone

Declaration

I, Jawad Ahmad, declare that the research contained in this thesis, unless otherwise formally indicated within the text, is the author's original work. The thesis has not been previously submitted to this or any other university for a degree and does not incorporate any material already submitted for a degree.

Signature: Jawad Ahmad

Date: 21/4/2025

BLANK

Abstract

The fifth-generation (5G) technology in Internet of Things (IoT) systems is enhancing modern developments owing to the faster communication and with minimal latency. In practice, two frequency bands are specifically allocated for 5G and futuristic communications. These include: FR1 sub-6 GHz band and the FR2 millimeter-wave (mmWave) band. The sub-6 GHz band has the capacity of wider coverage and better signal penetration, thus, it is more suitable for large-scale communication deployments. However, its limited bandwidth will not meet the rapidly increasing high-speed data transmission demand in emerging technologies. Alternatively, the mmWave band has significantly higher bandwidth, can support multi-gigabit per second data rates and growing IoT demands. However, owing to the smaller wavelength, the mmWave frequencies faces critical challenges. These include high path loss, blockages by obstacles, and atmospheric attenuation therefore restrict the mmWave communication range and its reliability. In general, only one antenna is mostly utilized for both transmission and reception in a conventional communication system. This approach is efficient but has limited channel capacity. Alternatively, the implementations of multi-input-multi-output (MIMO) can enhance the channel capacity, mitigate the mmWave blockages challenges and signal fading by incorporating multiple antennas at transmitter and receiver end. Multipath fading and blockages occurs when the transmitted signals from antennas reach to the receiver through reflecting off buildings, walls, and other obstacles. These multiple signals can interfere with one another, resulting in signal degradation. MIMO technology can mitigate this through spatial diversity, wherein multiple antennas transmit the same signal via different paths. This ensures that at least some portion of the signals will reach the receiver and with minimal distortion or fading. This way the communication in mmWave band will improves particularly in environments where there is significant non line of sight conditions.

The design and implementation of mmWave MIMO antennas present challenges. In mmWave MIMO systems, antenna elements are typically placed at half-wavelength intervals. However, the shorter wavelengths of mmWave frequencies, ranging from 10 to 1 millimeter, require closely spaced antenna elements. This close spacing increases electromagnetic interaction, known as mutual coupling, degrades system performance by affecting impedance bandwidth, radiation patterns, gain, and efficiency. Minimizing mutual coupling is crucial for achieving optimal performance in mmWave MIMO communication systems.

One method to reduce mutual coupling is to increase the inter-element spacing beyond half wavelength. Although this technique can decrease the mutual coupling, it will also increase the dimensions of a MIMO antenna, which is undesirable, particularly considering the futuristic device size constraints imposed by consumer device requirements. Thus, alternative mutual coupling reductions techniques are important. Therefore, this work aim to reduce mutual coupling by introducing advanced and novel techniques in MIMO antenna systems. These include defective ground structure (DGS), frequency selective surface (FSS), metasurface and metallic vias. An IoT application particularly wireless body area network (WBAN) was considered as application perspective of the designs. At first, a compact Vivaldi antenna was designed, comprising four-element Vivaldi patterns operating at 28 GHz and 30 GHz with a 36.44% fractional bandwidth. The design integrates a Vivaldi antenna with a FSS to reduce mutual coupling, achieving inter-element isolation below -20 dB within a compact 16×20 mm² size. Performance was assessed through simulations on Gustav's model and practical tests on the human body, evaluating parameters such as impedance bandwidth, gain, efficiency, and radiation patterns. The MIMO antenna demonstrated excellent diversity characteristics: low envelope correlation coefficient (ECC) < 0.24, diversity gain > 9.95 dB, and total active reflection coefficient below -10 dB. A hybrid approach combining DGS and FSS to minimize mutual coupling was also investigated. A dual-band antenna with a modified elliptical patch and rotating arms was ist designed. and then converted into a six-element dual-band MIMO antenna covering ISM and 5G NR bands (23.63–32.90 GHz and 36.68–40 GHz). This hybrid coupling achieved reduction of -33 dB between MIMO elements. The antenna demonstrated broadside radiation patterns. In this case, MIMO diversity performance was: TARC below -10 dB, ECC under 0.04, and DG exceeding 9.91 dB. Another novel hybrid technique for mutual coupling reduction in a compact dual-band mmWave MIMO antenna, incorporating metallic vias and a metasurface, was investigated. This work particularly addressed surface wave coupling and near-field interference. A dual-band antenna element was designed with modified K-shaped patch arms, achieving resonances at 27 GHz and 28 GHz. The MIMO antenna design process included multiple configurations. The baseline 2×2 MIMO array exhibited high mutual coupling (-13 dB). To mitigate this, metallic vias were introduced, reducing surface wave coupling and improving isolation to -22 dB. Further enhancement was achieved by integrating a metasurface above the MIMO2 antenna which reduced coupling to below -30 dB across both operating bands. Fabricated prototypes were evaluated and measurements were performed in an anechoic chamber. This technique of combining metallic vias and metasurface in compact spacing has not been previously reported in literature, and represents the first implementation of such a technique. These reduction techniques demonstrated excellent results and can be implemented further in mmWave MIMO antenna designs.

Acknowledgments

Completing this PhD has been a long and challenging journey, and I am deeply grateful to the many individuals who have supported me along the way.

First and foremost, I express my deepest gratitude to my supervisor, Professor Mohammad Hashmi, for his invaluable guidance, patience, and unwavering support throughout this research. His expertise and encouragement have been instrumental in shaping this work.

I am also profoundly grateful to my internal co-supervisor, Professor Galymzhan Nauryzbayev, and my external co-supervisor, Professor Francisco Falcone, for their insightful feedback, technical expertise, and constant motivation, which significantly contributed to the success of this thesis.

I gratefully acknowledge the fully funded scholarship from Nazarbayev University, which provided me with the financial support and resources necessary to dedicate myself fully to this research and pursue my academic aspirations.

My deepest appreciation goes to my family for their unconditional love, patience, and unwavering encouragement. Their emotional support has been my greatest source of strength throughout this journey.

I would also like to thank my lab mates and colleagues for their discussions and moral support.

Finally, to everyone who has contributed, directly or indirectly, to my academic and personal growth—thank you. Your kindness, advice, and encouragement have meant more than words can express.

Contents

List of Tables

List of Figures

List of Abbreviations

5G	Fifth-Generation
ADS	Advanced Design System
AI	Artificial Intelligence
AMC	Artificial Magnetic Conductor
AR	Axial Ratio
BW	Bandwidth
CMA	Characteristic Mode Analysis
CP	Circular Polarization
CST	Computer Simulation Technology
DGS	Defected Ground Structure
DG	Diversity Gain
DUT	Device Under Test
EIRP	Effective Isotropically Radiated Power
EBG	Electromagnetic Band Gap
ECC	Envelope Correlation Coefficient
EM	Electromagnetic
FCC	Federal Communications Commission
FSS	Frequency Selective Surface
HIS	High Impedance Surface
ICNIRP	International Commission on Non-Ionizing Radiation Protection
IEEE	Institute of Electrical and Electronics Engineers
IoMT	Internet of Medical Things
IoT	Internet of Things
ISM	Industrial, Scientific, and Medical
LHCP	Left Hand Circular Polarization
LM	Link Margin
LOS	Line of Sight

MIMO	Multiple Input Multiple Output
MISO	Multiple Input Single Output
ML	Machine Learning
mmWave	Millimeter-Wave
MS	Modal Significance
MTM	Metamaterials
MTS	Metasurface
NLOS	Non Line of Sight
OTA	Over The Air
PCB	Printed Circuit Board
PDMS	Polydimethylsiloxane
PEC	Perfect Electric Conductor
PMC	Perfect Magnetic Conductor
Q	Quality Factor
RF	Radio Frequency
SAR	Specific Absorption Rate
SISO	Single Input Single Output
SNR	Signal to Noise Ratio
VNA	Vector Network Analyzer
WBAN	Wireless Body Area Network

Chapter 1

Introduction

1.1 Millimeter wave antenna systems

The advancement of wireless communication in the (IoT) technology has increased the requirements of faster data transfer with reduced latency, and seamless connectivity in lower power devices [1]. Conventional and already established technology operating within the sub-6 GHz spectrum are increasingly congested and have bandwidth limitations, thus impeding efficient support for next-generation IoT applications [2]. To address these challenges, alternative frequencies such as millimeter-wave (mmwave) have been suggested [3]. The mmWave band offer substantially wider bandwidths and higher data rates, thereby has potential as a promising solution for fifth-generation (5G) and IoT wireless networks. However, the implementation and utilization of mmWave band posses significant challenges. Owing to the shorter wavelengths, the mmWave are significantly sensitive to higher propagation losses, atmospheric absorption, and blockage by physical obstacles [4].

Addressing the obstacles in mmWave communication necessitates the development of advanced antenna designs [5]. Antennas constitute critical elements in communication systems, facilitating the transformation of signals into electromagnetic (EM) waves for transmission and capturing incoming signals for reception. Different antenna typologies such as single-input single-output (SISO), multiple-input single-output (MISO), single-input multiple-output (SIMO), and multiple-input multiple-output (MIMO) are widely used for communication [6]. SISO is the most basic one where single antenna is used for both the transmission and reception. While it offers low hardware complexity and power consumption, it suffers from poor spectral efficiency, limited data rates, and vulnerability to fading. To overcome these limitations, multiple antennas at transmitter while single at receiver is used in a MISO system. This technique significantly improves signal reliability. However, it does not benefit from receive diversity, making it less effective in mitigating deep fades at the receiver end. Alternatively, a single transmitting antenna and multiple receiving antennas are used in a SIMO system. This approach improves link reliability and reception quality, but it does not take full advantage of spatial multiplexing, which limits its capacity improvement. Therefore, in MIMO antenna systems, multiple antennas are utilized at both the transmitter and receiver and has proved to be most reliable type of communication. It can increase channel capacity and improves spectral efficiency, and provides an efficient

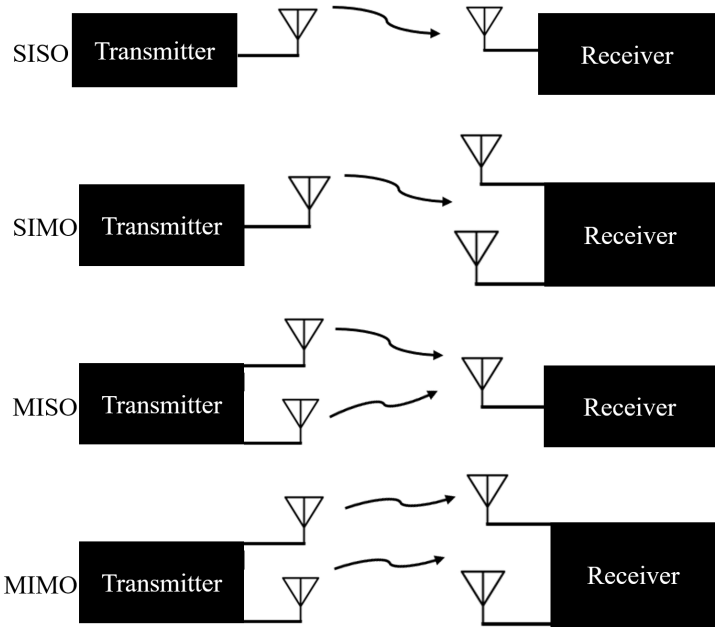

Figure 1.1: Overview of different antenna systems in a communication network.

communication even in severe fading environments [7]. Thus, MIMO antenna design is particularly beneficial in mmWave communication, where high directivity and massive MIMO techniques help compensate for severe propagation losses. Nevertheless, MIMO technologies come with increased complexity and higher energy consumption, rendering the implementation process more challenging. Fig. 1.1 shows antenna usage in communication systems, depicting various antenna configurations at both the transmitting and receiving sides.

In general, the choice of a suitable antenna setup in a communication system is typically determined by the specific application requirements and system limitations. While SISO remains suitable for low-complexity applications, MISO and SIMO provide diversity enhancements, and MIMO offers the best trade-off between capacity, reliability, and spectral efficiency for advanced applications such as 5G and beyond [8].

Despite the significant potential, implementing MIMO antenna in mmWave band communication presents several challenges, particularly from the design perspective [9]. One of the most critical issue in MIMO antenna is the presence of mutual coupling and less isolated antenna elements. This phenomenon occurs primarily when EM energy from one antenna element interferes with adjacent elements [10]. As the wavelength of mmWave frequencies is considerably smaller, ranging from 10 mm to 1 mm depending on the frequency, antenna elements become smaller, approximately the size of the wavelength or even less. Consequently, half-wavelength spacing between antenna elements results in significantly higher mutual coupling at mmWave frequencies. These increased antenna element interaction deteriorate the overall MIMO system performance, leading to issues such as reduced gain, poor impedance matching, and distorted radiation patterns. Addressing these challenges necessitates more innovative

antenna designs that minimize mutual coupling and enhance isolation within a compact space [11], [12]. Therefore, in this thesis, the primary focus is on developing mmWave MIMO antennas characterized by high isolation. The mutual coupling reductions methods have been comprehensively explored and employed in the antenna design process to enhance the performance and minimize interference between antenna elements.

Furthermore, MIMO antenna designs for mmWave IoT applications should follow certain design constraints. The increasing miniaturization demand for low-power portable and wearable devices requires antennas that not only exhibit superior performance but also possess characteristics such as lightweight, low profile, flexibility, and ease of integration into transmitters or receivers without introducing undue complexity [13]. Additionally, the production methods for MIMO antennas need to be cost-effective and suitable for mass production to meet commercial and industrial demands [14].

The mmWave spectrum offers new opportunities for the latest IoT technologies, like wireless body area network (WBAN) [15]. WBAN links wearable or implanted medical devices and can be used for continuous health monitoring in real-time. These networks facilitate the continuous tracking of vital signs and transmission of data to medical professionals for evaluation and diagnosis. By integrating mmWave MIMO antennas, WBANs can deliver faster data transfer, minimize latency, and enhance signal stability, thus ensuring uninterrupted communication even during body movement [16].

1.2 Motivation

MIMO antenna technology is critical for enhancing spectral efficiency, signal quality, and supporting high-capacity in mmWave band. However, designing compact MIMO antennas presents significant challenges of mutual coupling between closely placed antenna elements. This impact the antenna system performance, increase field correlation, and introduce interference, making effective decoupling strategies imperative. Several methodologies have been proposed to reduce mutual coupling, but each method comes with inherent drawbacks that limit its effectiveness in compact and high-performance mmWave MIMO designs. Parasitic shape elements have been used to reduce mutual coupling between antenna [17], [18], [19], [20], [21], [22]. However, these structures significantly increase the dimensions and are not suitable for compact and flexible designs in low power devices. Additionally, they may introduce unwanted resonance frequencies and impact the antenna's characteristics. Neutralization lines, another widely adopted method, work by introducing transmission lines to counteract coupling currents between adjacent elements [23], [24], [25], [26], [27], [28]. While these lines can enhance isolation, their effectiveness is highly dependent on precise

tuning, and any deviation in their design can lead to impedance mismatches, bandwidth degradation, or complex feed network integration. Decoupling networks have been utilized to suppress coupling by introducing lumped or distributed circuit elements[29], [30], [31]. However, these networks increase the complexity of the overall design, consume additional space, and may introduce unwanted losses, impacting the radiation efficiency and bandwidth of the MIMO system.

Considering the limitations constraints of traditional decoupling methods, this research is motivated by the necessity to create innovative approaches that successfully reduce mutual coupling while preserving a compact, efficient, and high-performing MIMO antenna system. Frequency Selective Surfaces (FSS) offer an effective approach by acting as band-reject or band-pass filters, selectively suppressing unwanted EM interactions between antenna elements. By optimizing FSS structures, this research aims to achieve significant isolation enhancement while maintaining the compact nature of the MIMO system. Another approach of utilizing metasurface has been introduced which offer precise manipulation of EM wave propagation. Additionally, their compatibility with flexible and conformal designs makes them ideal for wearable applications. Defected Ground Structures (DGS) modify the current distribution in the ground plane, thereby disrupting surface waves and reducing unwanted coupling between antenna elements. DGS structures have been introduced into MIMO antennas without major modifications to the radiation elements, preserving compactness while enhancing isolation. Metallic vias serve as vertical interconnects that suppress unwanted coupling paths by creating an artificial EM barrier between antenna elements. Thus this research aims to advance the development of next-generation MIMO antennas by addressing the critical issue of mutual coupling through enhanced decoupling techniques. Unlike most existing studies that focus solely on reducing mutual coupling, this research not only addresses coupling reduction but also implements the designed antennas in practical applications, specifically in WBAN systems, where promising results have been achieved.

1.3 Objectives

The primary objectives of this research are summarized as follows:

1. To design and develop a compact and high-performance MIMO antenna system that effectively integrates decoupling techniques such as FSS, DGS, metallic vias, and metasurfaces to achieve enhanced isolation and minimize mutual coupling.

2. To analyze and optimize the impact of mutual coupling on antenna performance, particularly in wide and dual-bands at mmWave.

3. To investigate the feasibility of integrating the designed MIMO antennas into practical applications, particularly in WBAN, while ensuring structural flexibility, low profile, and minimal interference from human-body interactions.

4. To evaluate and compare the proposed decoupling techniques in terms of isolation performance, bandwidth, efficiency, and fabrication feasibility, against other designs present in literature.

5. To fabricate and experimentally validate the designed MIMO antenna system by measuring key performance parameters such as S-parameters and radiation patterns, and to assess its effectiveness in real-world applications.

1.4 Key contributions

The key contributions of this research are as follows:

1. A significant contribution is the development of a compact four-element mmWave MIMO Vivaldi antenna specifically designed for wearable WBAN applications. The end-fire radiation pattern has been specifically utilized for device-to-device communication in WBAN. The design incorporates an FSS to enhance inter-element isolation, achieving isolation levels exceeding -20 dB while maintaining a low profile and high efficiency. Furthermore, the antenna exhibits a wide impedance bandwidth encompassing 24.25 to 27.50 GHz (n257) and 26.50 to 30 GHz (n258), ensuring compatibility with 5G mmWave communication. The MIMO antenna's performance was validated through on-body measurements on a human model, demonstrating stable gain, efficiency, and low absorption, thus establishing its suitability for WBAN applications.

2. A six-element dual-band mmWave MIMO antenna with an enhanced inter-element isolation technique for WBAN applications, thus advancing the state-of-the-art. The distinctive characteristic of this MIMO antenna is its functionality in two distinct mmWave bands: specifically, the 23.63–32.90 GHz and 36.68–40 GHz frequency bands. These bands have been licensed for the ISM and 5G NR bands. This antenna design incorporates a hybrid approach of DGS and a FSS to effectively suppress mutual coupling, achieving isolation levels of -33 dB, which is significantly higher than conventional techniques. Furthermore, the antenna exhibits a broadside radiation pattern with a high realized gain of approximately 9 dBi across the operating bands, along with excellent diversity results. The safety analysis of the antenna confirms compliance with on-body exposure limits for both 1 g and 10 g tissue standards. Additionally, the antenna underwent

experimental evaluation in a WBAN communication scenario, demonstrating an acceptable link margin and confirming its suitability for high-speed and reliable body-centric wireless communication systems.

3. Another significant contribution of this research is the novel integration of metallic vias and a metasurface for mutual coupling reduction in a dual-band mmWave MIMO antenna. This design utilizes metallic vias to effectively suppress surface wave-induced coupling, while the metasurface mitigates near-field interactions, ensuring substantially improved isolation. This hybrid approach achieves coupling levels below -30 dB. The metasurface, designed with dual-band band-pass characteristics, introduces negative permeability while maintaining positive permittivity, thus altering the propagation characteristics of EM waves to suppress near field coupling. The antenna exhibits stable broadside radiation patterns, excellent diversity performance, and high isolation across the 26.75-27.28 GHz and 27.77-28.19 GHz bands.

1.5 Publication list

The findings of this research have been published in the following journals and conferences.

Journal papers

- **J. Ahmad**, M. Hashmi, A. Bakytbekov and F. Falcone, "Design and Analysis of a Low Profile Millimeter-Wave Band Vivaldi MIMO Antenna for Wearable WBAN Applications," *IEEE Access*, vol. 12, pp. 70420-70433, 2024. doi: 10.1109/ACCESS.2024.3401865.
- **J. Ahmad** and M. Hashmi, "Reduced Inter-element Interference mmWave MIMO Antenna and its Application in WBAN," *IEEE Access*. April 2025. doi: 10.1109/ACCESS.2025.3562632.
- **J. Ahmad**, M. Hashmi and F. Falcone "A Hybrid Technique for Mutual Coupling Reduction in a Compact Dual-Band Millimeter-Wave MIMO Antenna," *IEEE Antennas and Wireless Propagation Letters*. March 2025. doi: 10.1109/LAWP.2025.3555397.

Conference papers

- **J. Ahmad** and M. Hashmi, "Mutual Coupling Mitigation Through Parasitic Structure in a Dual-Band Millimeter-Wave Flexible MIMO Antenna,"

in *International Conference on Engineering and Emerging Technologies (ICEET)*, Dubai, United Arab Emirates, 2024, pp. 1-6.

- **J. Ahmad**, G. Nauryzbayev and M. Hashmi, "Design of a Compact Millimeter Wave Band Antenna for Smartwatch WBAN Applications" in *IEEE Asia-Pacific Microwave Conference (APMC)*, Bali, Indonesia, 2024, pp. 1111-1113.
- **J. Ahmad** and M. Hashmi, "Design of Multi-Band 8-Port MIMO Antenna With Pattern Diversity for IoT Applications," in *IEEE International Symposium on Antennas and Propagation and INC/USNC-URSI Radio Science Meeting (AP-S/INC-USNC-URSI)*, Firenze, Italy, 2024, pp. 2047-2048.
- **J. Ahmad**, M. Hashmi, G. Nauryzbayev and F. Falcone, "A Multi-Band Efficient Metamaterial Absorber for Millimeter-Wave Band WBAN Applications," in *IEEE International Symposium on Antennas and Propagation and INC/USNC-URSI Radio Science Meeting (AP-S/INC-USNC-URSI)*, Firenze, Italy, 2024, pp. 1777-1778.
- **J. Ahmad** and M. Hashmi, "A Compact MIMO Antenna for WBAN Applications at Millimeter-Wave Frequencies," in *31st Telecommunications Forum (TELFOR)*, Belgrade, Serbia, 2023, pp. 1-4.
- **J. Ahmad**, M. Hashmi, G. Nauryzbayev and D. Rano, "Skin Cancer Detection Reflectometry Technique Using Millimeter-wave Antipodal Vivaldi Antenna," in *IEEE International Symposium On Antennas And Propagation (ISAP)*, Kuala Lumpur, Malaysia, 2023, pp. 1-2.
- **J. Ahmad**, M. Hashmi and G. Nauryzbayev, "Fabry–Perot Cavity Based Decagonal Shape Patch Antenna for Millimeter-Wave Band Applications," in *International Symposium on Networks, Computers and Communications (ISNCC)*, Doha, Qatar, 2023, pp. 1-4.

1.6 Thesis outline

The remaining parts of this thesis are organized as follows:

Chapter 2 is a comprehensive examination of the theoretical foundations and background studies related MIMO antenna systems. In addition, important parameters such as scattering, mutual coupling, bandwidth, gain, far-field, and efficiency are succinctly elucidated. Furthermore, the chapter offers a detailed exposition on mutual coupling and the significance of decoupling techniques. Moreover, the current challenges in mmWave MIMO antennas are delineated. Additionally, fundamental

diversity parameters, including total active reflection, correlation, and diversity gain are explained.

Chapter 3 presents the design, analysis, and experimental validation of a low-profile mmWave Vivaldi MIMO antenna for WBAN application. The chapter commences with an examination of the challenges associated with mutual coupling, on-body signal degradation, and compact antenna integration in WBANs. Initially, the design of a single element Vivaldi antenna is explained. The extension from single element to four element MIMO is subsequently discussed. A comprehensive analysis of the FSS design and its integration into the existing MIMO antenna is thoroughly elucidated. Following the development of a highly isolated MIMO antenna, on-body analysis is conducted, wherein investigations of various antenna parameters are performed. The final MIMO antenna is subsequently fabricated and experimentally evaluated on a human phantom to validate its on-body performance.

Chapter 4 explains the design, analysis, and optimization of a dual-band six-element MIMO antenna. The design process begins with an individual antenna element, carefully optimized for operation at dual mmWave bands. The progression from a single-element structure to a six-element MIMO array is subsequently explained. To mitigate mutual coupling, hybrid decoupling techniques of DGS and FSS are implemented and thoroughly explained. A comparative study is conducted to evaluate the impact of these techniques on key performance metrics such as S-parameters, gain, efficiency, and radiation patterns. The integration of these techniques demonstrates significant performance enhancements over conventional MIMO antenna designs. Furthermore, the fabrication and measured results analysis are explained. A real-world communication scenario of the designed MIMO antenna is explained and compared with a dipole for communication. Finally, the link margin analysis of the designed MIMO antenna is thoroughly investigated.

Chapter 5 demonstrates the design, analysis, and optimization of a dual-band MIMO antenna. This chapter particularly focuses on improving isolation. To overcome mutual coupling limitations, the designed MIMO antenna incorporates metallic via and metasurface -based decoupling approach. It is noteworthy that metallic vias were particularly utilized for surface waves reduction where as metasurface is used for near-field interactions. The integration of metasurfaces and metallic vias demonstrates significant performance improvements compared to conventional decoupling techniques.

Chapter 6 provides a brief summary of the overall research conducted and suggests future directions for further investigations.

Chapter 2

Literature Review

A communication system has a fundamental role in modern development as it is used for sending information over a given channel. A typical communication system consists of three key components: a transmitter, a communication channel, and a receiver, as depicted in Fig. 2.1. The transmitter processes the input information through modulation, amplification, and impedance matching before sending it to a channel via an antenna. The signal then propagates through the wireless channel (air), where it is subjected to attenuation, interference, and noise. The receiver antenna captures the incoming signal, which is then amplified, mixed with a local oscillator, and demodulated to retrieve the originally transmitted information. The antenna has a vital role in wireless communication systems as it is used for transmitting and receiving the maximum amount of information. Therefore, this chapter presents a comprehensive review of advanced antenna design techniques such as MIMO, mutual coupling reduction techniques in MIMO antennas at mmWave band, and implications for contemporary wireless communication systems, including applications in WBANs and IoT.

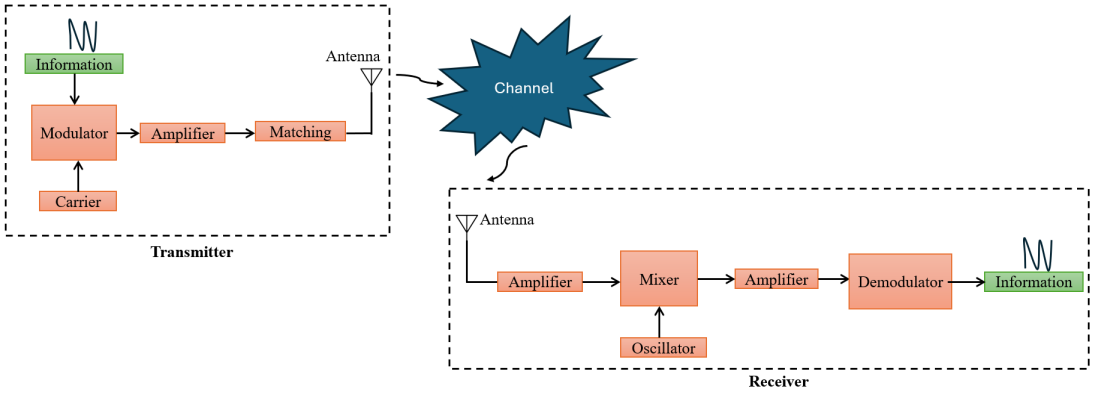

Figure 2.1: A generalized communication system modules.

2.1 The mmWave frequency band

The mmWave band is part of electromagnetic spectrum which spans from 30 GHz to 300 GHz, as illustrated in Fig. 2.2. However, the range between 24 GHz and 100 GHz is most commonly employed for modern mmWave band communication. In comparison with frequencies below 6 GHz, the mmWave band provides significantly higher data

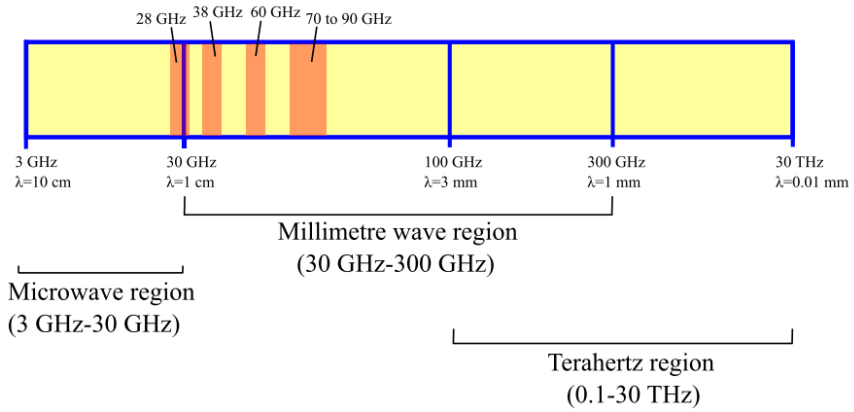

Figure 2.2: Illustration of the electromagnetic wave spectrum [32].

transmission rates, improved spectral efficiency, and less network congestion, making them an attractive option for 5G and futuristic IoT technologies.

A comparison between mmWave and lower-frequency bands in terms of key performance metrics is provided in 2.1.

Table 2.1: Comparison of mmWave and Sub-6 GHz band

Feature	**mmWave Band**	**Sub-6 GHz Band (Below 6 GHz)**
Data rate	Very high (multi-Gbps)	Moderate (Mbps–Gbps)
Spectral efficiency	High due to wide bandwidth	Limited by congestion
Path loss	High (rapid attenuation)	Lower (better propagation)
Penetration ability	Poor (blocked by walls and objects)	Strong (good outdoor coverage)
Antenna size	Small (wavelength is shorter)	Larger (longer wavelength)
Multipath effects	Severe (requires beamforming)	Moderate (fewer losses)
Interference	Lower (less congestion)	Higher (more occupied spectrum)
Applications	6G/5G, WBANs, IoT, satellite	LTE, Wi-Fi, traditional mobile networks

While the mmWave spectrum offers numerous benefits, its significant signal attenuation and limited penetration capabilities require the implementation of advanced technologies. These include MIMO systems and metasurface-based solutions to enhance the communication performance in this challenging frequency band.

2.2 MIMO technology

The MIMO technology uses multiple antennas at both transmitter and receiver side. This technique produce more than one data streams from transmitter which is received by multiple antennas at the receiver. A depiction of this technique is shown in Fig. 2.3

The received signal at each receiving antenna in an $N_t \times N_r$ MIMO system can be expressed as shown in Equations (2.1)–(2.3). Here, R_{N_r} and T_{N_t} denote the signals

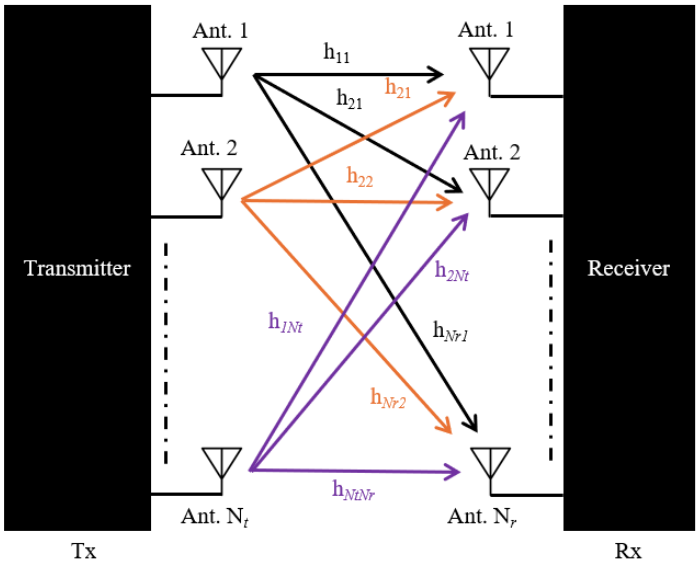

Figure 2.3: Configuration of a MIMO antenna system.

received and transmitted by the N_r receiving antennas and N_t transmitting antennas, respectively. The term $h_{N_rN_t}$ represents the channel coefficient that characterizes the transmission path between each transmitting and receiving antenna, while n_{N_r} accounts for the noise introduced at the receiver. The received signal model demonstrates that each receiving antenna captures a superposition of signals transmitted across multiple independent paths. This multi-path propagation is a fundamental principle of MIMO technology [32].

$$R_1 = (h_{11} \cdot T_1 + h_{21} \cdot T_2 + \cdots + h_{1N_t} \cdot T_{N_t}) + n_1 \tag{2.1}$$

$$R_2 = (h_{21} \cdot T_1 + h_{22} \cdot T_2 + \cdots + h_{2N_t} \cdot T_{N_t}) + n_2 \tag{2.2}$$

$$R_{N_r} = (h_{N_r1} \cdot T_1 + h_{N_r2} \cdot T_2 + \cdots + h_{N_rN_t} \cdot T_{N_t}) + n_{N_r} \tag{2.3}$$

The Shannon-Hartley theorem establishes the theoretical upper bound on data rate as a function of bandwidth and signal-to-noise ratio (SNR). In the case of a SISO system, the achievable channel capacity C in bits per second (bps) is given by:

$$C = B.W \log_2(1 + SNR) \tag{2.4}$$

where $B.W$ is the system bandwidth/ This equation indicates that capacity can be increased by expanding bandwidth or improving SNR. However, due to the logarithmic dependence on SNR, capacity improvements diminish at high SNR levels, leading to saturation. Beyond a certain point, increasing transmitted power does not significantly enhance capacity, making this approach inefficient. Alternatively, increasing bandwidth

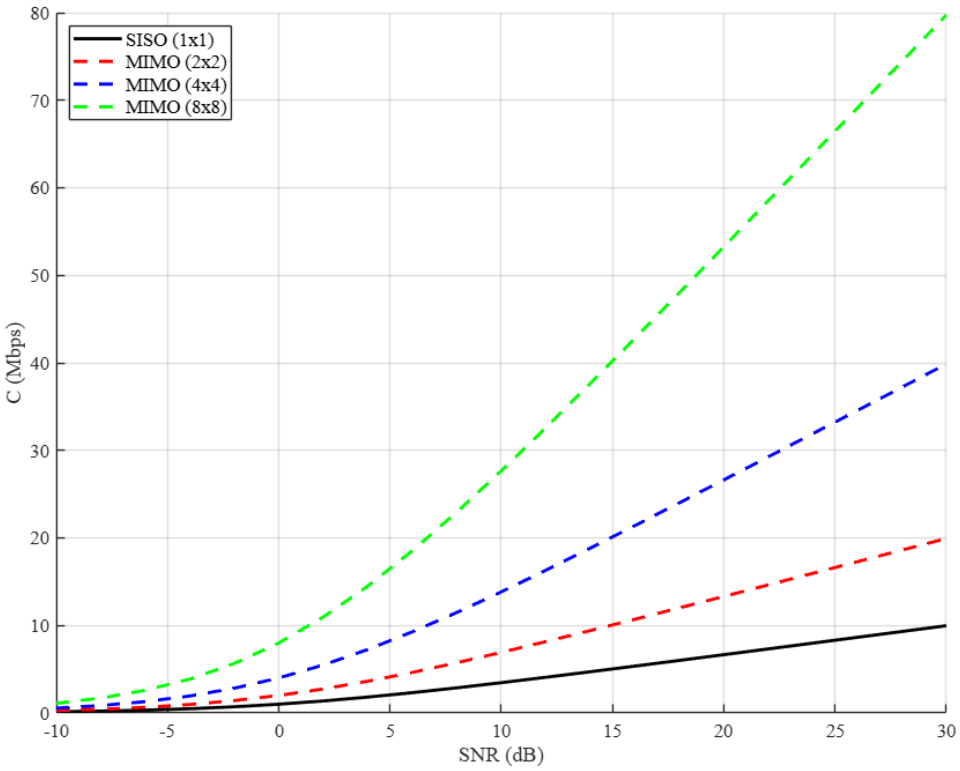

Figure 2.4: Comparison of SISO and MIMO channel capacity.

can enhance capacity, but practical constraints such as high spectrum acquisition costs and regulatory restrictions on transmission power limit the feasibility of this approach.

MIMO technology significantly enhances capacity compared to SISO systems by using multiple independent transmission paths. The channel capacity of a MIMO system can be expressed as [33]:

$$C = B.W \log_2 \det \left(I + \frac{SNR}{N_t N_r N_0} H H^H \right) \tag{2.5}$$

where SNR is the signal to noise ratio, N_t and N_r correspond to the number of transmitting and receiving antennas, respectively, and N_0 represents the noise power spectral density. The term H^H denotes the Hermitian transpose of the channel matrix H, and I is the identity matrix. The equation 2.5 highlights the determinant-based capacity scaling, demonstrating that how MIMO technique use spatial channels to enhance performance. At high SNR, the capacity of a MIMO system can be approximated as:

$$C \approx N_t B.W \log_2(1 + SNR) \tag{2.6}$$

Equation 2.6 reveals that capacity scales linearly with the number of transmit antennas, unlike SISO, which follows a logarithmic increase. Assuming a 1 MHz bandwidth, the comparison between SISO and MIMO capacity is depicted in Fig. 2.4. It is evident that capacity increases significantly as the number of antenna elements

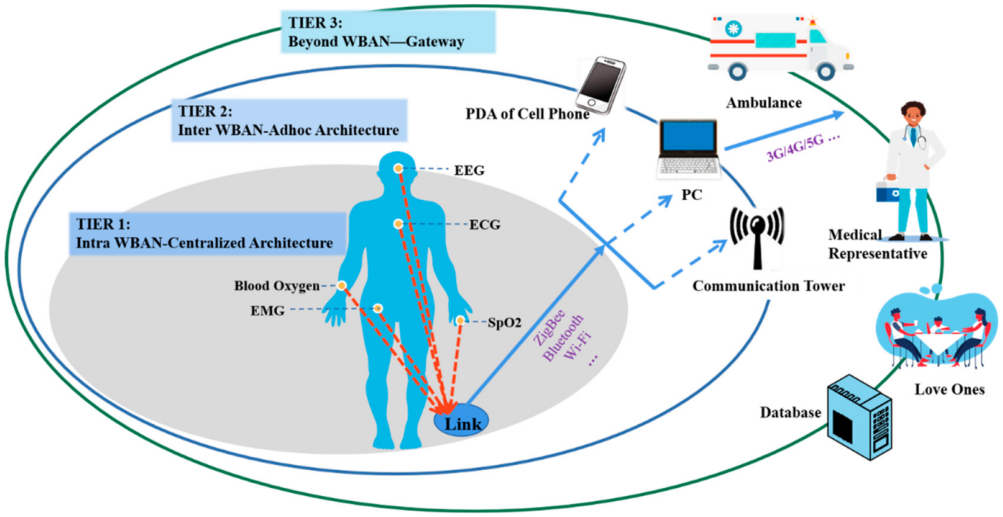

Figure 2.5: Different communication tiers in WBAN system [40].

grows, demonstrating that MIMO is a highly effective technique for improving data rates in wireless communication systems.

2.3 Applications of MIMO antennas

MIMO antennas have been extensively used in many applications, including wireless networks such as 5G and 6G [34], [35], satellite communications [36], and vehicular networks [37]. Moreover, MIMO technology plays a crucial role in IoT and wearable devices [38], [39]. In alignment with the thesis, the applications of MIMO antennas in mmWave WBAN are examined herein.

2.3.1 Introduction to WBAN

The WBAN consists of wearable and implanted devices that monitor physiological data such as heart rate, blood pressure etc. This information is subsequently transmitted to external healthcare professionals or physicians. WBANs improve patient care through continuous monitoring, early detection of health issues, and tailored treatment plans, while reducing the frequency of hospital visits. The communication within a WBAN can be categorized into several tiers [40], as illustrated in Fig. 2.5.

The Tier 1 or intra WBAN is human body centralized architecture which is particularly designed to gather physiological information from multiple sensors positioned on or inside the human body. These sensors mostly monitor EEG, ECG, SpO_2, and EMG behaviours. The sensed data is then sent to a central hub which usually is a wearable compact device. In Tier 2, the communication between the centralized hub and external devices such as a personal digital assistant (PDA) or a mobile phone

is established. This connection extends the communication beyond the body and is utilized for real-time data transmission to local devices such as a personal computer (PC) or local tower. This tier ensures that the data collected within the WBAN is accessible for preliminary analysis, storage, or forwarding through intermediate device communication, thus being widely recognized as inter-WBAN ad hoc architecture. In Tier 3, the sensed data from the body sensors is further transmitted through a communication tower using communication networks to remote locations such as hospitals, medical representatives, emergency services (ambulances), and even family members. This tier ensures that patient data is accessible to healthcare providers for real-time monitoring, diagnosis, and immediate intervention when necessary. Additionally, the data of users are also stored in centralized databases for the future analysis and provide also remote access for authorized personnel.

It is imperative to note that, although WiFi and Zigbee are well-established technologies, they face challenges, particularly for future advancements in the medical field [41]. WiFi is currently prone to saturation due to the fact that many devices are using this band, which has become congested. Moreover, WiFi's high power requirements make it unsuitable for wearable and body-centric applications. Alternatively, Zigbee consumes less power but has limited data transfer speeds and short range. Owing to these shortcomings, it will not meet the required high-speed data transmission in real-time monitoring in WBAN systems. These challenges will limit the capacity of WBAN communication [42].

A promising approach to answer these issues involves implementing mmWave MIMO antennas in WBANs. As previously discussed, the mmWave spectrum provides substantially greater bandwidth, faster data rates, and reduced latency. Simultaneously, MIMO antennas increase the channel capacity of communication. This combination of mmWave and MIMO antenna systems will support real-time monitoring, uninterrupted data transmission, and robust connectivity, even in dynamic and interference-prone environments. As a result, this approach effectively addresses the shortcomings of current wireless technologies in WBAN applications.

2.4 Challenges in mmWave MIMO antenna design

Several fundamental design challenges persist in implementing MIMO antennas for mmWave WBAN systems:

2.4.0.1 Challenges

1. **High path loss:** The substantial free-space attenuation experienced by mmWave frequencies necessitates the implementation of high-gain antenna designs to

maintain signal strength.

2. **Human body interaction:** Due to their shorter wavelengths, mmWave frequencies are only absorbed by the outer layers of skin, causing the human body to act as both an absorber and a reflector when MIMO antennas are placed on it. This interaction may potentially result in a decrease in signal quality.

3. **Antenna miniaturization:** As wavelengths become shorter antenna components shrink in size which is advantageous for miniaturization but introduces significant design challenges that complicate achieving desired radiation patterns, gain and efficiency.

4. **Mutual coupling:** When MIMO antenna elements are positioned in close proximity to maintain compactness, mutual coupling can occur. Consequently, effective isolation techniques are necessary to mitigate this effect.

5. **Material selection:** It is essential to develop antennas using substrates that are low in loss, flexible, and biocompatible. These characteristics are crucial for preserving antenna performance and ensuring user comfort.

6. **Bandwidth limitations:** Achieving wide bandwidths necessary for high data rates is challenging due to the inherently narrowband nature of many mmWave antenna designs.

7. **Environmental sensitivity:** The performance of antennas can be greatly affected by external conditions such as humidity, clothing, and user movement, making them highly susceptible to interference.

8. **Regulatory compliance:** mmWave MIMO antennas for WBANs must adhere to international standards for electromagnetic exposure and communication protocols. These standards include the guidelines set by the International Commission on Non-Ionizing Radiation Protection (ICNIRP) and the IEEE C95.1-2019 standard.

These challenges and their corresponding solutions are illustrated in Fig. 2.6.

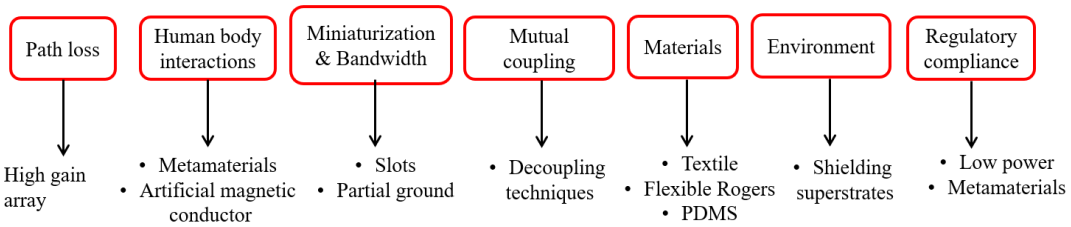

Figure 2.6: Challenges and its solution in literature.

2.5 Metamaterials and mmWave MIMO antenna designs

The signals experience free-space path loss due to rapid attenuation, which reduces communication range and signal strength at mmWave band. This phenomenon is particularly critical in WBANs, where antennas are in close proximity to the human body, which further absorbs and scatters the signals. Various antenna designs to enhance gain and improve performance in mmWave applications have been proposed. For instance, a study introduced a high-gain MIMO antenna array with enhanced isolation and decorrelated fields for 5G use, achieving a maximum gain of 12.5 dB and 91.5% radiation efficiency using a four-element configuration as shown in Fig. 2.7 [43].

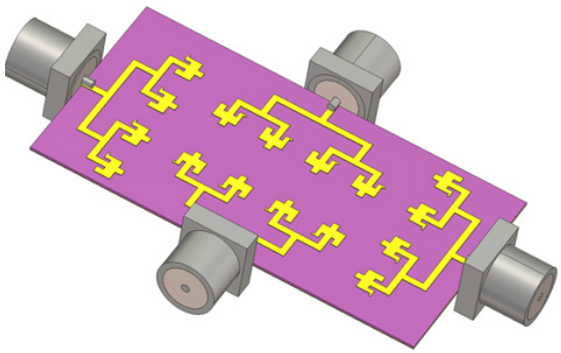

Figure 2.7: High gain four element MIMO antenna array [43].

An alternative method utilized a broadband, high-gain circularly polarized antenna array based on a substrate-integrated cavity structure [44]. This antenna achieved a peak gain of 26.10 dBic at 29.00 GHz, demonstrating its applicability in mmWave systems. Additionally, a dual-band end-fire MIMO antenna array incorporating a split-ring structure is proposed, achieving gains of 9.8 dB and 8.7 dB at its respective resonant frequencies while maintaining high radiation efficiency. [45]. Other antenna designs include graphene based designs [46], elliptical shape [47] and modified patch [48]. These antenna designs demonstrate the diverse approaches employed to enhance gain and efficiency in mmWave MIMO arrays, which are essential for the successful implementation of mmWave in 5G and future networks. However, it is imperative to note that with user movement, the high-gain antenna may lose line of sight due to the narrow beamwidth of the pattern. Thus, it is crucial to address these challenges when designing such antennas.

The human body significantly affects antenna performance by absorbing, reflecting, and scattering mmWave signals, which can degrade signal quality and reduce transmission efficiency. Additionally, the human body introduces high permittivity, causing impedance mismatch and increased losses.

2.5.1 Specific absorption rate (SAR)

One of the parameter to measure the absorption levels of human body is specific absorption rate (SAR). It investigates the absorption rate of electromagnetic energy by the human body when exposed to EM fields. This measurement is expressed in watts per kilogram (W/kg) and is defined in 2.7 [49]:

$$SAR = \frac{\sigma |E|^2}{\rho} \tag{2.7}$$

where σ is the conductivity of body tissue (S/m), $|E|$ is the electric field (V/m), and ρ is the mass density of body tissue (kg/m^3). SAR is a critical metric in WBANs and wearable devices, as prolonged exposure to high levels of electromagnetic radiation can cause tissue heating and potential health hazards. Regulatory bodies have established limits for acceptable SAR levels to ensure safety. The Federal Communications Commission (FCC) in the United States sets the limit at 1.6 W/kg averaged over 1 gram of tissue, while the International Commission on Non-Ionizing Radiation Protection (ICNIRP) recommends 2.0 W/kg averaged over 10 grams of tissue. Similarly, the IEEE C95.1 standard limits SAR to 1.6 W/kg, and the European Union Council enforces a 2.0 W/kg limit, both up to 300 GHz [50]. The SAR of a mobile handset antenna when placed near the ear on a head model at 28 GHz (left) and 38 GHz (right) is shown in Fig. 2.8. As can be seen at both frequencies, the SAR is under standard guidelines and maximum absorption is near to the hand region.

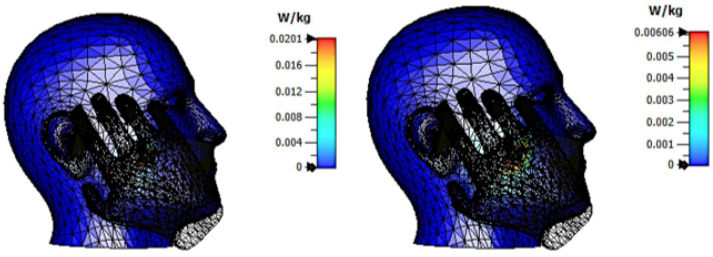

Figure 2.8: SAR of a mobile antenna [51].

In mmWave, although the penetration depth into human tissues is minimal, surface heating and skin absorption are significant concerns [52]. Techniques such as metamaterials based artificial magnetic conductors to reduce backward radiation are commonly employed. Additionally, low-loss substrates such as PDMS [53] or textile-based materials [54] are integrated to minimize surface wave effects and reduce SAR. These techniques are efficient and well-studied in the literature [55], [56] but fall outside the primary scope of this thesis. Therefore, metamaterial-based techniques for SAR reductions are primarily discussed.

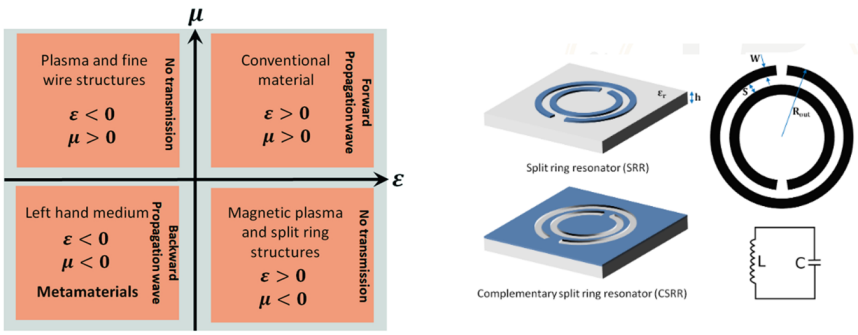

(a) (b)

Figure 2.9: MTMs (a) types and (b) structures.

2.5.2 Metamaterials

Metamaterials (MTMs) are artificially engineered three-dimensional structures designed to exhibit unique material properties that do not naturally occur in conventional materials. Unlike traditional materials, MTMs derive the properties from their structural design rather than the chemical composition.

In a conventional or natural material, the permittivity ε and permeability μ are positive. As shown in Fig. 2.9(a), MTMs can be classified into three types. If ε or μ are negative, it can be considered as single negative MTMs whereas when both are negative it can be considered as double negative MTMs. Negative ε is typically achieved using periodic arrays of thin metallic wires. When an external electric field is applied to these wires, they induce oscillating currents that oppose the incident field. This behaviour can be considered similar to free electrons in a plasma. This results in negative ε below a certain cut-off frequency (plasma frequency). The frequency-dependent permittivity can be approximated by 2.8 as follows:

$$\varepsilon(\omega) = 1 - \frac{\omega_p^2}{\omega^2} \tag{2.8}$$

where ω_p is the plasma frequency and ω is the operating frequency. For $\omega < \omega_p$, the effective permittivity becomes negative. Similarly, the negative μ is achieved using resonant structures such as split-ring resonators (SRRs) shown in Fig. 2.9(b). These SRRs behave like miniature LC circuits and resonate in response to the magnetic field component of incident EM waves. The circulating currents generated within the rings produce magnetic dipoles that oppose the incident magnetic field, resulting in an effective negative μ near the resonance frequency. When both ε and μ are negative over the same frequency range, the resulting refractive index also becomes negative (2.9).

$$n = \sqrt{\varepsilon\mu} \tag{2.9}$$

For negative ε and μ, the refractive index n becomes a real negative value. This leads to phenomena such as negative refraction, where EM waves bend in the opposite direction at structure interfaces [57], [58], [59].

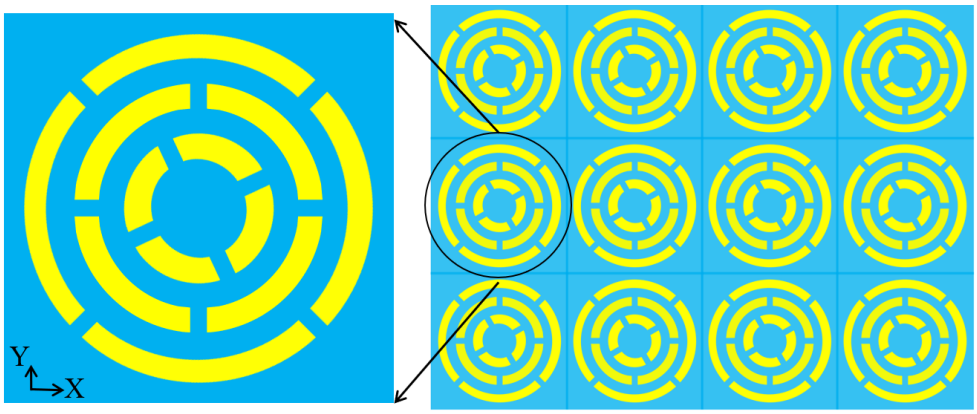

Figure 2.10: Design of a metasurface unit cell and array.

The applications of MTMs are diverse, ranging from invisibility cloaking devices that bend electromagnetic waves [60] to super lenses for advanced imaging [61]. Additionally, MTMs are utilized in sensors for improved biomedical and chemical detection [62], in systems for efficient wireless power transfer [63], and in various quantum technology applications [64].

Despite their potential, conventional 3D MTMs encounter several obstacles that hinder their widespread use in antenna design. A significant challenge lies in manufacturing process, which necessitates multiple layers and precise alignment, resulting in costly and time-intensive large-scale production. Furthermore, the nature of 3D metamaterials is bulky which makes them not suitable for wearable applications where flexibility is important. Another drawback is the substantial material losses at mmWave frequencies, which diminish their efficiency, particularly when integrated into compact systems like WBANs. Additionally, the increased thickness of 3D metamaterials introduces narrow bandwidths that limit wide-band performance [65].

In antenna design the use of metasurfaces (2D planar version of MTM) are mostly employed which is designed on a planner print circuit board (PCB) and do not require complex 3D fabrication facilities. Same like MTMs, the metasurfaces also consists of repeated sub-wavelength elements. In practice, first a unit cell is design with the required negative properties and then it is extended into desired array pattern normally in x or y directions as shown in Fig. 2.10. Recent advancements in metasurface technologies have significantly enhanced the performance of MIMO antennas, particularly in mmWave applications. Among these, some of the applications of metasurface can be broadly classified into six groups as shown in Fig. 2.11.

The artificial magnetic conductors (AMC) are engineered to produce in-phase reflections of electromagnetic waves. Unlike conventional metallic conductors that generate 180-degree out-of-phase reflections, AMCs reflect waves in phase, minimizing back radiation and increasing radiation efficiency. These structures are frequently utilized in MIMO antennas, particularly in compact and wearable systems where SAR

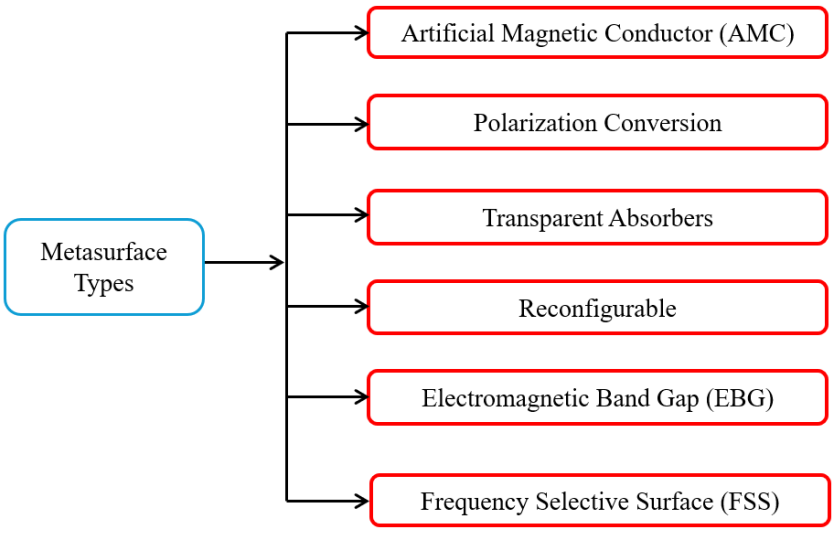

Figure 2.11: Types of metasurface according to applications.

is a critical consideration. The application of an AMC reflects the backlobes and constructively combines them with the main lobe, thereby reducing the SAR caused by backlobes. Additionally, it enhances the overall antenna gain. Fig. 2.12(a) illustrates an AMC-integrated fractal MIMO antenna [66]. The AMC structure significantly improved isolation, exceeding 27 dB, and increased gain by an average of nearly 55% dB throughout the operating band. This demonstrates the effectiveness of AMC-based metasurfaces in enhancing MIMO antenna gain. Another design, depicted in Fig. 2.12(b), AMC integration is specifically performed to reduce SAR. This technique has substantially reduced SAR by approximately 99% while maintaining a compact form factor [67]. It is essential to acknowledge that in WBANs, the integration of AMC layers comes with certain limitations. Firstly, incorporating AMC structures adds to the overall thickness of the antenna, which can be problematic for wearable and implantable applications where maintaining a compact and flexible form factor is crucial. Secondly, AMC structures can complicate the fabrication process and may alter the antenna's operational bandwidth due to user movement. Therefore, these factors must be carefully evaluated when designing AMC-based antennas for WBAN applications.

In addition to AMC, the gain can also be enhanced by employing a metasurface superstrate layer [68]. This method involves placing a near-zero refractive index-based metasurface at a central distance from the patch antenna, as illustrated in Fig. 2.13. The metasurface converts the radiating waves of the patches into planar waves by creating a Fabry-Perot cavity between the antenna and metasurface layers. The distance between the antenna and metasurface layer was varied, and its impact was observed. A summary of the effects on the antenna gain, efficiency, and voltage standing wave ratio (VSWR) is presented in Table 2.2. With the incorporation of the metasurface, the antenna gain was increased by 5.38 dBi at half wave length spacing, resulting in a total gain of 9.61

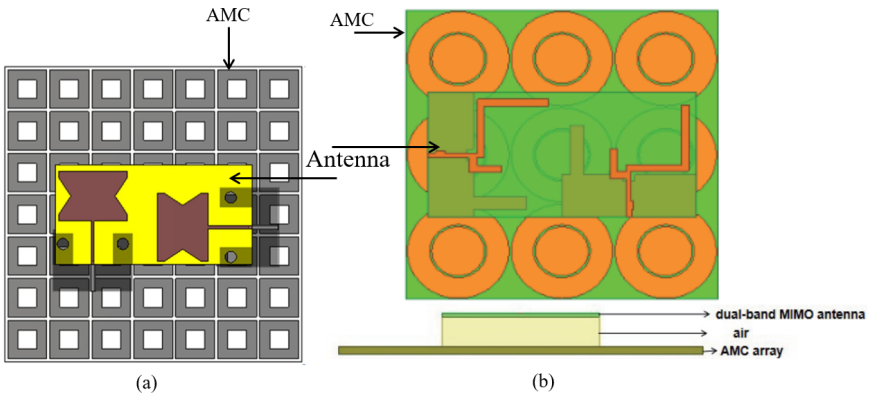

Figure 2.12: AMC backed MIMO antennas for (a) gain enhancement [66] and SAR reduction [67].

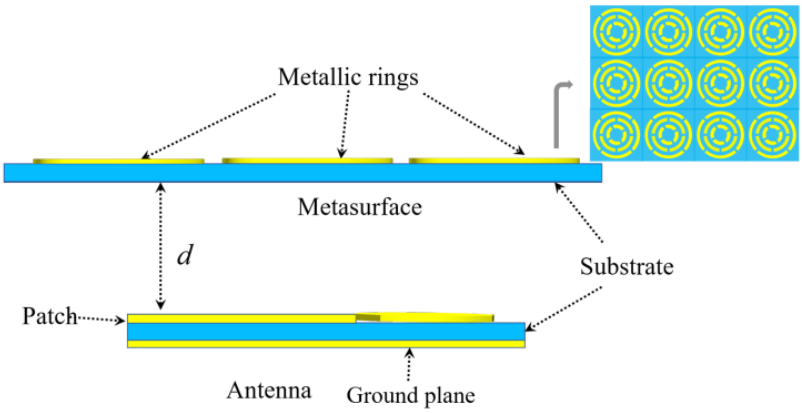

Figure 2.13: Gain enhancement of an antenna using superstate [68].

dBi. The total efficiency also improved from 0.69 to 0.93 without any notable increase in VSWR. Additionally, an enhancement of approximately 500 MHz in bandwidth was observed. These analysis show that superstrate and AMC layers are useful for increase gain in mmWave antenna designs.

Table 2.2: Impact of metasurface on antenna performance.

d (mm)	Gain (dBi)	Efficiency	VSWR
5.0	7.64	0.86	1.72
5.4	9.94	0.93	1.30
5.8	8.94	0.91	1.32
6.2	6.47	0.89	1.67
Antenna only	4.61	0.69	1.27
With metasurface ($d = 5.4$ mm)	9.94	0.93	1.30

Accordingly, the SAR can be reduced by employing a full ground plane and maintaining a specific distance between the MIMO antenna and the human body. In [69], a four-element MIMO antenna operating at 28 GHz was utilized for WBAN

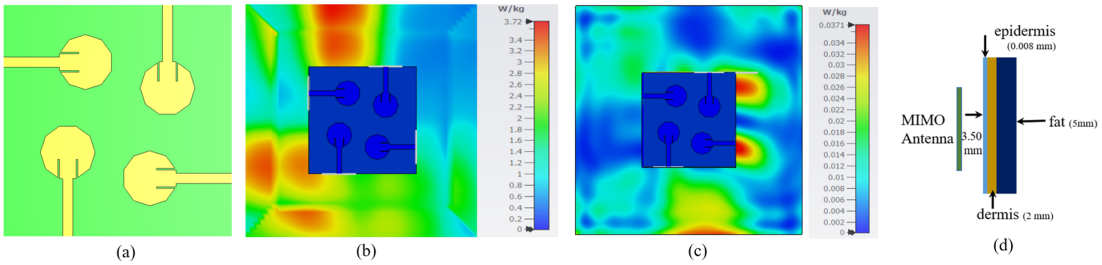

Figure 2.14: (a) MIMO antenna, (b) SAR without any space and (c) SAR with space. [68].

application and positioned on a three-tissue model comprising skin and fat layers, as illustrated in Fig. 2.14.

Two scenarios were investigated: one in which the antenna was placed directly on the tissue, and another where the antenna was positioned at a distance of 3.50 mm from the tissue. As evident from the SAR analysis in Fig. 2.14(b), elevated levels of SAR were observed. Despite the implementation of a full metallic ground plane, high levels of SAR were still detected due to increased main back lobe radiation. When the distance between the MIMO antenna and tissue model was increased, it was revealed that SAR levels were significantly reduced, indicating a decrease in back lobe penetration to the tissue model, which consequently lowered SAR values. It is noteworthy that most fabric is manufactured to this thickness, therefore, it can be suggested that this much gap can be accommodated by many daily usage clothing layers.

Polarization conversion is another type of metasurfaces that are used to manipulate the polarization of any electromagnetic wave. In particular, these metasurfaces are designed in a such a way that it converts any incoming linear polarized into circular polarization or it works apposite. By changing the phase response of electromagnetic waves, polarization conversion metasurfaces play a important role in enhancing the performance of antennas, particularly in MIMO antenna satellite systems. In [70], a highlghly efficient polarization conversion metasurface has been designed which converts both type of polarization i.e, linear to circular and circular to linear. As shown in Fig. 2.15(a), the unit cell design of this metasurface features an asymmetric structure that enables efficient polarization manipulation. Thus, high conversion efficiency in the Ku, K, and Ka frequency bands are achieved. Experimental results demonstrated that the metasurface maintains a polarization conversion ratio exceeding 90% across the targeted frequency ranges. This show its potential for applications in advanced communication systems and electromagnetic compatibility solutions. In a separate study, a wideband cross-polarized converter was designed on a flexible polydimethylsiloxane (PDMS) substrate as shown in Fig. 2.15(b) [71]. The design, comprising three layers with the PDMS substrate between resonating and ground layers, achieves linear-to-circular and circular-to-cross polarization conversions. It demonstrates over 99% polarization conversion ratio (PCR), ensuring high conversion efficiency. The device maintains a

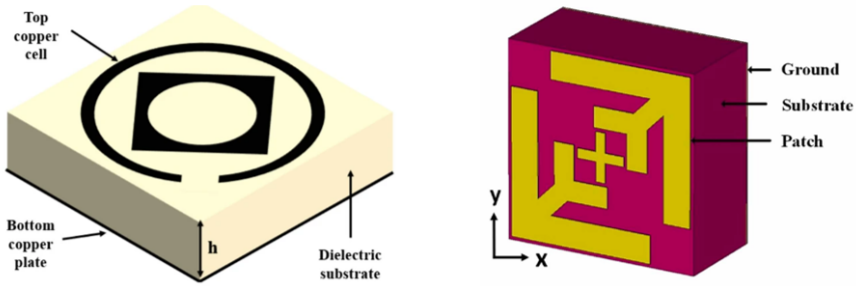

(a) (b)

Figure 2.15: PCR unit cells (a) triple band [70] and (b) PDMS based [71].

PCR above 99% for incidence angles from 0° to 60°, exhibiting strong angular stability, and retains performance under bending up to 60°. The study illustrates the metasurface's suitability for radar, antenna, and communication systems requiring high polarization purity and wide-angle performance [71].

Metasurface absorbers are two-dimensional engineered surfaces designed to achieve near-perfect absorption of electromagnetic waves by manipulating wave interactions at the sub wavelength scale. These structures typically consist of patterned metallic structures arranged on a dielectric substrate with a metallic ground plane to block full wave transmission. Their primary mechanism relies on impedance matching to free space, ensuring minimal reflection and maximum absorption [72]. Metasurface absorbers are widely utilized in energy harvesting, radar cross-section reduction, and wireless communication systems due to their compact size, lightweight properties, and ability to operate over multiple frequency bands. The absorption of a metasurface based absorber can be calculated using following equations.

$$A(\omega) = 1 - R(\omega) - T(\omega) \tag{2.10}$$

where $A(\omega)$ is the absorptivity, $R(\omega)$ is the reflectivity, and $T(\omega)$ is the transmissivity. For metasurface absorbers with a metallic ground plane, $T(\omega) = 0$, hence:

$$A(\omega) = 1 - R(\omega) \tag{2.11}$$

$$R = |S_{11}|^2 \tag{2.12}$$

where S_{11} is the reflection coefficient obtained from the scattering parameters. Similarly the absorber efficiency and quality factor can be formulated as:

$$\eta = \frac{P_{\text{absorbed}}}{P_{\text{incident}}} \tag{2.13}$$

here η is the absorption efficiency, P_{absorbed} is the absorbed power, and P_{incident} is the incident power.

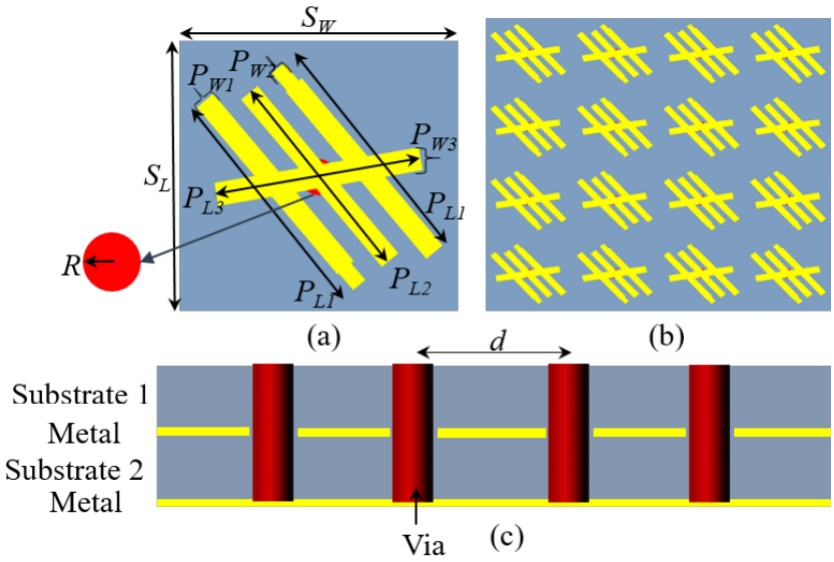

Figure 2.16: Multi-band absorber (a) unit cell, (b) array and (c) side view [73].

$$Q = \frac{\omega_0}{\Delta\omega} \tag{2.14}$$

where Q is the quality factor, ω_0 is the resonant frequency, and $\Delta\omega$ is the bandwidth.

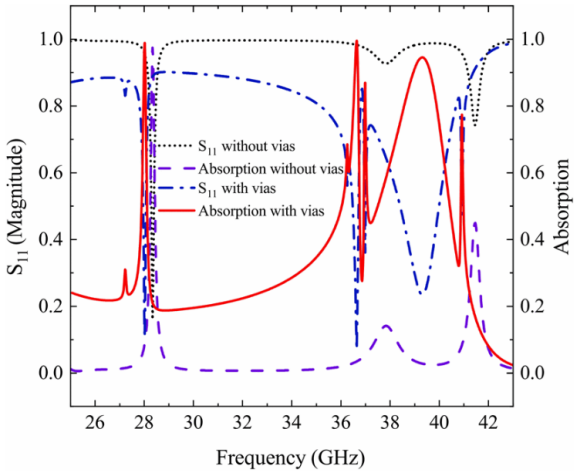

Figure 2.17: Reflection and absorption of the multi-band absorber.

Several studies have demonstrated the effectiveness of metasurface absorbers for mmWave applications. a dual-band metamaterial absorber operating at 28/38 GHz for 5G applications, achieving high absorption with a compact design [74]. Similarly, introduced a broadband microwave absorber optimized using multi-objective techniques, highlighting the potential for wideband performance. Additionally, a wideband microwave absorber incorporating E-shaped fractal metamaterials to enhance absorption in the mmWave band is developed [75] . These works illustrate the versatility of metasurface absorbers in achieving multi-band and broadband responses, crucial for modern communication systems.

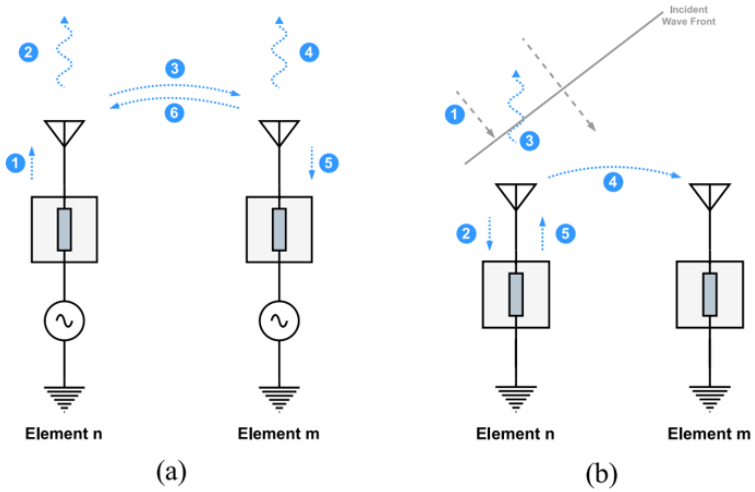

Figure 2.18: Mutual coupling interaction in (a) transmission and (b) reception modes.

Furthermore, a multi-band metasurface based absorber specifically designed for WBAN in the mmWave band is introduced [73] and is shown in Fig. 2.16. The absorber employs a multilayered structure with two Rogers RT5880 substrates and two copper layers. A critical innovation is the inclusion of metallic vias that connect the top patch to the ground plane without intersecting the first metal layer. Initially, a unit cell without and metallic via was designed but had only two bands near 28 GHz and 41 GHz. However the inclusion of metallic vias produced multi-band absorption capabilities. As shown in Fig. 2.17, the design achieves impressive absorption rates of 0.98, 0.99, and 0.94 at 28 GHz, 36.64 GHz, and 39 GHz, respectively. The absorber also exhibited double-negative permittivity and permeability properties. The unit cell parameters in mm were: $(S_W, S_L = 5.40, P_{L1} = 4.64, P_{L2} = 4.22, P_{L3} = 4.04, P_{W1} = 0.40, P_{W2} = 0.30, P_{W3} = 0.44, R = 0.70, d = 5.40)$. It is noteworthy that the unit cell was then converted into 4×4 array to have maximum rate of absorption.

2.6 Mutual coupling and its reduction techniques in mmWave MIMO antennas

When antenna radiating elements are positioned in close proximity in a MIMO antenna system, energy from one element is transferred to another. This phenomenon results in mutual coupling, which is present in both transmission and reception modes. The mutual coupling is primarily influenced by the spacing, radiation pattern interactions, and the various placement orientations of the MIMO antenna system. A simple representation of this phenomenon in a two antenna element (m×n) MIMO antenna system and for both transmission and reception modes is presented in Fig. 2.18. This illustration can also be implied for more than two elements. For a two closely spaced MIMO antenna

elements, the inter-element interaction in both transmitting and receiving modes can be summarized as follows [76]:

1. **Transmitting Mode**
    1. The signal is generated by a source and is travelling to Element n.
    2. Radiated signal from Element n into free space.
    3. Some of the radiated energy from Element n reaches Element m, causing mutual coupling.
    4. Element m re-radiates the energy received from Element n.
    5. The re-radiated energy from Element m reaches to Element n.
    5. Some of the received energy travel into Element m.
2. **Receiving Mode**
    1. An external incident electromagnetic wave reaches both antennas.
    2. Element n receives the incident wave and converts it into a signal.
    3. Part of the received wave reflects back from the antenna.
    4. Some of the received energy from Element n reaches Element m, causing mutual coupling.
    5. The received electromagnetic waves going back to radiate.

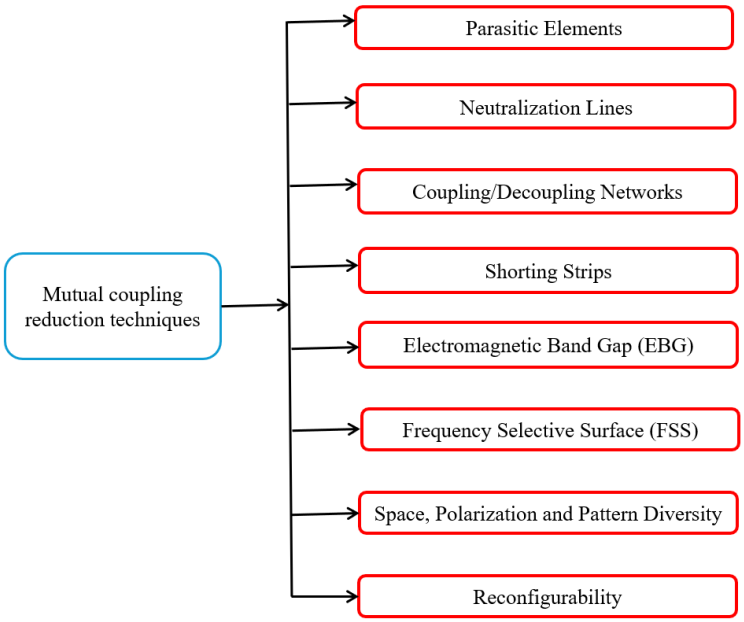

Figure 2.19: Mutual coupling and reduction techniques in MIMO antennas.

Some of these redistributions are not necessary, particularly those causing mutual coupling. Although the processes of the interactions are difficult to predict and change

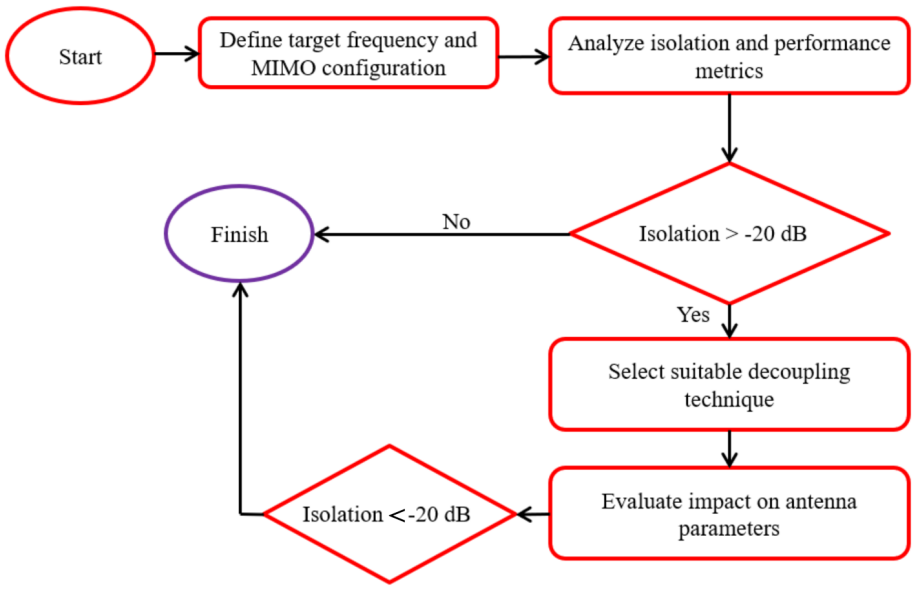

Figure 2.20: The systematic methodology of implementing the decoupling techniques in MIMO antennas.

with respect to design and frequency parameters, such interactions can be reduced, particularly for the surface current distributions in microstrip antennas. Techniques to suppress or at least diminish the effect of surface currents and consequently reduce mutual coupling and increase inter-element isolation are essential. Several mutual coupling reduction techniques are illustrated in Fig. 2.19, which have been extensively documented in the literature. These include parasitic element [73], [76], [77], [78], [79], [80], neutralization lines [81], [82], [83], [84], decoupling networks [85], [86], [87], shorting strip [88], MTMs based EBG [89], [90], [91], FSS [92], [93], [94], using antenna diversity [95] and reconfiguration [96].

In practice, the designs of these decoupling techniques follows almost a similar systematic approach and is shown in Fig. 2.20. It begins with defining the target frequency and MIMO configuration, followed by analysing isolation and performance metrics. If isolation is more than -20 dB threshold, suitable decoupling techniques are implemented and their impact on antenna parameters is evaluated. The process iteratively continues until the isolation meets the desired standard. This approach ensures efficient performance enhancement through structured assessment and refinement. A summary featuring the advantages and limitations of decoupling techniques is also provided in Table 2.3. Various techniques, including parasitic elements, neutralization lines, decoupling networks, shorting strips, EBG structures, and reconfigurable methods, offer advantages such as enhanced isolation, improved diversity, and increased compactness. However, these approaches also present challenges, including frequency shifts, ohmic losses, reduced gain, and complex configurations. Despite the aforementioned methods, FSS and DGS emerged as superior techniques due to their capacity to provide wideband isolation enhancement and minimal

Table 2.3: Advantages and limitations of mutual reduction techniques.

Ref.	Techniques	Advantages	Limitations
[73]-[77]	Parasitic elements	- Control the isolation	- Shift in frequency
[78]-[81]	Neutralization lines	- Acceptable matching - Proper diversity	- Lower frequency band
[82]-[84]	Decoupling network	- Easy decoupling - Enhance far-field	- Additional spacing - Generate ohmic losses
[85]	Shorting strips	- Compactness - Proper diversity	- Low gain
[86]-[89]	EBG	- Easy layout - Acceptable isolation	- Short bandwidth - Low gain
[92], [93]	Diversity and Reconfigurable	- Appropriate isolation - High gain	- Losses - Complex configuration

interference with antenna radiation patterns. Consequently, FSS and DGS represent more effective solutions for mitigating MIMO antenna systems.

2.7 Performance and diversity indicators of MIMO antenna systems

Typically, the assessment of single antenna element is conducted using S-parameters and far-field radiation patterns. However, these metrics alone are insufficient for a comprehensive evaluation of MIMO antenna systems. Therefore, several performance indicators are defined to accurately characterize the behaviour of MIMO antennas.

2.7.1 S-parameters and mutual coupling

An antenna can be model as a two-port network, where each port functions as an interface for signal transmission or reception. This approach can be extended to MIMO antenna systems to analyse key parameters such as reflection coefficients, transmission characteristics, and mutual coupling effects. In a two-port representation, Port 1 is typically the input where the signal is fed, and Port 2 is either another antenna element or the output. The relationship between incident and reflected waves at each port is expressed using S-parameters. These parameters form a matrix that characterizes how power propagates through the antenna system. For the analysis, a two port MIMO antenna system is shown in Fig. 2.21(a) whereas the respective two port of network for this setup is given in Fig. 2.21(b). The two-port network is represented by a voltage source V_s and an impedance Z_s, and it is connected to a load Z_0. The S-parameters can then be expressed as [97]:

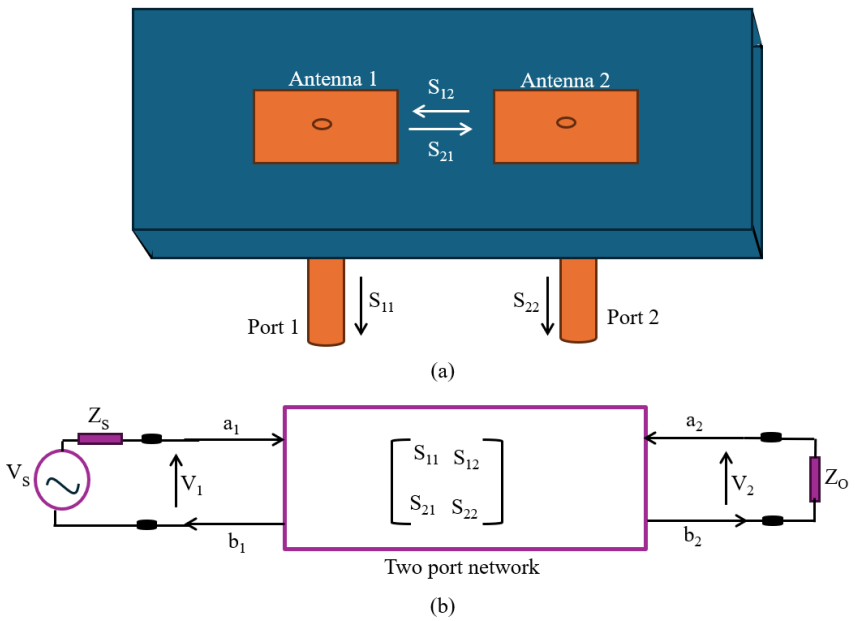

Figure 2.21: Demonstration of S-parameters (a) in two element MIMO antenna and (b) two port network representation.

Input Reflection Coefficient (S_{11}) with $a_2 = 0$:

$$S_{11} = \frac{b_1}{a_1} \tag{2.15}$$

Output Reflection Coefficient (S_{22}) with $a_1 = 0$:

$$S_{22} = \frac{b_2}{a_2} \tag{2.16}$$

Forward Transmission Coefficient (S_{21}) with $a_2 = 0$:

$$S_{21} = \frac{b_2}{a_1} \tag{2.17}$$

Reverse Transmission Coefficient (S_{12}) with $a_1 = 0$:

$$S_{12} = \frac{b_1}{a_2} \tag{2.18}$$

In practice, the two port network matrix can be further written as:

$$\begin{bmatrix} b_1 \\ b_2 \end{bmatrix} = \begin{bmatrix} S_{11} & S_{12} \\ S_{21} & S_{22} \end{bmatrix} \times \begin{bmatrix} a_1 \\ a_2 \end{bmatrix} \tag{2.19}$$

$$b_1 = S_{11}a_1 + S_{12}a_2 \tag{2.20}$$

$$b_2 = S_{21}a_1 + S_{22}a_2 \tag{2.21}$$

The reflection and transmission coefficients can be calculated as:

$$\text{Reflection coefficient} = 10\log_{10}(|S_{ii}|) \tag{2.22}$$

$$\text{Transmission coefficient or mutual coupling } = 10\log_{10}(|S_{ij}|) \tag{2.23}$$

2.7.2 Total active reflection coefficient (TARC)

The TARC ((Γ_a^t)) is a key metric for evaluating MIMO antenna performance, as it accounts for both amplitude and phase variations across e input ports. TARC provides a comprehensive measure of overall signal reflections in MIMO antennas [98]. It can be defined as:

$$\Gamma_a^t = \sqrt{\frac{\text{Reflected power}}{\text{Total available power}}} \tag{2.24}$$

TARC ranges from 0 (perfect radiation) to 1 (complete reflection), where lower values indicate improved antenna efficiency. In multi-port systems, TARC is expressed as:

$$\Gamma_a^t = \sqrt{\frac{\sum_{i=1}^{N} |b_i|^2}{\sum_{i=1}^{N} |a_i|^2}} \tag{2.25}$$

Incorporating mutual coupling phase variations, TARC becomes:

$$\Gamma_a^t = \frac{\sqrt{|S_{11} + S_{12}e^{j\theta}|^2 + |S_{21} + S_{22}e^{j\theta}|^2}}{\sqrt{2}} \tag{2.16}$$

Equation 2.16 shows the overall reflection of the system which includes input signals phase variations and mutual coupling due to closely spaced MIMO antenna elements.

2.7.3 Envelope correlation coefficient (ECC)

In communication systems, channels should ideally remain isolated and free from interference. In MIMO antenna systems, this isolation is quantified using the ECC results which measures the degree of correlation between the radiation patterns of antenna elements. The ECC can be expressed using far-field as follows [98]:

$$\begin{aligned} ECC(j,k) = & \frac{\left(\int_0^{2\pi}\int_0^{\pi}\left\{X_{PR}.E_{\theta_j}E_{\theta_k}^{*}P_{\theta} + E_{\phi_j}E_{\phi_k}^{*}P_{\phi}\right\}d\Omega\right)^2}{\int_0^{2\pi}\int_0^{\pi}\left\{X_{PR}.E_{\theta_j}E_{\theta_j}^{*}P_{\theta} + E_{\phi_j}E_{\phi_j}^{*}P_{\phi}\right\}d\Omega} \\ & \times \int_0^{2\pi}\int_0^{\pi}\left\{X_{PR}.E_{\theta_k}E_{\theta_k}^{*}P_{\theta} + E_{\phi_k}E_{\phi_k}^{*}P_{\phi}\right\}d\Omega \end{aligned} \tag{2.26}$$

Where

- E_{θ_j} and E_{ϕ_j} are the far-field radiation patterns of the j-th antenna element in the θ- and ϕ- polarization, respectively.
- E_{θ_k} and E_{ϕ_k} are the far-field radiation patterns of the k-th antenna element in the θ- and ϕ- polarization, respectively.
- X_{PR} is the cross-polarization ratio.
- P_{θ} and P_{ϕ} are the power patterns in the θ- and ϕ-polarization, respectively.

In the case of high efficiency MIMO antennas (more than 0.90), the ECC can be defined from S-parameters as following:

$$\text{ECC} = \frac{|S_{ii}S_{ji}^{*} + S_{ii}S_{ji}^{*}|^2}{(1 - |S_{ii}|^2 - |S_{ji}|^2)(1 - |S_{jj}|^2 - |S_{ij}|^2)} \tag{2.27}$$

where S_{ii} and S_{ij} represents the reflection and transmission coefficients. In an ideal communication system, the ECC should be zero, signifying perfect isolation and completely uncorrelated radiation patterns between MIMO antenna elements. However, due to mutual coupling and other practical limitations, achieving zero ECC is not possible. Consequently, in real-world applications, an ECC value of no more than 0.5 is generally considered acceptable for ensuring efficient MIMO system performance.

2.7.4 Diversity gain (DG)

The DG is an important performance metric in MIMO systems, representing the improvement in signal reliability when multiple antennas are employed to mitigate fading. It quantifies the additional power a single-antenna system would need to achieve the same outage probability as a system utilizing spatial diversity [99]. In MIMO systems, DG is closely related to the ECC, as both parameters influence the effectiveness of diversity techniques. Their relationship is expressed as [100]:

$$DG = 10 \times \sqrt{1 - ECC^2} \tag{2.28}$$

It can be observed that as the ECC increases, the DG decreases, as higher correlation between antenna elements diminishes the benefits of spatial diversity. This show that ECC and DG are inverse with each other. For efficient MIMO communication, ECC should remain below 0.5 to minimize signal correlation, while a DG of at least 10 dB will achieve reliable MIMO system performance in fading environments.

2.8 Conclusion

This chapter provided a comprehensive review of the literature and background theories related to mmWave MIMO antenna technology and its various applications. The discussion began with an overview of communication challenges in the mmWave band, followed by an explanation of MIMO technology through its theoretical framework, emphasizing its role in enhancing channel capacity. The applications of mmWave MIMO antennas, particularly in WBAN were also briefly introduced. Subsequently, the challenges associated with the design and implementation of mmWave MIMO antennas were examined. This included an introduction to MTMs and their various types, highlighting their potential benefits in antenna design. A significant focus was placed on mutual coupling, its impact on MIMO antenna performance, and various

techniques for its reduction. Among these, DGS and FSS were identified as particularly effective solutions for mitigating coupling in wideband mmWave MIMO antenna designs. Furthermore, key performance parameters such as S-parameters and mutual coupling characteristics were analysed. In addition, the theoretical background and standardization of MIMO diversity performance metrics, including TARC, ECC, and DG were thoroughly explained. This chapter establishes the fundamental basis in this thesis for understanding the key design considerations and challenges in mmWave MIMO antennas.

Chapter 3

Performance Analysis of a Four-Element Vivaldi MIMO Antenna for WBAN

3.1 Introduction

Wireless Body Area Network (WBAN) systems typically utilize two distinct forms of communication: off-body and on-body [101]. Off-body communication involves the transmission of data between devices worn on the body and external systems, such as base stations or control unit. Conversely, on-body communication encompasses the interactions among sensors and devices situated on or near the body. For off-body device communication, antennas with broadside radiation patterns are preferred. These patterns provide a directional transmission range, thus, facilitate effective communication between a body-mounted central node (such as a wearable device) and external nodes. While in on-body communication, where sensors need to communicate with each other, omnidirectional and endfire radiation patterns are commonly utilized. Omnidirectional patterns antennas are advantageous due to their capacity to transmit almost in all directions. Nonetheless, the use of omnidirectional radiation patterns results in significant energy waste particularly in unintended directions. This inefficiency is especially challenging for wearable devices, which often have limited power resources due to factors like compact batteries and restricted transmission power. As a result, the energy dispersed in unnecessary directions not only decreases the overall effectiveness but also heightens the potential for interfering with neighbouring devices. These constraints highlight the importance of developing more targeted radiation patterns, such as endfire, which directs energy along the body's surface, aligning with typical sensor placement in WBAN systems. This focused energy transmission minimizes power loss and can enhances communication efficiency, especially when sensors are arranged linearly or along curved body structures. Furthermore, the endfire pattern exhibits reduced susceptibility to external interference as well, as its radiation is primarily confined to the intended path on the body. Consequently, the endfire radiation pattern presents a significant advantage for sensor-to-sensor communication in WBAN systems.

Wearable devices frequently employ single-antenna elements due to their compact

design and ease of integration [102]. Reliable wireless connectivity in these devices necessitates careful antenna selection and support for multi band or wideband operation. Furthermore, wearable antennas must conform to the body's contours to ensure comfort and functionality. To enhance flexibility, researchers have investigated various materials and designs, including elastomeric polydimethylsiloxane (PDMS) [103], conductive fabrics [104], and fractal structures [105]. However, challenges such as durability, environmental sensitivity, complex tuning, and soldering limitations persist.

To address these challenges, innovative designs have been proposed. For instance, a multi band, all-textile microstrip circular patch antenna combining a conductive fabric layer with denim was developed for WBAN applications [106]. This ultra-thin design is well-suited for low-frequency wearable applications. Similarly, a study assessed a patch antenna's performance through on-body measurements at various locations, including the chest, back, arm, and leg, demonstrating stable radiation patterns and effective impedance matching [107]. Another investigation [108] introduced a compact textile antenna with a full ground plane operating within the 3.1–10.6 GHz frequency range, fabricated using a cost-effective FR4 substrate and copper tape. Further research on a one-turn circular patch antenna array highlighted stable radiation patterns and good impedance matching but also emphasized the human body's significant influence on antenna performance. Additionally, a flexible design using copper tape achieved a 100 MHz bandwidth with stable radiation patterns [109]. Despite these advancements, bandwidth limitations remain a challenge, hindering the simultaneous transmission of multiple data types, such as biological signals and communication data. While traditional body-worn sensors like ECG and EEG operate effectively with low data rates below 100 kbps, next-generation WBAN applications demand substantially higher bandwidth to support advanced functionalities. Emerging WBAN scenarios such as real-time wireless transmission of medical imaging often involve the simultaneous transmission of multiple data streams in real-time. For instance, wearable ultrasound devices designed for continuous cardiovascular monitoring generate substantial data streams that must be transmitted with low latency and high resolution to ensure clinical reliability. These systems often require data rates in the order of several megabits to gigabits per second. In such scenarios, narrow bandwidth constraints can lead to signal degradation and low latency. Consequently, antennas with wide bandwidth becomes essential to support such high-data-rate wearable diagnostic tools within WBAN environments.

The development of wearable antennas that minimize radiation exposure to the human body introduces additional complexities. Compliance with SAR safety standards is essential to ensure user safety. Some researchers have proposed solutions such as metamaterial bandgap structures and AMC layers placed behind the antenna [110], [111], [112], [113]. However, these approaches often increase device thickness and

require a quarter-wavelength gap between the antenna and the AMC layer, complicating integration with other wearable device components [114]. As an alternative, antennas such as Vivaldi antennas have demonstrated potential in reducing the need for additional metamaterial-backed layers due to their inherent end-fire radiation pattern, which propagates parallel to the human body. While studies have investigated end-fire antennas operating in the 2.4 GHz ISM band and ultra-wideband (UWB) [115], [116], [117], these frequency ranges are increasingly congested due to the proliferation of electronic devices. Consequently, the mmWave band are garnering interest for WBANs. However, mmWave systems face challenges such as sensitivity to path loss and increased susceptibility to multipath fading and obstructions caused by the human body, which can impair performance. To address these MIMO antenna systems have been proposed as a viable solution.

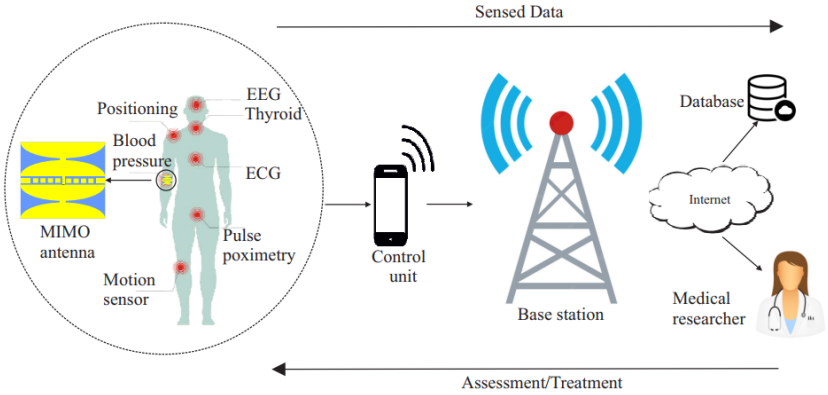

Figure 3.1: Application overview of designed MIMO antenna in WBAN system.

This chapter thoroughly investigates the design of mmWave band MIMO antenna for WBAN applications, addressing endfire communication scenarios. The application scenario of designed MIMO in a WBAN environment is shown in Fig. 3.1. The structure of this chapter is as follows: Initially, it presents the design and examination of a single Vivaldi antenna element with a broad frequency range from 23.45 GHz to 33.59 GHz. The design is subsequently expanded to incorporate two and four elements. In the four-element configuration, significant mutual coupling was observed between Antennas 1 and 4, particularly along the vertical axis. To mitigate this phenomenon, a FSS was implemented, effectively reducing the coupling and achieving an improvement of over -30 dB across the entire bandwidth. The chapter then evaluates the final MIMO antenna design's performance in terms of bandwidth, gain, efficiency, and radiation characteristics, specifically when positioned on the Gustav human body model. The antenna's behaviour under bending conditions is also examined to determine its suitability for wearable applications. The chapter discusses the results of S-parameters and radiation patterns obtained from testing the fabricated antenna. Lastly, the chapter explores the diversity performance of the MIMO antenna and conducts a safety analysis regarding SAR compliance.

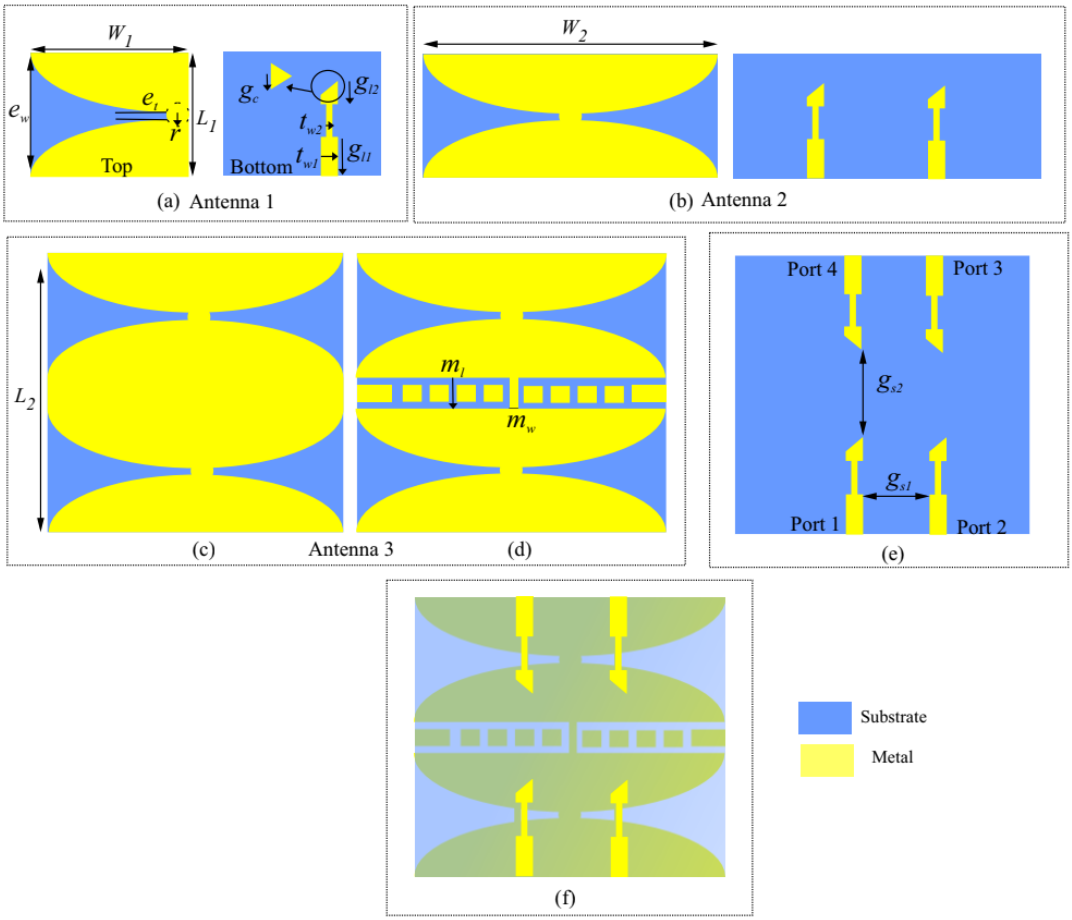

Figure 3.2: Vivaldi MIMO antenna design configuration (a) Antenna 1: single element, (b) Antenna 2: two elements, (c)-(d) Antenna 3: four element without and with FSS, (e) input ports, and (f) perspective view.

3.2 Vivaldi MIMO antenna design

The Vivaldi antenna is distinguished by its exponentially tapered slot profile, which offers two key advantages: broadband impedance matching and wide operational bandwidth. These characteristics make Vivaldi antennas highly suitable for demanding applications such as ultra-wideband radar systems, 5G/6G GHz phased arrays, and medical imaging. Despite these advantages, Vivaldi antennas have not been extensively explored for WBAN applications, particularly in the mmWave band where broadband performance, compact size, and endfire radiation patterns are critical. Therefore, in this chapter, a Vivaldi MIMO antenna is proposed and evaluated within a WBAN application scenario. The proposed Vivaldi MIMO antenna was designed in CST Studio Suite which is a widely recognized and industry-standard simulation software for electromagnetic devices design. It also provides a number of solvers such as time-domain and frequency-domain.

Time-domain solvers are efficient for wideband simulations as they capture the broadband response in a single run, while frequency-domain solvers are more precise

Table 3.1: Optimized parameters of the MIMO antenna.

Parameters	Values (mm)	Parameters	Values (mm)	Parameters	Values (mm)	Parameters	Values (mm)
W_1	10.00	W_2	20.00	L_1	7.00	L_2	16.00
e_t	0.41	r	0.71	g_{l1}	2.70	g_{l2}	1.00
t_{l1}	0.65	t_{l2}	0.25	g_c	0.61	m_l	2.00
g_{p1}	3.08	g_{p2}	6.18	w_c	0.30	g_{s1}	6.35
e_{gw}	1.05	e_{gl}	1.50	g_{s2}	6.10		

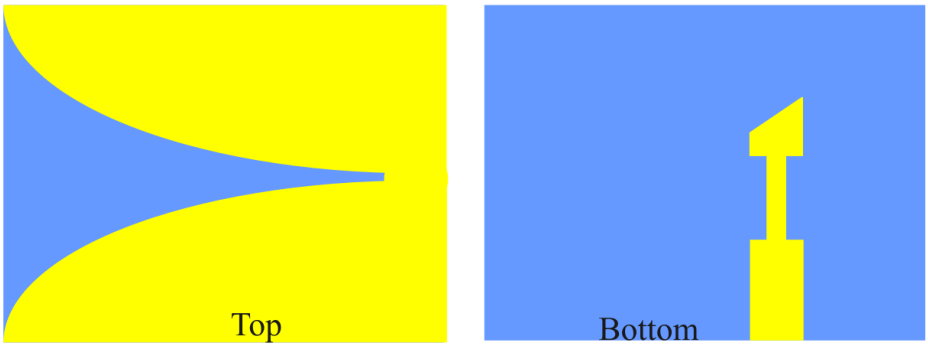

Figure 3.3: Structure of single element Vivaldi antenna.

for narrowband designs. These solvers are well-suited for simulating complex antenna structures with high accuracy. Additionally, CST is particularly effective for modeling antennas in proximity to the human body, as it supports detailed human tissue phantoms models which can be used for on-body effects and SAR calculations. The design of Vivaldi MIMO antenna encompasses several stages as shown in Fig. 3.2. The design starts with a single element and expands to two and four element. Finally, a decoupling structure is added to minimize the mutual coupling. The optimized parameters of the design are provided in Table 3.1.

3.2.1 Single antenna design

The structural layout of the single element Vivaldi antenna printed on a semi-flexible substrate, Rogers RT5880 (permittivity of 2.2, loss tangent of 0.0009), is illustrated in Fig. 3.3. The thickness of the substrate was 0.79 mm, whereas that of the copper metal was 0.017 mm. The antenna is fed by EM coupling between the microstrip and the slot line, where the microstrip line is connected to the input port. The antenna top face employs a tapered slot design that efficiently directs EM energy. The antenna's structure has two radiating flares that converge into a tapered profile. These flares connect at a circular section with a radius *r*, which serves as a critical design parameter and significantly influences the resonance frequencies. The antenna is excited through EM coupling between the microstrip line and the slot line. To achieve

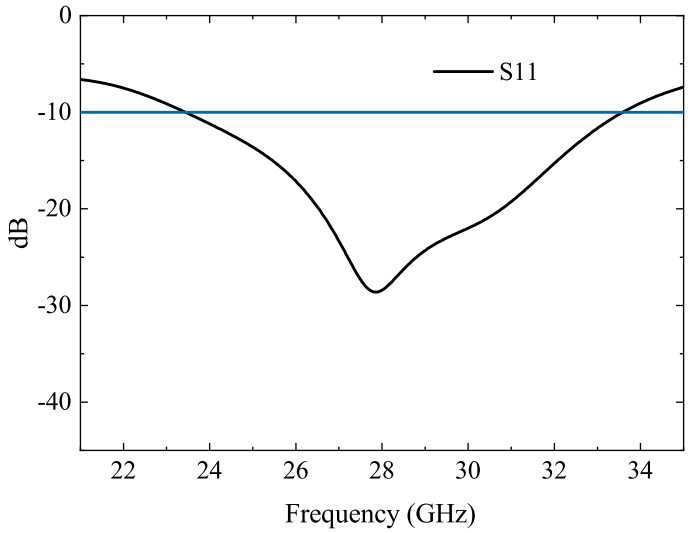

Figure 3.4: Reflection coefficient of single antenna.

optimal impedance matching across the operational bandwidth, the microstrip line's width is divided into two distinct sections. A triangular cut (gc) on the upper section of the microstrip line on the bottom side further enhances the antenna's performance. This cut introduces additional reactive tuning, improving impedance matching and expanding the operational bandwidth. Furthermore, the triangular cut aids in maintaining stable radiation patterns across the desired frequency range. A tapering slot configuration on the top face was utilized using equation3.1 [118].

$$y = c_1 e^{rx} + c_2 \tag{3.1}$$

Here r id the opening rate of the flares which are determined by c_1 and c_2 at two points of p_1 $(x1, y1)$ and p_2 $(x2, y2)$ as given in equations 3.2 and 3.3.

$$c_1 = \frac{y_2 - y_1}{e^{rx_2} - e^{rx_1}} \tag{3.2}$$

$$c_2 = \frac{y_1 e^{rx_2} - y_2 e^{rx_1}}{e^{rx_2} - e^{rx_1}} \tag{3.3}$$

The exponential taper curve exhibits a minimum point at p_1, defined by the coordinates (x_1, y_1), and a maximum point at p_2, defined by (x_2, y_2). Utilizing the values of y_1 and y_2, the cut-off frequencies of the Vivaldi antenna can be derived based on the aperture width, e_w, as expressed in equation 3.4. The opening rate, represented by r, serves as the exponential factor governing the beam-width of the Vivaldi antenna, while c_1 and c_2 are constants associated with the taper curve.

$$e_w = \frac{c}{f_{min}\sqrt{\epsilon_r}} \tag{3.4}$$

Where, the speed of light is c, and ϵ_r represents the dielectric constant of the substrate material. Any modifications to these values will result in alterations to the antenna and its characteristics. The simulated reflection coefficient (S_{11}) of the single element

antenna design is shown in Fig. 3.4. The results demonstrate that the antenna design exhibits an impedance bandwidth exceeding 10 GHz. This wide bandwidth ranges from 23.45 GHz to 33.59 GHz and covers the 24 GHz ISM and 28 GHz of 5G bands within the mmWave spectrum.

3.2.1.1 Parametric analysis

A parametric analysis is conducted to evaluate the influence of key geometric variables on the antenna's performance, with a focus on S_{11}. While multiple factors contribute to performance, this study concentrates on g_c and t_{w2}. The results of modifying g_c parameter are presented in Fig. 3.5(a). Four distinct values of g_c are examined: 0.4 mm, 0.6 mm, 0.8 mm, and 1.0 mm. The findings indicate that increasing g_c results in a minor shift in resonance frequency and expanded bandwidth. A smaller g_c (e.g., 0.4 mm) yields more pronounced resonance and deeper S_{11}, indicating superior impedance matching. Conversely, larger gaps (e.g., 1.0 mm) produce a shallower S_{11} curve, suggesting reduced matching performance. This trend in shifting suggests that the precise adjustment of g_c is critical for achieving both wide bandwidth and enhanced resonance characteristics. Fig. 3.5(b) illustrates the impact of varying the taper width of transmission t_{w2} on S_{11}. The taper width is analyzed at three values: 0.15 mm, 0.25 mm, and 0.35 mm. Larger t_{w2} values shift resonance frequencies higher and widen the bandwidth. A narrower t_{w2} (e.g., 0.15 mm) yields a smaller bandwidth and more pronounced S_{11}, while wider taper widths (e.g., 0.35 mm) result in significantly higher S_{11}. These results underscore the significance of t_{w2} in adjusting the antenna's impedance bandwidth and resonance frequency. The parametric analysis demonstrates that both g_c and t_{w2} significantly influence the vivaldi antenna's performance, particularly its impedance bandwidth and resonance characteristics. Through precise tuning of these two parameters, high-performance vivaldi antennas with optimized matching and bandwidth for any desired frequency range can be designed.

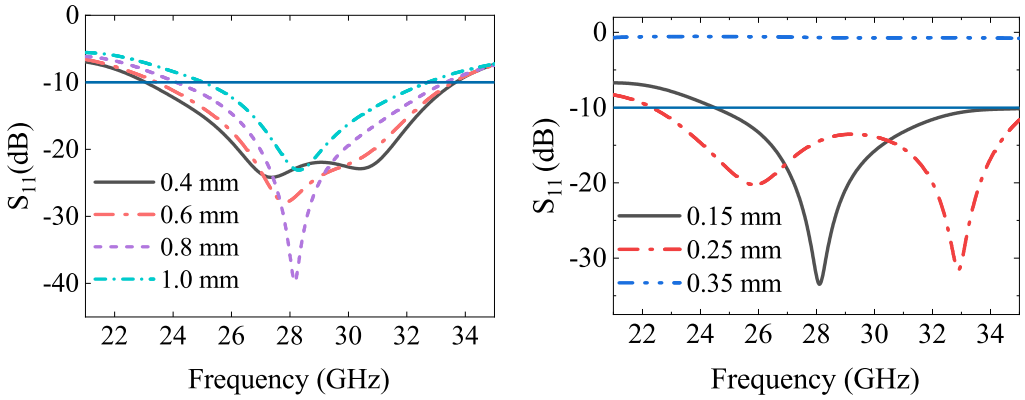

Figure 3.5: Parametric analysis of variables g_c and t_{w2}.

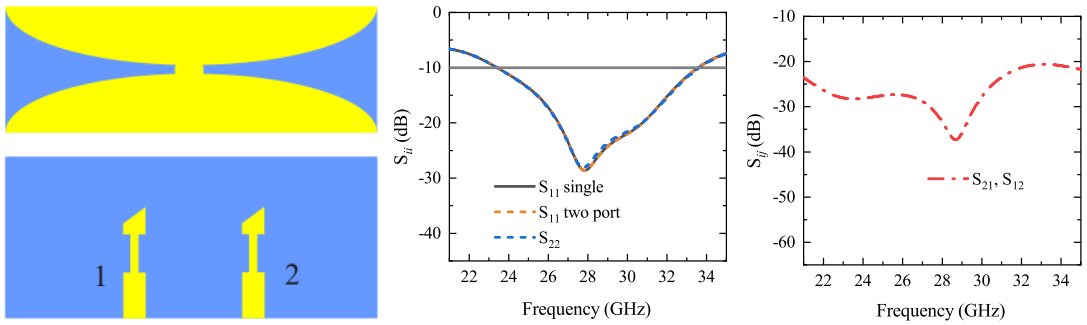

(a) (b)

Figure 3.6: Two element vivaldi antenna (a) structure and (b) reflection and transmission coefficients.

3.2.2 Multi element design without FSS

3.2.2.1 Two element design

The two-element MIMO design from a single-element Vivaldi antenna necessitates the replication of the fundamental Vivaldi structure and its positioning in the opposite orientation, as depicted in Fig. 3.6(a). The upper face of this design maintains the exponentially tapered slot configuration for each element, thereby preserving its broadband radiation characteristics. The lower face incorporates two feeding ports, each corresponding to an individual antenna element. These ports are strategically positioned to optimize impedance matching and ensure efficient power transmission to each antenna component. The elements are separated by a specific distance to achieve high isolation while minimizing mutual coupling between them.

The S-parameters of the two-element Vivaldi antenna are presented in Fig. 3.6(a). The reflection coefficient results exhibit a similar trend compared to the single antenna element. The impedance bandwidth of this design for both elements is 23.61GHz-33.52 GHz (fractional bandwidth = 34.69%). Both single-element and two-element configurations demonstrate a pronounced minimum in the S11 curve near 28 GHz, indicating effective impedance matching and efficient power transfer at this frequency. The transmission coefficients, which quantify the power transfer between the two ports and serve as a measure of mutual coupling between antenna elements, are depicted in the right-hand plot of Fig. 3.6(a). This parameter remain below -20 dB throughout the analyzed frequency range and reach -37 db near 28 GHz, indicating minimal mutual coupling. The low transmission coefficients suggest that the two-element array achieves satisfactory port isolation, reducing undesired interactions and maintaining efficient performance across the target frequency band.

The low mutual coupling can also be analyzed through the E-field and surface current distribution between two antenna elemnts. This is shown in Fig. 3.7 along with far-field radiation patterns particulalry at 28 GHz and 30 GHz. The E-field and

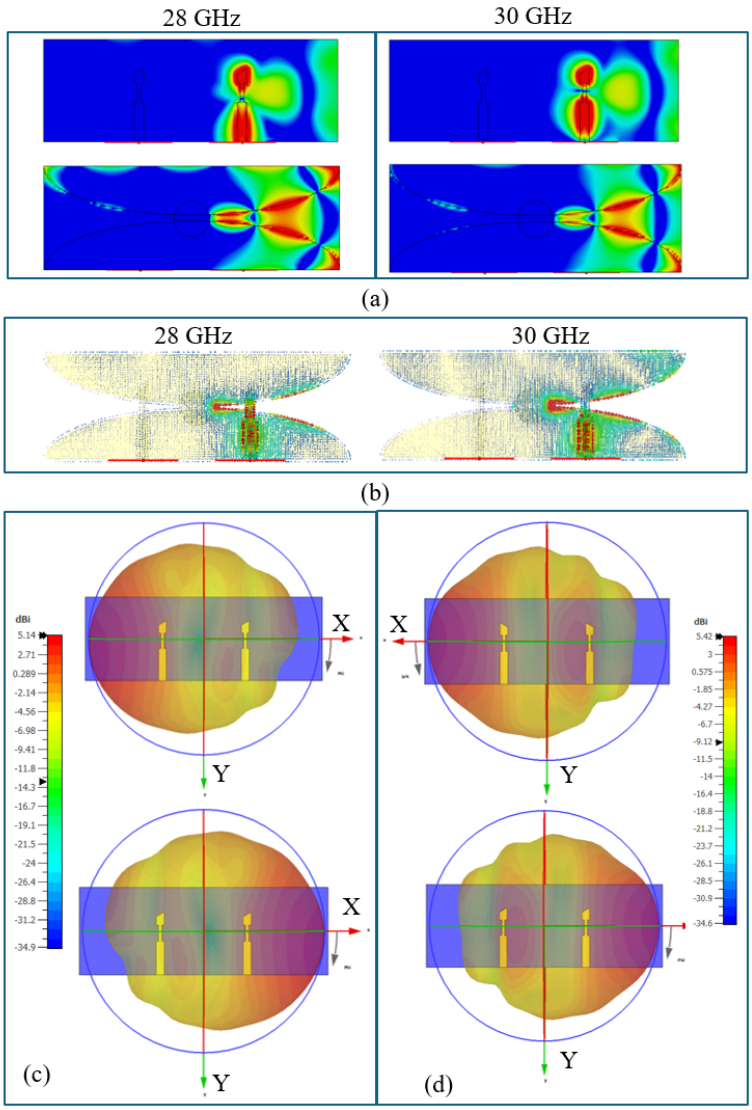

Figure 3.7: (a) E-field, (b) surface current when antenna 1 is operating, (c) far-field at 28 GHz, and (d) far-field at 30 GHz.

surface current distribution of antenna 1 at both frequencies and on the top and bottom faces are not much impacting the other antenna as evident in Fig. 3.7(a-b). The E-plane radiation characteristics of the dual-element depicted in 3.7(c-d) exhibit radiation patterns with primary lobes oriented along the +x and -x axes, demonstrating effective energy emission perpendicular to the antenna plane. The patterns display smooth, symmetrical lobes, indicating consistent E-plane directivity. The max gain at both frequencies are 5.14 dBi and 5.42 dBi which is almost same. The distinct lobes for each element suggest minimal interference between them.

3.2.2.2 Four element design

To enhance performance, the two-element structure is subsequently replicated and arranged in a linear configuration comprising four elements with uniform inter-element spacing as shown in Fig. 3.8(a). The top face exhibits an identical exponentially tapered

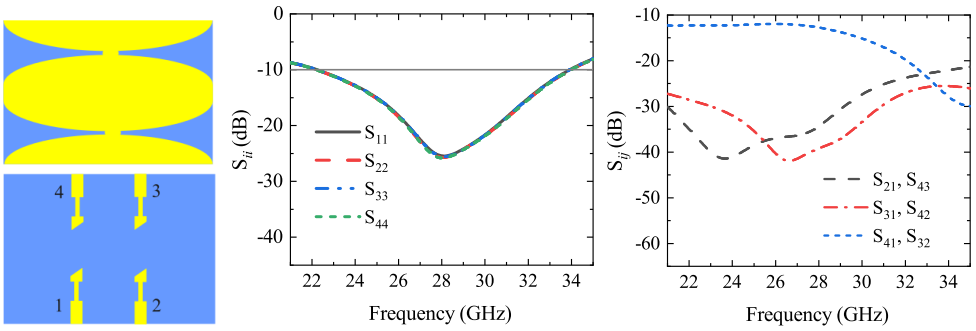

(a) (b)

Figure 3.8: Four element vivaldi antenna (a) structure and (b) reflection and transmission coefficients.

slot configuration, while the lower surface incorporates designated ports 1, 2, 3, and 4, which serve to excite each element. The reflection and transmission coefficients of this design are shon in 3.8(b). The implementation of a multi-port design resulted in a marginal enhancement of the antenna's impedance bandwidth, with the four-port configuration encompassing a range from 22.97 GHz to 33.91 GHz. Consequently, the proposed MIMO antenna achieved a fractional bandwidth of approximately 38.46%. The isolation between antenna elements radiating in opposite directions, such as S_{21}, S_{43}, S_{31}, S_{42}), remains more than -30 dB indicating effective decoupling between these ports. However, the antennas radiating in the same direction, represented by S_{41}, S_{32}, exhibit lower isolation levels, with values exceeding -14 dB. This reduced isolation may potentially compromise the overall performance of the MIMO antenna system. Therefore, further refinements in the antenna design are necessary to enhance the isolation between these ports and optimize the MIMO performance.

3.2.3 FSS design

a) Background

It is worth noting that natural EM media generally possess positive values of permeability and permittivity. However, artificial periodic structures known as FSS can exhibit negative effective permeability and permittivity at specific frequencies. This attribute enables these structures to manipulate EM waves in novel and potentially valuable ways. The incorporation of FSS into antenna designs can significantly reduce mutual coupling between adjacent antenna elements by serving as an EM barrier or band-stop filter. When positioned between antenna elements, an FSS can suppress unwanted surface waves and attenuate the interaction of radiated fields among neighboring components, thus minimizing mutual coupling and enhance interelement isolation. The wave-number k for such materials becomes imaginary, unlike that of natural EM media [119]. When EM waves travel through such metamaterials, they

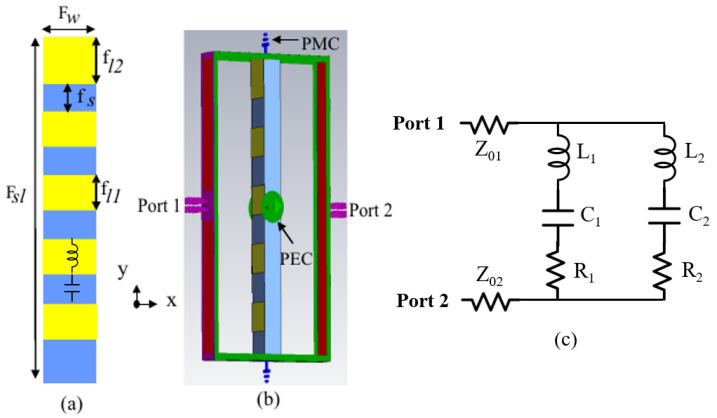

Figure 3.9: FSS unit cell design (a) structure, (b) boundary conditions, and (c) equivalent circuit model.

become evanescent decay due to the FSS negative characteristics. For instance, the activation of antenna 1 can induce currents on neighboring antennas because of a strong x-component of the electric field, resulting in inter-element mutual coupling. By positioning an FSS with negative permeability between antenna elements, a zone of negative permeability and positive permittivity ($\mu_r < 0, \varepsilon_r > 0$) is established, which aids in reducing mutual coupling by attenuating the electric field between the elements. In equation 3.5, the wave-number *k* is expressed within the region defined by $\mu_r < 0$ and $\varepsilon_r > 0$ [120]:

$$k = k_0 \cdot \sqrt{-|\mu_r| \cdot |\varepsilon_r|} = jk_0 \cdot \sqrt{|\mu_r| \cdot |\varepsilon_r|} \tag{3.5}$$

The associated x-component of the electric field, represented by $A_0 \cdot e^{jkx}$, propagating in the negative x-direction, can be formulated as shown in in equation 3.6.

$$A_0 \cdot e^{jkx} \cdot e^{j\omega t} = A_0 \cdot e^{-k_0\sqrt{|\mu_r| \cdot |\varepsilon_r|}} \cdot e^{j\omega t} \tag{3.6}$$

In this context, A_0 signifies the E-field's amplitude, while ω represents the angular frequency. As demonstrated in Equation 3.6, EM waves will exhibit decaying behaviour along the negative x-axis on the FSS. This rapid attenuation of wave amplitude results in improved isolation between antenna components.

b) Design and Results

Fig. 3.9(a) depicts the proposed FSS configuration designed to reduce mutual coupling, specifically between antennas 1 and 4, as well as antennas 2 and 3. The performance of Vivaldi antennas, in terms of bandwidth and radiation, is significantly influenced by the response of their radiation flares or tapering structures and presence of slots [118]. Consequently, the FSS structure was designed to minimize its impact on the antenna's performance. The dimension of FSS, particularly the width was chosen to be smaller than the wavelength of the desired bandwidth frequencies. It was done to follow the

design criteria of MTM unit cells which states that the unit cell dimensions must remain sub wavelength with respect to the operational frequency band. Specifically, the unit cell size must be chosen to less than half the wavelength $(\lambda/2)$, and preferably less than one-quarter of the wavelength $(\lambda/4)$, where λ is the wavelength of operating frequencies. This is done to ensures that the FSS behaves as an effective or homogenized surface rather than an array of discrete scatterers. Additionally, the sub wavelength dimensions of unit cells also ensure consistent performance over different incidence angles. The FSS structure was designed on same RT5880 substrate and comprises rectangular patches with inter spacing of f_s. The FSS's spatial filtering characteristics are determined by its periodicity along the y-axis, facilitating selective transmission or reflection of EM waves at specific frequencies. The optimized parameters and dimensions of the FSS are as follows: f_{sl} = 10.50, f_W = 1.30, f_s = 1.08 f_{l1}= 1.05, and f_{l2}= 1.50 (mm). The unit cell was subsequently simulated in the CST Studio Suite environment, as illustrated in 3.9(b). The FSS unit cell was positioned between two ports (Port 1 and Port 2) to analyse its transmission and reflection characteristics. Perfect magnetic conductor (PMC) boundaries were applied along the x-axis, while perfect electric conductor (PEC) boundaries were applied along the y-axis. This configuration ensures the appropriate behaviour of a periodic structure under normal incidence. The ports are used to excite the structure and measure the S-parameters and frequency-selective behaviour of the FSS. The designed FSS can also be represented by an equivalent RLC circuit model, as illustrated in Fig. 3.9(c). This circuit model employs inductors (L_1 and L_1), capacitors (C_1 and C_2), and resistors (R_1 and R_2) to simulate the frequency-dependent characteristics of the FSS unit cell. The inductors represent the width and length of the patches (f_{l2}) and generate currents in response to incident EM waves (magnetic response). The capacitors model the gap between patches (f_s) and store electric energy due to potential differences between two patches. The resistors represent the losses and energy dissipation within the FSS. In the circuit, both Port 1 and Port 2 are designated as Z_{01} and Z_{02}, respectively, and are considered equivalent to the free space impedance of 377 Ω.

The results of simulated S-parameters, along with extracted material parameters including ε, μ, and n of the designed FSS are shown in Fig. 3.10. The reflection and transmission coefficient both for EM simulated and ADS circuit showing almost same results in Fig. 3.10(a). High reflection (near 0 dB) and lower transmission across most of the frequency band can be observed, with exceptions at 25.50 GHz and 31.82 GHz. This high reflection can be attributed to the band-reject characteristics of the filter, whereas the frequencies exhibiting lower reflection can be considered band-pass frequencies. Similarly, results of both real and imaginary ε components are provided in Fig. 3.10(b). The results indicate that the real part is positive whereas the imaginary part is negative in most of the band of interest. The real part represents the material's electric

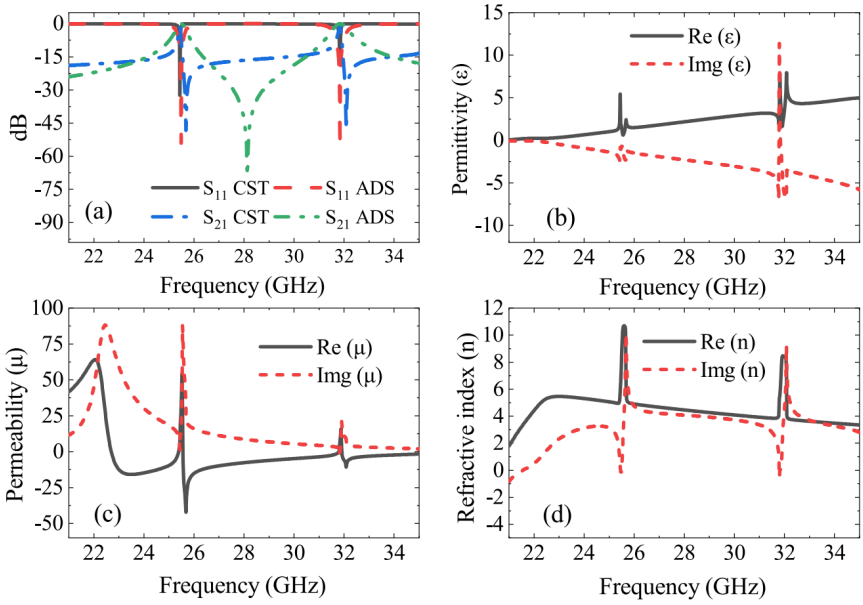

Figure 3.10: FSS unit cell (a) S-parameters (b) ε, (c) μ, (d) n.

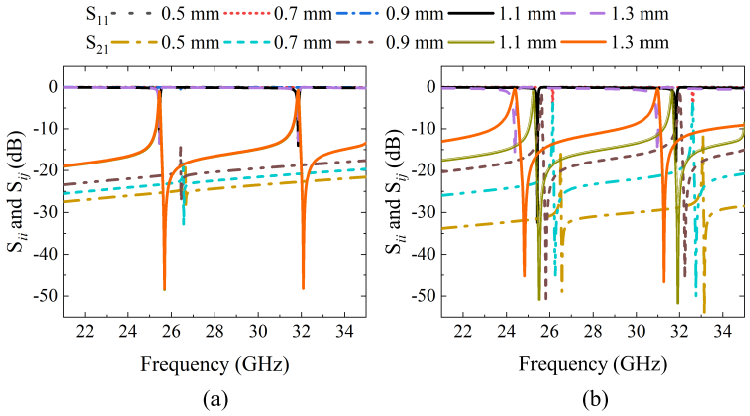

Figure 3.11: Parametric analysis of the FSS (a) separation f_s and (b) gap F_w.

energy storage capacity, whereas the imaginary part indicates energy loss within the material. Correspondingly, the real part of μ is negative at all frequencies except within the transmission range as shown in 3.10(c). The real value of n is positive as shown in 3.10(d). The negative permeability values confirm the FSS's ability to manipulate EM waves through magnetic responses, and can be classified as single negative MTM.

The FSS unit cell was further evaluated through a parametric analysis, focusing on the influence of patch separation (f_s) and patch width (F_w) on the reflection and transmission coefficients, as shown in Fig. 3.11. The results in Fig. 3.11(a) indicate that changes in the separation between patches do not significantly affect the resonance frequency, and an approximately constant behavior can be observed. Similarly, the impact of patch width (F_w) was analyzed as shown in 3.11(b), and it was determined that increasing the patch width from 0.5 mm to 1.3 mm resulted in a notable shift in both parameters. Wider patches facilitated increased EM wave transmission through the FSS structure, thereby enhancing the transmission performance. However, the widening of the patches also induced a shift in the resonance frequency, which may

necessitate careful adjustments to align with the desired frequency bands. Overall, the parametric analysis demonstrates that both patch separation and width play a crucial role in determining the frequency-selective behavior of the FSS unit cell. These parameters must be carefully optimized to ensure that the structure achieves the desired filtering characteristics while minimizing undesired reflections or losses.

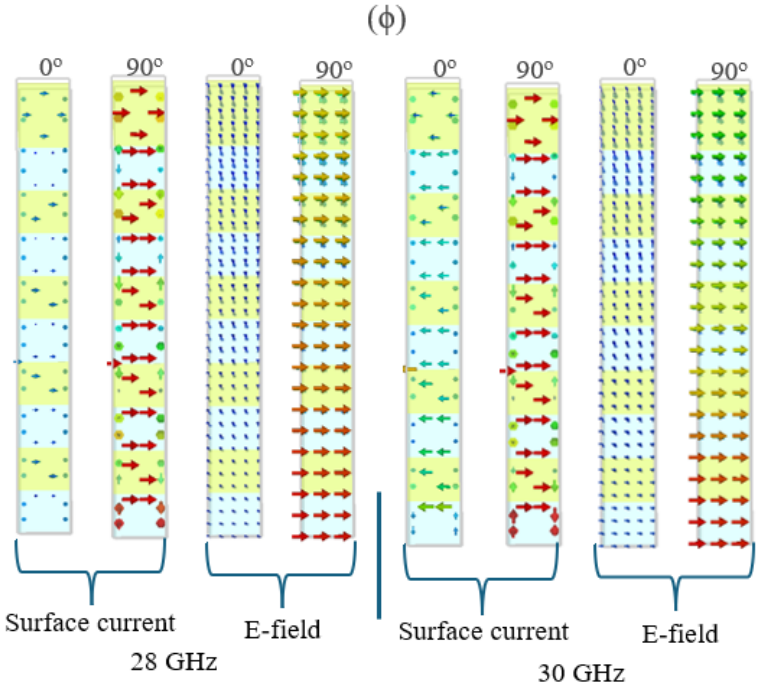

Figure 3.12: FSS unit cell surface current and E-field distributions.

Fig. 3.12 illustrates the distribution of surface currents and E-fields for the designed FSS, depicting results at frequencies of 28 GHz and 30 GHz for both 0° and 90° phase angles. At both frequencies and 0° , both the surface current distribution and E-field have inward flow along the FSS unit cell. The current vectors demonstrate alignment at 90° shows effective interaction with incident EM waves. The corresponding E-field distribution at 28 GHz reveals a significant concentration of electric fields along the patch edges, suggesting the FSS's capacity to confine electric fields in the desired direction. The 30 GHz frequency presents a similar pattern in surface current distribution. The alignment of surface currents and E-fields indicates consistent resonant behavior across various polarizations. At 30 GHz, the E-field distribution demonstrates that electric field vectors remain concentrated along the patch edges. The observed surface current and E-field distributions corroborate the FSS structure's frequency-selective behavior at the target frequencies. The alignment of currents and electric fields at both 0° and 90° demonstrates the FSS effective response to EM waves across different polarization, thus showing excellent performance as a frequency-selective filtering surface.

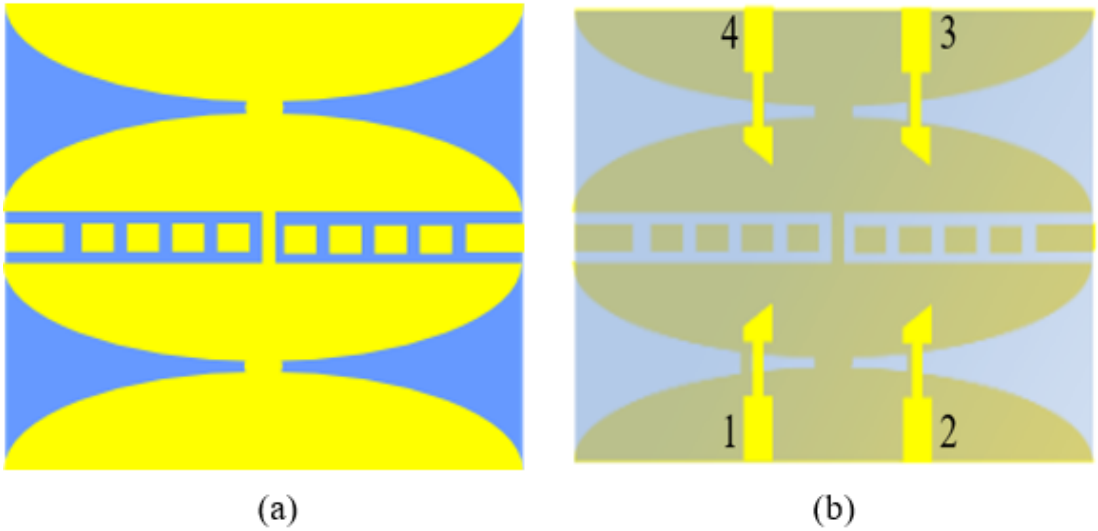

Figure 3.13: Final four element vivaldi antenna structure (a) top and (b) bottom faces.

3.2.4 Vivaldi MIMO antenna with FSS

Following the design of FSS with the desired characteristics, it was then integrated into the four element vivaldi MIMO antenna configuration. The perspective view of the final antenna design is illustrated in Fig. 3.13, while the corresponding S-parameter results are presented in Fig. 3.14. The analysis reveals that all antenna elements exhibit a comparable impedance bandwidth with no significant shift in the resonance behavior. The FSS integrated design achieved a bandwidth of 22.85 GHz to 33.96 GHz, corresponding to a fractional bandwidth of approximately 40.7%. The integration of the FSS structure significantly enhanced the isolation between MIMO antenna elements. Specifically, the isolation between ports 1 and 4, which was initially approximately -14 dB without the FSS, improved to exceed -31 dB across the majority of the bandwidth after FSS incorporation, achieving a maximum isolation of -50 dB at 30 GHz. Furthermore, substantial improvements in isolation were observed between ports 1 and 2 as well as ports 1 and 4, both surpassing -25 dB. These enhancements in isolation and the reduction in mutual coupling substantiate the efficacy of the proposed FSS decoupling and inter element isolation.

The isolation enhancement between antenna elements can also be analysed by comparing the E-field and surface current distributions with and without the inclusion of FSS as shown in 3.15. The regions designated as “A” and “B” in both the E-field and surface current plots illustrate the impact of the FSS. As demonstrated in 3.15(a) without the FSS, a stronger coupling effect is observed between antenna elements, particularly in the highlighted regions, notably between ports 1 and 4, where the E-field generated by port 1 perturbs the adjacent field of port 4. This excessive coupling contributes to higher mutual coupling between these ports, as previously discussed. The incorporation of the FSS structure effectively mitigates this coupling,

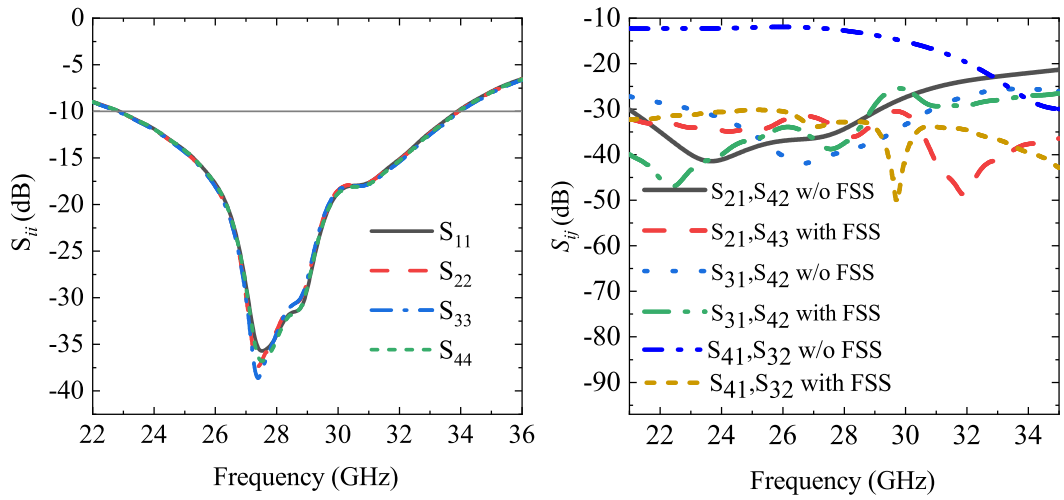

Figure 3.14: S-parameter results of the final stage four element MIMO antenna.

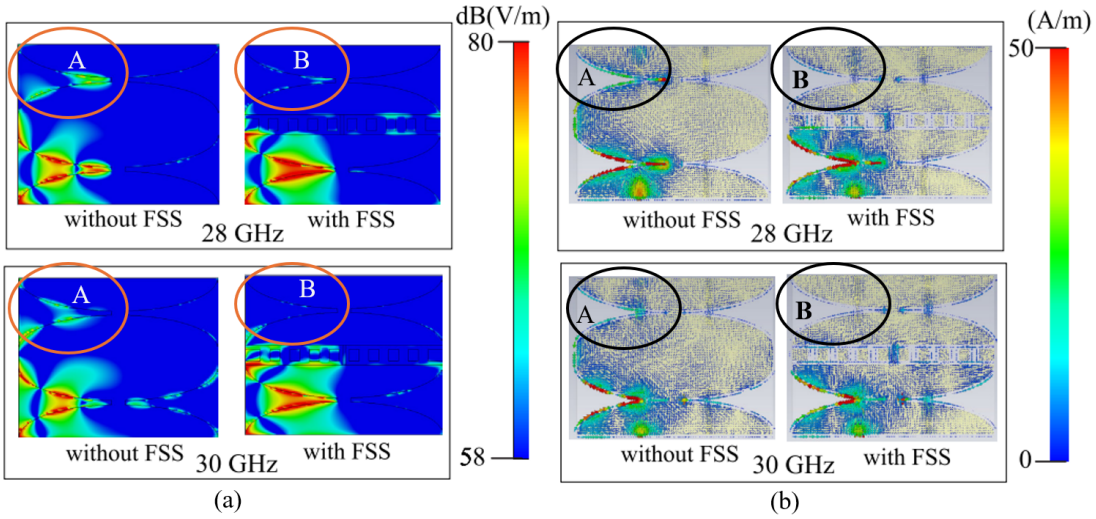

Figure 3.15: E-field and surface current distribution with and without FSS (a) E-field and (b) surface current when antenna 1 is operating.

thereby enhancing the directional generation of the electric field. The surface current distribution, illustrated in Fig.3.15(b), demonstrates that the current flows to the adjacent antenna in the absence of the FSS. This concentration is significantly reduced in the presence of the FSS, indicating that the coupling is reduced due to the bandstop characteristics of the FSS.

Moreover, the integration of the FSS has a minimal impact on the antenna's gain and efficiency, as shown in Fig. 3.16. The gain performance improves with the FSS structure, reaching a peak gain of 5.73 dBi at 28 GHz. Similarly, the efficiency shows a slight improvement, with maximum values exceeding 86 at 28 GHz and 87 at 30 GHz. These enhancements demonstrate that the proposed FSS structure contributes positively to both the radiation performance and efficiency of the MIMO antenna without introducing significant losses.

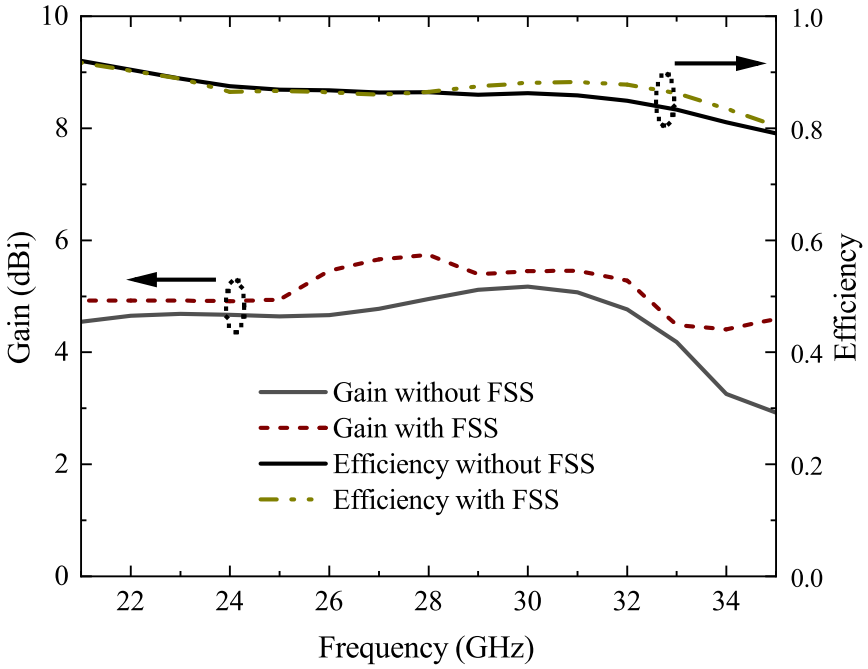

Figure 3.16: Simulated gain and efficiency with and without FSS

3.2.5 Bending analysis

The bending analysis of the MIMO antenna is essential for wearable device applications, as it can be affected by the body's curvature when placed on body parts such as the chest, hand, or leg. To assess this, the antenna's performance was tested when antenna was bent along the x-axis in free air and on the cylinder model with different radii Rx (80 mm, 65 mm, 50 mm, and 35 mm) as shown in Fig. 3.17. The bending in x-direction was performed in two different scenarios: first bending in positive x-direction while another scenario consisted of bending in both positive and negative x-directions. this was performed in free space conditions. In cylinder case, the MIMO antenna was placed on a cylinder showing bending in both directions.

The MIMO antenna's S-parameters for these cases are provided in Fig. 3.18. Due to symmetry and identical antenna structure, the results of ports 1 and 4 are presented, although similar results were observed for the other two ports. From the results in Fig. 3.18(a), it can be observed that when the antenna is bent in the positive x-direction, the antenna bandwidth is slightly shifted towards lower frequencies. Consequently, the impedance bandwidth in this case ranges from 22.5 GHz to 34 GHz. The transmission coefficient in Fig. 3.18(b) indicates that the coupling levels are slightly increased compared to the flat antenna case. Nevertheless, the average coupling levels remain below -25 dB, with a maximum isolation of -70 dB observed near 29 GHz. Similarly, the bandwidth exhibited a more pronounced shift when the antenna was bent in both directions, as illustrated in Fig. 3.18(c), where the bandwidth extended from 23 GHz to 31 GHz. In addition to the bandwidth shift, increased reflection was observed in this case, while an average coupling of approximately -28 dB was noted, as shown in

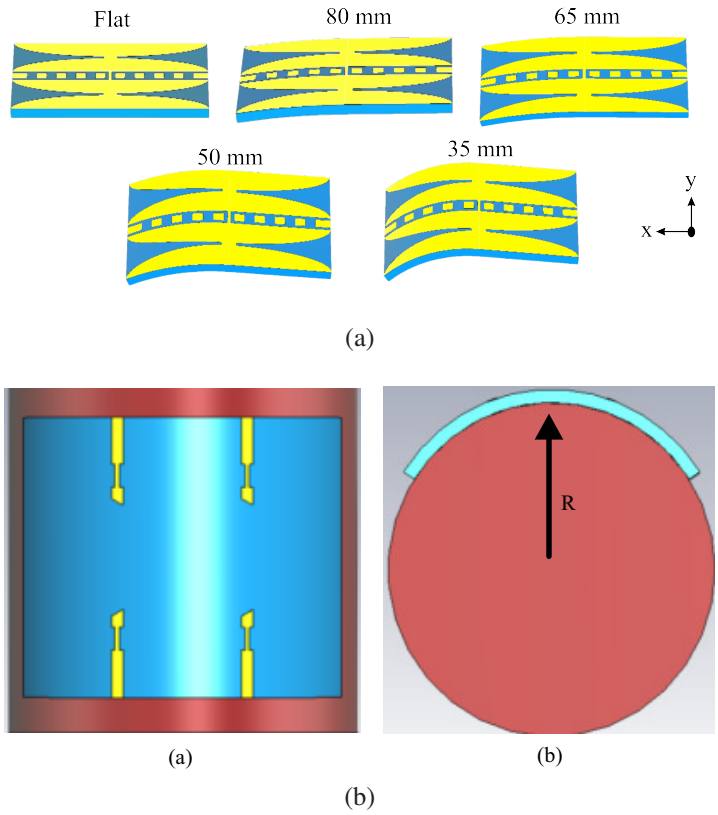

Figure 3.17: Bending of MIMO antenna (a) x-direction in free space and (b) on a cylinder shape.

Fig. 3.18(d). A different bandwidth was observed when the antenna was placed on a cylinder, as depicted in Fig. 3.18(e), whereas no significant change in coupling was noted, as illustrated in Fig. 3.18(f). This shift to lower frequencies is anticipated due to the elongation of the current path on the radiating patch resulting from bending in both directions. However, in all cases, the proposed MIMO antenna continues to cover most frequencies, particularly 28 GHz and 30 GHz, respectively, under all bending conditions while maintaining excellent isolation levels. Furthermore, as shown in Fig. 3.19, an almost constant efficiency of 0.84 was observed in all bending scenarios and does not decrease significantly, maybe due to reduced unwanted coupling between the elements caused by bending of the proposed MIMO antenna. At 28 GHz, a constant gain of 5.52 was observed, whereas at 30 GHz, the gain was significantly reduced when the antenna was subjected to more pronounced bending on the cylindrical shape.

The simulated radiation patterns of the E-plane at frequencies of 28 GHz and 30 GHz, in comparison with a flat MIMO antenna, for various bending conditions are shown in Fig. 3.20. The results indicate that the designed MIMO maintains endfire radiation patterns across all bending scenarios. This demonstrates that the radiation pattern exhibits minimal susceptibility to bending conditions in free space.

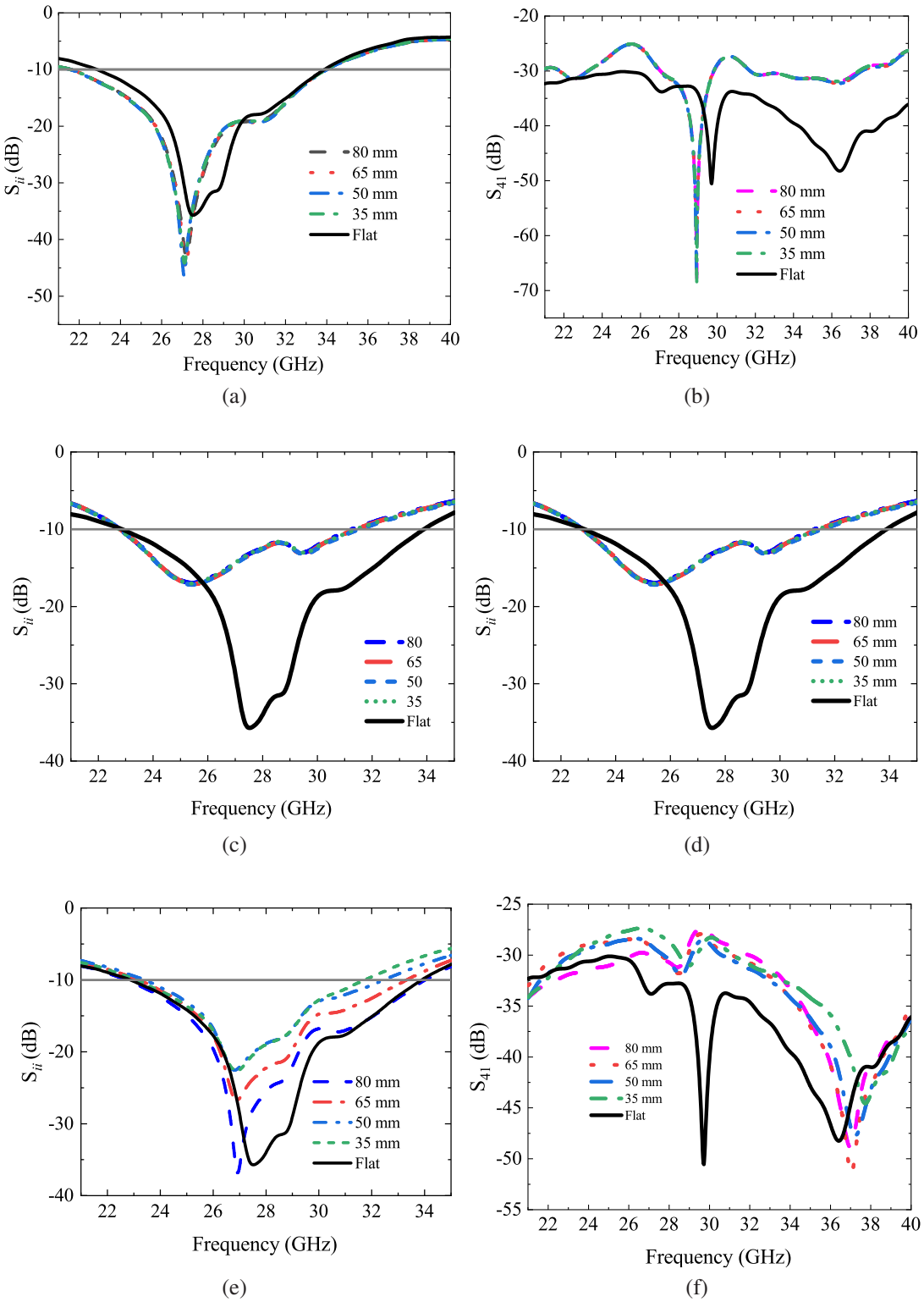

Figure 3.18: Reflection and transmission coefficients results of bending in (a) and (b) positive x-direction , (c) and (d) both positive and negative x-direction, (e) and (f) cylinder case. (S_{ii} represent S_{11} and S_{44}).

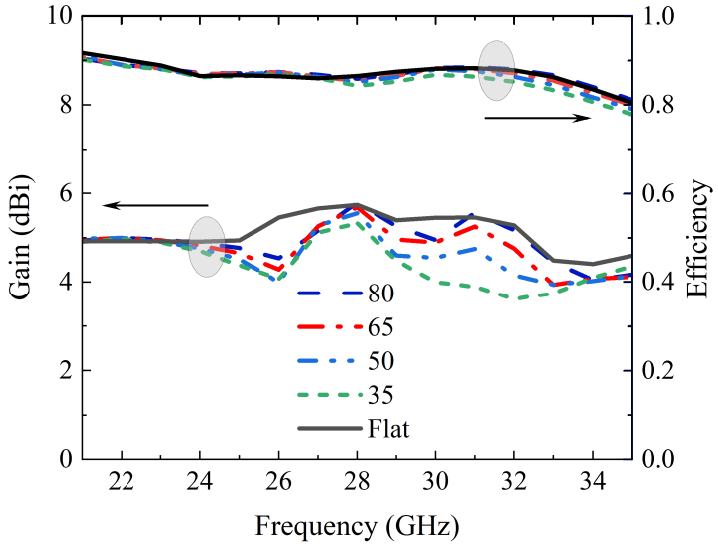

Figure 3.19: Gain and efficiency during bending conditions.

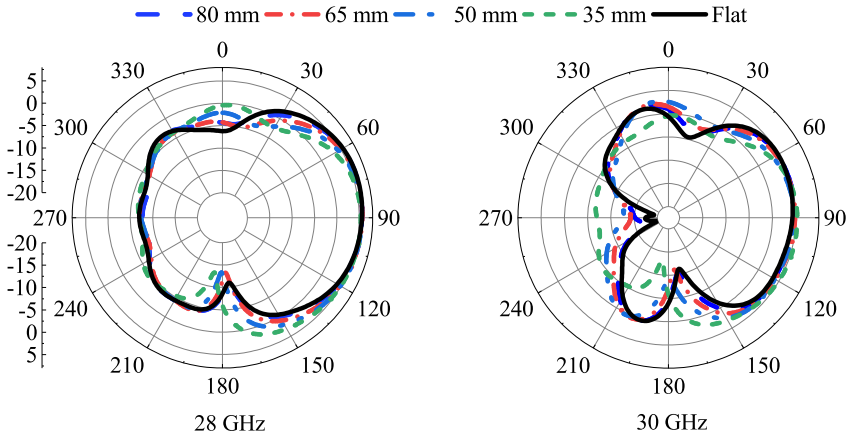

Figure 3.20: E-plane radiation pattern during bending conditions.

3.2.6 Antenna on-body analysis

To analyse the impact of the human body on the performance of the designed MIMO antenna, the S-parameters, radiation patterns, efficiency, and gain were examined when antenna was placed on a human body voxel model called Gustav from CST Studio Suite bio models. The simulated setup is illustrated in 3.21. The antenna was positioned on the chest, arm, and leg regions. These regions were selected due to their potential as central nodes during communication in WBAN. It is important to note that the distance between the antenna and voxel body was 4.50 mm. This spacing was implemented to prevent maximum radiation absorption beneath the antenna elements by the body. Furthermore, this gap approximates the thickness of clothing, thus representing wearable realistic scenarios. Each scenario is discussed in details in following sections.

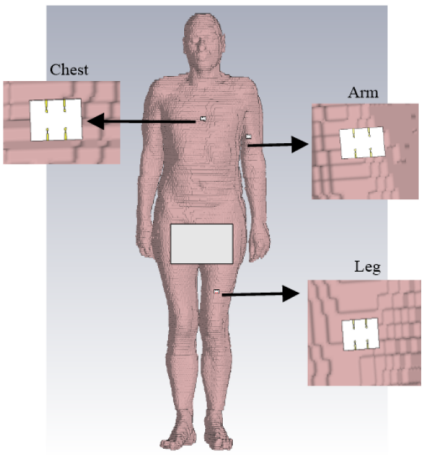

Figure 3.21: MIMO antenna on the chest, arm, and leg of the Gustav body model.

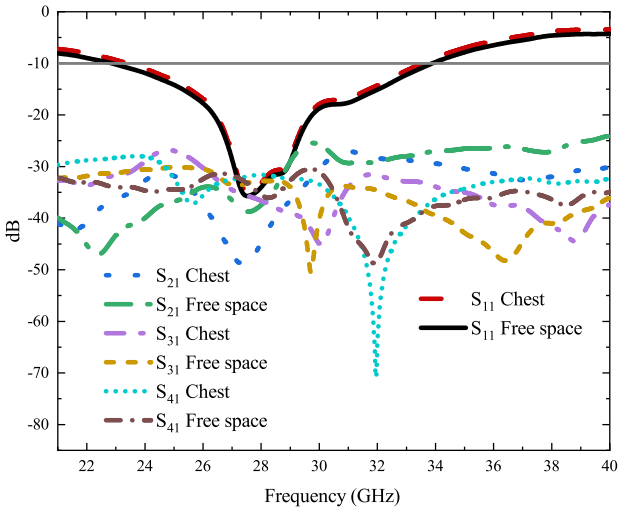

Figure 3.22: S-parameters when MIMO antenna is placed on chest region.

3.2.6.1 MIMO antenna on chest

The simulated S-parameters results when the MIMO antenna was placed on the chest region are shown in Fig. 3.22. The impedance bandwidth of the MIMO antenna when placed on the chest region exhibits approximately the same impedance bandwidth. The transmission coefficient indicates variations due to absorption and reflections of the chest region, which affect the current flow between antenna elements. Nevertheless, the mutual coupling remains below -25 dB in impedance bandwidth. Similarly, the two principle E and H radiations when MIMO antenna is placed on chest are compared with free space and are shown in Fig. 3.23(a). The radiation patterns for both E- and H-planes exhibits a consistent endfire radiation pattern in E plane whereas broadside in H-plane across both scenarios. However, the minor pattern distortions primarily attributed to the interaction between the antenna's near field and the lossy human tissue. Nevertheless, the antenna maintains its overall directional characteristics. Fig. 3.23(b) presents an analysis of the antenna's gain and efficiency. The peak gain of roughly 5.8

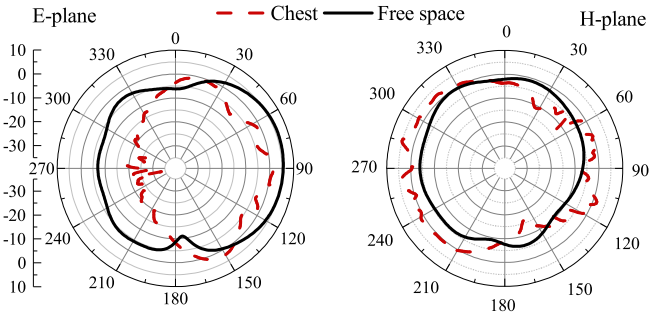

(a)

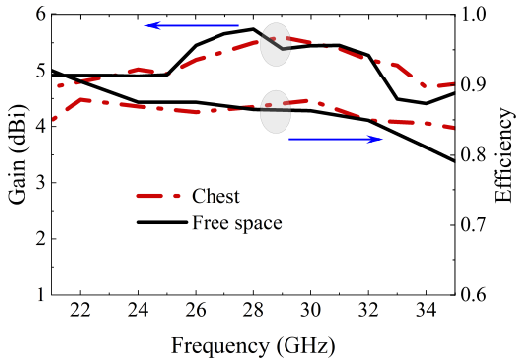

(b)

Figure 3.23: On chest results (a) E and H planes and (b) gain and efficiency.

dBi in free space was marginally reduced to 5.2 dBi. The efficiency remains high in both scenarios, exceeding 0.85. A minor efficiency decrease is observed which can be attributed to the lossy nature of human chest tissues.

3.2.6.2 MIMO antenna on arm

Figure 3.24 shows the S-parameter results for the MIMO antenna placed on the arm region compared to free-space conditions. The impedance bandwidth experienced a slight shift due to the proximity to the arm, spanning from 24.30 GHz to 33.79 GHz. Despite this shift, the antenna successfully covers most of the target frequency range. Importantly, the mutual coupling levels remain consistently below -25 dB. These results confirm that the interaction with the arm region primarily impacts the impedance bandwidth, while the desired frequency coverage and mutual coupling characteristics are largely preserved.

A comparative analysis of the performance of the MIMO antenna concentrating on the radiation patterns in the E- and H-planes as well as the gain and efficiency metrics are shown in Fig. 3.25. In both the E-plane and H-plane in Fig. 3.25(a), the antenna shows minor variations in planes. Although the fundamental shape of the patterns is preserved, the antenna has still endfire and broadside radiation patterns. The gain and efficiency in Fig. 3.25(b) indicate a marginal decrease in performance. The gain

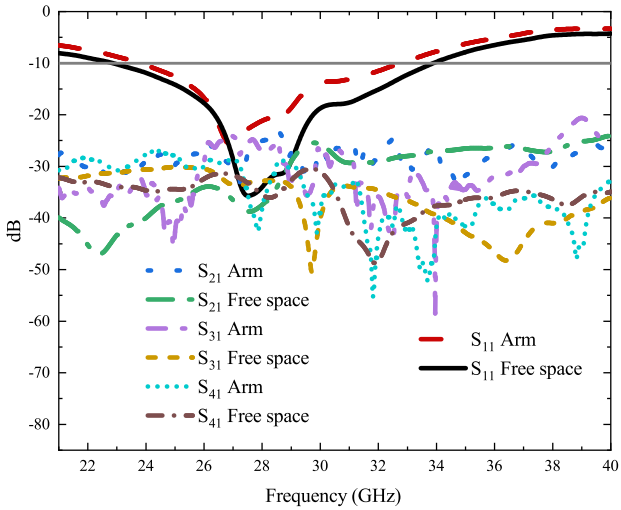

Figure 3.24: S-parameters when MIMO antenna is placed on arm region.

diminishes by approximately 0.5-1 dB across the operational frequency spectrum, with a peak gain of 5 dBi in free space decreasing to nearly 4.5 dBi upon arm placement. Correspondingly, the efficiency experiences a slight reduction from approximately 85% in free space to around 80% when situated on the arm.

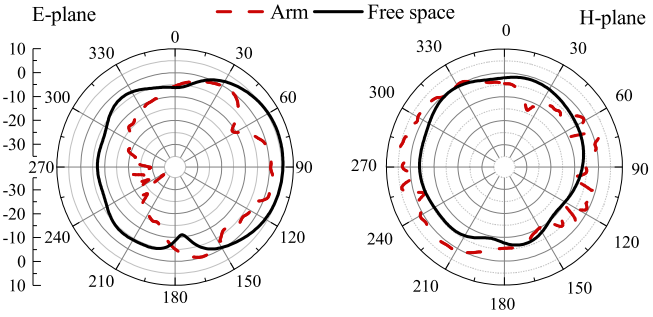

(a)

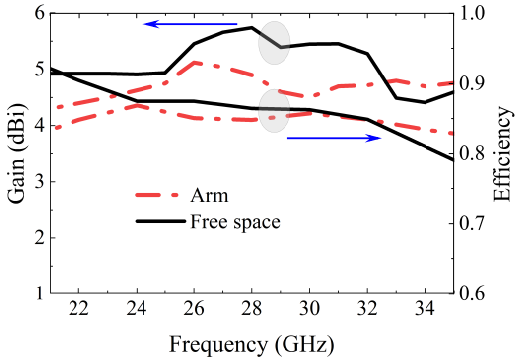

(b)

Figure 3.25: On arm results (a) E and H planes and (b) gain and efficiency.

3.2.6.3 MIMO antenna on leg

The performance of the MIMO antenna when placed in the leg region are shown in Figs. 3.26 and 3.27. The S-parameters in Fig.3.26(a) indicate a marginal alteration in impedance bandwidth. In this case the impedance bandwidth range from 24.10 GHz to 33.50 GHz. Compared to placement on the chest and arm regions, this case also posses the mutual coupling less than -25 dB in average across most part of the impedance bandwidth.

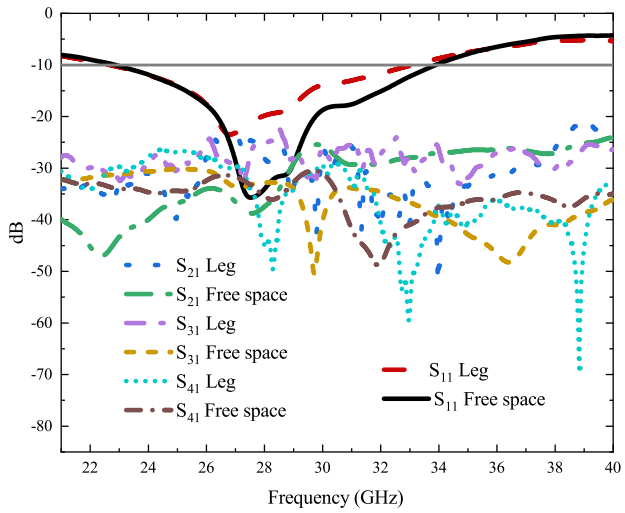

Figure 3.26: S-parameters when MIMO antenna is placed on leg region.

The radiation patterns presented in Fig.3.27(a) shows more distortions in the E- and H-planes when the antenna is positioned on the leg. These distortions arise from bending curvature of the leg region; however, they do not substantially impair the overall endfire and broadside directional capabilities of the designed MIMO antenna. Similarly, the Fig. 3.27(b) shows the gain and efficiency of the antenna across both free space and on the leg region. The results show that the gain experiences a reduction of approximately 0.5-1 dB in the bandwidth when MIMO antenna was placed on the leg compared to free space. Here, a peak gain of approximately 5 dBi on the leg in contrast to 5.50 dBi in free space was observed. The efficiency also exhibits a slight reduction from approximately 85% in free space to a range to around 78% during antenna placement on the leg region. Despite these reduction, the adesigned MIMO antenna still upholds acceptable performance metrics for wearable applications.

In conclusion, the key findings results from all three MIMO placement on Gustav model are summarized in 3.2. Although the proximity to the human body induces minor alterations in bandwidth and slight reductions in gain and efficiency, the antenna retains its mutual coupling, impedance matching, and overall operational efficacy. This substantiates its appropriateness for wearable applications, even within the constraints of challenging body-worn environments.

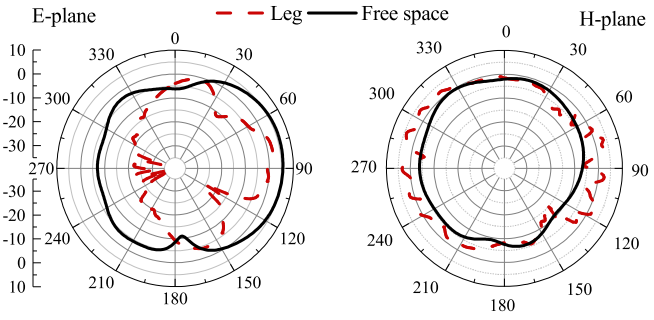

(a)

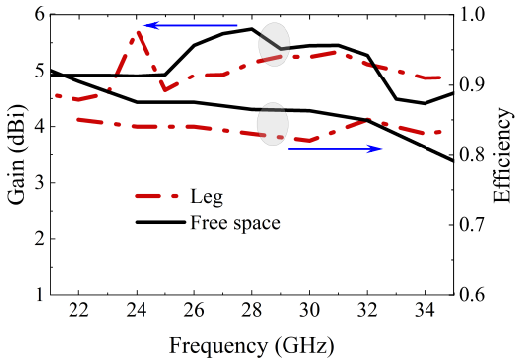

(b)

Figure 3.27: On leg and free space comparison (a) E and H planes, (b) gain and efficiency.

Table 3.2: Summary of results when MIMO antenna is placed on Gustav model.

Placement	Impedance Bandwidth (GHz)	Peak Gain (dBi)	Efficiency (Avg)	Mutual Coupling (dB)
Free space	22.97 - 33.91	5.73	0.87	< -30
Chest	23.12 - 33.86	5.61	0.87	< -25
Arm	24.30 - 33.79	5.25	0.80	< -25
Leg	24.60 - 33.85	5.13	0.78	-25

3.2.7 Investigation of the MIMO antenna on denim fabric material

As the designed MIMO intended for wearable applications, fabric analyses were conducted specifically to examine the bandwidth and mutual coupling. The wearable fabric materials can induce signal scattering and reflection, thereby potentially altering the antenna impedance. To investigate this phenomenon, a denim fabric was designed and positioned beneath the antenna without any spacing as shown in Fig. 3.28. The permittivity of the denim fabric was selected to be 1.79 [121] within the operational bandwidth of the antenna. The thickness (d) of the denim fabric was varied from 1 mm to 6 mm, and the impact on S-parameters was observed. As previously noted, most garments have a maximum thickness of up to 5 or 6 mm; therefore, the results were

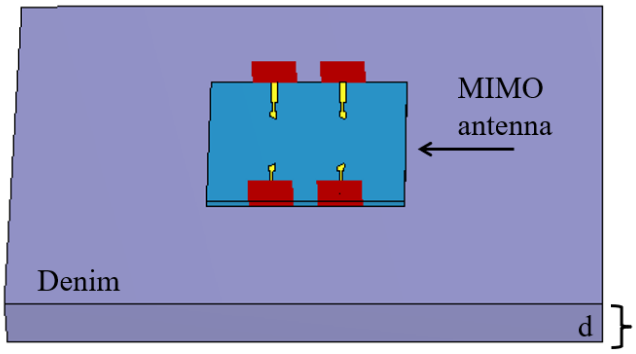

Figure 3.28: Placement of MIMO antenna on denim fabric material.

considered only up to this thickness.

The impedance bandwidth results of each antenna element with variations in thickness are presented in Fig. 3.29(a). The results demonstrate that an increase in thickness does not significantly alter the bandwidth shift in frequencies. Although a lower reflection (-70 dB at 28 GHz) was observed in the case of 1 mm, while approximately equivalent reflection was noted for all other frequencies. This effect diminished as the thickness increased, and the antenna approached the free space condition at approximately 6 mm. The impact of mutual coupling levels with variations in denim thickness are provided in Fig. 3.29(b)-(d). The coupling level between antennas 1 and 2 (S_{21}) almost remains below -22 dB in whole impedance bandwidth and has minimal impact as thickness of denim increases. In this case the coupling levels are extremely low near 27 GHz and 28 GHz. Similarly, S_{31} between antennas 1 and 3 the coupling levels are below -25 dB, although it exhibits some more sensitivity (in terms of reduction) to increasing fabric thickness, particularly beyond 3 mm. The coupling between antennas 1 and 4 (S_{41}) exhibits the more coupling levels but decreases as thickness increases. the overall mutual coupling remains decreasing with increasing the thickness. This can be attributed to the presence of more permittivity quantity as it adds with the permittivity of the substrate (2.2 + 1.78 = 3.98). From the mutual coupling investigation it can be observed that surface waves can be significantly reduced in high permittivity materials. Hence, while slight resonance frequency shifts and coupling variations are observed, the designed MIMO antenna maintains adequate impedance matching and low mutual coupling across all tested thicknesses.

3.3 Experimental and measurement results analysis of Vivaldi MIMO antenna

The MIMO antenna was fabricated utilizing an LPKF PCB prototype machine, and subsequent measurements were conducted using a vector network analyzer (VNA)

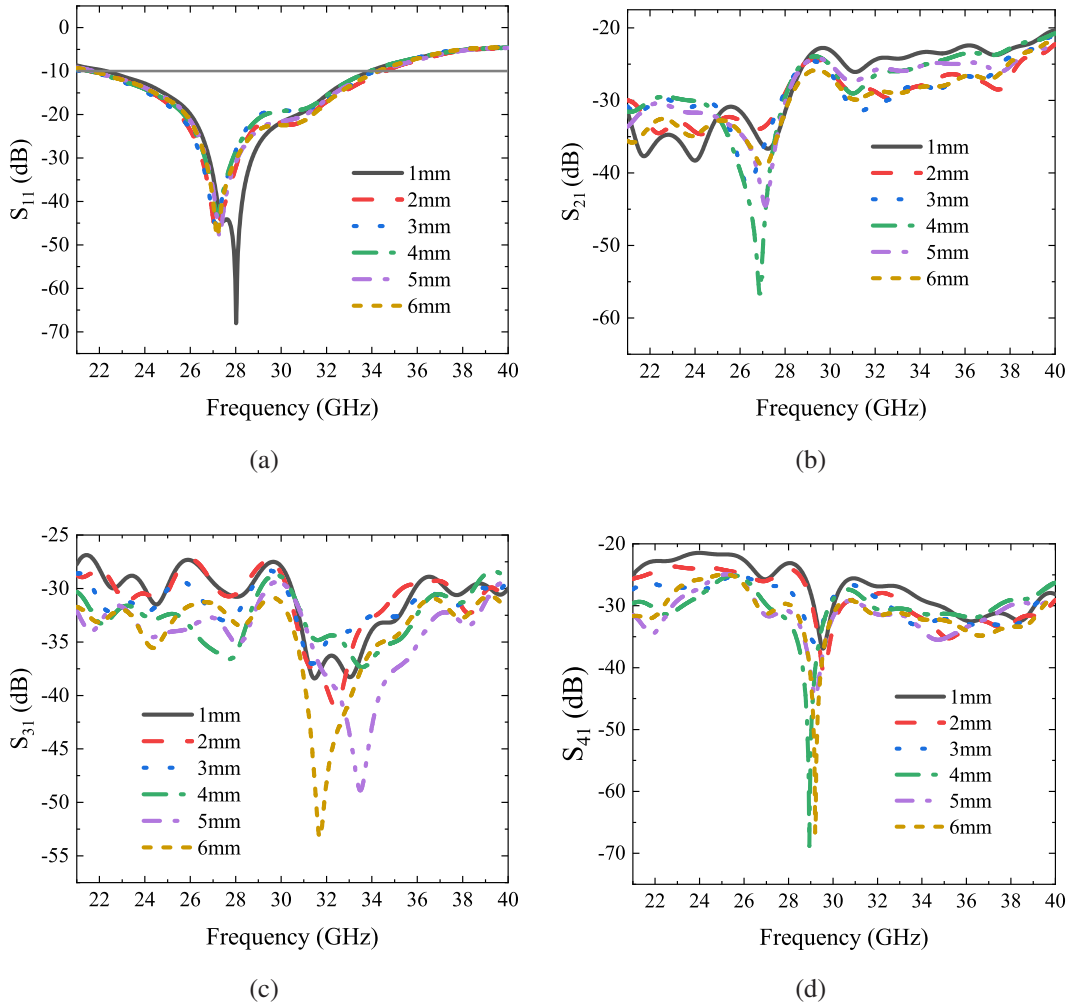

Figure 3.29: Impact of denim thickness on MIMO antenna (a) reflection coefficients of antenna 1 (b) coupling between antenna 1 and 2, (c) coupling between antenna 1 and 3, and (4) couping between antenna 1 and 4.

from the Keysight series PNA-X N5247B. As the VNA is extensively employed for S-parameter and transmission coefficients (mutual coupling) analysis in this thesis, a brief introduction to VNA usage and theory is provided.

3.3.1 Introduction to VNA

Calibration of any VNA is a critical step before utilizing it to measure S-parameters. Two primary calibration methodologies exist: the conventional approach employing mechanical connectors and the more contemporary electronic calibration (E-cal). The mechanical method typically utilizes open, short, load, and through connectors. While efficacious, this technique is time-intensive and susceptible to human error. Conversely, E-cal instruments offer a highly efficient and precise calibration process, mitigating systematic errors caused by cable losses, connector mismatches, and other measurement setup imperfections. E-cal modules automate the procedure, rendering

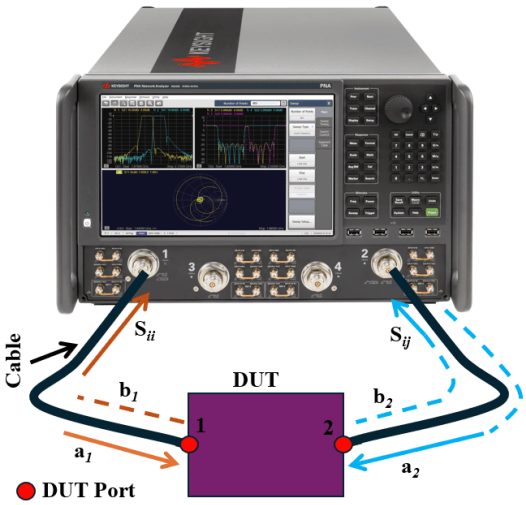

Figure 3.30: S-parameters measurements of DUT using VNA.

it more expeditious and less error-prone compared to mechanical calibration. For all measurements in this thesis, a Keysight E-cal module compatible with the PNA-X N5247B VNA was employed.

Subsequent to calibration, the measurement process commences by connecting the DUT, typically an antenna, to the VNA ports. The VNA functions by generating a known RF signal at a port and analyzing the DUT's effect on this signal. The setup of measuring a two port DUT using VNA is shown in Fig. 3.30. VNA assesses the DUT's frequency response by measuring both the amplitude and phase of transmitted and reflected signals. This analysis yields valuable information regarding antenna characteristics, including impedance, return loss, transmission, group delay etc.

A VNA measures the S-parameter as follows:

$$S_{11} = \frac{b_1}{a_1} = \text{input reflection coefficient}$$

$$S_{12} = \frac{b_1}{a_2} = \text{reverse transmission coefficient (mutual coupling in MIMO antenna)}$$

$$S_{21} = \frac{b_2}{a_1} = \text{forward transmission coefficient (mutual coupling in MIMO antenna)}$$

$$S_{22} = \frac{b_2}{a_2} = \text{reverse reflection coefficient}$$

Where a_1 = incident signal on port 1, a_2 = incident signal on port 2, b_1 = reflected signal from port 1, and b_2 = reflected signal from port 2. In the analysis of multi-port devices such as MIMO antennas, a VNA facilitates both reflection and transmission measurements. In reflection measurements (S_{11}, S_{22} etc.), the VNA measures the magnitude of signal reflected back to the input source, thereby showing the quality of perfect impedance matching scenarios in the MIMO antenna. The optimal matching of antenna typically have a reflection coefficient below -10 dB. Conversely,

transmission measurements (S_{21}, S_{31}, etc.) involve the VNA quantifying the signal propagation from one port to another, thus enabling the assessment of mutual coupling or isolation between antenna elements.

3.3.2 Measurement results analysis

The prototype of the fabricated Vivaldi MIMO antenna, shown in Fig. 3.31, includes its top and bottom views (a) and the measurement setup (b). Using a VNA, S-parameters were measured under free-space conditions to evaluate the antenna's impedance matching and mutual coupling performance.

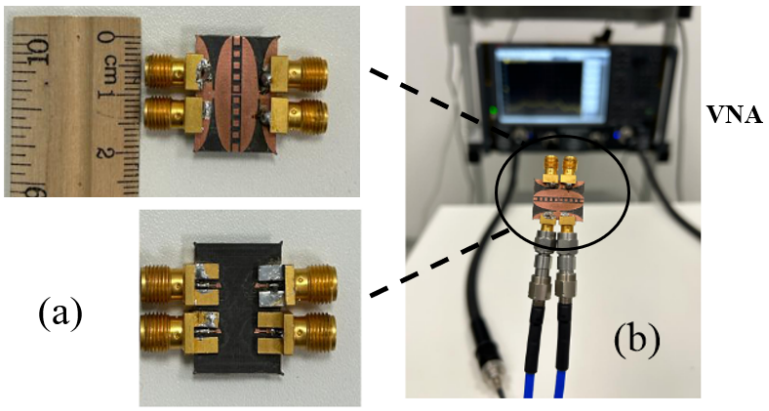

Figure 3.31: (a) Prototype of Vivaldi MIMO antenna bottom and top faces and (b) S-parameter measurements using a VNA.

The S-parameter results of the MIMO antenna for all four elements in free space conditions are presented in Fig.3.32. The simulated reflection coefficients are compared with measurement results and are illustrated in Fig.3.32(a). The results demonstrate strong agreement between simulation and measurement, with the measured data confirming an impedance bandwidth of 23–34 GHz. Fig.3.32(b) shows the mutual coupling between antenna elements. Both simulated and measured results indicate that mutual coupling values remain below -20 dB across the entire impedance bandwidth, ensuring high isolation between elements. While minor discrepancies are observed between simulated and measured results, these are within acceptable limits, likely attributable to fabrication tolerances and environmental factors during measurement. The measured results confirm that the fabricated prototype meets the design requirements established by the simulation results.

The performance of the designed MIMO antenna under wearable conditions particularly on the chest, arm and leg region was assessed as shown in Fig. 3.33(a). The reflection coefficients results for these on-body placements are compared against free space conditions in Fig. 3.33(b). The results demonstrates that the MIMO antenna placement on the body still maintains a operational impedance bandwidth as of free

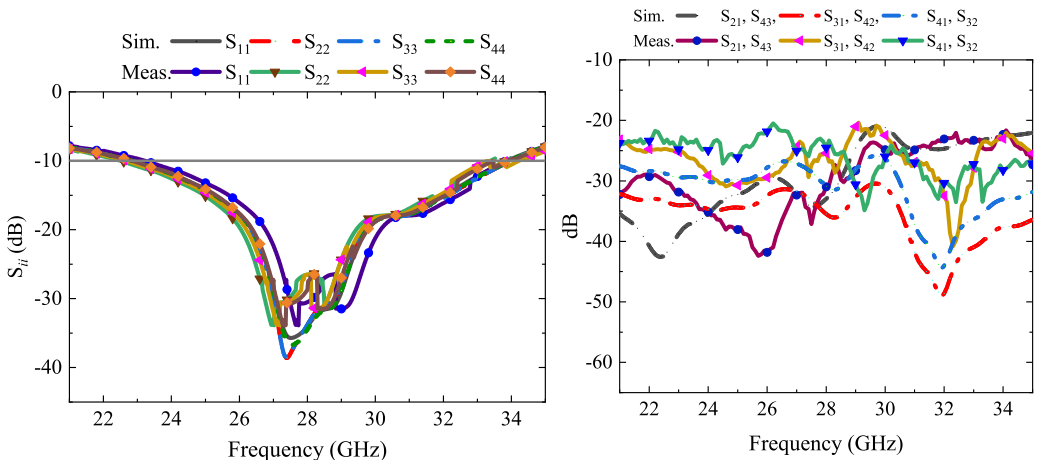

Figure 3.32: Simulation and measured S-parameters comparison (a) reflection coefficients and (b) transmission coefficients.

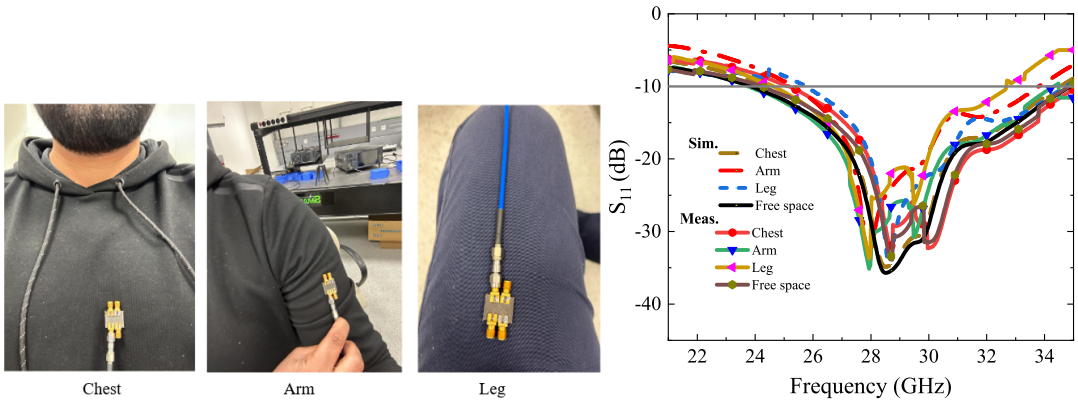

Figure 3.33: (a) MIMO antenna position on chest, arm and leg positions (b) and respective reflection coefficients.

space conditions in all tested scenarios, indicating effective impedance matching. However, on-body placements exhibit slight shifts in resonance frequencies and minor variations in return loss compared to free space. As discussed earlier in the simulation data part that these changes are attributed to the interaction of em waves with the human body and placement on the fabric material. The arm and leg placements show somewhat more pronounced effects than the chest placement. Nevertheless, the antenna still exhibits satisfactory bandwidth performance across all conditions, demonstrating its robustness and suitability for wearable applications.

3.3.2.1 Gain measurements in anechoic chamber

The gain measurements of MIMO antenna were conducted in a Rhodes & Schwarz RS®ATS1800C 5G anechoic chamber. The chamber constitutes an advanced testing

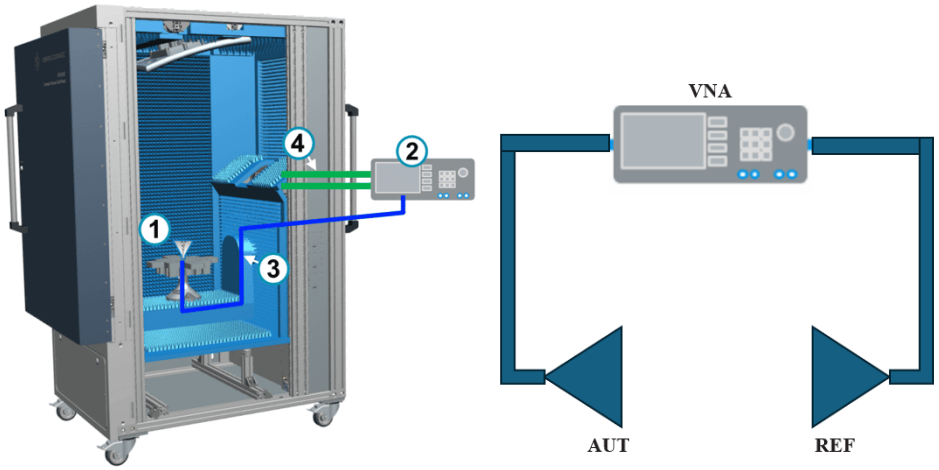

(a) (b)

Figure 3.34: (a) Anechoic chamber view and (b) depiction of gain transfer method.

platform for conducting over-the-air (OTA) measurements on 5G devices and antennas. This chamber establishes an isolated, noise interference-free environment for evaluating devices in the mmWave frequency spectrum, particularly at Ka band (26-40 GHz), which is crucial for 5G technology. Incorporating state-of-the-art reflectors and absorbers, it facilitates precise assessment of radiation patterns and gain measurements. The side view of the anechoic chamber connected to a VNA is shown Fig. 3.34(a) where different points are highlighted, the details of which are as follows: 1 = Reference antenna, 2 = VNA, 3 = RF cable from VNA to reference antenna, and 4 = Two RF cables from VNA to feed antenna. This chamber uses gain transfer method for measurements of gain and principle radiations patterns as shown in Fig. 3.34(b). In this method, a set of reference antennas (typically a horn antenna) is used with known gain. The reference antenna provides a known received power P_{ref}, and has a known gain, G_{ref}. The power reception is then measured for AUT antenna. The received power of the AUT, denoted as P_{AUT}, is measured under identical conditions. The difference between the received powers of the AUT and the reference antenna (P_{AUT} and P_{ref}) corresponds to the difference in their gains. Using this difference, the gain of the AUT, G_{AUT}, can be calculated with the following equations 3.7 and 3.8 as follows:

$$G_{\text{AUT(dB)}} = G_{\text{ref(dB)}} + \Delta_{\text{(dB)}} \tag{3.7}$$

where

$$\Delta_{\text{(dB)}} = P_{\text{AUT(dB)}} - P_{\text{ref(dB)}} \tag{3.8}$$

Two sets of measurements were conducted for gain measurements of the designed MIMO antenna. First, free-space analysis was performed by measuring the received power levels in both E and H planes. As the MIMO antenna is intended for use in wearable applications, in the second set, a phantom (meat) was placed behind

the fabricated MIMO, and the same measurement analysis was performed. The measurement setup for both cases is shown in Fig. 3.35.

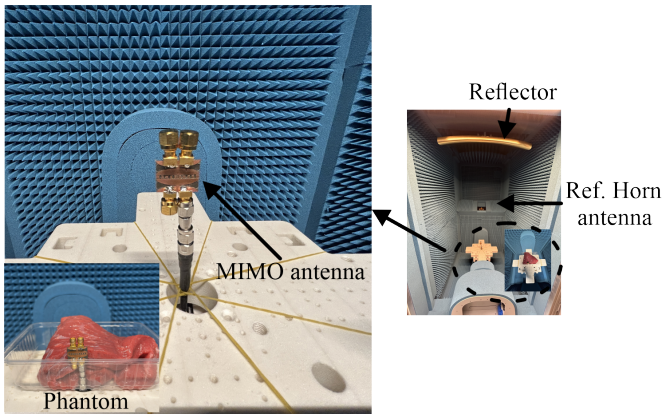

Figure 3.35: MIMO antenna gain measurement in free space and on a meat phantom inside an anechoic chamber.

The MIMO antenna's E-plane and H-plane radiation patterns were evaluated at 28 GHz and 30 GHz, with measured results compared to simulations as shown in Fig. 3.36. The comparison revealed excellent correlation between simulated and measured data, especially in end-fire and broadside radiation directions, validating the antenna design and simulation models under free-space conditions. Nevertheless, significant discrepancies were noted when measurements were conducted with a meat tissue-mimicking phantom present which can be explained by multiple factors. Firstly, manufacturing imperfections in misalignment may impact antenna gain performance. Secondly, the phantom creates a more lossy environment than free space, resulting in increased absorption and scattering of EM waves. Despite these differences, the antenna maintained its fundamental radiation characteristics, indicating that the design is resilient and appropriate for wearable applications, even when interacting with lossy environments. The MIMO antenna's measured gain and efficiency were determined at various frequencies, both in free space and when positioned on the phantom. These results are presented in Fig. 3.37. It is imperative that the MIMO antenna, when positioned on the human body, should not undergo significant alterations and should maintain consistent gain and efficiency. The designed MIMO antenna demonstrates almost same gain and efficiency across its operational impedance bandwidth, even in the presence of the phantom both in simulations and measurements.

3.4 Diversity analysis of the designed MIMO antenna

This section analyses the performance of the designed MIMO antenna through an assessment of the diversity parameters, including the TARC, ECC, and DG.

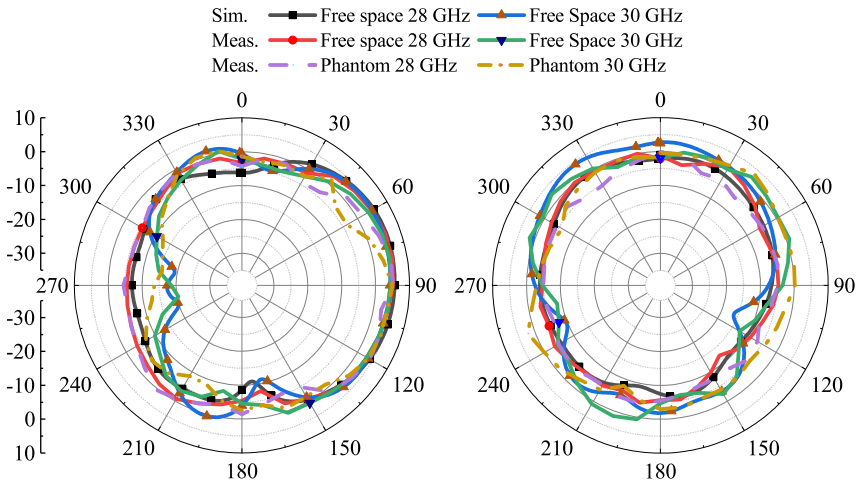

Figure 3.36: Simulated and measured radiation patterns of the MIMO antenna compared at 28 GHz and 30 GHz: on the left is E-plane whereas H-plane on the right side.

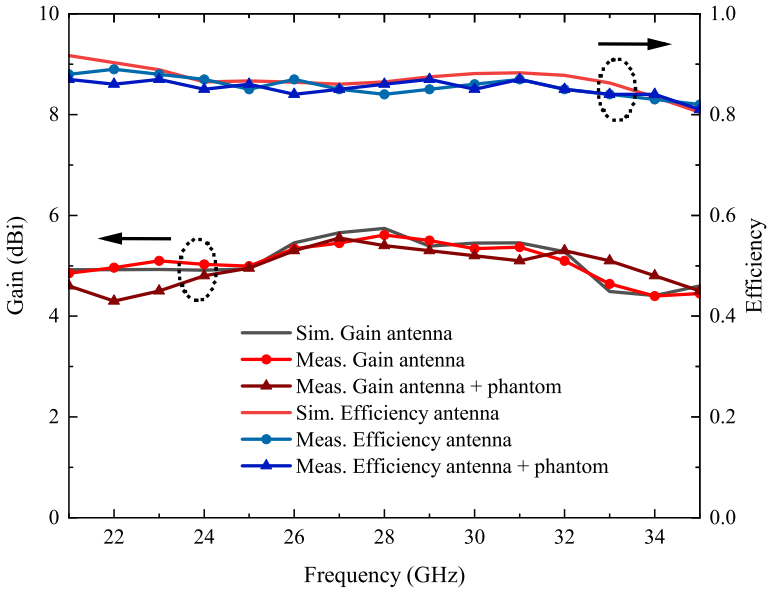

Figure 3.37: Simulated and measured gain and efficiency of the MIMO antenna.

3.4.1 TARC analysis

The TARC of the designed MIMO antenna was analyzed for $0°$, $45°$, and $90°$ under two scenarios: free space conditions and on-body placement. The results demonstrated in Fig. 3.38 that the TARC remains below -10 dB across the entire operational bandwidth in free space, spanning from approximately 22 GHz to 34 GHz. This indicates that the antenna maintains efficient signal transmission and reception with minimal power losses due to changes in input. In free-space conditions, the TARC exhibits consistent behaviour. Conversely, the TARC values for on-body placement, while marginally higher than in free space, still remain below the critical threshold of -10 dB. The minor

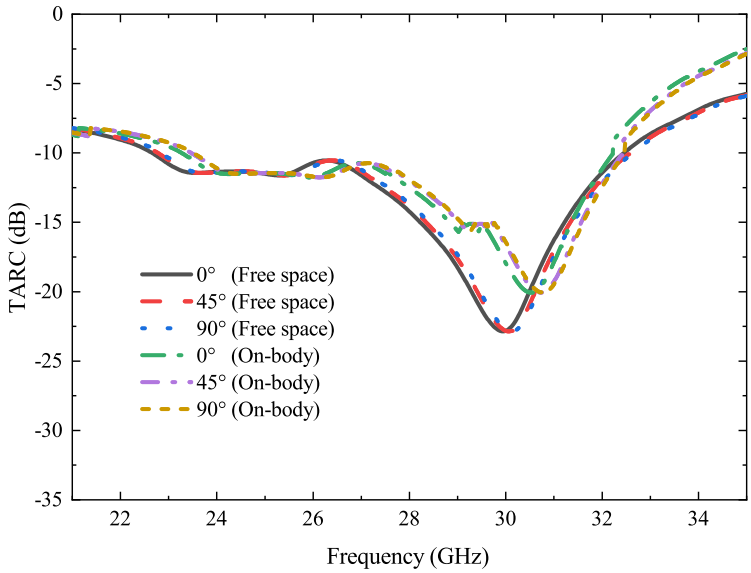

Figure 3.38: TARC of the MIMO antenna in free space and on the body.

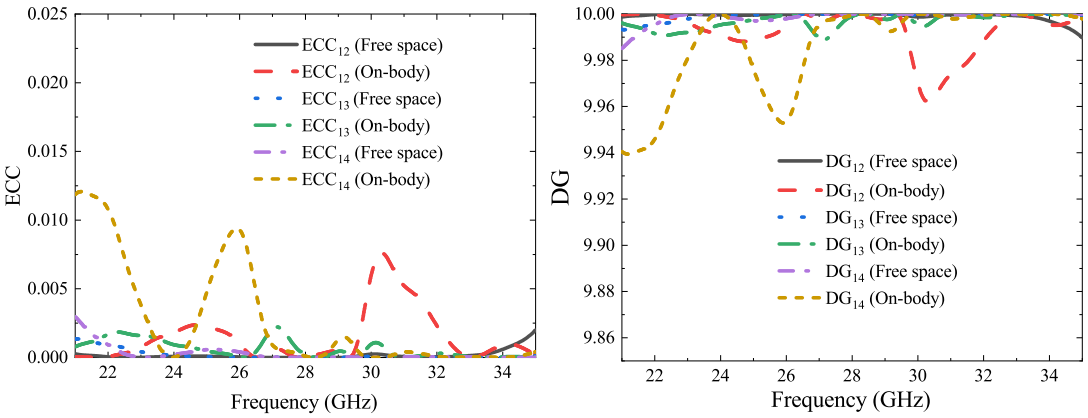

(a) (b)

Figure 3.39: (a) ECC and (b) DG of the MIMO antenna.

variations in on-body measurements are attributed to the lossy nature of human tissue, which affects the EM environment. Despite these variations, the antenna continues to perform efficiently, demonstrating its resilience to the challenging on-body environment.

3.4.2 ECC and DG analysis

The results of the ECC and DG both in free space and on the body are shown in Fig. 3.39. ECC in both cases are significantly below the acceptable threshold value of 0.5 across the entire operational bandwidth. This indicates minimal correlation between the radiation patterns of the antenna elements, even in on-body scenarios, ensuring effective spatial diversity. Furthermore, the DG values consistently approach the ideal value of 10 dB, demonstrating the antenna's capacity to achieve near-optimal diversity performance. The results substantiate that the proposed MIMO antenna maintains

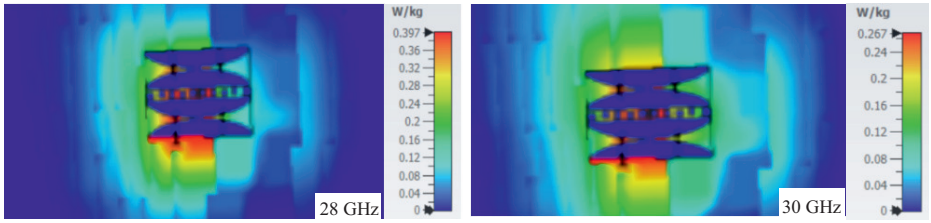

Figure 3.40: SAR distribution of the MIMO antenna.

Table 3.3: Designed Vivaldi MIMO antenna comparison with other reported works.

Ref. No	[122]	[123]	[124]	[125]	Designed
Type	Yagi	Rectangle	Microstrip	Circular	Vivaldi
Band	mm-wave	mm-wave	ISM	mm-wave	mm-wave
Bandwidth (GHz)	0.9	0.80	2.80	0.01	10.94
Substrate	Single	Two	Single	Single	Single
Dimensions (mm)	14.9×17.4	5 × 19	14 × 17	60 × 60	16 × 20
Gain (dBi)	5.20	6.00	7.50	0.82/2.83	5.65
Efficiency	–	0.80	0.80	0.60	0.86
Bending analysis	Yes	Yes	No	Yes	Yes
Antenna elements	-	2	-	-	4

robust performance in both free space and on-body conditions, rendering it suitable for wearable applications.

3.5 SAR analysis

The designed Vivaldi antenna MIMO antenna was positioned 4.50 mm above the arm region of the Gustav voxel model within CST Studio Suite for SAR analysis. The evaluation followed the IEEE C95.1-1999 standard, which defines a maximum permissible SAR of 1.6 W/kg for 1g of biological tissue. To maintain consistency with typical wearable device power levels, an input power of 17 dBm (50 mW) was applied during the simulation. The SAR distribution was analyzed at 28 GHz and 30 GHz, as depicted in Fig. 3.40. The highest levels of EM energy absorption were recorded directly beneath the MIMO antenna. The maximum SAR values at 28 GHz and 30 GHz were found to be 0.397 W/kg and 0.267 W/kg, respectively. These values remain significantly below the regulatory threshold of 1.6 W/kg, confirming that the Vivaldi MIMO antenna design is safe for wearable WBAN applications.

A comparative analysis of the desgined MIMO antenna with other antenna designs is reported in 3.3. The designed Vivaldi MIMO antenna demonstrates significant advantages over existing designs in terms of bandwidth, efficiency, flexibility, and MIMO capability. Notably, the antenna achieves a wide bandwidth of 10.94 GHz,

which is substantially higher than the reported Yagi [122] , rectangular [123], microstrip [124], and circular antennas [125]. Additionally, the proposed antenna attains a gain of 5.65 dBi, ensuring stable performance across the operating frequency bands. While the microstrip antenna in [124] exhibits a slightly higher gain 7.50 dBi, it lacks flexibility and is unsuitable for wearable applications. Another key advantage of the designed antenna is its compact size (16 $\times$ 20 mm), which is considerably smaller than [125] while maintaining a wider operational bandwidth. Unlike the rectangular antenna in [123], which requires a two-layer substrate, this design employs a single-layer structure, leading to a simpler and more cost-effective fabrication process. Furthermore, the Vivaldi MIMO antenna is designed for bending analysis, ensuring its suitability for flexible and wearable applications, whereas the microstrip antenna in [124] lacks this capability. The antenna also achieves an efficiency of 0.86 which is more than most existing designs. Additionally, its 4-element MIMO configuration enhances spatial diversity and signal robustness, a feature absent in most of the reported antennas. This superior performance, coupled with its high efficiency and compact form factor, makes the designed Vivaldi MIMO antenna an excellent candidate for next-generation wearable and flexible mmWave communication systems, including 5G, IoT, and WBAN.

3.6 Conclusion

This chapter presented the design and analysis of a low-profile mmWave Vivaldi MIMO antenna for wearable WBAN applications. The design incorporates a four-element MIMO structure that operates within the mmWave band, specifically targeting the 28 GHz and 30 GHz frequencies, with a fractional bandwidth of 36.4%. The chapter also highlighted the challenges of mutual coupling and a FSS based decoupling technique. The Vivaldi antenna's wide bandwidth and directional end-fire radiation patterns reduce the requirement for additional metamaterial-backed layers, which are frequently employed to mitigate heat absorption by the human body. Conformability analysis was evaluated under various bending conditions to simulate real-world usage on different body parts. The results indicate that the antenna maintains consistent efficiency and radiation characteristics even when bent, demonstrating its suitability for wearable applications. Additionally, the chapter discusses the impact of fabric on antenna performance, noting that denim, used as a substrate, has minimal effect on performance up to a certain thickness. The design also ensures that the SAR remains within safe limits when placed on the human body. Overall, the designed MIMO antenna offers a compact, efficient, and safe solution for wearable WBAN applications, with high DG and low ECC and TARC values. A comparative analysis with other reported work demonstrated that the designed MIMO exhibits superior characteristics compared to other works.

Chapter 4

High-Isolation Dual-Band mmWave MIMO Antenna for WBAN: Design and Coupling Reduction with DGS and FSS

4.1 Introduction

The introduction of 5G technology has transformed the IoT ecosystem owing due to the fact that it facilitates fast data processing and transmission. This technology shift is essentially advantageous for various IoT applications, including intelligent urban environments, self-driving vehicles, and medical services [126]. For efficient 5G communication in a IoT smart city, the mutli-band MIMO antennas are essential as shown in Fig. 4.1.

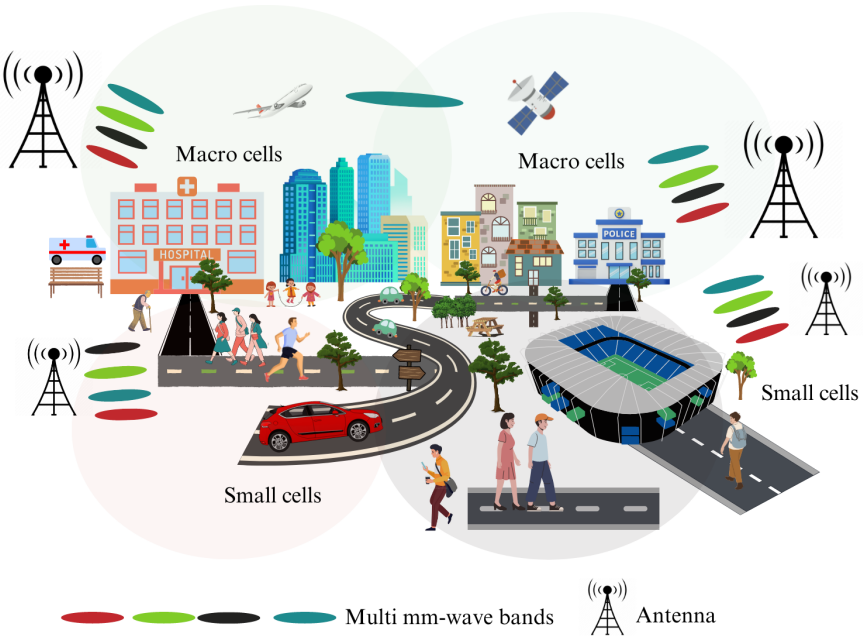

Figure 4.1: Applications of multi mmWave bands antennas in IoT smart city environment.

Multi-band antennas play a crucial role as they function effectively without interference by dynamically switching between frequency bands. Furthermore, multi-band antennas maximize spectrum utilization by allocating different frequency bands to various services. By distributing users and applications across multiple frequency bands, multi-band antennas also mitigate congestion, particularly in high-traffic zones such as stadiums, commercial areas, and healthcare facilities [127]. This results in enhanced network reliability and reduced service interruptions, rendering multi-band mmWave antennas an essential component of smart city infrastructure.

The design and implementation of multi-band MIMO antennas present numerous challenges [128]. A significant issue is the complexity of antenna design and fabrication, as optimizing antenna geometry for multiple frequency bands poses considerable difficulties. Mutual coupling constitutes another challenge. The dimensions and integration constraints are also critical factors, as multi-band antennas tend to be larger, thus complicating their incorporation into compact devices such as wearable and IoT sensors. Ensuring wide band impedance matching across multiple frequency bands presents an additional challenge, as variations in radiation patterns and impedance can result in signal losses. Addressing these challenges necessitates advanced antenna designs and techniques that have capabilities of multi-band operations .

To overcome these limitations, in this chapter a high-isolation six-element MIMO antenna operating at two distinct mmWave bands is thoroughly discussed. The antenna is made of a modified elliptical patch with rotating arms which achieve dual-band functionality, covering the ISM (24-24.25 GHz) and multiple 5G NR bands (24.25-27.50 GHz, 26.50-30 GHz, and 37-40 GHz). Inter-element isolation is enhanced through the integration of DGS and FSS, achieving isolation exceeding -33 dB while maintaining compact dimensions. The antenna demonstrates broadside radiation patterns, high gain, and excellent MIMO diversity parameters, including ECC below 0.012 and DG exceeding 9.96 dB. Furthermore, the design is validated through simulations, measurements, and SAR analysis, ensuring its suitability for wearable and IoT applications.

4.2 Design of single antenna element

The antenna was designed in the CST Studio and comprises multiple stages, as shown in Fig. 4.2 (a-d). A semi-flexible Rogers RT5880 substrate (dielectric constant = 2.2 and a loss tangent = 0.0009) is used with dimensions of $16 \times 16 \times 0.79$ mm^3. The copper thickness of 0.017 mm was utilized for the full ground plane and top patch. In the step 1 design, an elliptic-shaped patch was fed by a microstrip feed line. Similarly in the step 2, the elliptical shape patch was modified and cut in half. An extended arm was introduced in step-3, whereas step-4 incorporates two arms that are positioned and

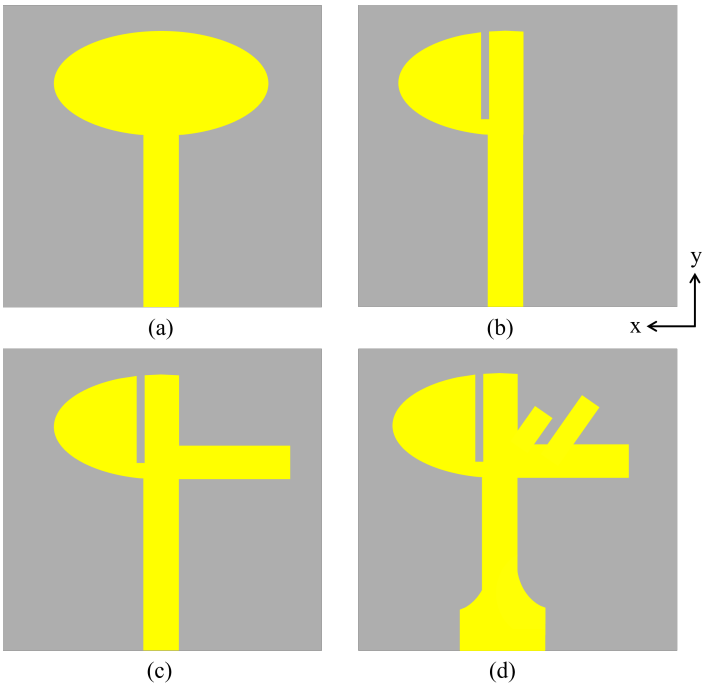

Figure 4.2: Development steps of antenna (a) step 1, (b) step 2, (c) step 3, and (d) step 4.

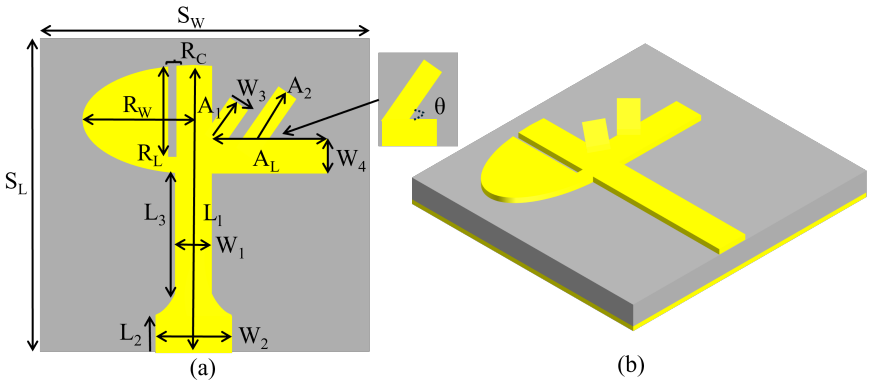

Figure 4.3: Final stage 4 single antenna: (a) dimensions, and (b) 3D view.

rotated. It is important to note that all these steps were performed in order to achieve the desired dual-band. Each of these steps were thoroughly analysed using CMA analysis in the following subsequent subsections. The final optimized single antenna element parameters are shown in Fig.4.3, whereas the values of each parameter are provided in 4.1. The 3D layout of the final stage design are presented in Fig.4.3.

The resonant frequency of an elliptical patch antenna can be calculated using equation 4.1 [129]. Here, $f_{11}^{e,o}$ refers to the two dual even- and odd-resonant frequency modes and ε_{r} represents the relative permittivity of the substrate. Variable e signifies the eccentricity of the elliptical shape, and $q_{11}^{e,o}$ is an approximated Mathieu function of the dominant TM11^{e,o} mode expressed in 4.2 and 4.3.

$$\mathrm{f_{11}}^{e,o} = \frac{15}{\pi e \mathrm{a_{eff}}} \sqrt{\frac{q_{11}^{e,o}}{\varepsilon_{\mathrm{r}}}} \tag{4.1}$$

Table 4.1: Parameters and dimensions of final single element antenna.

Parameter	Dimensions (mm)	Parameter	Dimensions (mm)
S_W	16.00	S_L	16.00
W_1	0.70	W_2	3.00
W_3	0.70	W_4	0.95
A_1	1.05	A_2	1.58
A_L	3.78	L_1	14.00
L_2	2.40	L_3	5.05
θ	130°	R_W	3.71
R_C	0.54	R_L	3.40

$$q^{11e} = -0.0049e + 3.7888e^2 - 0.7278e^3 + 2.314e^4 \tag{4.2}$$

$$q^{11o} = -0.0063e + 3.8316e^2 - 1.1351e^3 + 5.2229e^4 \tag{4.3}$$

The parameter a_{eff}, as defined in equation 4.4, represents the effective semi-major axis (measured in centimeters) and is used to account for the stored energy within the fringing field of an elliptical shape patch antenna [129].

$$a_{\text{eff}} = \left[a^2 + \frac{ha}{0.3525\pi\epsilon_{\text{eff}}}\left\{\ln\left(\frac{a}{2h}\right) + (1.41\epsilon_{\text{eff}} + 1.77) + \frac{h}{a}(0.268\epsilon_{\text{eff}} + 1.65)\right\}\right]^{\frac{1}{2}} \tag{4.4}$$

where *a* denotes the semi-major axis, *h* represents the substrate height, and ϵ_{eff} is the effective permittivity, as given by equation 4.5.

$$\epsilon_{\text{eff}} = \epsilon_r - 0.35\epsilon_r\left(\frac{h}{a} + \frac{h}{b} + \frac{h}{ab}\right) \tag{4.5}$$

4.2.1 CMA analysis

The CMA is a useful method for evaluating the surface current of a structure by determining its eigenvalue (λ_n) and the corresponding eigen current (J_n). In the field of antenna design, CMA is an effective tool because it predicts the radiation behaviour of an antenna structure by analysing the surface current without requiring any external excitation [130]. Accordingly, all four stages in were progressively analysed using CMA by using CST Multilayer solver.

The CMA theory explain that the random bodies through orthogonal characteristic modal currents and weighted eigenvalues can result in the support of multi-characteristic modes [131] as in equation 4.6.

$$XJ_n = \lambda_n RJ_n \tag{4.6}$$

In this context, λ_n denotes the eigenvalue, J_n refers to the surface current, and $[R, X]$ represents the real and imaginary parts of the impedance operator $Z(J_n)$ in 4.7.

$$Z(J_n) = R(J_n) + jX(J_n) \tag{4.7}$$

Here, $X(J_n)$ signifies the characteristic modes associated with energy storage. To ensure the dominance of these modes, it is crucial to minimize $X(J_n)$ to zero, thereby making the impedance real. This can be achieved by modifying the current pattern at the different regions of the designed structure by incorporating slots, which cause the mode to become entirely real. The imaginary surface current $X(J_n)$ is derived from the characteristic angle (α_n), which depends on λ_n and is defined by equation 4.8.

$$\alpha_n = 180^\circ - \tan^{-1}(\lambda_n) \tag{4.8}$$

The summation of all surface or characteristic currents is symbolized by (J), as shown in equation 4.9. Modal significance (MS) can be calculated by utilizing weighted λ_n as specified following in equation 4.10.

$$J = \sum_{n=1}^{\infty} \lambda_n \alpha_n \tag{4.9}$$

$$\text{MS}_n = \frac{1}{\sqrt{1 + |\lambda_n|^2}} \tag{4.10}$$

When the MS is equal to 1, it represents the prevalent resonant modes of the structure. However, not all modes in structures exhibit resonance; some are capacitive while others are inductive and store energy. The investigation of such modes can be facilitated through the use of λ_n and α_n. An efficient mode is characterized by $\lambda_n = 0$ and α_n = 180°, implying that it efficiently radiates the majority of the coupled energy. For modes where λ_n is less than zero and α_n is between 180 degrees and 270 degrees, the mode functions as a capacitive mode and stores electric field energy. Conversely, for modes where λ_n is positive and α_n ranges between 90 and 180 degrees, the mode predominantly retains magnetic field energy and behaves as an inductive mode. To suppress the inductive and capacitive modes, it is necessary to alter the surface current flow in the structures. This can be accomplished by modifying the structure itself. Each respective mode's surface current generates distinct radiation patterns, thereby illustrating the role of CMA in aiding antenna development and achieving the required radiation pattern.

The initial five modes have been selected due to the fact that a considerable number of resonating modes can be distinguished within this range, while very few modes are detectable beyond it. As a result, the first five modes of each stage of the proposed antenna are explained in following subsequent sub-sections.

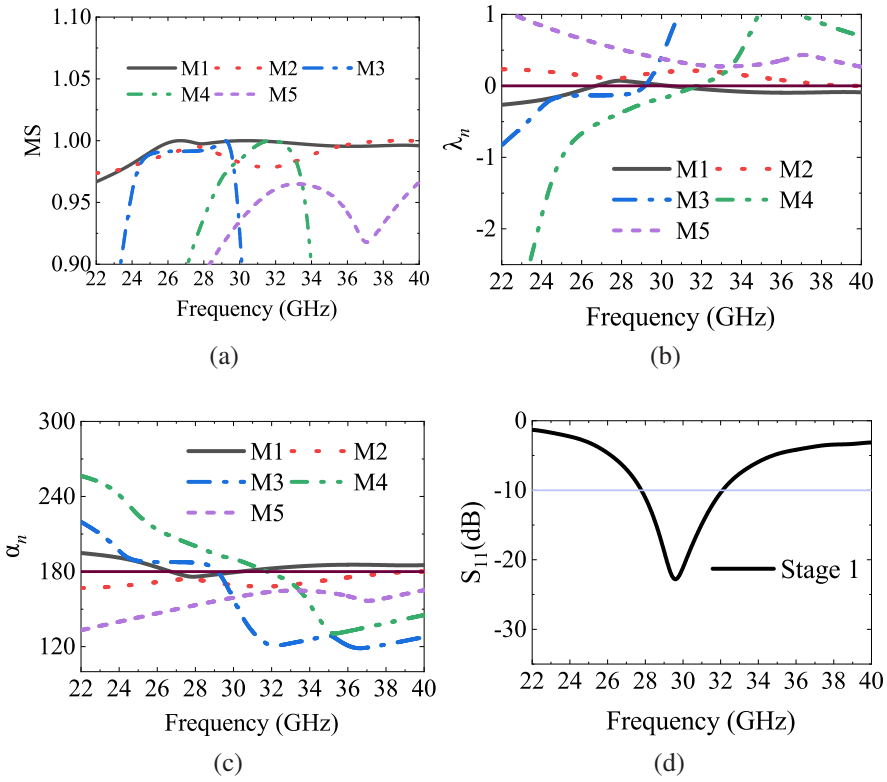

Figure 4.4: CMA results of step 1: (a) MS, (b) λ_n, (c) α_n, and (d) reflection coefficient.

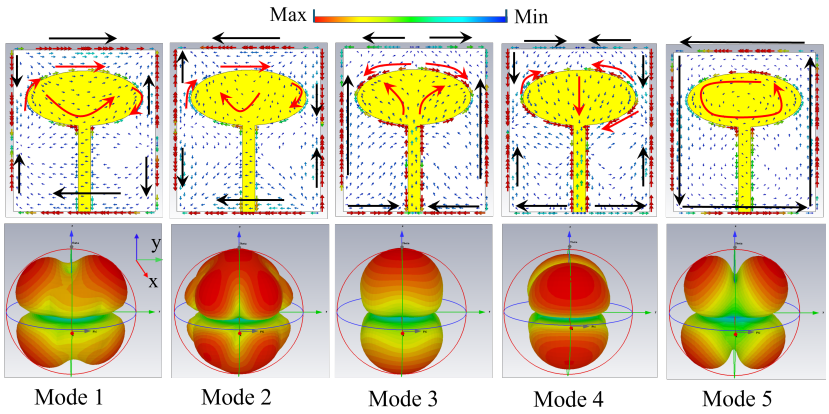

Figure 4.5: Current flow behaviour and radiation profile of the Step 1 antenna.

4.2.1.1 CMA of step 1 antenna

The CMA analysis of step 1 antenna design is shown in Fig. 4.4. The MS of stage 1 in Fig. 4.4(a) signifies that all five Modes are highly significant, with a value close to 1. However, the λ_n and α_n in Figs. 4.4(b) and 4.4(c) reveal that Modes 1 and 2 are efficient resonant modes at 28 GHz, while Modes 3 and 4 are resonant at 29 GHz and 32 GHz, respectively. Beyond these frequencies, these modes become capacitive and inductive. Specifically, Modes 1, 3, and 5 are capacitive for frequencies below 28 GHz, while all modes, excluding Mode 1, are inductive.

The surface current gives insight into the radiation pattern of the modes at each stage. For all modes of step 1 1, the current distribution and radiation patterns are shown in Fig. 4.5, where the current for top patch and ground plane are shown in red and blue arrows. The current distribution in mode 1 is in phase at the top edge of the elliptical patch with the ground plane, while it is anti-phase at the outer left and right edges, resulting in quad-beam and bidirectional radiation patterns at the angles of $\phi = 0°$ and $\phi = 90°$. The current distribution in mode 2 is the same as in mode 1, but in the opposite direction. In modes 3 and 4, the current distributions are in-phase except at the center of edges, generating bidirectional radiation patterns. In mode 5, the distribution is in phase in all areas, producing quad-beam patterns in all four planes. Based on the results displayed in Fig. 4.4(d), it is apparent that the stage 1 antenna design has an impedance bandwidth of 4.29 GHz, encompassing the frequencies of 28 GHz and 30 GHz. However, in order to achieve multiple bands operation that covers the 24 GHz (ISM band) and 38/39 GHz frequency bands, the design has been modified with multiple stages and is further explained in the following subsections.

4.2.1.2 CMA of step 2 antenna

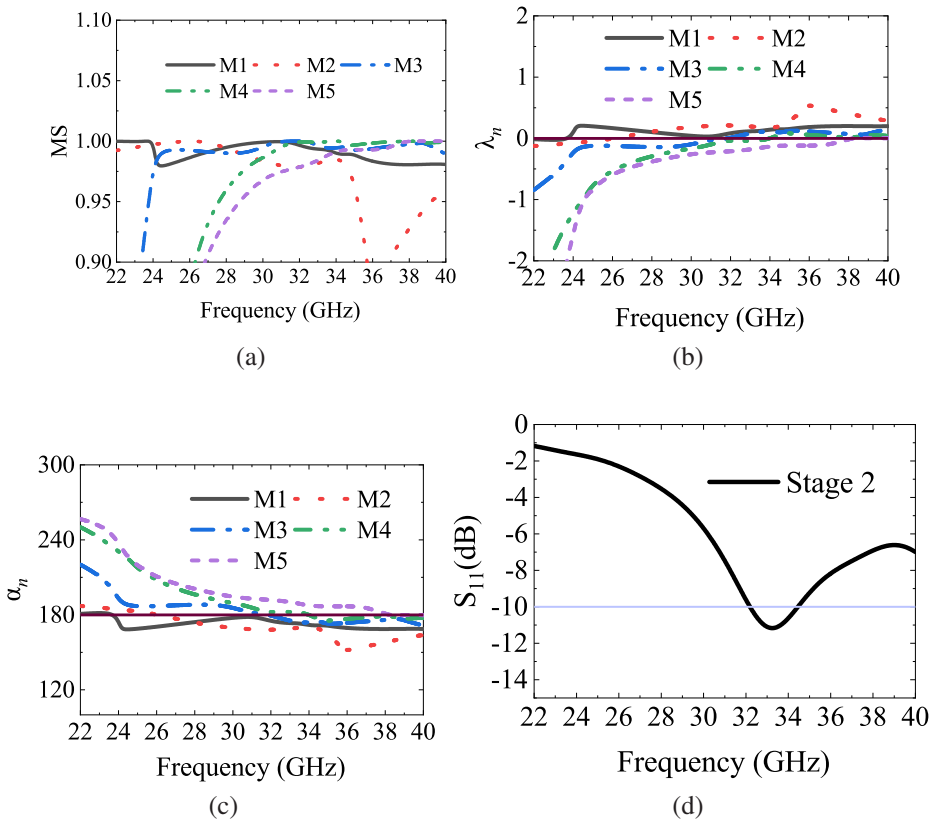

Figure 4.6: CMA results of step 2: (a) MS, (b) λ_n, (c) α_n, and (d) reflection coefficient.

In this stage, the ellipse is divided in half along its centre, and then another cut is made while maintaining the width of the transmission line. The outcome of the first five

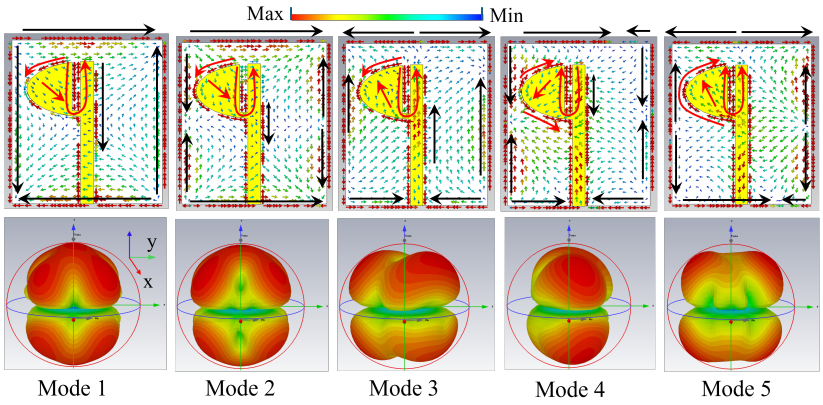

Figure 4.7: Current flow behaviour and radiation profile of the Step 2 antenna.

modes and the reflection coefficient are depicted in Fig. 4.6. The results in Fig. 4.6(a) show that all five modes are significant at all frequencies. The eigenvalues in Fig. 4.6(b) indicate that the first four modes converge to zero, particularly at 32 GHz and 34 GHz, respectively, while mode 5 converges after 40 GHz. However, the results in Fig. 4.6(c) suggest that all modes exhibit capacitive behavior at the required resonant frequencies, except for the 32-GHz-34GHz band. This is also evident from the reflection coefficient in Fig. 4.6(d) that this design has impedance bandwidth of 2 GHz covering 32-34 GHz frequencies only.

In Fig. 4.7, the current distribution and radiation patterns for all modes of step 2 are displayed. For mode 1, the current distribution is anti-phase at the top edge and left side of the elliptical patch, resulting in a quad-beam pattern. Conversely, mode 2 has in-phase current distribution which leads to a bidirectional radiation pattern. Similarly, modes 4, 5, and 6 produce quad-beam patterns due to their anti-phase current distributions.

4.2.1.3 CMA of step 3 antenna

In this stage, an additional strip line is added to the main ellipse in the x-direction. Fig. 4.8 shows the results of the first five modes and their respective reflection coefficients for the structure. As can be seen in Fig. 4.8(a), all five modes are significant at different frequencies. For instance, mode 1 is significant from 27GHz to 29 GHz, while mode 2 is significant from 26 GHz to 35 GHz. Likewise, modes 3 and 5 are significant almost at all frequencies from 28 to 40 GHz, whereas mode 4 is significant near 29 GHz. The λ_n in Fig. 4.8(b) indicate that the first two modes converge to zero, particularly at 28 GHz and 31 GHz, while modes 3 and 4 converge at 32 GHz and 36 GHz, respectively. However, mode 5 does not converge. Nevertheless, the results in Fig. 4.8(c) suggest that all modes exhibit capacitive behaviour at the required resonant frequencies, except for modes 1 and 2. As shown in Fig. 4.8(d), which indicates that this design has an approximate impedance bandwidth of 5 GHz, covering the 25-30 GHz band only.

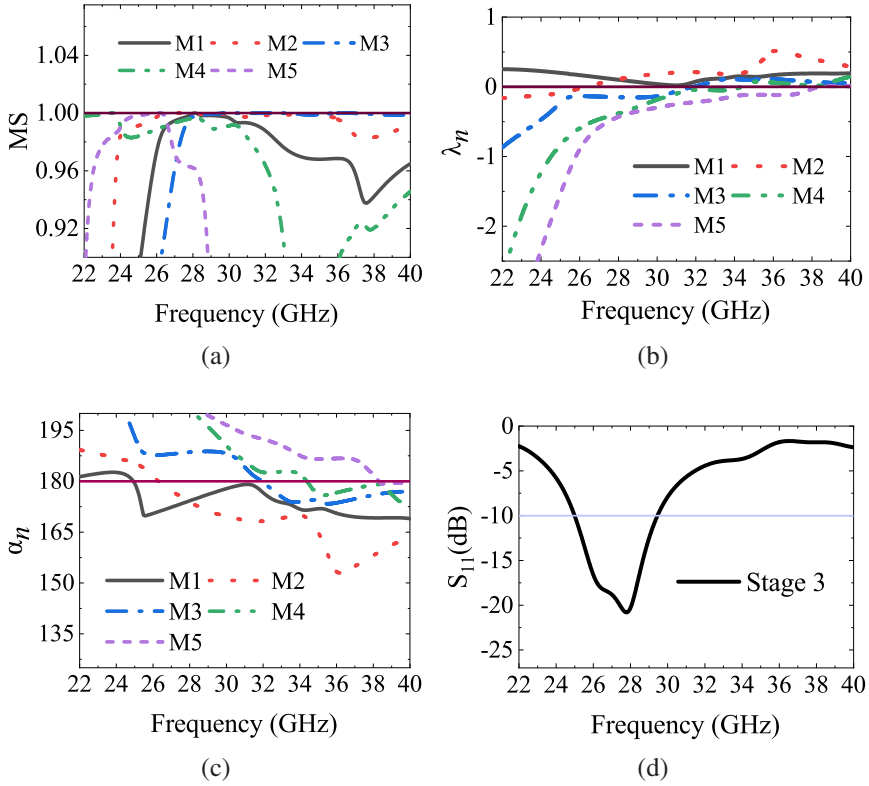

Figure 4.8: CMA results of step 3: (a) MS, (b) λ_n, (c) α_n, and (d) reflection coefficient.

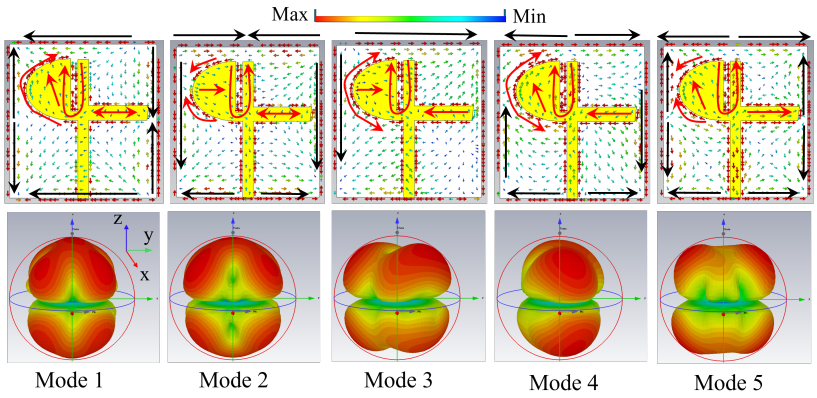

Figure 4.9: Current flow behaviour and radiation profile of the Step 3 antenna.

Fig. 4.9 displays the current distribution and radiation patterns for all modes of stage 3. For mode 1, the current distribution is anti-phase at the top edge and left half side of the elliptical patch, resulting in a quad-beam pattern. Conversely, mode 2 has in-phase current distribution, leading to a bidirectional radiation pattern. Similarly, modes 4, 5, and 6 produce quad-beam patterns due to their anti-phase current distributions.

4.2.1.4 CMA of step 4

The third stage of the design covers the lower mm-wave band, ranging from 25 GHz to 30 GHz. To make it multi band and cover the 38 GHz band, arms were designed and

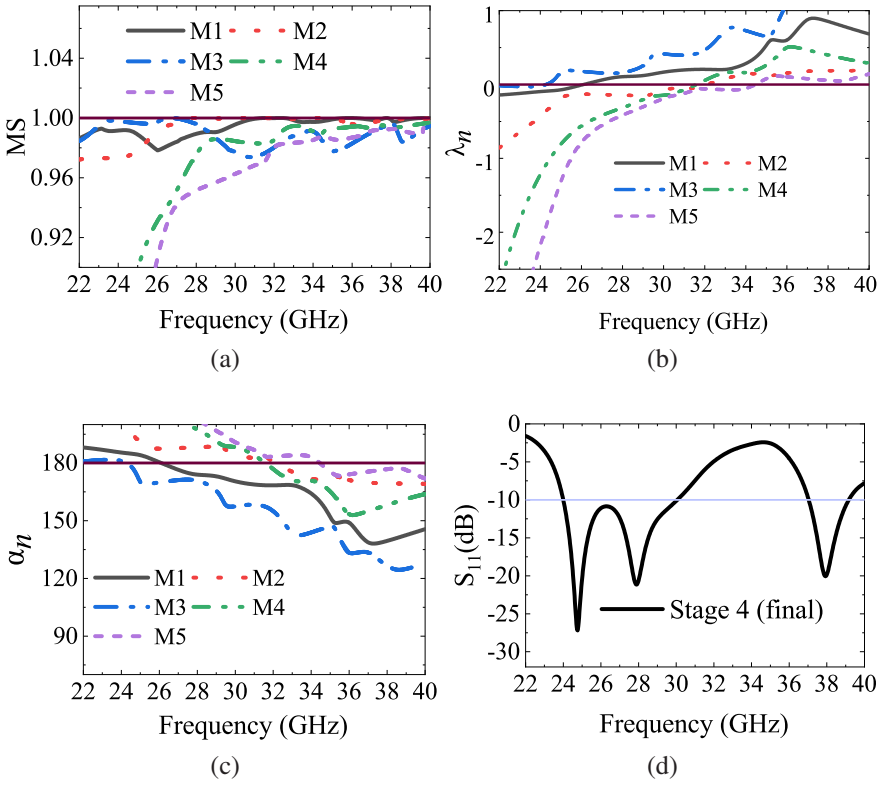

Figure 4.10: CMA results of step 4: (a) MS, (b) λ_n, (c) α_n , and (d) reflection coefficient.

placed on a microstrip line, with the width of the transmission line increased near the port. Fig. 4.10 shows the results of the first five modes and their respective reflection coefficients for the structure. As can be seen in Fig. 4.10(a), the first three modes are significant at all frequencies, while modes 4 and 5 become significant from 33 GHz and 36 GHz, respectively. The λ_n in Fig. 4.10(b) indicate that the first two modes converge to zero, particularly at 24 GHz and from 28 GHz, while modes 3, 4 and 5 converge at 32 GHz and 34 GHz, respectively. Nonetheless, results in Fig. 4.10(c) suggest that there are both capacitive and inductive behaviours in different stages, particularly modes 1 and 5 are capacitive, mode 4 is capacitive up to 34 GHz, while modes 2 and 3 are inductive after 34 GHz and 36Hz, respectively. This can also be seen in the reflection coefficient in Fig. 4.10(d), which indicates that this design has now multiple frequency bands covering 24 GHz-30 GHz and 37 GHz-39 GHz mm-wave bands. Fig. 4.11 displays the current distribution and radiation patterns for all modes of stage 4. For the first mode, the current distribution is both in- and anti-phase at the top edge while anti-phase at the left half side of the elliptical patch, resulting in a six-beam pattern. Modes 2 and 3 have in-phase and anti-phase surface currents at the top and left half side of the elliptical patch, respectively, resulting in a quad-beam pattern. Modes 4 and 5 have anti-phase surface currents at the top while in-phase and anti-phase currents near the elliptical patch, resulting in bi-directional beams.

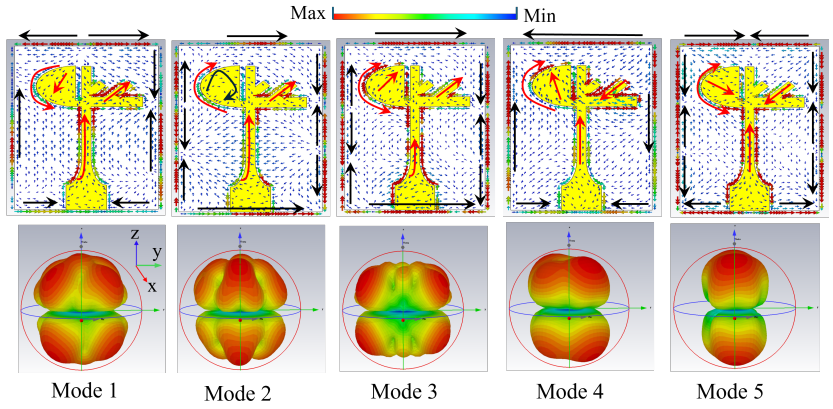

Figure 4.11: Current flow behaviour and radiation profile of the Step 4 antenna.

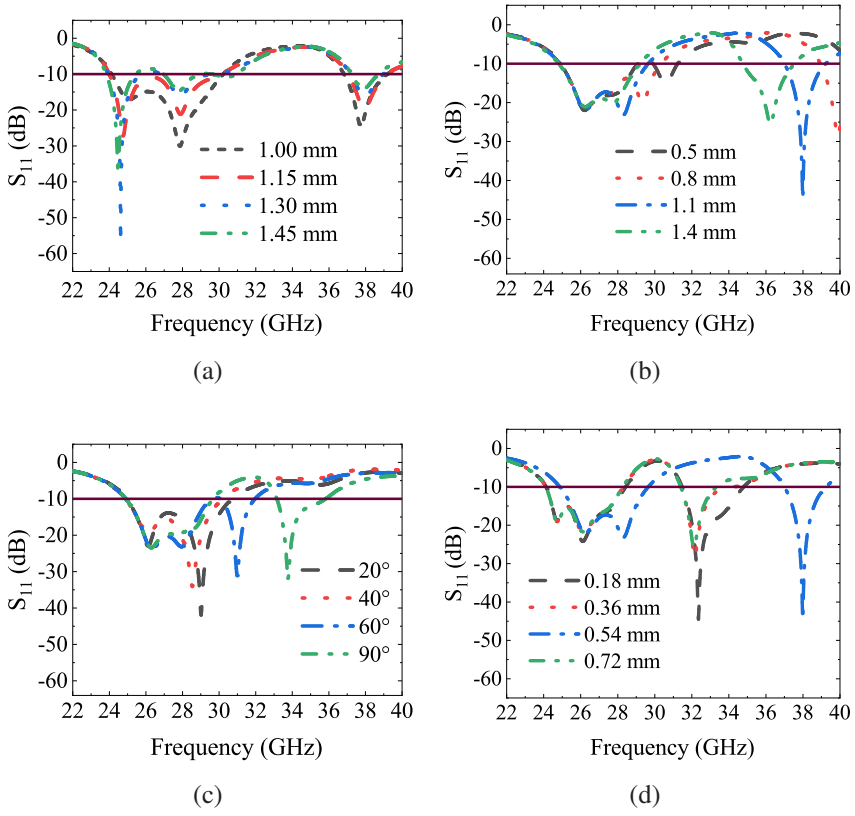

Figure 4.12: Parametric analysis: (a) L_2, (b) W_3, (c) θ, and (d) R_C

4.2.2 Parametric analysis

In parametric analysis, antenna performance is examined by assessing the effects of key design variables on the reflection coefficient. In this context, different antenna parameters were altered, and the impact are shown in Fig. 4.12.

From the Fig. 4.12(a), the parameter L_2 demonstrates that increasing its value leads to a decrease in both the magnitude and impedance bandwidth. Conversely, the parameter W_3 has an inverse relationship, affecting the upper frequency band of 38 more than the lower band, and by increasing its size, the frequency shifts to the left side

of the band as shown in Fig. 4.12(b). Furthermore, the rotation of the arm also impacts the bandwidth, as demonstrated in 4.12(c). Additionally, the analysis of the variable R_C exhibits similarities, as shown in Fig. 4.12(d). It is evident from the results that dual-band characteristics were achieved at 0.54 mm.

4.2.3 Generation of circular polarization

The electric field, time-phase difference $\Delta\theta$, and axial ratio (AR) can be considered as indicators that the propagation of the antenna is circular polarization (CP). Thus, when the electric field vector of an EM wave moves in a circular path as it propagates then it is considered as circular polarization. The electric field components (E_x and E_y) generated through diverse resonant modes oriented in the x and y directions of an elliptical patch antenna can be written as [129]:

$$E_x = \frac{\cos(\pi \cdot\ x_1 \cdot a)}{\omega^2 - \omega_{11}^{e,o}(1 + jQ_{11}^{-1})} \tag{4.11}$$

$$E_y = \frac{\cos(\pi \cdot\ y_1 \cdot b)}{\omega^2 - \omega_{11}^{e,o}(1 + jQ_{11}^{-1})} \tag{4.12}$$

In the equations above, ω represents the phase rate of an oscillating electromagnetic wave, while $\omega_{11}^{e,o}$ denotes the angular resonant frequency. Additionally, Q_{11}^{-1} corresponds to the antenna's quality factor. Circular polarization is achieved when the magnitudes of the two orthogonal field components are equal and their phase difference is an odd multiple of $\pi/2$, as expressed in the following condition:

$$|E_x| = |E_y| \tag{4.13}$$

and

$$\Delta\theta = \theta_x - \theta_y \tag{4.14}$$

$$\begin{cases} +\left(\frac{1}{2} + 2k\right)\pi \cdot k = 0, 1, 2, \ldots, \text{ for LHCP} \\ -\left(\frac{1}{2} + 2k\right)\pi \cdot k = 0, 1, 2, \ldots, \text{ for RHCP} \end{cases}$$

The CPs of elliptical patch antenna can be written in terms of axial ratio (AR) as:

$$AR = \frac{|E_y|}{|Ex|} = 1 \tag{4.15}$$

Both linear and circular polarizations exhibit advantages in the context of IoT-based smart cities. While linear polarization (LP) is typically preferred for line-of-sight and high-gain applications, circular polarization (CP) is more effective in mobile and dynamic situations, offering better signal penetration, reduced multipath interference, and orientation independence. Using antennas that support both LP and CP across various frequencies can significantly enhance the performance and versatility

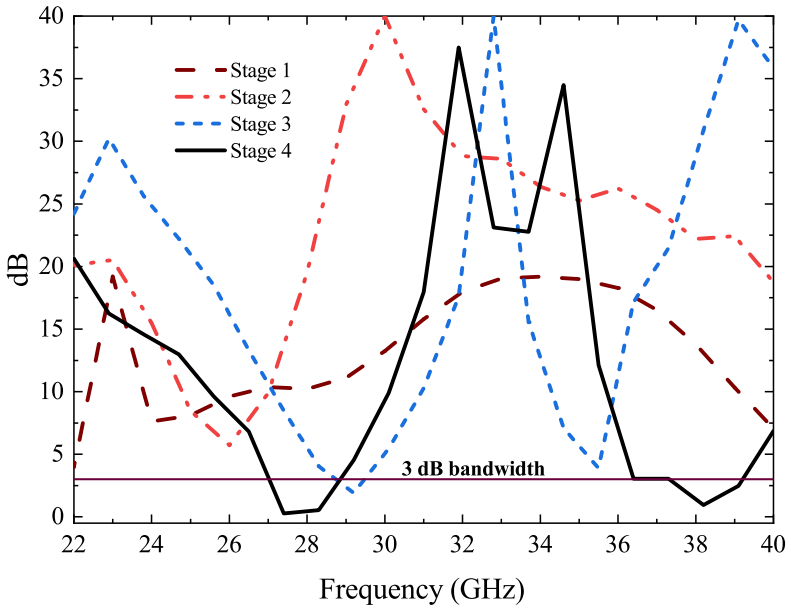

Figure 4.13: Axial ratio of all stages.

of communication systems in smart cities. This dual-polarization feature of antennas is particularly beneficial for addressing the dynamic communication requirements of a smart city environment. In this context, the proposed antenna exhibits dual polarization, as evidenced by the axial ratio (AR) results shown in Fig. 4.13. The final stage of the design achieves AR 3 dB bandwidth of 2 GHz, spanning from 27 GHz to 29 GHz, and 1.5 GHz, covering the 37.5 GHz to 39 GHz range. These bands align with the standard 5G frequencies at 28 GHz and 38 GHz. As a result, this antenna design supports CP within these frequency bands, while LP is applicable at other frequencies.

4.3 MIMO design

The designed single element antenna is expanded to a six-element MIMO design. The final MIMO antenna design is completed through three separate stages: the MIMO antenna with a full ground plane ($MIMO_1$), the MIMO antenna with a DGS ($MIMO_2$), and the FSS structure incorporation in DGS ($MIMO_3$). Each of these antenna elements is arranged in a hexagonal configuration. The characteristic of this design is useful for designing compact MIMO antenna, especially in applications with strict size requirements, such as in small IoT devices.

4.3.1 Design of six-element MIMO antenna

The initially designed single antenna has been adapted into a six-element MIMO array on a hexagonal substrate. Fig. 4.14 illustrates the top and bottom configurations of the

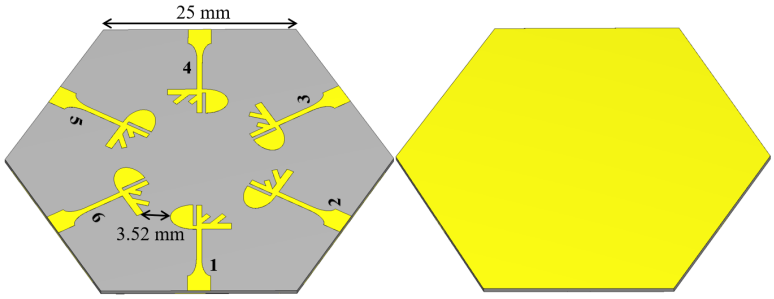

Figure 4.14: $MIMO_1$ antenna (a) top and (b) bottom faces.

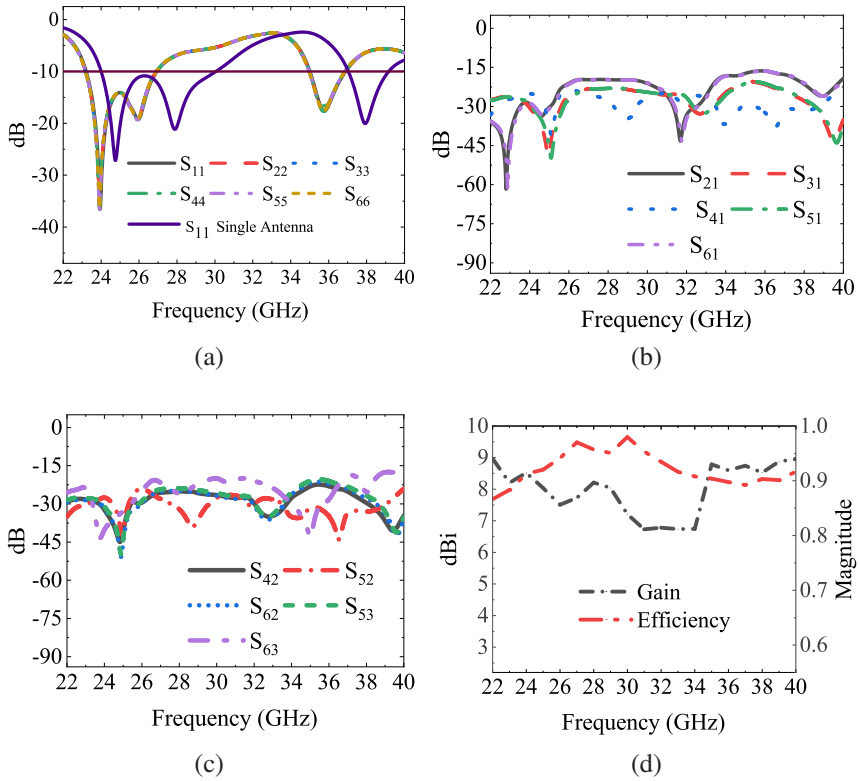

Figure 4.15: Results of $MIMO_1$ antenna (a) reflections, (b) and (c) transmission coefficients, and (d) gain and efficiency.

MIMO antenna. The edge-to-edge spacing between adjacent antenna elements was 3.52 mm which is less than half wavelength of operating frequencies.

Subsequent to the arrangement of the antenna elements, simulations were conducted, with the results presented in Fig. 4.15. These results depict the s-parameters, gain, and efficiency of the MIMO design. As evident from Fig. 4.15(a), the hexagonal substrate has induced a slight shift in the resonance frequencies. Specifically, the lower frequency band has shifted from 23.95-30.05 GHz to 23.18-26.89 GHz. Similarly, the upper frequency band has shifted from 37.05-39.13 GHz to 34.97-36.85 GHz. This alteration in the impedance bandwidth is undesirable, as it should correspond to the bandwidths of the single antenna element. Conversely, as shown in Figs. 4.15(b-c), the inter-element isolation and mutual coupling demonstrate an average of more than -20

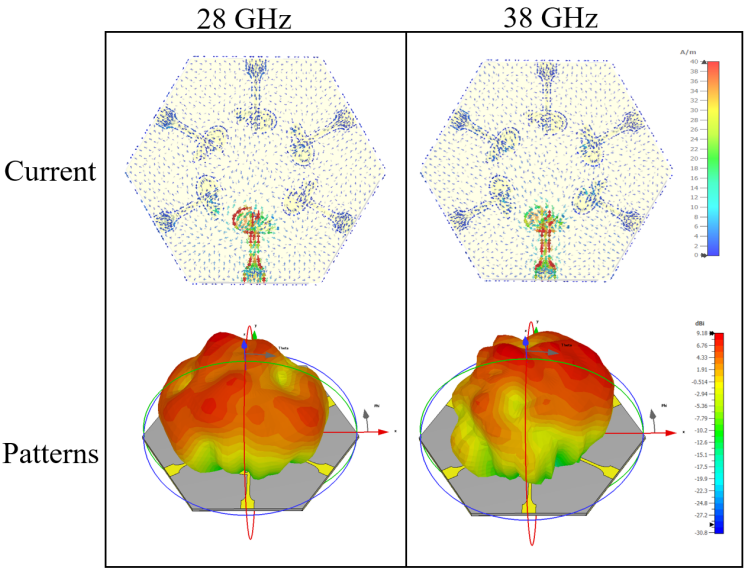

Figure 4.16: Surface current and radiation patterns of MIMO antenna 1 at 28 GHz and 38 GHz.

dB. Furthermore, an average realized gain of approximately 8 dBi was observed in both bands, while efficiency values exceeding 0.90 were noted across both dual bandwidths, as illustrated in Figure 4.15(d).

The surface current distribution and radiation patterns when antenna 1 is active is shown in Fig. 4.16. The top row of the figure shows the distribution of surface current, while the bottom row presents the corresponding 3D radiation patterns. To elucidate the behaviour of current distribution and radiation patterns, only two frequencies (38/38 GHz) are presented, as the trends remain consistent across other frequencies. At 28 GHz, the distribution exhibits strong current concentration around the feed point and along the and half-elliptical patch. Notably, the current is also observed on adjacent antenna elements, indicating the presence of mutual coupling. This coupling behaviour suggests that energy is partially transferred to neighbouring elements, which may influence the impedance characteristics and overall isolation performance. The radiation pattern at 28 GHz shows a well-defined main lobe in the z-direction. At 38 GHz, the surface current distribution appears more dispersed along the antenna arm structure and extended arm. The coupling effect is also noticeable at this frequency. However, the radiation pattern at 38 GHz maintains strong directivity with a slightly broader main lobe and minor side lobes, which is expected due to frequency-dependent changes in the antenna response.

4.3.2 Design of six-element MIMO antenna with DGS

To further reduce the mutual coupling and optimize the impedance bandwidth shift, in this stage DGS technique was employed as shown in Fig. 4.17. The ground plane incorporates a cross-shaped structure of periodic rectangular slots. These slots, with

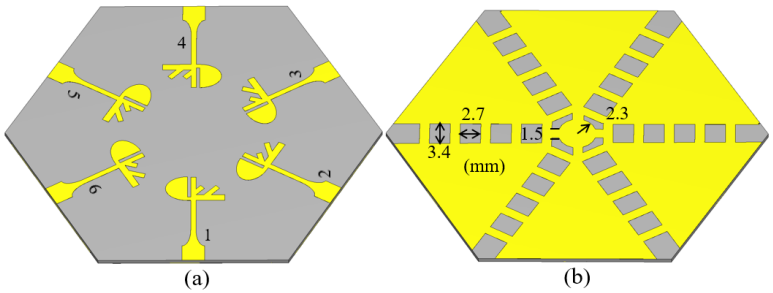

Figure 4.17: $MIMO_2$ antenna (a) top and (b) bottom views.

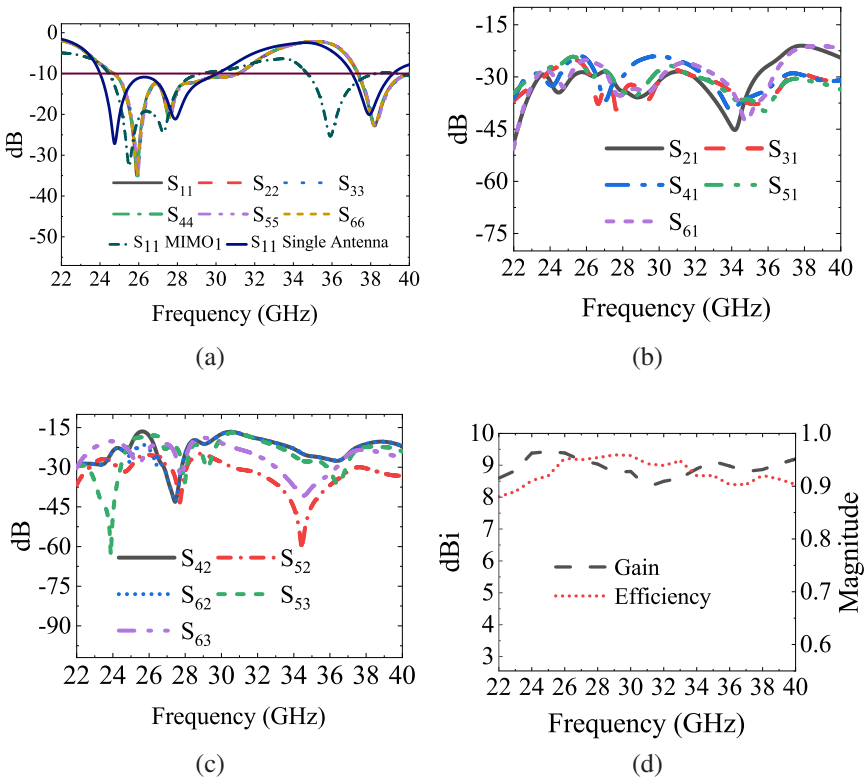

Figure 4.18: Results of $MIMO_2$ antenna (a) reflection, (b) and (c) transmission coefficients, and (d) gain and efficiency.

dimensions of approximately 2.7 $\times$ 3.4 (mm^2) and interspaced by 1.5 mm, serve multiple functions. A primary advantage of this DGS implementation is the reduction in mutual coupling between adjacent MIMO antenna elements. By disrupting the uniformity of the ground plane, these periodic slots alter the surface current distribution, effectively suppressing surface waves and mitigating undesired EM interference. Moreover, the DGS improves impedance matching by modifying the antenna's effective capacitance and inductance, thereby enhancing signal transmission efficiency across operational frequency bands. The cross-shaped DGS pattern facilitates multi-directional decoupling, ensuring optimal isolation among various antenna elements positioned around the hexagonal substrate. Furthermore, the disruption of surface currents

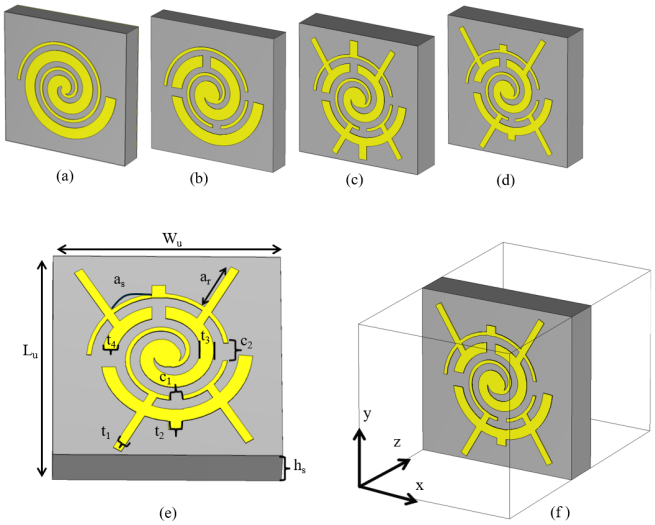

Figure 4.19: FSS design: (a) first stage, (b) second stage, (c) third stage, (d) final stage (stage 4), (e) detailed dimensions of stage 4, and (f) Floquet boundary excitation.

can result in increased bandwidth and enhanced radiation efficiency, consequently improving overall gain performance. In essence, the DGS structure in this MIMO antenna represents a calculated design feature aimed at optimizing isolation and impedance matching.

The s-parameters, gain and efficiency results of DGS based MIMO antenna is shown in Fig. 4.18. In this case, as shown in Fig. 4.18(a) the impedance bandwidth is now enhanced, covering now 24.61-31.61 GHz and 37.30-40.05 GHz. The results indicate efficient impedance matching, with the MIMO antenna now demonstrating similar bandwidth performance compared to a single-element antenna. Although, high isolation (> -20) dBi is observed particularly between antenna 1 and all other elements as shown in Fig. 4.18(b), however the level mutual coupling is more in elements as can be seen from results S_{42}, S_{62}, S_{53}, and S_{63} as shown in Fig. 4.18(c). Although, good isolation was observed at 28 GHz, however 38 GHz was more prone to mutual coupling. With incorporation of slots, the gain and efficiency is also increased and more than 8.50 gain and 0.90 efficiency are also observed in the both frequency bandwidth, as indicated in Fig. 4.18(d).

4.3.3 MTM based FSS design

The challenge posed by mutual coupling, especially at mmWave frequencies where the antenna element spacing is just a few millimetre and the coupling is consequently pronounced, is of paramount importance. The utilization of traditional methods for mitigating coupling, which require the dimensions of the substrate of FSS to be half the wavelength of the operating frequency, has been found to be insufficient in achieving the desired high isolation at mmWave band. Consequently, this work presents a design of FSS to develop a broadband structure with dimensions significantly smaller than

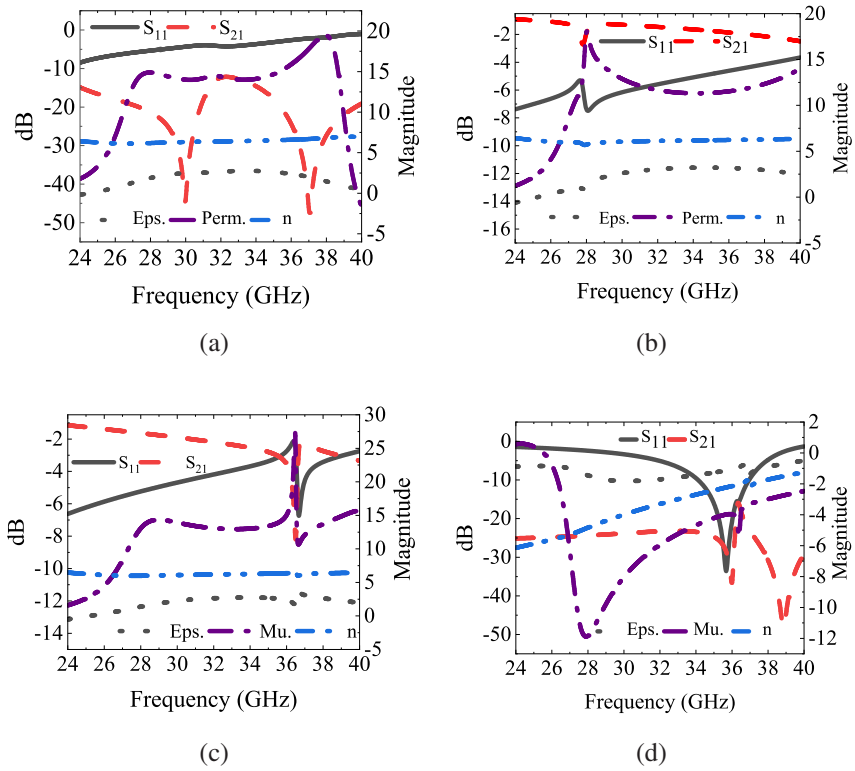

Figure 4.20: FSS unit cell results: (a) first stage, (b) second stage, (c) third stage, and (d) final stage.

the half wavelength, exhibiting exceptional band rejection properties particularly at impedance bandwidth frequencies. The metamaterial FSS unit cell is inspired by spiral shape resonator design. The final design was achieved through different stages as shown in Fig. 4.19. The optimized parameters of the unit cell are as follows: L_U = 3.95, W_U = 3.95, t_1 = 0.14, $t_2 = t_3 = c_1 = c_1$ = 0.21, a_s = 0.68, a_r = 0.68, a_r = 0.61, t_4 = 0.07, g_r = 0.16, g_r = 0.14, and h_s = 0.79 (mm). The simulation of the unit cell was facilitated by employing Floquet boundary conditions in CST Studio Suite. Floquet boundary conditions are used to simulate periodic structures such as MTM unit cells. These boundaries consider the simulation of an infinite array by modeling just a single unit cell. When Floquet boundaries are applied in the transverse directions (typically x and y), they assume that the fields on opposite sides of the unit cell are periodic. A Floquet port is then used to excite a standard plane wave, usually propagating in the z-direction, allowing the extraction of S-parameters under periodic excitation. This setup is ideal for analysing how a MTM unit cell interacts with EM waves under plane-wave excitations. The s-parameters and effective parameters (permittivity (eps.), permeability (perm.) and refractive index (n)) results of each stage are shown in Fig. 4.20.

In the initial design, two spiral rings were implemented, with the width of the smaller ring being one-third of the larger ring. This stage produced significant reflection and transmission, as shown in Fig. 4.20(a), without negative values of effective parameters.

Consequently, the FSS objective of increased reflection and decreased transmission with negative effective parameters was not achieved at this stage. Therefore, necessary adjustments were performed in subsequent stages. Four cuts with a width of c_1, positioned 90 degrees apart, were made on both rings. This stage did not significantly impact the results, as shown in 4.20(b). In stage 3, six arms connected to both smaller and wider rings were introduced. This produced a resonant frequency band near 36 GHz where decreased reflection and increased transmission were observed, as can be seen in 4.20(c). Although the reflection was greater at resonant frequencies with acceptable transmission, negative effective parameters were still not achieved. Thus, in the final stage 4, necessary changes were implemented. As shown in 4.20(d) results, all FSS objectives were achieved. The unit cell demonstrates reflection of more than -5 dB and transmission of less than -23 dB up to 35.6 GHz, and transmission of -30 dB or more beyond 37 GHz frequencies. Additionally, the design features negative values for permittivity, permeability, and refractive index, as illustrated in Fig. 20(b). The Kramers-Kronig algorithm was used to calculate the effective permittivity, permeability, and refractive index of the FSS design [132]. It is noteworthy that the FSS was designed on a substrate without a ground plane.

4.3.4 $MIMO_3$ final design

In this instance, the designed metamaterial based FSS was placed between the antenna elements on the top face and in the ground plane, as shown in Fig. 4.21. Each antenna element on the top surface is surrounded by multiple FSS unit cells, while the bottom face incorporates a DGS in conjunction with periodic FSS elements. To suppress surface waves, enhance gain, and improve isolation, the FSS structures are optimally positioned at intervals of 1.4 mm. The DGS on the bottom face is configured in a cruciform pattern, with FSS elements symmetrically distributed to form a periodic lattice. This engineered configuration contributes to bandgap filtering and reduces mutual coupling.

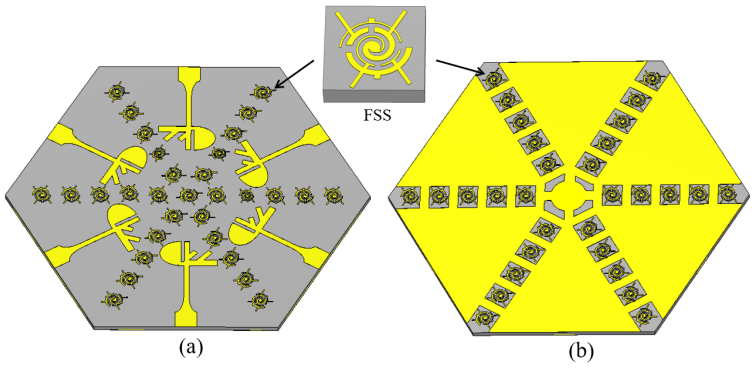

Figure 4.21: $MIMO_3$ antenna (a) top and (b) bottom views.

The integration of FSS and DGS in the six-element MIMO antenna design leads to significant improvements in impedance matching, isolation enhancment and mutual coupling reduction, as shown in 4.22. The reflection coefficient results in Fig. 4.22(a) demonstrate a noticeable enhancement in impedance bandwidth due to the incorporation of FSS. Specifically, the lower impedance band now ranges from 23.63 GHz to 32.90 GHz, while the upper frequency band covers the frequency range from 36.68 GHz to beyond 40 GHz. This expanded bandwidth indicates the FSS and DGS capability in the bandwidth enhancement of designed MIMO antenna. The transmission coefficient results in Figs. 4.22(b-c) further validate the enhanced isolation between the antenna elements. In most cases, isolation exceeds -33 dB, indicating significant suppression of mutual coupling. The periodic FSS structures contribute to this isolation by acting as EM bandgap structures, thereby reducing surface wave propagation and minimizing unwanted inter element interactions. However, slightly reduced isolation is observed for elements S41 and S42, where the transmission coefficient reaches approximately -23 dB. Despite this, the overall MIMO antenna exhibits excellent isolation characteristics.

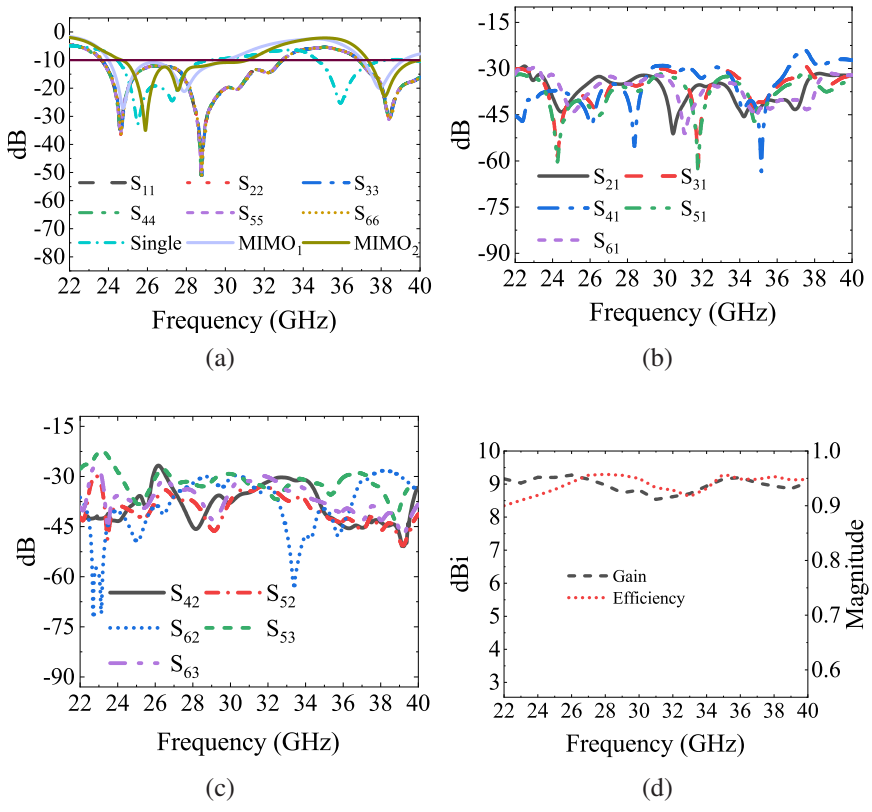

Figure 4.22: Results of MIMO antenna with FSS and DGS: (a) reflection coefficients, (b) and (c) transmission coefficients, and (d) gain and efficiency.

Moreover, the gain and efficiency characteristics, as depicted in Fig. 4.22(d), reveal a consistent improvement across the operating frequency range. The antenna achieves a peak gain exceeding 8.90 dBi, while the efficiency remains above 0.92, indicating minimal losses and high radiation efficiency. These enhancements can be attributed

to the optimized placement of the FSS elements, which not only improve impedance matching but also enhance radiation performance by reducing undesired back radiation. The stable gain and efficiency values further validate the robustness of the proposed design. In summary, the observed enhancements in mutual coupling reduction, gain augmentation, and efficiency optimization demonstrate the efficacy of the proposed antenna for advanced wireless communication applications, including 5G, Internet of Medical Things (IoMT), and other high-data-rate wireless systems.

4.3.5 Surface current and electric field distribution

4.3.5.1 Single element

The surface current distribution of the designed single antenna element at 26 GHz, 28 GHz, 30 GHz, and 38 GHz is shown in Fig. 4.23. It is observed that the primary concentration of surface current occurs in the half elliptical region at 26 GHz. At 28 GHz, the current is more pronounced in both the elliptical shape and rotating arms, indicating the origin of the resonance. Similarly, at 30 GHz, the current is more concentrated in the transmission line, while at 38 GHz, it is more prominent in the rotating arms region. It can be observed that the CP is primarily generated at the half-elliptical patch and rotated arms region of the single element antenna. Moreover, the LP is dominantly generated in the remaining region. This demonstrates that a single antenna can be designed for the generation of different polarization by utilizing a half-elliptical patch and introducing rotating arms to it.

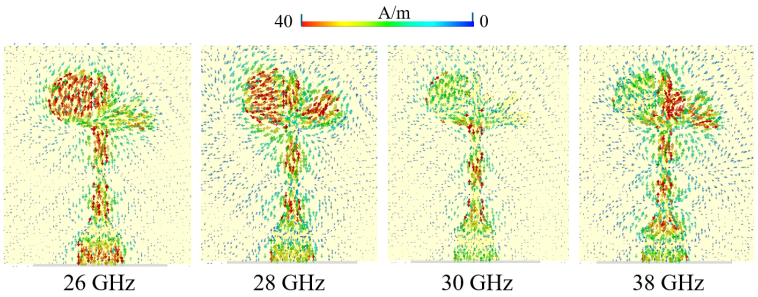

Figure 4.23: Surface current distribution of the single antenna element.

4.3.5.2 MIMO distributions

Figs. 4.24(a)-(d) illustrate the surface current distribution with and without FSS, considering port 1 as active while all other ports are terminated with a 50Ω load. As anticipated, the surface current density distribution is higher when FSS is absent, resulting in increased mutual coupling. However, when FSS is inserted between antenna elements, it significantly reduces the impact of surface current, leading to increased current concentration at FSS locations. This, in turn, enhances the isolation and

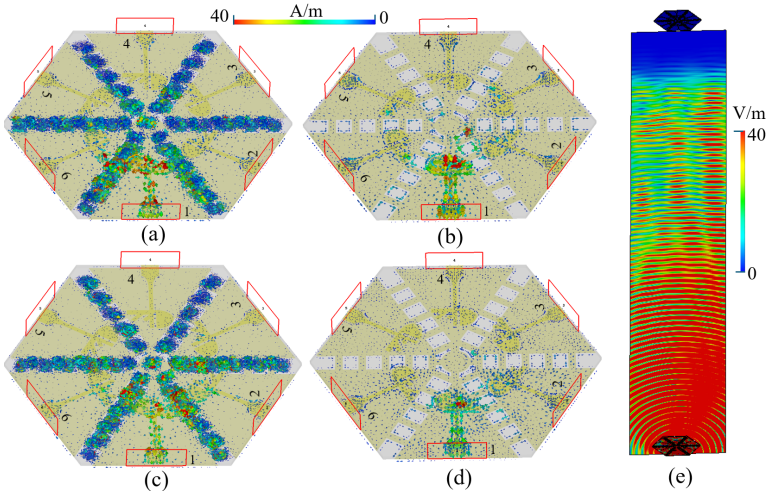

Figure 4.24: Surface current distribution (a) 28 GHz with FSS, (b) 28 GHz with DGS, (c) 38 GHz with FSS, (d) 38 GHz with DGS, and (e) e-filed at 28 GHz.

showcases the effectiveness of FSS-based metamaterials in MIMO antenna systems. The free space electric field is also shown in Fig. 4.24(d). In order to observe the far-field electric field, two proposed MIMO antennas were placed 50 cm apart, with one serving as a transmitter and the other as a receiver. The results clearly demonstrate that the field is effectively generated and flows efficiently from the transmitter to the receiver antenna.

4.4 Measured results

The final $MIMO_3$ antenna was fabricated and Fig. 4.25. showing both structural design and measurement setup. The top face in Fig. 4.25(a) shows fabricated antenna and integrated with FSS structures, while the bottom face in Fig. 4.25 presents the DGS with periodic FSS for mutual coupling suppression. Fig. 3. 4.25(c) displays the assembled antenna with connectors attached. The measurement setup in Fig. 4.25(d) involves a Keysight network analyzer (PNA-X, N5247B) to evaluate the antenna's s-parameters, including reflection and transmission coefficients. The small vias in the fabricated prototype were created for the connections of the SMA connector.

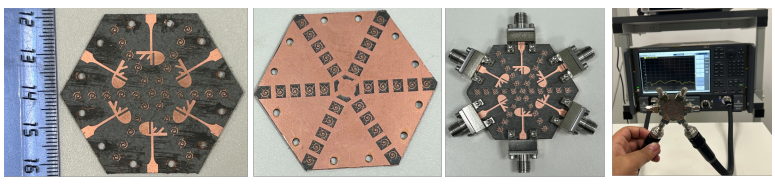

Figure 4.25: Fabricated prototype of the MIMO antenna: (a) top view, (b) bottom view, (c) assembled with connectors, and (d) S-parameter measurements using a VNA.

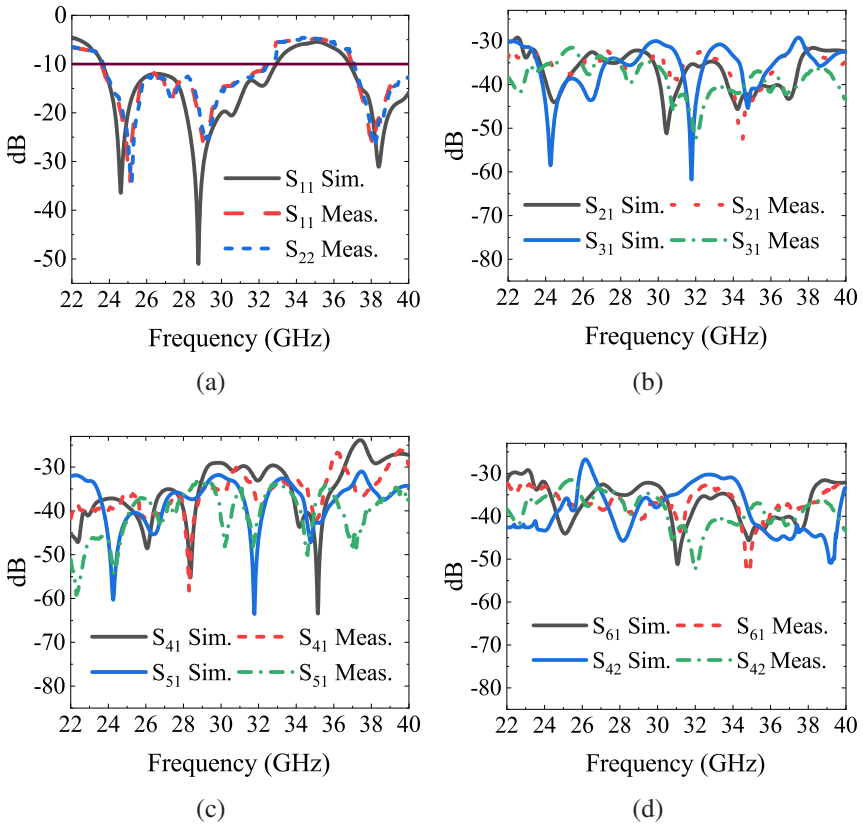

Figure 4.26: Comparison of simulation and measurement results (a) reflection, (b), (c) and (d) transmission coefficients.

The s-parameters outcomes, encompassing reflection and transmission coefficients are shown in Fig. 4.26. As shown in Fig. 4.26(a), the measured results for the initial two antenna components closely follow the simulation data trends, with slight differences attributed to manufacturing tolerances, and connector losses. Despite these variations, the measured impedance bandwidth aligns with the simulated performance, spanning 23.65 GHz to 32.51 GHz for the lower band and 37.1 GHz to over 40 GHz for the upper band. These findings confirm that the antenna design maintains its multi-band functionality after fabrication. It's important to note that during measurements, all inactive ports were connected to 50 Ω loads to eliminate unwanted reflections, ensuring precise and dependable results across all antenna components. The designed MIMO antenna supports multiple operating bands and exhibits strong isolation between adjacent antenna elements, as evidenced in Figs. 4.26(b-d). The transmission coefficients reveal that mutual coupling remains under -33 dB throughout most of the frequency range, validating the effectiveness of the FSS in reducing unwanted EM interference. The FSS's periodic structure inhibits surface wave propagation, thereby minimizing undesired interactions between elements. The effective decoupling between antenna elements not only boosts radiation efficiency but also ensures each element's independent contribution to the MIMO system's performance.

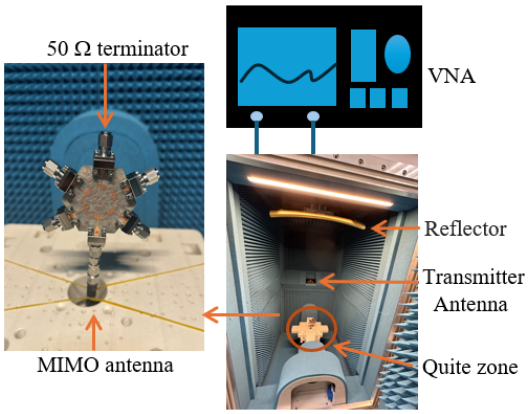

Figure 4.27: MIMO antenna gain measurement performed in the anechoic chamber.

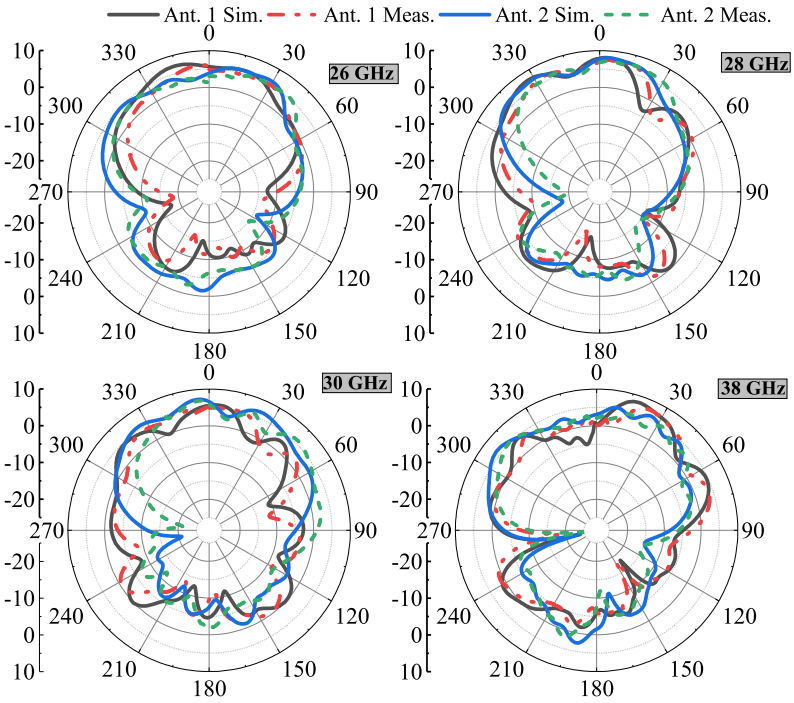

Figure 4.28: Comparison of simulation and measured results in azimuth E-plane (a) 26 GHz (b) 28 GHz (c) 30 GHz, and (d) 38 GHz.

Radiation pattern measurements were performed in the Rhodes & Schwarz RS®ATS1800C anechoic chamber, as shown in Fig. 4.27. This chamber offers a controlled, echo-free setting for accurate gain and radiation pattern measurements, reducing external interference. To measure the antenna's gain, the gain transfer method was employed, using a mm-wave reference horn antenna with known gain as a standard. The reference horn antenna was first placed in the quiet zone to minimize multipath effects, and its received power was measured for both E-plane and H-plane. The MIMO antenna then replaced the reference antenna in the same quiet zone, and its received power was recorded under identical conditions. The MIMO antenna's gain was accurately determined by comparing the difference in received power between these two measurements. During testing, 50 Ω terminators were attached to the MIMO antenna's

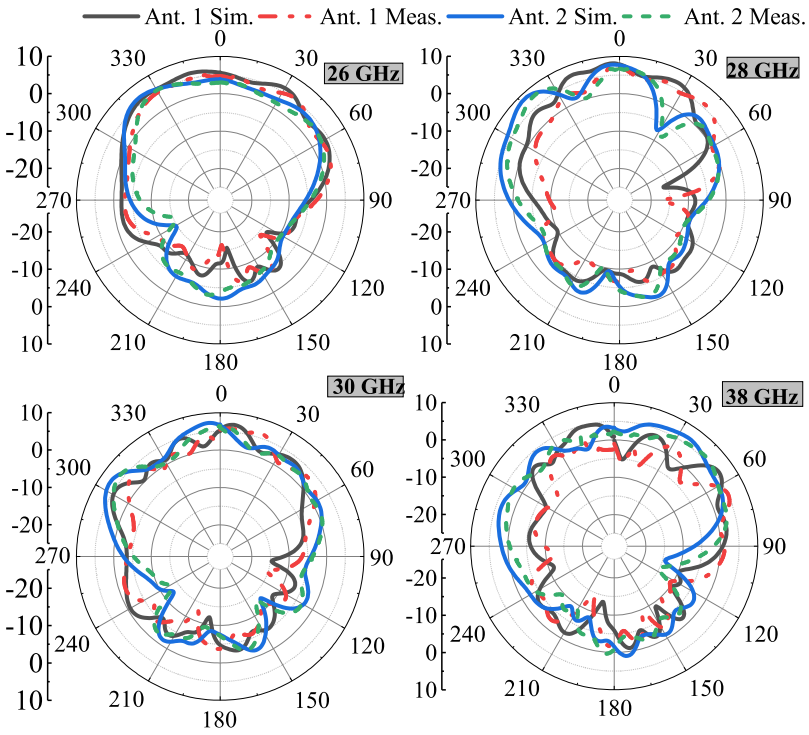

Figure 4.29: Comparison of simulation and measured results in elevation H-plane: (a) 26 GHz (b) 28 GHz (c) 30 GHz, and (d) 38 GHz.

unused ports to eliminate unwanted reflections and ensure reliable results. A VNA was used to capture received signals and analyse gain response across the antenna's operational frequency range. The anechoic chamber also contained a strategically positioned reflector and transmitting antenna to improve measurement accuracy and direct the incident wave towards the MIMO antenna. This methodology allowed for the creation of a detailed radiation pattern for the MIMO antenna across various angles. The measured gain and radiation characteristics were subsequently compared with simulation results to verify the fabricated prototype's performance.

The MIMO antenna radiation patterns were evaluated in both the azimuth E-plane (phi = 0) and elevation H-plane (phi = 90) at frequencies of 26 GHz, 28 GHz, 30 GHz, and 38 GHz and are presented in Fig. 4.28 and Fig. 4.29. The results demonstrate broadside radiation patterns with significant correlation between the simulated and measured results, confirming the MIMO antenna design's reliability in practical gain scenarios. However, minor discrepancies are observed, potentially attributable to manufacturing tolerances, measurement setup misalignments, and connector losses. Additionally, the efficiency and antenna gain of the MIMO antenna are given in Fig. 4.30. The measured results show a considerable match with the simulation. Hence, the gain values for 26 GHz, 28 GHz, 30 GHz, and 38 GHz were 9.12 dBi, 9.19 dBi, 8.80 dBi, and 8.77 dBi. Similarly, the efficiency values were 0.92, 0.94, 0.94, and 0.95.

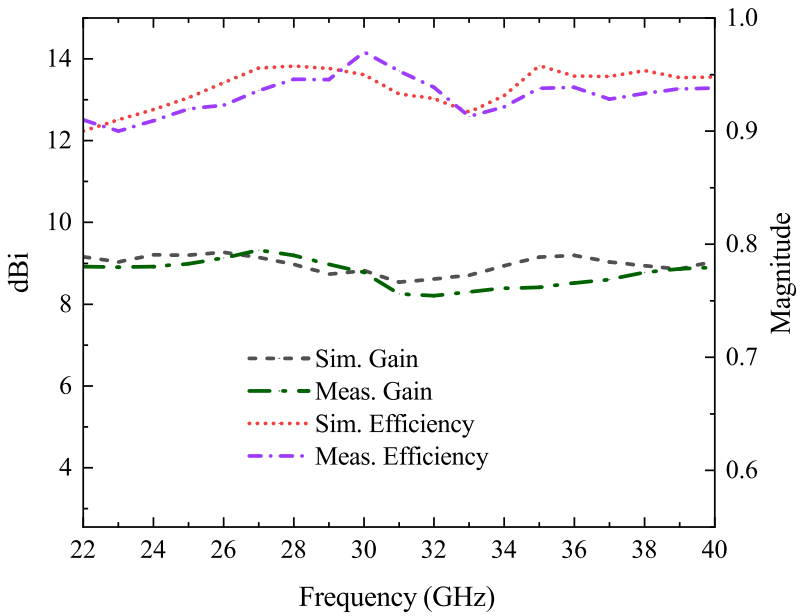

Figure 4.30: Comparison of simulated and experimental results for the gain and efficiency of the MIMO antenna.

4.5 MIMO Diversity analysis

4.5.1 TARC analysis

The TARC is a is a metric used to determine the operational frequencies of a MIMO antenna when its input signal phase is altered. The TARC is calculated by dividing the square root of the sum of all outgoing powers at the ports by the sum of all incident powers at the ports of an N-port antenna. For a six-element MIMO antenna, the TARC can be mathematically represented [133] as follows:

$$TARC = \frac{\sqrt{\sum_{i=1}^{6} |R_i|^2}}{\sqrt{\sum_{i=1}^{6} |I_i|^2}} \tag{4.16}$$

Where, R_i and I_i are the reflected and incident signals. Hence, the scattering matrix of a six-elemnt MIMO antenna can be written as:

$$\begin{bmatrix} R_1 \\ R_2 \\ R_3 \\ R_4 \\ R_5 \\ R_6 \end{bmatrix} = \begin{bmatrix} S_{11} & S_{12} & S_{13} & S_{14} & S_{15} & S_{16} \\ S_{21} & S_{22} & S_{23} & S_{24} & S_{25} & S_{26} \\ S_{31} & S_{32} & S_{33} & S_{34} & S_{35} & S_{36} \\ S_{41} & S_{42} & S_{43} & S_{44} & S_{45} & S_{46} \\ S_{51} & S_{52} & S_{53} & S_{54} & S_{55} & S_{56} \\ S_{61} & S_{62} & S_{63} & S_{64} & S_{65} & S_{66} \end{bmatrix} \begin{bmatrix} I_1 \\ I_2 \\ I_3 \\ I_4 \\ I_5 \\ I_6 \end{bmatrix} \tag{4.17}$$

The values of TARC can be further calculated as following:

$$TARC = \frac{\sqrt{\sum_{p=1}^{6} \left| R_{i1} + \sum_{p=1}^{6} R_{ip} e^{j\theta_{p-1}} \right|}}{\sqrt{6}} \tag{4.18}$$

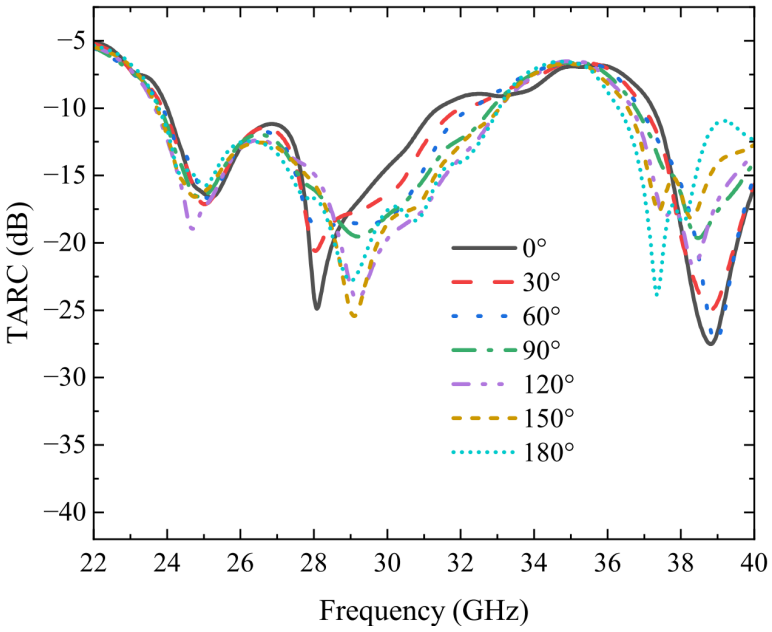

Figure 4.31: Calculated TARC values of the MIMO antenna.

$$TARC = \frac{\sqrt{\zeta_1 + \zeta_2 + \zeta_3 + \zeta_4 + \zeta_5 + \zeta_6}}{\sqrt{6}} \tag{4.19}$$

Where the coefficients of each element are:

$$\begin{aligned}
\zeta_1 &= |S_{11} + S_{12}e^{j\theta} + S_{13}e^{j\theta_1} + S_{14}e^{j\theta_2} + S_{15}e^{j\theta_3} + S_{16}e^{j\theta_4}|^2 \\
\zeta_2 &= |S_{21} + S_{22}e^{j\theta} + S_{23}e^{j\theta_1} + S_{24}e^{j\theta_2} + S_{25}e^{j\theta_3} + S_{26}e^{j\theta_4}|^2 \\
\zeta_3 &= |S_{31} + S_{32}e^{j\theta} + S_{33}e^{j\theta_1} + S_{34}e^{j\theta_2} + S_{35}e^{j\theta_3} + S_{36}e^{j\theta_4}|^2 \\
\zeta_4 &= |S_{41} + S_{42}e^{j\theta} + S_{43}e^{j\theta_1} + S_{44}e^{j\theta_2} + S_{45}e^{j\theta_3} + S_{46}e^{j\theta_4}|^2 \\
\zeta_5 &= |S_{51} + S_{52}e^{j\theta} + S_{53}e^{j\theta_1} + S_{54}e^{j\theta_2} + S_{55}e^{j\theta_3} + S_{56}e^{j\theta_4}|^2 \\
\zeta_6 &= |S_{61} + S_{62}e^{j\theta} + S_{63}e^{j\theta_1} + S_{64}e^{j\theta_2} + S_{65}e^{j\theta_3} + S_{66}e^{j\theta_4}|^2
\end{aligned} \tag{4.20}$$

The computed TARC for the proposed MIMO antenna design is shown in Fig. 4.31. In the TARC analysis, the phase of the input signal at the first port was kept constant at 0°, while the phases at the other six ports were varied from 0° to 180° in 30° steps. The TARC measurements consistently fall well under the conventional 10 dB threshold, demonstrating excellent impedance matching and minimal reflection-induced power losses. Despite a minor uptick in TARC at 39 GHz, the values remain within acceptable ranges, indicating that the antenna maintains effective decoupling even at higher frequencies. The TARC's stability across various phase angles further confirms the antenna's ability to accommodate diverse signal excitations without performance degradation. Moreover, the consistent TARC response ensures the antenna's efficient operation in dynamic settings where phase variations are prevalent, such as in beamforming and spatial multiplexing scenarios.

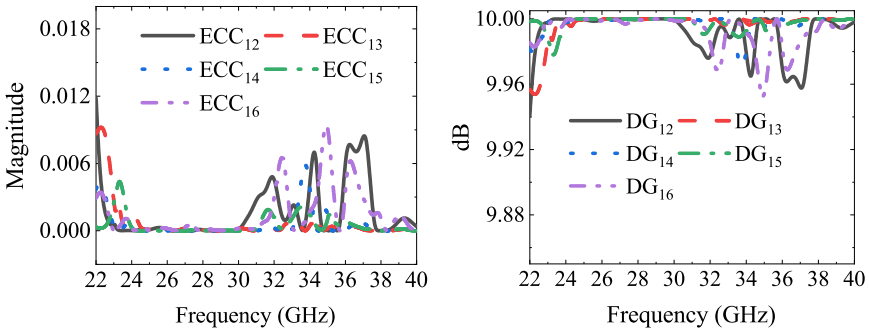

Figure 4.32: Comparison of ECC and DG performance for the MIMO antenna.

4.5.2 ECC and DG analysis

The ECC is an another essential metric for the investigation of MIMO antenna systems. It quantifies the degree of correlation between the radiation patterns of antenna elements in a MIMO configuration. The ECC values are ideally within the range of 0 and 1. A value of zero signifies no correlation, while a value less than 0.5 is generally considered acceptable in practical applications. The ECC values for the antenna elements are calculated using far-field and are shown in Fig: 4.32. The ideal value of DG is supposed to be 10 dB, which signifies the absence of any correlation between the antenna elements. The ECC and DG parameters of the MIMO antenna are depicted in Fig. 31. In Fig. 31(a), it is evident that the ECC values fall well below the standard of 0.5 and approach zero across most frequencies of the impedance bandwidth. Similarly, as shown in Fig. 31(b), the MIMO antenna exhibits exceptional DG values surpassing 9.98 dB, which are nearly in line with the standard threshold of 10 dB throughout the impedance bandwidth.

4.6 Designed MIMO antenna application scenario

The proposed MIMO antenna can be utilized in WBAN applications, as shown in Fig. 4.33. In a medical care context, WBAN is employed to remotely monitor patients by medical professionals. To this end, biosensors are placed on the patient's body which collect and transmit crucial physiological data to a central hub. The hub subsequently collects the data and wirelessly sends it to an access point, which is integrated into the hospital's local network infrastructure. This information is then transmitted over the internet, allowing medical professionals to access it remotely and facilitating real-time monitoring and remote consultation. The proposed MIMO antenna, due to its compactness and semi-flexible substrate, can be mounted on the human body.

The antenna was placed on the human body arm, chest, and leg regions, as depicted in Fig. 4.34, to evaluate its performance in realistic wearable conditions. The reflection

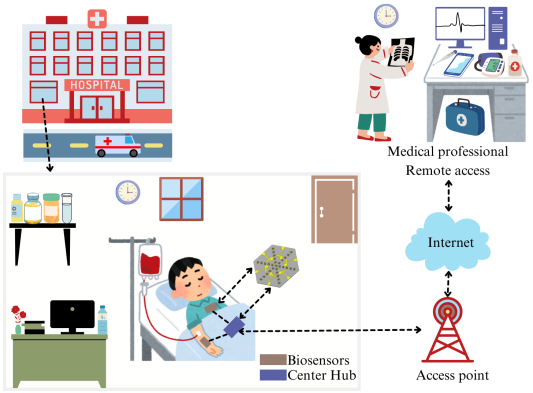

Figure 4.33: An application overview of the proposed MIMO antenna in WBAN system.

Figure 4.34: MIMO antenna placement on the arm, chest, and leg regions.

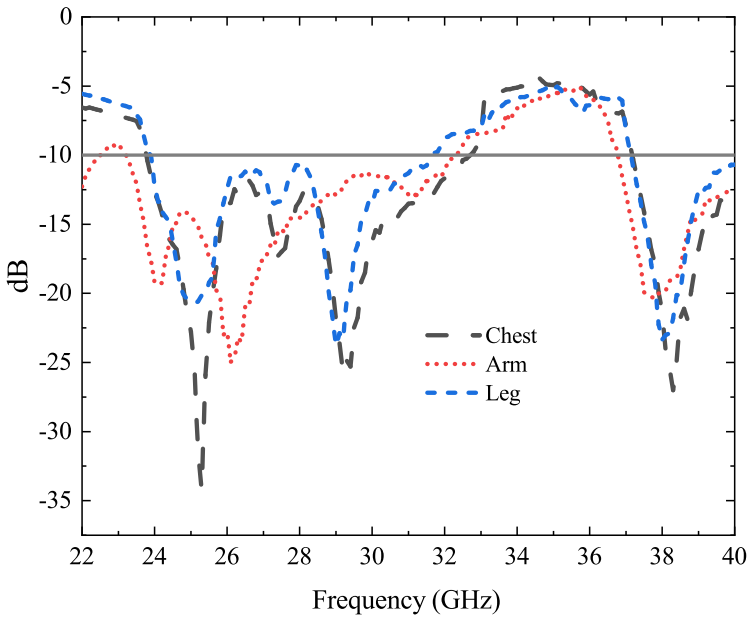

Figure 4.35: Comparison of the MIMO antenna reflection coefficients when placed on chest, arm, and leg regions.

coefficient results for these different placements are presented in Fig. 4.35. A slight impedance bandwidth shift is observed across all cases in the results, however: the desired operating frequencies, including 26 GHz, 28 GHz, 30 GHz, and 38 GHz, remain well covered in all cases. The frequency shift is most noticeable when the antenna is placed on the arm region. This can be attributed to the increased bending and muscle

movement in the arm, which introduces additional variations in the antenna's effective permittivity and impedance characteristics. In contrast, the chest and leg placements exhibit relatively smaller shifts, likely due to their more stable and uniform surface profiles, resulting in fewer perturbations to the antenna's EM properties. Despite these shifts, the antenna maintains its dual-band functionality across all three placements, confirming its robustness for on-body applications. The minimal performance variation suggests that the design effectively mitigates the impact of body loading effects, which is a critical factor for wearable antenna applications. Thus the design MIMO antenna is well-suited for integration into WBAN and other wearable communication systems.

4.6.1 Safety analysis

Evaluating the absorption of EM radiation by human tissue is essential for any antenna designed for on-body use. This evaluation ensures the safety and protection of the human body. The SAR serves as a critical metric, indicating the amount of EM energy absorbed by human tissue. The designed MIMO antenna was positioned on various parts of the CST Hugo model, which was obtained from the CST voxel library, as shown in Fig. 4.36.

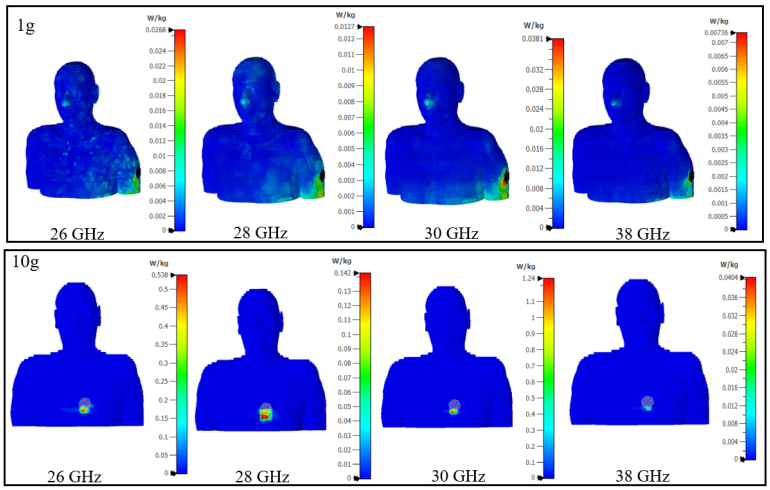

Figure 4.36: SAR values at arm and chest regions.

SAR assessment was performed at 500 mW power, a reasonable level for practical wearable communication systems. The MIMO antenna's SAR values were examined at 26 GHz, 28 GHz, 30 GHz, and 38 GHz. The 1g SAR measurements were 0.0268, 0.028, 0.031, and 0.0037 W/kg, respectively. Correspondingly, the 10g SAR measurements were 0.538, 0.142, 1.24, and 0.040 W/kg, respectively. These findings demonstrate that the proposed MIMO antenna exhibits low SAR values across the tested frequency ranges, staying well within the IEEE and ICNIRP safety guidelines for wearable communication devices. The slightly elevated SAR at 30 GHz in the 10g evaluation might be due to localized absorption caused by the antenna's proximity to the body, but

the values remain within acceptable limits. Thus, these results confirm the designed MIMO antenna's suitability for on-body WBAN applications without presenting significant health risks to the human body.

4.6.2 Communication link analysis

To analyse the communication efficiency of the proposed MIMO antenna, communication assessments were performed for two different scenarios and at two different resonant frequencies of 28 GHz and 38 GHz. Analysing the communication capacity of the MIMO antenna is essential in WBAN applications scenarios.

Scenario 1:

In this scenario, it was assumed that the MIMO antenna is positioned on the chest and operates as a transmitter (Tx), while an ideal $\lambda_o/2$ dipole antenna functions as a receiver (Rx) situated in free space at a distance (d) from the Tx. The received power (P_r) is calculated based on the path loss (PL_{dB}) using the following equations [134]:

$$P_r(\mathrm{dBm}) = P_t(\mathrm{dBm}) + G_t(\mathrm{dB}) + G_r(\mathrm{dB}) - \mathrm{PL}_{dB}(\mathrm{dB}) \tag{4.21}$$

$$\mathrm{PL}_{dB}(d) = 10n \log_{10}\left(\frac{d}{d_0}\right) + 20 \log_{10}\left(\frac{4\pi d}{\lambda_0}\right) + X_\sigma \tag{4.22}$$

where P_t represents the transmitted power, G_t is the transmitter antenna gain, G_r denotes the receiver antenna gain, and n is the path loss exponent that varies based on the communication scenario (LOS or NLOS). The parameter d represents the distance between the Tx and Rx antennas, while X_σ is a Gaussian-distributed random variable with a standard deviation accounting for environmental variations. For this evaluation, P_t was considered at three levels: 10 dBm, 20 dBm, and 30 dBm, with G_r set at 2 dBi to simplify the communication path analysis. The G_t value was chosen as 8.98 dBi, representing the average of the measured gains at 28 GHz (9.12 dBi) and 38 GHz (8.77 dBi). The path loss exponent (n) was set to 1.5 for LOS conditions and 3.0 for NLOS conditions, reflecting multipath propagation environments. Additionally, X_σ was assigned a value of 0 dBm, and the reference distance (d_0) was set at 1.0 m. The distance d was varied up to 30 m to assess the communication performance.

The results, presented in Fig. 4.37, demonstrate that when operating at a high transmit power of 30 dBm, the MIMO antenna enables the dipole antenna with 2 dBi gain to receive more than -60 dBm of power at distances up to 15 meters in both LOS and NLOS scenarios for 28 GHz and 38 GHz. At a lower transmit power of 10 dBm, the dipole antenna can still receive power greater than -75 dBm at a distance of up to 15 meters in LOS conditions at 28 GHz. However, at 38 GHz, the received power is significantly reduced for the 10 dBm input power in both LOS and NLOS links, which

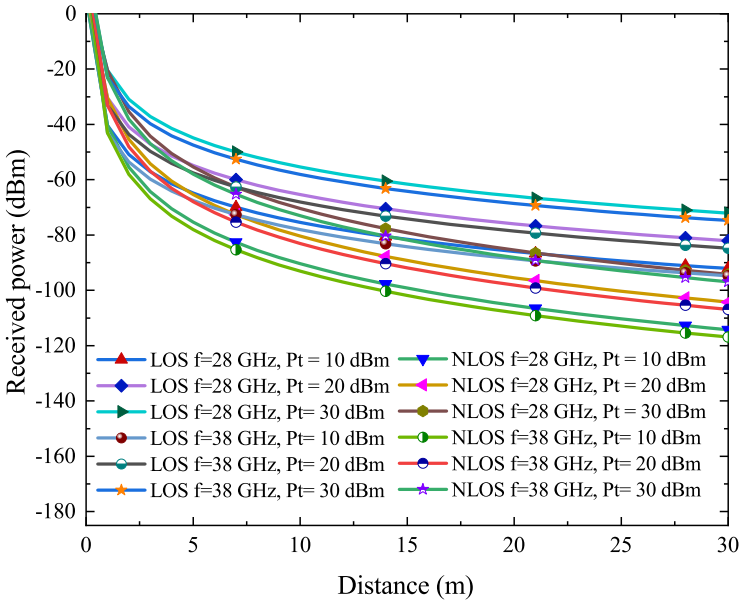

Figure 4.37: Impact of Tx-Rx distance on received power in LOS and NLOS uplink communication using a dipole antenna.

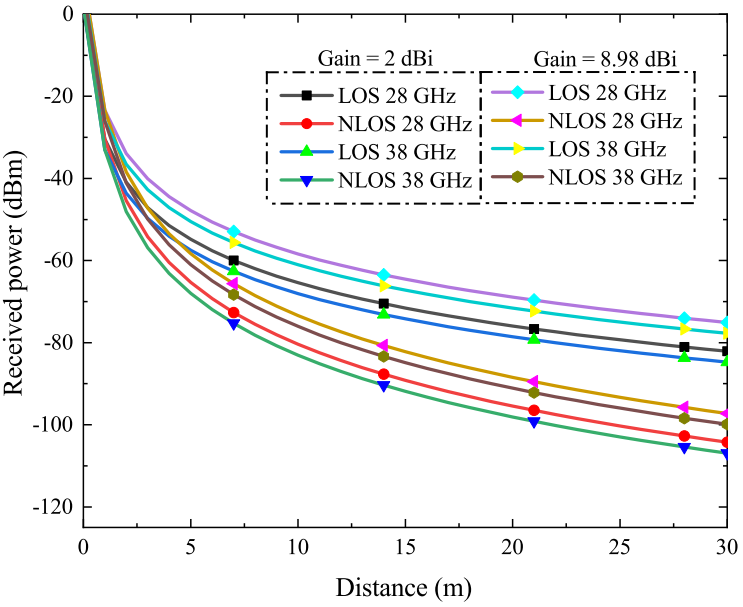

Figure 4.38: Received power comparison of the dipole and proposed antenna with a 20 dBm transmitter power.

can be attributed to higher free-space path losses and increased atmospheric absorption at higher frequencies.

Case 2:

In this case the proposed MIMO design was regarded both as the transmitter and receiver antenna. The results were then compared with those of Case 1 for P_t = 20 dBm, and shown in Fig. 4.38. An improvement in power reception of almost 7 dBm was recorded at all distance points beyond 5 m. Consequently, if the same type of antennas are used at both the transmitting and receiving ends, it can lead to even better

reception of power. In accordance with the significance of human safety, the maximum power limit for wearable antennas has been set at 17 dBm. The results of the SAR analysis presented in Fig. 35 and the calculations of the received power in both LOS and NLOS scenarios indicate that the proposed antenna is capable of achieving effective communication while also ensuring the safety of human tissues during operation.

Table 4.2: Link budget parameters.

Transmitter conditions	
Parameter	**Value**
Operating frequency, f (GHz)	28/38
Transmitted power, P_t (dBm)	17
Transmitter antenna gain, G_t (dBi)	9.12/8.77
EIRP ($P_t + G_t$) (dBm)	26.12/25.77
Propagation environment conditions	
Distance, d (m)	0-100
Free space loss, L_f (dB)	Adaptive (distance)
Receiver conditions	
Receiver antenna gain, G_r (dBi)	8.98 (average)
Ambient temperature, T_0 (K)	293
Boltzmann constant, k	1.38×10^{-23} W/m K
Noise power density, N_0 (dB/Hz)	-203.9
Signal conditions	
Bit rate, B_r (Mb/s)	1, 10, 50, 100
Bit error rate	1×10^{-5}
E_b/N_0 (ideal PSK), (dB)	9.6
Coding gain, G_c (dB)	0
Fixing deterioration, G_d (dB)	2.5

Link Margin: The link margin analysis is of great importance in wireless communication. This measure represents the difference between the received signal strength and the minimum necessary signal strength for effective communication. It is typically expressed in decibels (dB) and functions as a safety margin, while ensuring reliable data transmission even in a noisy communication channel. The link margin is determined using equations (25-30) at two resonance frequencies of 28 and 38 GHz, and the link budget parameters are presented in Table 1 [135].

$$L.M\,(dB) = Link\left(\frac{c}{N_0}\right) - Required\left(\frac{c}{N_0}\right) \tag{4.23}$$

$$Link\left(\frac{c}{N_0}\right) = EIRP - L_f + G_r - N_0\,[\mathrm{dB/Hz}] \tag{4.24}$$

$$Required\left(\frac{c}{N_0}\right) = \frac{E_b}{N_0} + 10\log_{10}(B_r) - G_c + G_d\,[\mathrm{dB/Hz}] \tag{4.25}$$

$$L_f = 20\log_{10}\left(\frac{4\pi d}{\lambda}\right)(\mathrm{dB}) \tag{4.26}$$

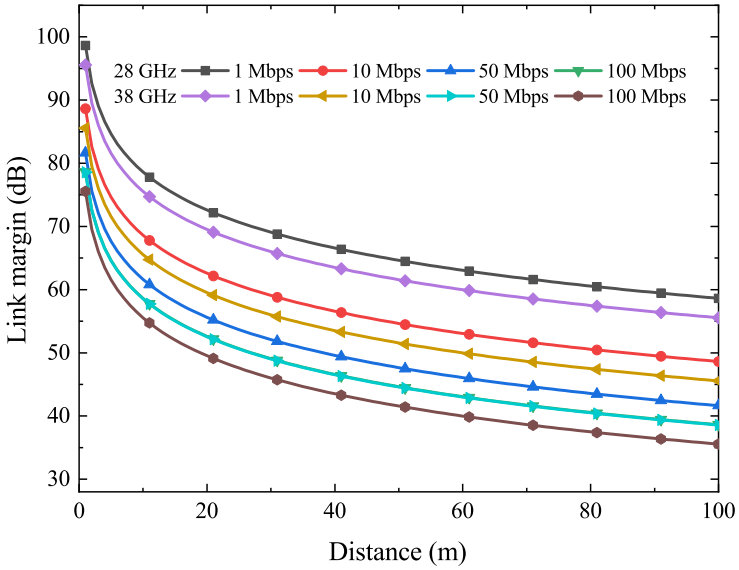

Figure 4.39: Link margin results.

$$N_0 = 10\log_{10}(k) + 10\log_{10}(T_i)\,[\mathrm{dB/Hz}] \tag{4.27}$$

$$T_i = T_0\,(NF - 1)\,[K] \tag{4.28}$$

In this study, we have taken into account an input power of 17 dBm to ensure safety. The calculated link margin is depicted in Figure 38. The calculated link margin indicates that as the communication distance increases, the margin decreases. At a frequency of 28 GHz, a higher link margin was observed compared to a frequency of 38 GHz for the same data rate. The reduction in link margin can be attributed to the increased path loss at 38 GHz compared to 28 GHz. However, the link margin improves to 55 dB when the separation distance is below 10 meters, which is a typical distance for wearable antenna communication. The proposed antenna can transmit and receive data at a rate of 100 Mbps up to 100 meters for both resonant frequencies of 28/38 GHz, with a link margin of over 35 dB. The proposed MIMO design effectively demonstrates its capacity to process significant amounts of data at 28/38 GHz mm-wave bands.

The table presents a comparative analysis of the designed dual-band MIMO antenna against previously reported designs in Table 4.3. The proposed antenna, with six ports and dimensions of 25 × 43 × 0.79 mm³, is relatively compact compared to larger designs such as [141] (104 × 104 × 0.51 mm³) and [143] (54 × 54 × 0.8 mm³). It offers a wide impedance bandwidth spanning 23.63–32.90 GHz and 36.68–40 GHz, which is significantly broader than many existing antennas, including [136] (28.80–29.80 GHz) and [142] (27.5–28.50 GHz). The presence of multiple resonant bands enhances its suitability for multi-band communication applications, unlike some designs that operate within a single frequency range. In terms of isolation, the proposed antenna achieves greater than 33 dB, which is higher than many designs such as [142] (>20 dB) and [141] (>16 dB). While some designs, such as [136] (>36 dB), offer slightly better isolation,

Table 4.3: Performance comparison of the designed six-element MIMO antenna with other reported MIMO antennas.

(a) Comparison of dimensions, impedance bandwidth, and isolation.

Ref.	Port	Dimensions (mm^3)	Bandwidth (GHz)
[136]	2	11.4×5.3×0.8	28.80-29.80
[137]	4	32.5×32.5×0.51	36.83-40.0
[138]	2	15×15×0.52	23.6–24.9
[139]	4	20×20×0.20	26.9-29/34.5-41
[140]	4	9.8×38.64×0.508	36.5-39.28
[141]	4	104×104×0.51	22-30
[142]	4	18×18×0.79	27.5-28.50
[143]	8	54×54×0.8	23.30-27.60
[144]	4	24×20×1.85	24.10-27.18
Prop.	6	25×43×0.79	23.63-32.90/36.68-40

(b) Comparison of isolation, gain, ECC, and decoupling techniques.

Ref.	Isolation (dB)	Gain (dBi)	ECC
[136]	>36	6	<0.0001
[137]	>25	6.5	0.001
[138]	>25	6.1	NR
[139]	>23	9.5	0.0001
[140]	>30	10	3×10^{-5}
[141]	>16	10	0.0001
[142]	>20	7.50	0.0025
[143]	>26	8.6	<0.0004
[144]	>16	3.01	<0.01
This work	>33	9.12/8.77	<0.0010/0.009

they may have trade-offs in bandwidth and gain. The proposed antenna exhibits a gain of 9.12 dBi at one frequency and 8.77 dBi at another, making it comparable to high-performance designs such as [139] (9.5 dBi) and [140] (10 dBi) while outperforming designs like [144] (3.01 dBi) and [142] (7.50 dBi). Additionally, its ECC values remain below 0.0010 and 0.009, indicating excellent MIMO performance with minimal correlation between antenna elements. Most existing designs, such as [136] (<0.0001) and [139] (0.0001), exhibit similarly low ECC values, but some, like [142] (0.0025), show slightly higher correlation. Overall, the proposed six-port multi-band MIMO antenna achieves a well-balanced trade-off between compact size, wide bandwidth,

high isolation, and good gain performance. Its multiple resonances allow for operation across different frequency bands, making it suitable for applications in 5G, IoT, and high-speed wireless communication.

4.7 Conclusion

A six-element MIMO antenna design which features a modified elliptical shape and optimized by utilizing CMA is thoroughly explained. The antenna design incorporates a thin copper layer for the ground plane and top patch, with modifications to the elliptical patch to achieve the desired impedance bandwidth. The chapter explained the MIMO configuration development in three stages: full ground plane, DGS, and FSS integration. The fabricated prototype measurements demonstrate strong agreement with simulations, exhibiting high isolation due to the FSS decoupling effect. Radiation pattern evaluations confirm stable gain and efficiency, while diversity performance, assessed through TARC, ECC, and diversity gain, indicates minimal correlation and robust MIMO characteristics. The antenna is further evaluated in IoT-based WBAN applications, particularly placement on the human body results in minor impedance shifts. Safety analysis confirms that SAR values remain within regulatory limits. Communication link evaluations at 28 GHz and 38 GHz demonstrated effective power reception and reliable data transmission up to 100 meters, with satisfactory isolation and gain. These results show the potential of the designed MIMO antenna for 5G-enabled IoT and WBAN applications.

Chapter 5

Mutual Coupling Mitigation in compact Dual-Band mmWave MIMO Antenna

5.1 Introduction

Mutual coupling in MIMO arises primarily from near-field interactions and surface wave coupling between adjacent antenna elements [145]. For instance, when one antenna is operational, it generates surface waves propagating along the substrate which interact with adjacent antennas, resulting in coupling. Moreover, near-field coupling can occur between the radiated fields of the active antenna and adjacent elements, intensifying mutual coupling. In the previous chapters, the utilization of DGS and FSS partially reduced mutual coupling, for example, through surface current distribution. These approaches primarily address the coupling caused by surface waves between radiating elements while largely overlooking the impact of near-field interactions. Furthermore, these techniques are predominantly applicable in scenarios where the spacing of antenna elements is at least greater than half-wavelength. An alternative approach could be a hybrid method where the surface current is reduced with previously discussed techniques and a MTS for near-field interaction. This approach has the potential to mitigate both types of coupling.

In this chapter, a novel hybrid technique to reduce coupling in a closely spaced dual-band MIMO antenna, targeting both surface waves and near-field radiation interactions has been discussed. Initially, metallic vias are employed to reduce surface currents. Subsequently, a MTS placed above the MIMO antenna can reduce near-field radiation interactions. The dual-band MIMO antenna (designated $MIMO_1$) exhibits a high level of mutual coupling of -13 dB due to close spacing. The incorporation of vias in the design ($MIMO_2$) reduces the surface current and achieves a reduced coupling of -25 dB, whereas the final design ($MIMO_3$) incorporating both the vias and MTS achieves an excellent coupling reduction to the level of -30 dB. It is thus evident that the proposed hybrid design approach is capable of significant reduction in the surface wave coupling and near-field interactions.

5.2 Single antenna element design

The single antenna element antenna was designed in CST Studio and on a Rogers RO4003C substrate. The antenna featured a circular shape with a 6.80 mm radius and was built on a substrate measuring 1.52 mm in thickness. The substrate material had a relative permittivity of 3.55 and a loss tangent of 0.0027. The goal was to develop a dual-band antenna with bands in close proximity around 27/28 GHz 5G mmWave bands. The narrow bands are advantageous for applications such as energy harvesting at mmWave frequencies. This is attributed to the fact that narrow bands with optimal matching can mitigate out-of-band noise [146]. Similarly, narrowband rectification is preferred owing to its high efficiency and optimized matching [147]. To achieve desired dual-band operation goal while ensuring optimal impedance matching, an iterative design approach was adopted, as shown in Fig. 5.1. The results of reflection coefficient and each stage's impact on the bandwidth is shown in Fig. 5.2. Initially, a circular copper patch radiator (thickness = 0.035 mm) was implemented. While this design provided a fundamental resonance, it exhibited significant reflection losses and poor impedance matching due to the lack of resonant-enhancing structures. To address this issue, the circular patch was modified into a semi-circular shape in the second step. This alteration aimed to enhance resonance characteristics by modifying the current distribution, but the high reflection losses persisted, indicating the need for additional structural modifications.

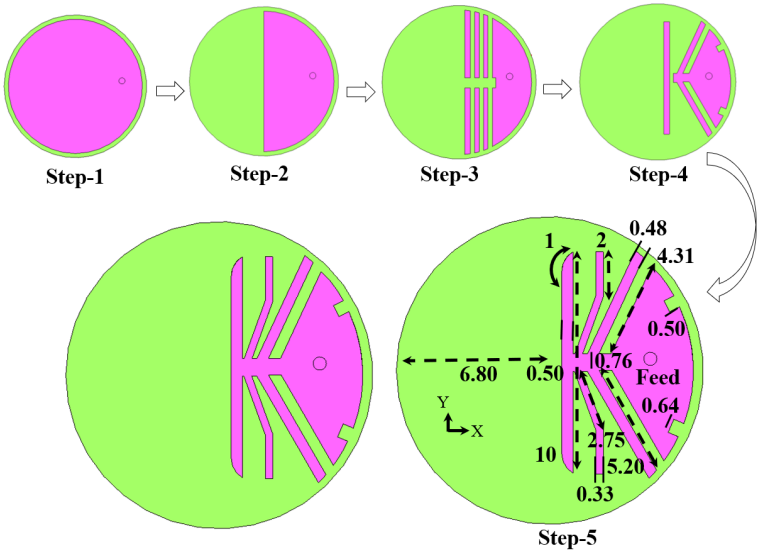

Figure 5.1: Iterative design steps of the single element mmWave dual-band antenna.

In the third step, three strip lines were introduced and positioned at specific intervals to improve bandwidth characteristics and support resonance near 27 GHz. These strip lines functioned as resonance-enhancing structures, influencing the effective electrical length of the antenna. However, the reflection characteristics exhibited minimal improvement, and the targeted dual-band response was not yet achieved. To

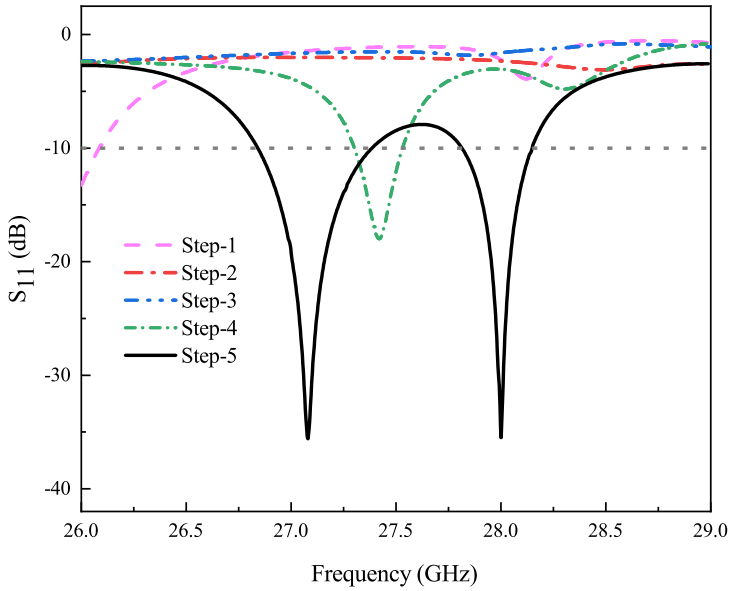

Figure 5.2: Reflection coefficients comparison of each design steps of the single element antenna.

further refine the design, the middle strip line was removed, and the first strip line was rotated to form a tapered structure in the fourth step. This modification successfully generated a resonance frequency near 27.5 GHz, confirming the role of the tapered structure in improving impedance matching. Nevertheless, dual-band operation was still not realized. In the final step, the middle strip line was reintroduced with further refinements applied to the strip endpoints. Specifically, the middle strip line was maintained in a straight configuration, while the endpoints of the third strip line were chamfered, resulting in a K-shaped structure with a tapered base. These modifications successfully enabled dual-band operation at 27 GHz and 28 GHz, with significantly enhanced impedance matching.

5.2.1 Analytical circuit model of the single element dual-band mmWave antenna

The analytical circuit representation of the single element dual-band mmWave antenna is achieved through an equivalent RLC circuit model and is shown in Fig. 5.3. In order to investigate the dual-bands of antenna impedance characteristics, the circuit model utilizes passive electrical components, including resistor (R), inductor (L), and capacitor (C). The circuit model provides resonance and impedance bandwidth behavior of the antenna without relying solely on full-wave EM simulations. The designed circuit model consists of a combination of RLC elements arranged in series and parallel configurations to replicate the distributed effects of the physical antenna structure, including the patch geometry, slot patterns, and feed line coupling.

The inductive elements in the circuit correspond to the current flow along the strip

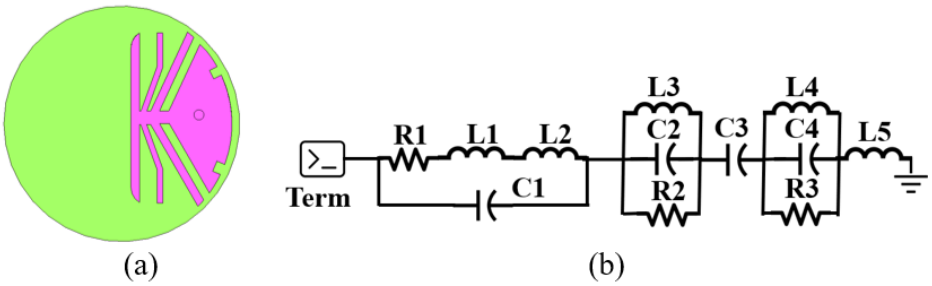

Figure 5.3: (a) Designed EM model in CST and (b) ADS circuit model of dual-band mmWave antenna.

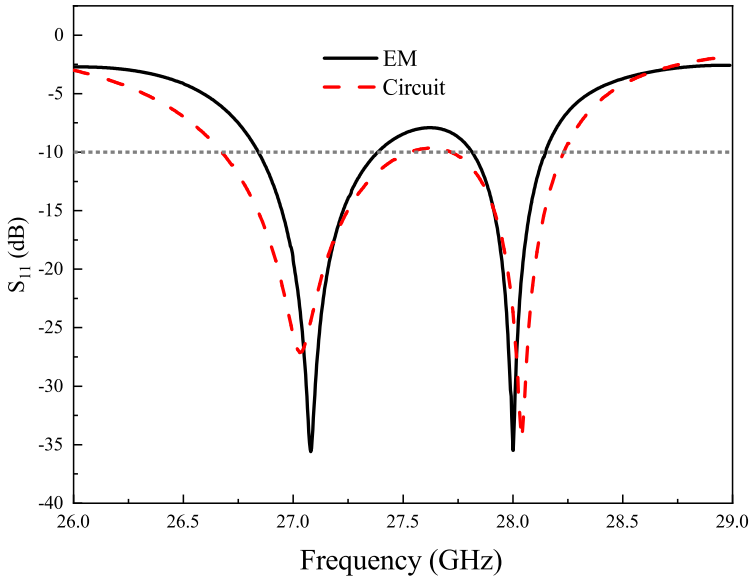

Figure 5.4: Comparison of the reflection coefficient between EM and circuit based designs.

lines and conductive paths of the antenna, with multiple inductors accounting for different resonant sections of the design. The capacitive elements model the gap capacitance created by the slots and tapered edges in the radiating structure, playing a key role in defining the frequency selectivity of the antenna. The inclusion of resistivity elements accounts for various loss mechanisms, such as dielectric, conductor, and radiation losses, ensuring that the model accurately represents practical attenuation effects. Additionally, the transmission line feeding structure is modeled through a series and parallel LC circuits.

A comparison of the results of the both EM and circuit model are shown in Fig. 5.4. It can be demonstrated that the circuit based model is showing almost similar results. Minor discrepancies between the two models arise due to higher-order effects and fringing fields, which are more accurately accounted for in EM simulations but are approximated in the lumped-element circuit model. Despite these slight variations, the circuit model proves to be a valuable tool for design optimization, providing a faster means of analysing resonance behaviour and fine-tuning frequency responses

without extensive computational simulations. In the circuit analysis, the coaxial feeding was examined separately (R1, L1, L2, and C1), whereas the resonant behaviour of the antenna was analysed as parallel RLC circuits. The capacitor C3 represents the spacing between strip lines, while L5 demonstrates the inductance of strip lines. The circuit was optimized in the Keysight ADS schematic environment. In ADS, antenna behaviour can be model using an equivalent RLC circuit that represents its input impedance characteristics. The ADS optimization tool is then used to adjust the RLC component values so that the reflection coefficient of the circuit model closely matches that of the CST-based full-wave electromagnetic (EM) model. The final optimized RLC circuit parameters value are as follows: Term = 50Ω (matching), R1 = 62.08, R2 = 62.54, R3 = 52.50 (Ω), L1 = 974.26 (pH), L2 = 0.97, L3 = 0.005, L5 = 0.016, L4 = 0.010 (nH), C1 = 0.51, C2 = 5.56, C3 = 0.19, and C4 = 3.27 (pF).

5.2.2 Parametric analysis of the dual-band mmWave antenna

The reflection coefficient results of the designed dual-band mmWave antenna were examined for various parameter modifications, as shown in Fig. 5.5. The analysis specifically focused on four critical design variables: y_m, x_m, t_w, and b_r, and their effects on resonance behavior, although additional factors also influenced the results.

Fig. 5.5(a) demonstrates how altering y_m, which denotes the vertical feed position in the radiating element, impacts the antenna's performance. Adjusting y_m causes a notable frequency shift in both resonant bands, with an increase in y_m primarily affecting the first resonance frequency while minimally impacting the second band. The impact of x_m, representing the horizontal feed location, is shown in Fig. 5.5(b). Increasing x_m results in shifts in both resonance frequencies. This suggests that x_m is critical in regulating the higher-frequency resonance, possibly due to its effect on the radiating structure's effective electrical length. Fig. 5.5(c) shows the strip line width t_w for different values. As can be seen that the larger t_w is creating a downward shift in the 27 GHz frequency band, while the 28 GHz resonance band remains relatively stable. Changes in t_w also affect the impedance bandwidth, with narrower widths resulting in slightly better matching. This indicates that t_w mainly influences the frequencies around 27 GHz and helps in optimizing impedance matching at these frequencies. The effect of b_r, which represents the stripline curvature, is analyzed in Fig. 5.5(d). Variations in b_r cause changes in both resonant frequencies, with a more pronounced effect on the lower band. The results show that optimizing b_r is crucial for fine-tuning impedance matching in both bands while maintaining a consistent bandwidth. Higher b_r values slightly shift both resonances upward. The parametric analysis demonstrates that each structural modification distinctly influences the dual-band mmWave antenna's impedance bandwidth characteristics. Consequently, to achieve the desired frequencies in other bands, these parameters can be fine-tuned accordingly.

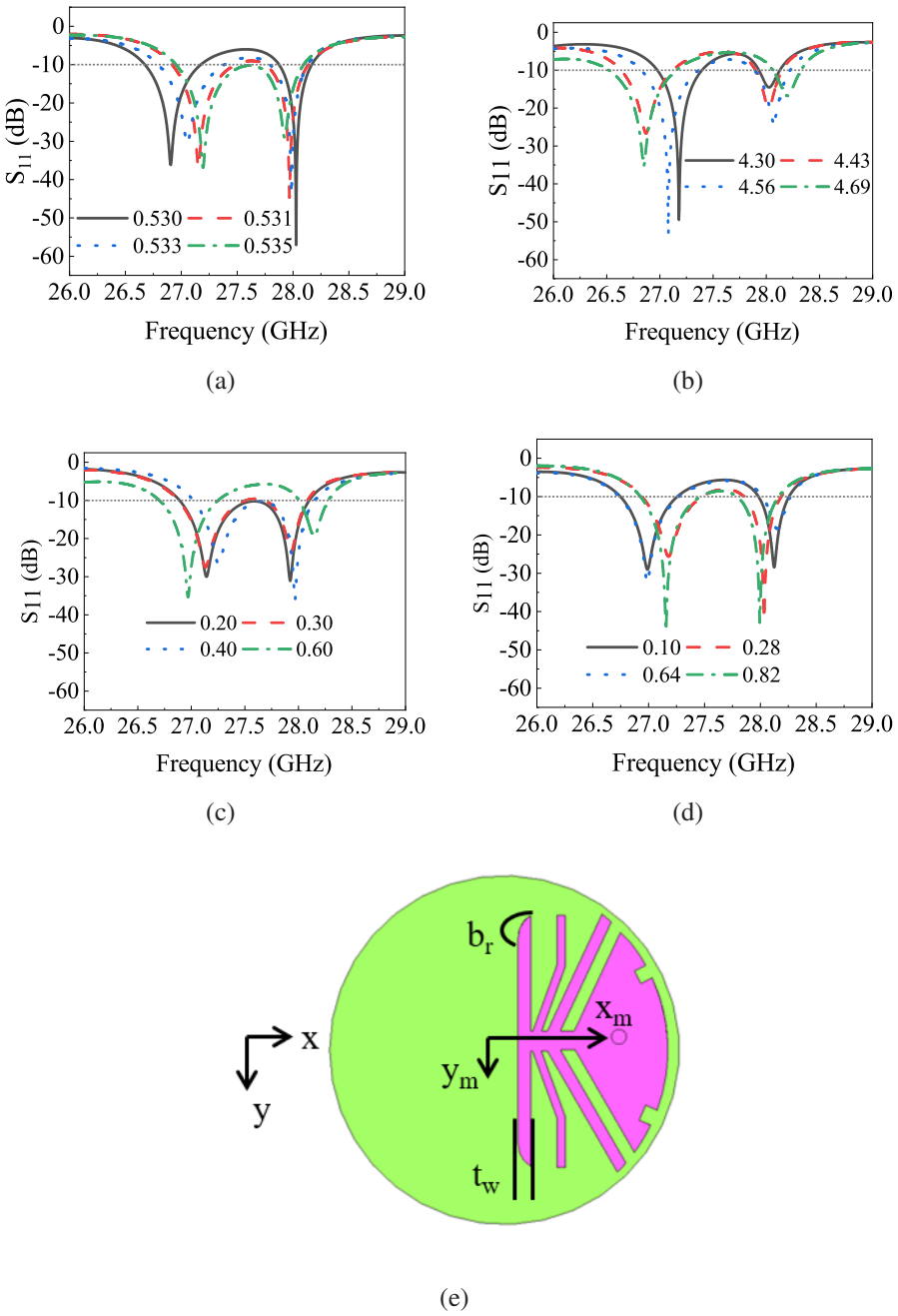

Figure 5.5: Parametric results of (a) y_m, (b) x_m, (c) t_w, (d) b_r, and (e) the structure illustrating the parameters.

The surface current distribution and 3D radiation H-plane pattern of the dual-band mmWave antenna at 27 GHz and 28 GHz are shown in Fig. 5.6. The current distribution in Fig. 5.6(a) demonstrates that, at 27 GHz, a more pronounced current distribution is observed near the lower sections (left side) of the K-shaped structure. This observation indicates that this region contributes significantly to the 27 GHz frequency band. At 28 GHz, the current shifts slightly towards the upper strip (right) elements, illustrating their influence in exciting the second resonance. Similarly, the far-field radiation patterns shown in Fig. 5.6(a) for both 27 GHz and 28 GHz frequencies exhibit a stable broadside

radiation characteristic, with a well-defined main lobe directed along the broadside. The maximum gain of 4.79 dBi and 5.39 dBi at 27 GHz and 28 GHz was noticed.

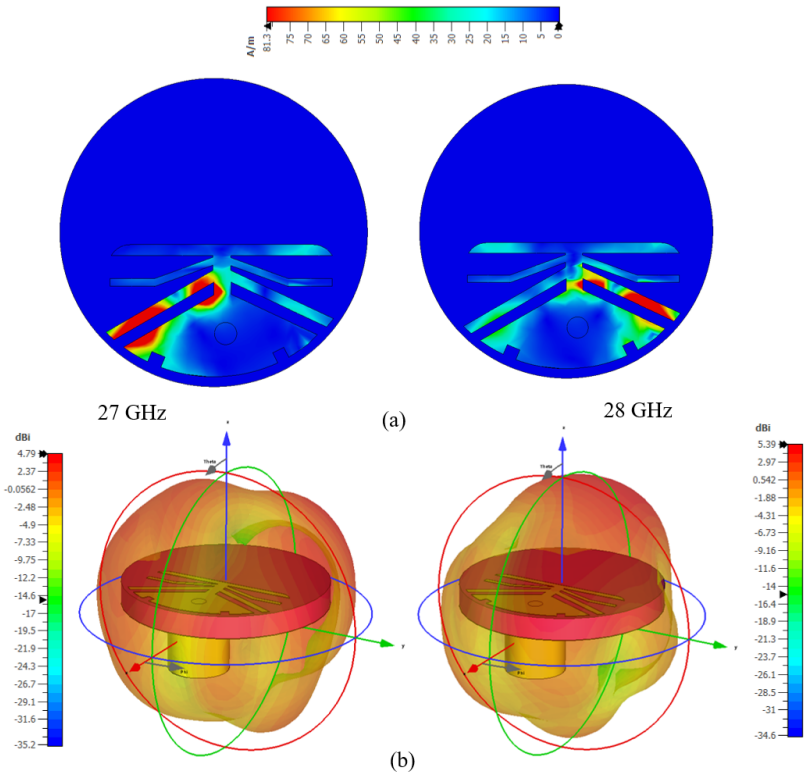

Figure 5.6: (a) Surface current and (b) H-plane.

5.3 MIMO antenna evolution and final dual-band mmWave design

The final MIMO antenna was achieved after three stages as illustrated in Fig. 5.7. This process was performed to achieve improved isolation, reduced mutual coupling, and enhanced radiation performance. The design stages are summarized as follows:

- **MIMO**$_1$ represents the initial 2×2 MIMO configuration with a closely spaced antenna layout. Owing to the close spacing, high mutual coupling was noticed in this stage.
- **MIMO**$_2$ introduces metallic vias between antenna elements to suppress surface wave propagation, reducing unwanted interactions and improving isolation.
- **MIMO**$_3$ incorporates a MTS structure, strategically placed above the antennas to further mitigate mutual coupling and enhance radiation characteristics. The MTS, shown in both front and back views, functions as a frequency-selective structure that enhances decoupling while maintaining a compact footprint.

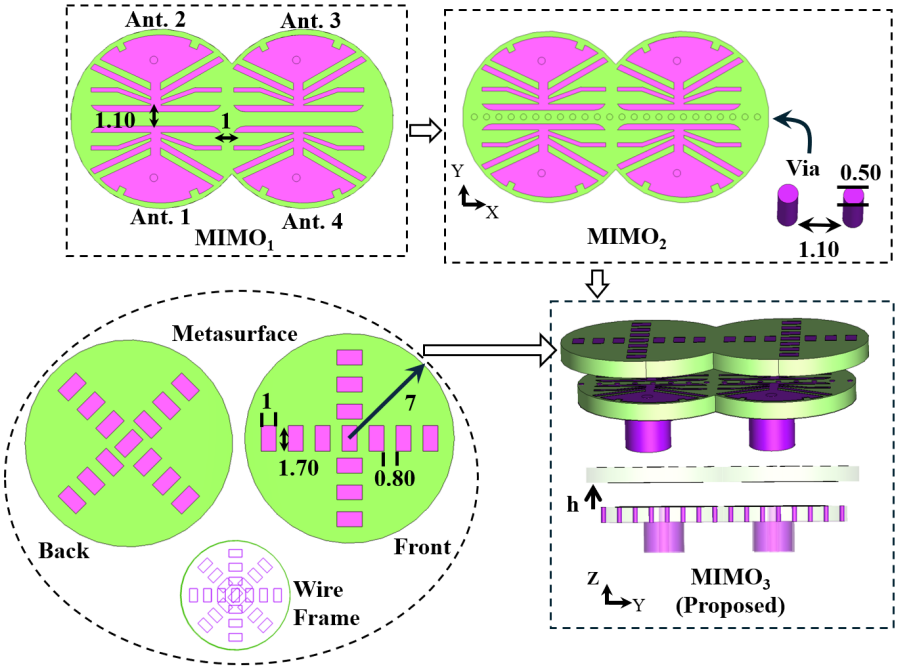

Figure 5.7: Design evolution of the MIMO antennas.

5.3.1 Dual band Four-element $MIMO_1$ design

The single antenna element was transformed into a four-element $MIMO_1$ antenna design and configured in a 2×2 arrangement as illustrated in Fig. 5.8. It is important to note that the spacing in the X- and Y-direction was 1.1 mm and 1 mm, respectively. To meet the increasing demands for compactness in modern electronic and portable devices, this smaller distance was maintained. It should be noted that this distance in both directions is significantly smaller than the half-wavelength of both desired resonance frequencies.

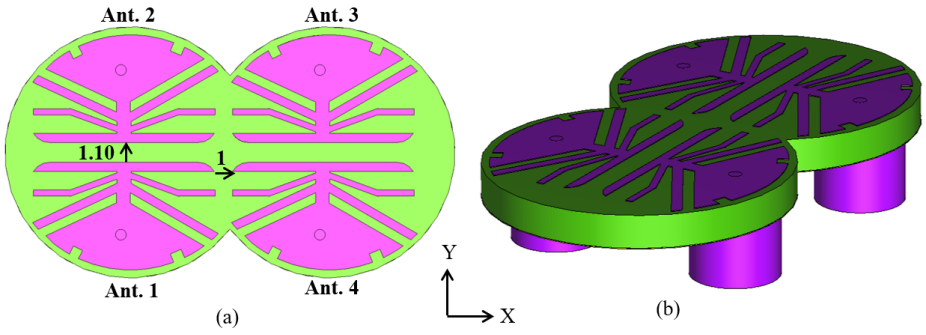

Figure 5.8: $MIMO_1$ antenna (a) top face and (b) perspective view.

The reflection and transmission coefficient results for the $MIMO_1$ antenna configuration are presented in Fig. 5.9. The results are compared with the S_{11} of a single antenna. The results in Fig. 5.9(a) show almost the same behaviour compared to single element antenna. The dual-band resonance is clearly observed at 27 GHz and 28 GHz, with return loss levels reaching below -30 dB. A slight bandwidth shift in S_{22} and S_{33} is evident. The observed frequency shift is primarily attributed to the placement

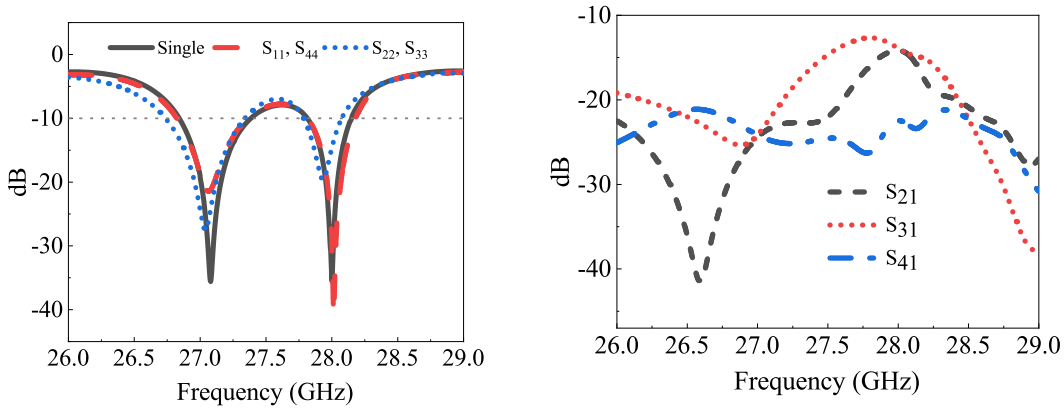

(a) (b)

Figure 5.9: MIMO$_1$ (a) reflection and (b) transmission coefficients results.

of antennas 2 and 3. Their position in the upper half of the structure results in more EM boundary interactions, which shifts the bandwidth. The impedance bandwidth for antenna 1 and 2 was: 26.83 GHz to 27.38 GHz and 27.81 GHz to 28.51 GHz. Likewise, the frequency range for impedance bandwidth between antennas 2 and 3 was measured to span from 26.72 GHz to 27.34 GHz, as well as from 27.79 GHz to 28.05 GHz.

The transmission coefficients or mutual coupling results of of MIMO$_1$ antenna is shown in Fig. 5.9(b). At 27 GHz, the coupling levels remain below -20 dB, suggesting acceptable isolation between all antenna elements. However, at 28 GHz, only S_{41} maintains coupling levels below -20 dB, while S_{21} and S_{31} exhibit higher coupling of -13 dB. This elevated coupling indicates that strong interactions occur, likely due to the close spacing and shared surface currents as can be seen in Fig. 5.10(a). The current distribution highlights the flow of surface current when antenna 1 is active while others are matched with 50Ω. At both 27 GHz and 28 GHz frequencies, more surface currents are concentrated in other antenna elements, which contribute to mutual coupling. These elevated coupling levels may significantly impair system performance, necessitating efforts to mitigate them. One approach to mitigate these couplings is to increase the spacing between antenna elements; however, this will increase the size constraints of the antenna, which may not be suitable for devices with limited space requirements. Thus, alternate techniques are required to decrease the coupling levels without increasing the antenna's spacing. The H-plane radiation pattern for antenna 1 element is also shown in Fig. 5.10(b). The results show maximum gain 7.06 dBi at 28 GHz.

5.3.2 Proposed technique for mutual coupling mitigation

For the two antenna elements (I_{th}, j_{th}) shown in Fig. 5.11, mutual coupling arises from radiated (S^{ij}_{Ra}) and surface (S^{ij}_{Sur}) waves. Thus, the total mutual coupling (S^{ij}_{Total}) is given by equation 5.1.

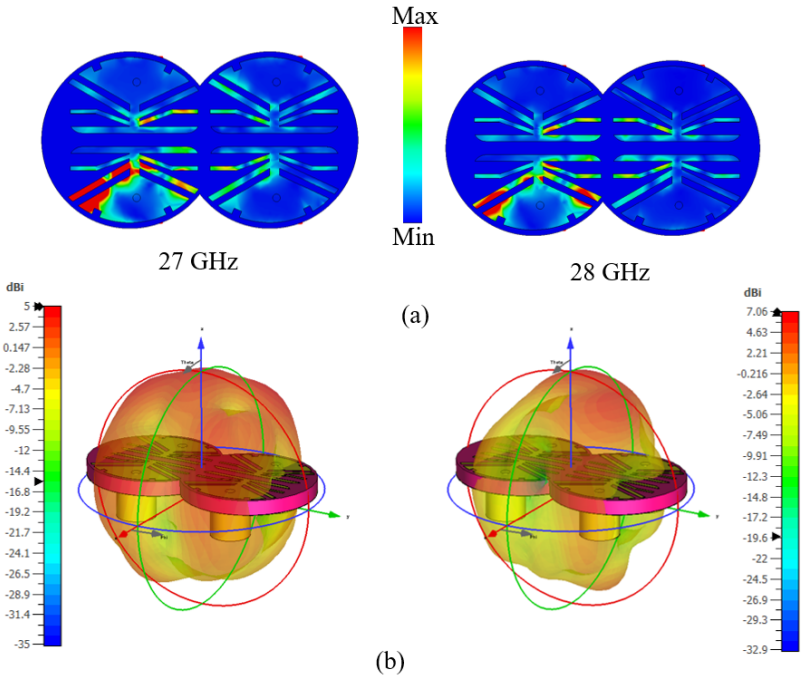

Figure 5.10: $MIMO_1$ antenna (a) current and (b) far-field radiation patterns.

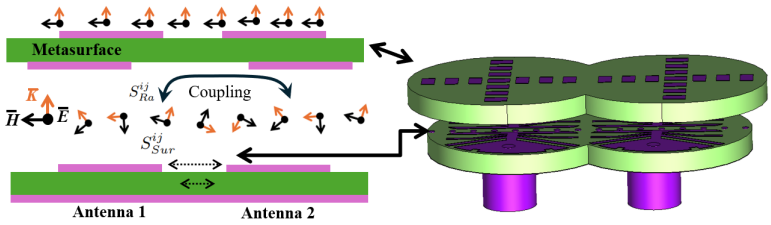

Figure 5.11: Mutual coupling basis and proposed decoupling techniques.

$$S_{Total}^{ij} = S_{Ra}^{ij} + S_{Sur}^{ij} \tag{5.1}$$

When S_{Ra}^{ij} and S_{Sur}^{ij} are equal in magnitude but out of phase, a smaller S_{Total}^{ij} is achieved. To mitigate S_{Sur}^{ij}, metallic vias between antenna elements can be used. EM waves between antennas induce currents on these vias, generating secondary fields that interfere with the original wave, reducing overall field strength at the other antenna. Similarly, to reduce S_{Ra}^{ij}, a MTS can be deployed. The coupling arises from the stray EM component $A_0 e^{jk_0}$, which propagates along the negative X-direction and induces currents in antenna 2. To mitigate this effect, a suspended MTS can be positioned above the MIMO antenna. This MTS generates a region with negative permeability and positive permittivity ($\mu_r < 0$, $\epsilon_r > 0$), thus altering the propagation characteristics of the EM waves [120]. In this region, the wavenumber is expressed as in equations 3.5 and 3.6. Equation 3.6 demonstrates that EM waves traveling along the MTS's negative x-direction exhibit evanescent behavior, leading to their attenuation. This effectively suppresses the wave contributing to mutual coupling between antennas. Conversely, when EM waves propagate along the z-direction with their magnetic field aligned along

the x-axis, the anisotropic characteristics of the MTS enable effective radiation and minimize mutual coupling.

5.3.3 Dual band Four-element MIMO$_2$ design

In order to reduce S_{Sur}^{ij} between antenna elements, metalic vias were introduced along the x-direction between the antenna elemnts in MIMO$_2$ design. The top face and 3D perspective of this design are shown in Fig. 5.12. The radius of metallic vias was determined based on two criteria: firstly, to ensure that the vias do not come into contact with the antenna radiating elements, and secondly, to adhere to via fabrication limitations. The placement of the vias was established through an optimization process, with the proposed spacing yielding the most favorable results among all options considered. The s-parameter results of MIMO$_2$ design is shown in Fig. 5.13.

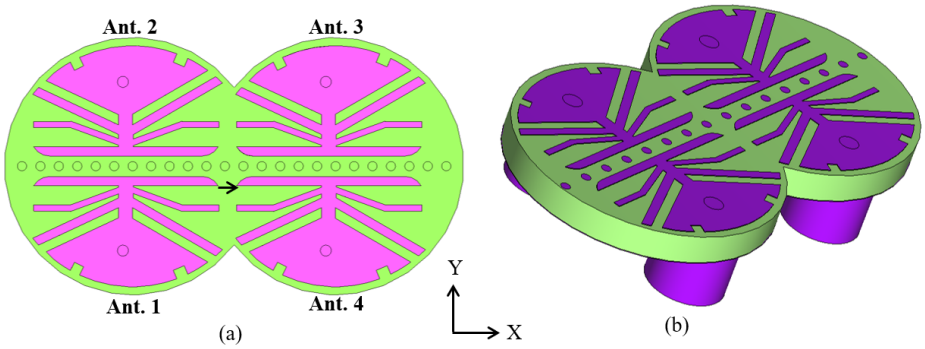

Figure 5.12: MIMO$_2$ antenna (a) top face and (b) perspective view.

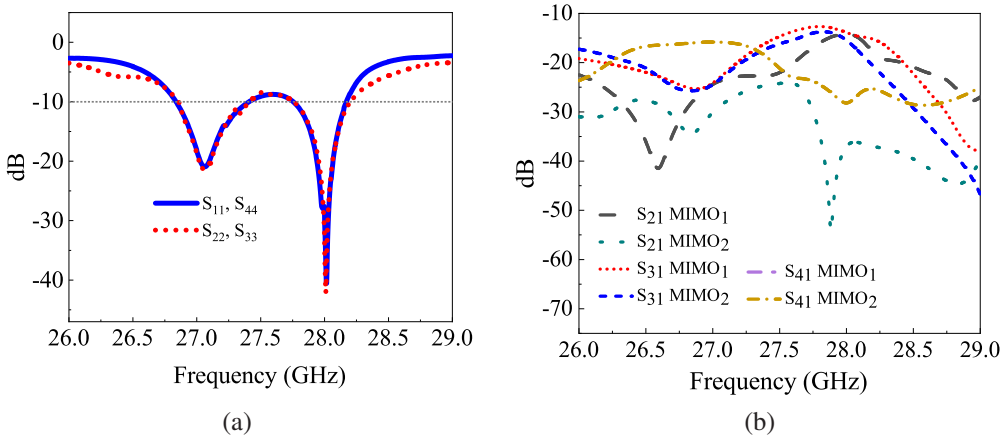

Figure 5.13: MIMO$_2$ results (a) reflection and (b) transmission coefficients.

From the results in Fig. 5.13(a), is evident that the MIMO$_2$ antenna maintains a nearly identical operational bandwidth of 26.85–27.50 GHz and 27.75–28.18 GHz across all elements, confirming that the introduction of vias does not compromise impedance matching. The improvement in mutual coupling is also noticed from the

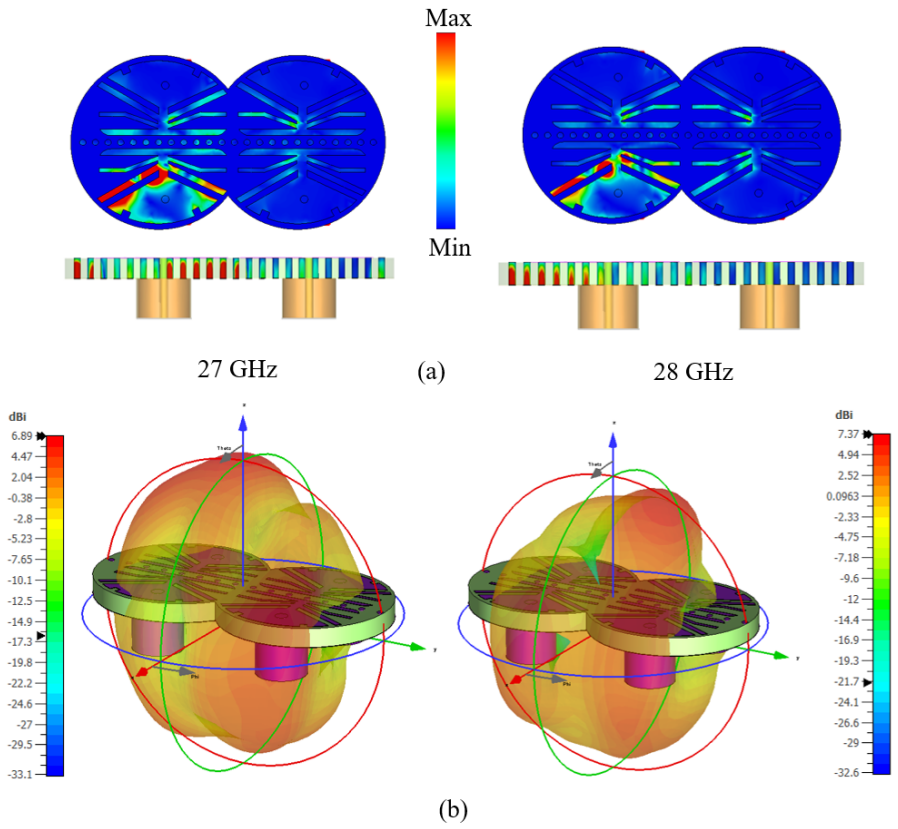

Figure 5.14: $MIMO_2$ results when antenna 1 is active (a) current and (b) far-field radiation patterns.

transmission coefficient results in Fig. 5.13(b), which shows a reduction in inter-element coupling. Specifically, the coupling between antenna 1 and antenna 2 improved by approximately -11 dB at 27 GHz (from -22 dB to -33 dB) and -22 dB at 28 GHz (from -14 dB to -36 dB). Additionally, the coupling between antenna 1 and antenna 3 at 28 GHz was reduced by -19 dB, with no significant changes at 27 GHz. The coupling between antenna 1 and antenna 4 also improved by -5 dB at 27 GHz and -10 dB at 28 GHz, validating the effectiveness of metallic vias in mitigating EM interactions. The decrease in mutual coupling can be explained by the interaction of EM waves and of vias in the designed compact MIMO antenna:

- *Suppression of Surface Wave Propagation:* The vias introduce localized high-impedance paths, which effectively disrupt surface waves that would otherwise propagate between adjacent antenna elements. This suppresses unwanted current interactions, hence, reduce coupling effects.

- *Common Ground Path for Current Flow:* The metallic vias alter the surface current distribution by providing a low-impedance return path (to ground plane), thereby reducing direct coupling between antenna elements. This effect is clearly observed in the surface current distribution results in Fig. 5.14(a), where current

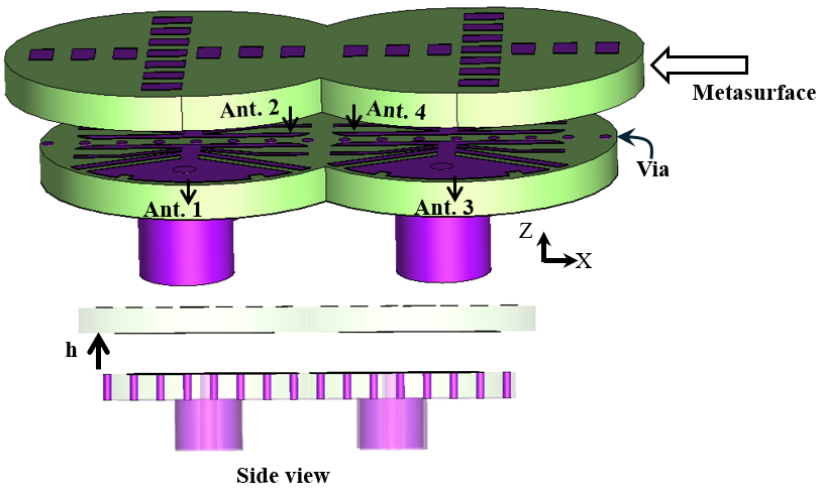

Figure 5.15: $MIMO_3$ (final)antenna design.

concentrations around adjacent antennas are significantly reduced compared to $MIMO_1$.

- *EM Field Disruption:* The vias act as artificial obstacles, disrupting coupling by altering the electric field distribution around the antenna elements. This effect is particularly evident at 28 GHz, where coupling was initially higher in $MIMO_1$ but has been significantly reduced in $MIMO_2$.

- *Reduction of Inductive and Capacitive Coupling Components:* The presence of vias modifies the effective inductive and capacitive coupling between elements by introducing additional parasitic reactance. This contributes to improved isolation between antenna elements.

The effectiveness of metallic vias in reducing mutual coupling is further analyzed through the surface current distribution shown in Fig. 5.14(a) at both 27 GHz and 28 GHz, with antenna 1 active while the other elements are matched to 50Ω. The side view of the metallic vias clearly illustrates the presence of current flow, which effectively reduces the current distribution on adjacent antenna elements. Figure 5.14(b) shows the H-plane far-field radiation patterns for antenna 1. The gain has exhibited a slight increase, with values of 6.89 dBi and 7.37 dBi at 27 GHz and 28 GHz, respectively. Although this reduction in coupling by decreasing S_{Sur}^{ij} has achieved high isolation, the subsequent design enhances coupling further through MTS integration.

5.3.4 Dual band Four-element $MIMO_3$ design

The $MIMO_3$ antenna design, as shown in Fig. 5.15, incorporates metallic vias and a MTS to significantly enhance isolation and minimize mutual coupling. The MTS, positioned above the antenna elements suppressing unwanted near-field EM interactions.

5.3.4.1 Design of MTS

The design, boundary setup, and circuit model of the MTS unit cell, which is integrated into the $MIMO_3$ antenna, is presented in Fig. 5.16(a). It comprises rectangular patches arranged in a plus shape on the top face and rotated 45 degrees on the bottom face. The front and back views illustrate the distribution of these patches, which are designed to function as a band stop and band pass filter. For the full-wave EM simulation of the unit cell under periodic boundary conditions, it's important to note that Floquet boundary conditions are utilized, as illustrated in Fig. 5.16(b). The propagation direction of the EM waves is defined by the Z_{min} and Z_{max} planes. The unit cell can also be analyzed as an analytical equivalent LC circuit, where L represents the inductances of the patches, and C represents the separation between patches. As the unit cell is designed to operate on two dual-band frequencies, two series-parallel LC circuits are utilized. This lumped-element circuit model was optimally designed in ADS schematic environment and helps in understanding the resonance behavior and filtering characteristics of the MTS. The circuit model elements values are as follows: with the optimized LC circuit values of C1 = 0.5, C2 = 0.45, C3 = 1.24, C4 = 1, C5 = 1.59 (pF), L1 = 0.07, L2 = 8.86, L3 = 189.58, L4 = 2.37 (nH), and T1=T2 (377 Ω free space impedance).

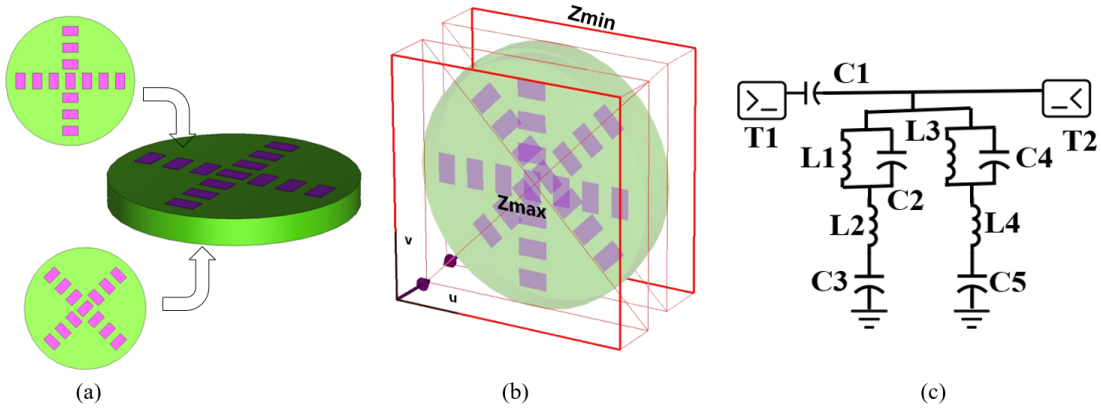

Figure 5.16: MTS (a) side view, (b) floquet boundary, and (c) circuit model.

Fig. 5.17 presents a comparison of the results derived from EM and circuit simulations models. The primary objective of the MTS in this design is to facilitate signal transmission at 27 GHz and 28 GHz while effectively attenuating frequencies within the 27.40–27.80 GHz range. In addition to its filtering functionality, the unit cell is expected to exhibit negative permeability values in the pass band, ensuring its capacity to manipulate EM wave propagation. A detailed examination of the results confirms that the designed MTS successfully meets these requirements. In the stop-band region, a significant variation in permeability (μ) is observed, indicating the presence of a magnetic resonance phenomenon. Simultaneously, a notable change in permittivity (ε) confirms the dielectric characteristics of the MTS. These variations in material properties contribute to the selective filtering behavior which allow only the desired

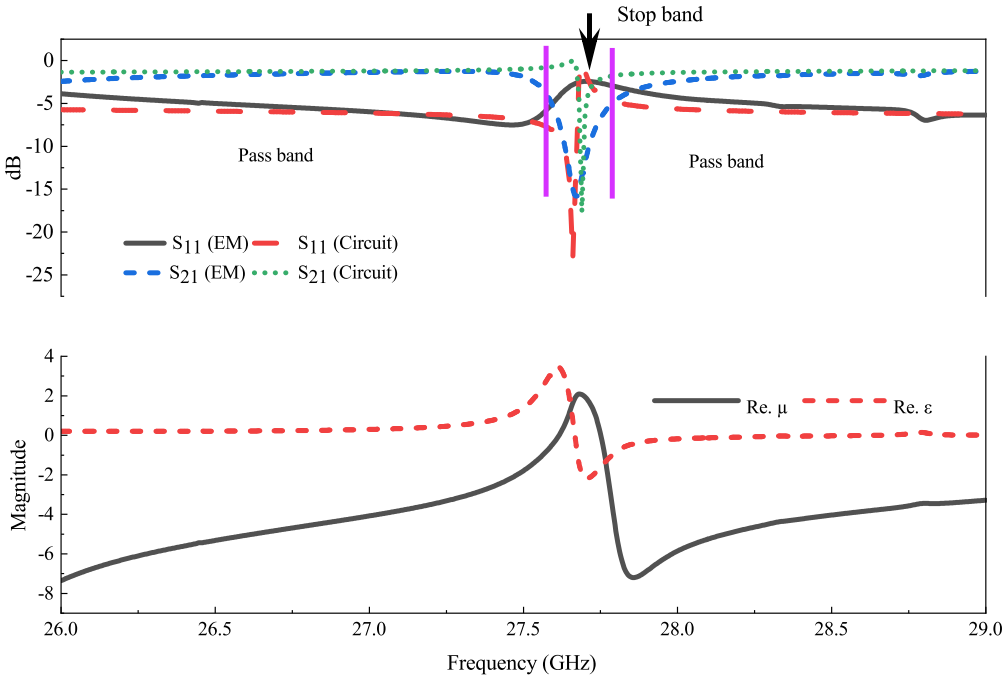

Figure 5.17: MTS s-parameters, permittivity and permeability.

frequency band to pass through while blocking the others. The close agreement between the EM simulation results and the circuit model confirms that the proposed unit cell design is effective in reducing mutual coupling. The unit cell was converted into MTS and placed above the MIMO antenna the details of which are given in following section.

5.3.4.2 Result of $MIMO_3$

In this stage, the designed MTS was optimally positioned 3.50 mm above the antenna. It is important to note that this was the optimal location in terms of isolation, although variations can be observed when the placement height is altered. Thus, the presence of metallic vias in the antenna substrate, combined with the MTS on top, renders the proposed design a hybrid approach. The results in terms of S-parameters are presented in Fig. 5.18.

It can be observed that the inclusion of the MTS has led to minor variations in impedance matching across the operational bands. The bandwidth of antennas 1 and 4 were 26.75 GHz-27.28 GHz and 27.77-28.19 GHz, whereas 26.69-27.28 GHz and 27.68-28.23 GHz was recorded for antennas 2 and 4. These values indicate that the introduction of the MTS does not significantly degrade impedance performance but slightly shifts the resonance frequencies due to EM interactions with the periodic structure. The transmission coefficient results in Fig. 5.18(b) further confirm the effectiveness of the MTS in mitigating mutual coupling. The inclusion of the MTS has resulted in a noticeable reduction in coupling across all antenna pairs, with values

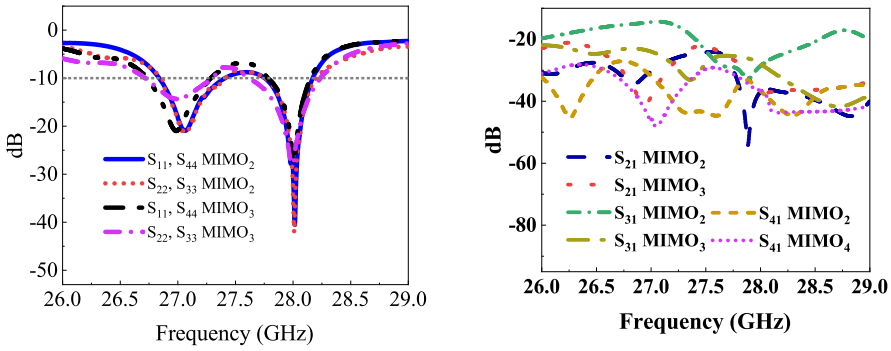

(a) (b)

Figure 5.18: $MIMO_3$ results (a) reflection and (b) transmission coefficients.

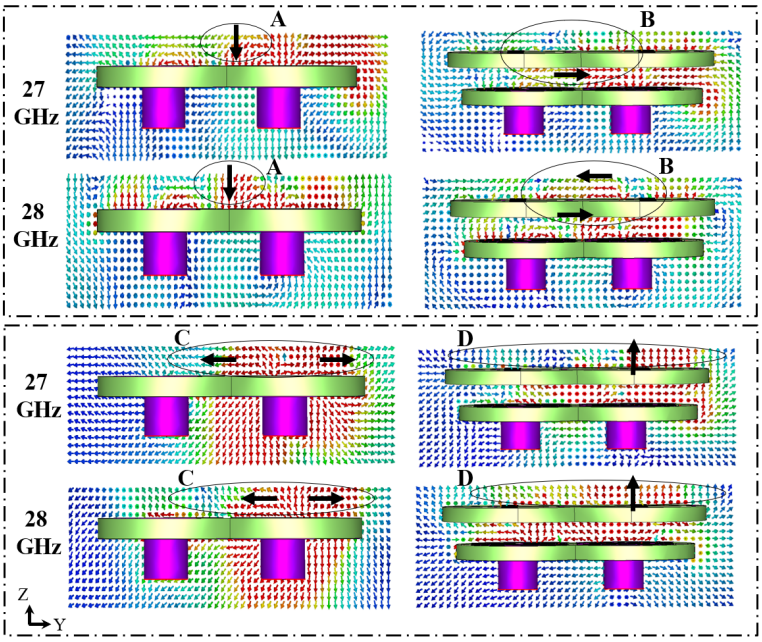

Figure 5.19: Distributions of H-field (first two rows) and Poynting vectors (last two rows) without and with MTS when antenna 1 is active.

consistently below -30 dB throughout the operational bandwidth. Notably, S_{31} exhibits a substantial decrease in coupling levels, reinforcing the impact of the MTS in suppressing unwanted inter-element interactions. These findings validate the design approach, demonstrating that the integration of a MTS in the $MIMO_3$ configuration effectively enhances isolation without significantly compromising impedance bandwidth.

To assess the impact of the MTS on EM wave propagation and the reduction of mutual coupling, a comprehensive examination of the magnetic field (H-field) and Poynting vector [148] distributions was conducted along the YZ-plane. The results, illustrated in Fig. 5.19, provide a comparative assessment of the MIMO antenna behavior with and without the incorporation of the MTS at 27 GHz and 28 GHz. In the absence of the MTS, the H-field in region A exhibits an irregular and unconfined rotational pattern at both 27 GHz and 28 GHz. This unregulated field behavior results in strong mutual coupling between antenna elements, as stray magnetic fields interact with adjacent

antennas, leading to performance degradation. However, upon the integration of the MTS, a distinct improvement is observed in region B, where the H-field vectors become more structured and aligned. The rotational effects are significantly diminished, and the field components are directed more effectively along the Y-axis. This regulated field behavior indicates that the MTS acts as a guiding structure, suppressing undesired field interactions and contributing to improved isolation between antenna elements. The last two rows of Fig. 5.19 illustrate the corresponding Poynting vector distributions, further validating the influence of the MTS on EM energy flow. Without the MTS, the Poynting vectors in region C predominantly propagate laterally along the Y-direction, causing unwanted power leakage and reinforcing mutual coupling. This lateral energy dispersion can be detrimental to MIMO antenna performance, as it results in reduced radiation efficiency and increased interference among elements. Conversely, when the MTS is introduced, the Poynting vectors in region D exhibit a reoriented distribution, where energy propagation is redirected towards the Z-direction. This alignment ensures that the radiated power follows the desired path, effectively minimizing lateral coupling and enhancing isolation between the antenna elements. By regulating the H-field distribution and controlling the directionality of the Poynting vectors, the MTS mitigates mutual coupling effects while ensuring efficient energy transmission.

5.4 Measured results of dual-band MIMO$_3$ antenna

The dual-band MIMO$_3$ antenna was fabricated and experimentally evaluated using a VNA. The measurement setup, top and bottom faces are shown in Fig. 5.20(a). During the measurement process, all non-active antenna elements were terminated with 50Ω loads to ensure proper impedance matching and minimize unwanted reflections. Furthermore, a polystyrene foam layer with a thickness of 3.50 mm was placed between the antenna and the MTS to maintain physical support. It is noteworthy that the foam layer permittivity is almost 1 thus it also mimic the free space spacing in simulation. Figs. 5.20(b-c) compares the simulated and measured results of the reflection coefficient and transmission coefficients.. The simulated 10 dB impedance bandwidth for antennas 1 and 4 spans from 26.75 GHz to 27.28 GHz and 27.77 GHz to 28.19 GHz, respectively. The measured results demonstrate a similar impedance bandwidth, ranging from 26.73 GHz to 27.33 GHz and 26.77 GHz to 28.16 GHz. Furthermore, antennas 2 and 3 exhibit nearly identical simulated and measured bandwidths, though minor shifts in resonance frequencies and slight reductions in reflection levels are observed. The effectiveness of the proposed antenna is further confirmed by the transmission coefficient findings. Throughout the operational frequency range, both simulated and measured coupling levels consistently remain under -30 dB, indicating exceptional isolation between antenna components. There is a strong correlation between the

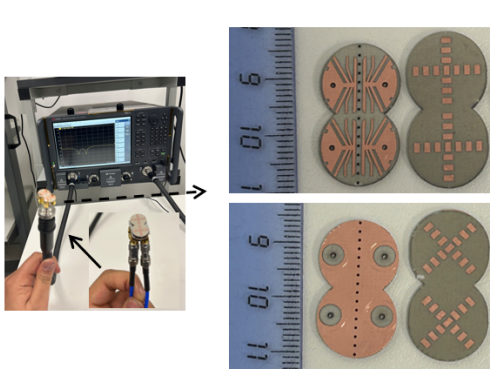

(a)

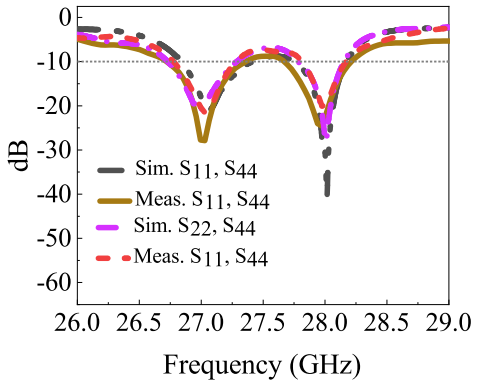

(b)

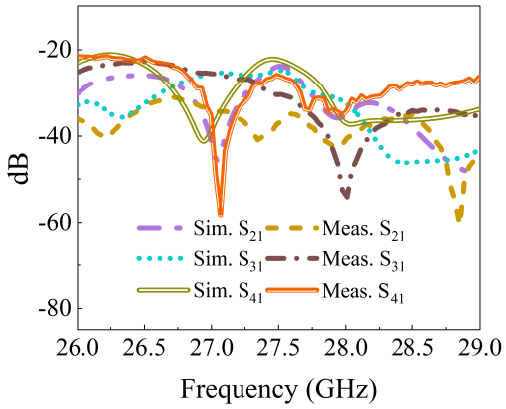

(c)

Figure 5.20: $MIMO_3$ measured results (a) reflection and (b) transmission coefficients.

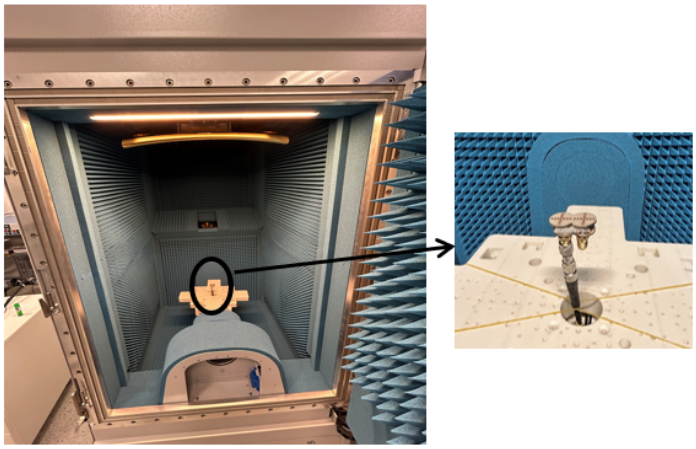

Figure 5.21: Gain measurement of fabricated $MIMO_3$ antenna in anechoic chamber.

simulations and measurements, despite some minor variations. These slight differences can be explained by manufacturing tolerances, measurement inaccuracies, and potential misalignment when positioning the foam layer. Nonetheless, the overall performance aligns closely with the simulation.

The gain and radiation pattern measurements were performed in the anechoic

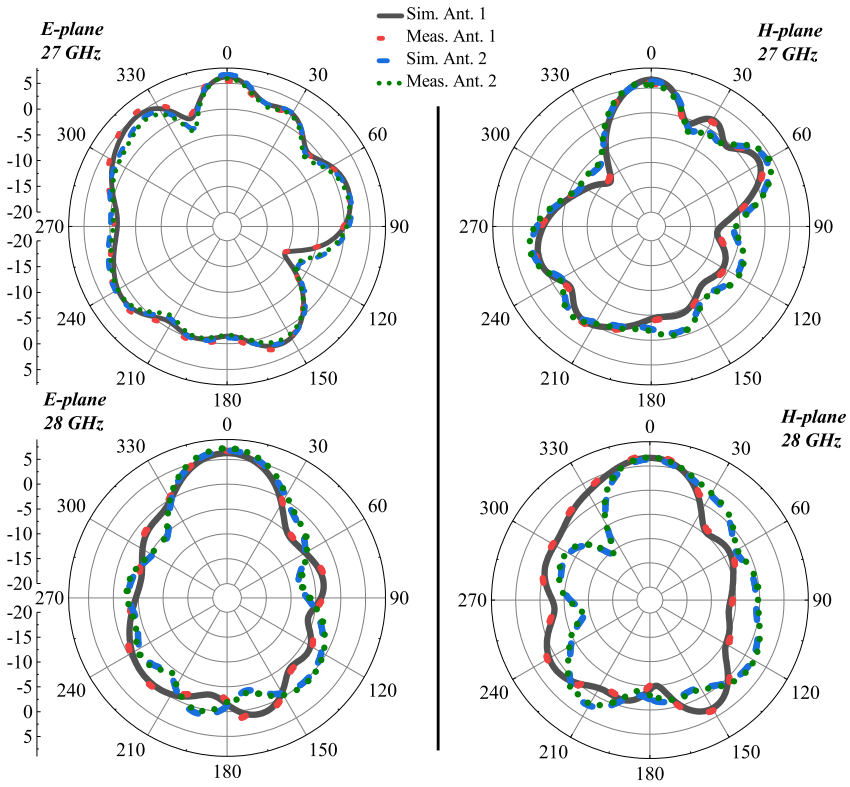

Figure 5.22: Radiation patterns results of MIMO$_3$ at 27 Ghz and 28 GHz.

chamber using gain transfer method. The fabricated antenna placement and measurement setup is shown in Fig. 5.21. A detailed comparison between the simulated and measured far-field radiation patterns at 27 GHz and 28 GHz are provided in Fig. 5.22. The radiation patterns were analysed in both the E-plane and H-plane to evaluate the consistency between simulations and practical measurements. At 27 GHz, both the the E-plane and H-plane, with only minor variations observed in the measured data. These slight shifts can be attributed to fabrication imperfections and experimental uncertainties. The measured gain at 27 GHz was almost 6.52 dBi. At 28 GHz, the radiation patterns exhibit broader main lobes and slightly suppressed side lobes compared to 27 GHz. The maximum measured gain at this frequency is 6.74 dBi, which closely aligns with the simulated results. The similarity between the radiation characteristics at both frequencies confirms that the MTS integration effectively regulates the antenna's far-field behaviour while maintaining high reflectivity across the dual-band spectrum. Additionally both antenna elements of MIMO$_3$ exhibit strong correlation, which indicates minimal mutual coupling effects., as evident in the results. This strong correlation signifies minimal mutual coupling effects, ensuring independent radiation from each element. The well-aligned simulated and measured radiation characteristics, along with the minimal distortions in both E-plane and H-plane, validate the efficacy of the MTS in optimizing radiation performance and suppressing unwanted coupling.

5.5 Diversity analysis of the dual-band MIMO antenna

5.5.1 TARC analysis

In MIMO antenna analysis, TARC demonstrates the overall reflection performance of all ports when simultaneously excited with varying phase angles. Lower TARC values, measured in dB, shows enhanced impedance matching and reduced signal reflections in response to phase angles. Fig. 5.23 shows the TARC outcomes for the final $MIMO_3$ antenna across phase angles of 30°, 60°, 90°, and 120°. The TARC exhibits a minor increase as the phase rises, suggesting greater reflection losses. Nevertheless, the TARC is less than standard -10 dB across all scenarios in both bands.

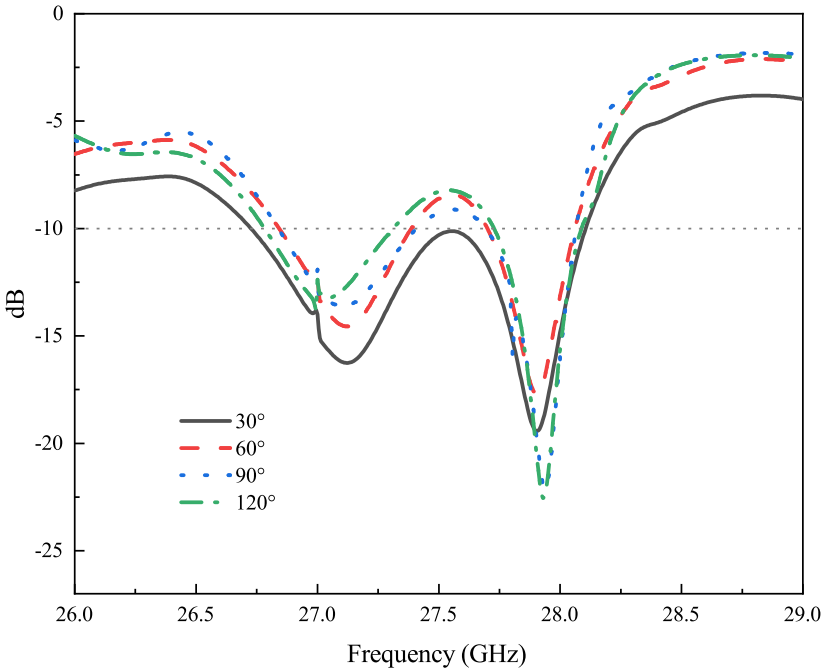

Figure 5.23: TARC results of the $MIMO_3$ antenna.

5.5.2 ECC and DG analysis

Figure 5.24 presents the ECC and DG results for the $MIMO_3$ antenna configuration. The results in Figure 5.24(a) demonstrate that the ECC remains well below the threshold of 0.5 wherein all antenna elements the ECC values are less than 0.03. The low ECC values at both operational bands confirm that the $MIMO_3$ antenna ensures independent radiation patterns and high spatial diversity, which are essential for achieving robust MIMO performance in mmWave communications.

Similarly in Figure 5.24(b), the DG values for antenna pairs 1-2, 1-3, and 1-4 consistently remain above 9.97 dB in both frequency bands. Thee results confirms that the antenna system effectively maintains high diversity gain. A minor variation is observed around 27 GHz, where DG for the antenna pair 1-3 experiences a slight

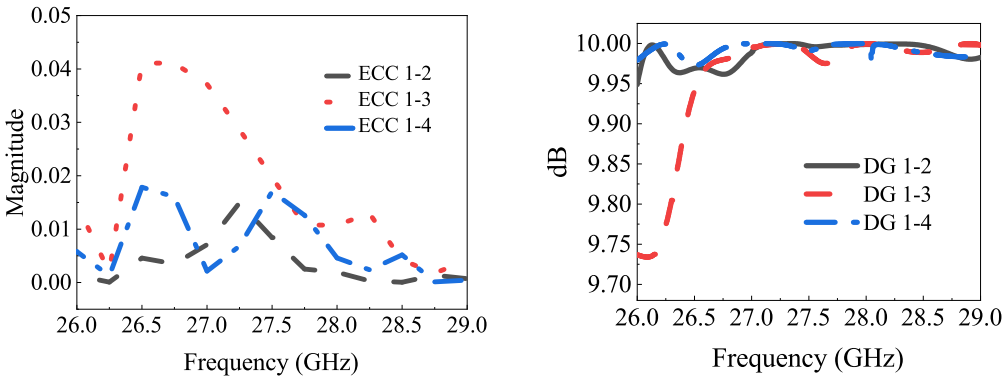

Figure 5.24: $MIMO_3$ (a) ECC and (b) DG results.

Table 5.1: Comparison of the dual-band MIMO with reported works.

Ref.	Size (λ)	Center freq.	Isolation (dB)	Technique	Gain (dBi)
[149]	1.81×1.81	28	>-24	Strip	3.5
[150]	4.08×4.08	28	>-23	FSS/DGS	8.6
[151]	1.96×0.55	26	>-30	Bar-L	5.8
[152]	2.15×0.61	28	>-20	MTS	12
[153]	0.69×2.56	25	>-20	CSRR	NA
Prop.	1.96×1.25	27/28	>-30	Vias+MTS	6.52/6.74

decrease to approximately 9.75 dB. However, this frequency does not include in the desired dual band/. The combination of low ECC and high DG values validates the efficiency of the $MIMO_3$ antenna in minimizing mutual correlation while maximizing diversity gain. These characteristics make the dual-band design highly suitable for mmWave MIMO applications, where maintaining low inter-element correlation and high diversity gain is essential for improving channel capacity and link reliability.

The designed MIMO antenna is compared with previously reported designs to highlight its advantages in terms of size, operating frequency, isolation, and gain performance in Table 5.1. Compared to other antennas, the proposed design offers a more compact footprint while maintaining operation at dual 27/28 GHz bands, which is beneficial for mmWave applications requiring multi-band functionality. One of the key strengths of this design is its high isolation, exceeding 30 dB, which is superior to several reported designs that typically achieve isolation between 20–24 dB. While some existing designs, such as the one in [152], achieve higher gain values (12 dBi), they often come with the trade-off of larger physical dimensions, which may not be suitable for space-constrained applications like wearable technology, IoT, and compact energy harvesting systems. The proposed antenna balances size reduction and performance optimization, achieving a gain of 6.52/6.74 dBi, which is competitive given its smaller form factor. Additionally, unlike some reported designs that operate in a single frequency band, the proposed work provides dual-band functionality, increasing its versatility in applications

such as 5G, wireless power transfer, and sensor networks. By offering a combination of high isolation, moderate gain, and compact size, the proposed antenna is well-suited for high-density wireless communication environments where minimizing interference and maximizing spectral efficiency are crucial.

5.5.3 Conclusion

This chapter presented the design and development of a dual-band MIMO antenna for mmWave applications. To address the mutual coupling issues of surface waves and near-field interactions, a novel hybrid approach incorporating metallic vias and MTS was proposed to enhance isolation while maintaining a compact size. To achieve dual-band resonance, a K-shaped patch with metallic strips was introduced. The impedance bandwidths of the antenna range from 26.84–27.37 GHz and 27.81–28.16 GHz. The design was extended to a 2 × 2 MIMO configuration, where coupling levels were analysed. A significant level of mutual coupling was observed, particularly at 28 GHz. The decoupling method involved integrating metallic vias to suppress surface waves and utilizing MTS to modify wave propagation, which significantly reduced mutual coupling. Measurement results from the fabricated prototype confirmed the effectiveness of the design, with bandwidths closely matching simulations and coupling levels below -30 dB, indicating excellent isolation. Radiation patterns and diversity performance, evaluated through ECC analysis, demonstrated strong agreement with simulations. The findings highlight the potential of the proposed approach for next-generation wireless communication systems.

Chapter 6

Conclusion and Future Work Directions

6.1 Conclusion

In recent technological advancements, the achievement of rapid data transmission and stable wireless connectivity has emerged as a critical objective. To address these increasing demands, mmWave MIMO antenna systems have been implemented. The mmWave band offers extensive bandwidth availability, whereas MIMO antenna systems enhance channel performance. Consequently, the significant path losses in mmWave can be mitigated through MIMO antennas, wherein multiple antennas are utilized. The employment of multiple antennas facilitates multiple data streams. To ensure channel independence and reduce interference, it is necessary to maintain adequate spacing between antenna elements. Although increasing the distance between radiating components improves isolation, this method is not practical due to the size limitations of contemporary communication devices, which require more compact designs. Thus, the close placement of antenna elements in the mmWave band produces mutual coupling, which becomes more critical when antenna elements are placed less than half-wavelength spacing. The mutual coupling impacts the MIMO antenna system performance, as it produces more correlation and disturbs the radiation patterns, impedance matching, and decreases the efficiency and gain. Therefore, it is imperative to minimize the coupling levels while considerably reducing the antenna dimensions to meet the compactness demands of modern devices. Consequently, it is essential to incorporate decoupling techniques that decrease the mutual coupling and enhance the inter element isolation without impacting the antenna performance in a MIMO communication system. To overcome mutual coupling challenges, various decoupling techniques have been utilized. These techniques include the FSS, DGS, and MTS designs for single, wideband, and dual-band MIMO antenna configurations. In particular, hybrid approaches were considered for mutual coupling reductions. It is important to note that the FSS and DGS primarily reduce the coupling which occurs due to the surface current present between antenna elements. Alternatively, the MTS reduces the interactions of near-field interactions.

A detail analysis were performed for effective on-body communication, a Vivaldi

antenna was designed. This antenna comprised four-element Vivaldi patterns operating at 28 GHz and 30 GHz with a 36.44% fractional bandwidth. The design integrates a Vivaldi antenna with a FSS to reduce mutual coupling. This combination achieved inter-element isolation below -20 dB within a compact 16×20 mm² size, which represents a significant advancement compared to other reported works. The performance was assessed through simulations on Gustav's model (chest, hand, and leg) and practical tests on the human body, evaluating parameters such as impedance bandwidth, gain, efficiency, and radiation patterns. The MIMO antenna demonstrated a low ECC < 0.24, high DG of more than 9.95 dB, and a TARC below -10 dB. Additionally, SAR analysis confirmed safe operation with values of 0.397 W/kg at 28 GHz and 0.267 W/kg at 30 GHz. The results highlighted the antenna's suitability for wearable WBAN applications and its ability to maintain an endfire radiation pattern even when placed on the human body.

A hybrid approach combining DGS and FSS to minimize mutual coupling is thoroughly investigated. Initially, a dual-band antenna with a modified elliptical patch and rotating arms was created using CMA. Building on this design, a six-element dual-band MIMO antenna covering the ISM and 5G NR bands (23.63–32.90 GHz and 36.68–40 GHz) was developed. The isolation technique achieved a coupling reduction of -33 dB between the MIMO elements. The antenna demonstrated broadside radiation patterns with peak realized gains of 9.12 dBi, 9.19 dBi, 8.80 dBi, and 8.77 dBi at 26 GHz, 28 GHz, 30 GHz, and 38 GHz, respectively. MIMO performance metrics included TARC below -10 dB, an ECC under 0.04, and a DG exceeding 9.91 dB. Safety evaluation through SAR analysis confirmed compliance with limits for both 1g and 10g tissue models. Additionally, the designed MIMO antenna's performance was validated in a WBAN communication scenario, demonstrating high gain, strong isolation, dual-band capability, reliable diversity and excellent power reception as well as LM characteristics.

A novel hybrid technique for mutual coupling reduction in a compact dual-band mmWave MIMO antenna, incorporating metallic vias and a metasurface, has been investigated. The research addresses challenges in MIMO antenna design, such as surface wave coupling and near-field interference resulting from compact element spacing. Initially, a dual-band antenna was designed utilizing a Rogers RO4003C substrate with modified K-shaped patch arms, achieving resonances at 27 GHz and 28 GHz. An equivalent RLC circuit model was developed to analyse the dual-band response, with results from the circuit closely corresponding to full-wave simulations. The MIMO antenna design process encompassed multiple configurations. The baseline 2×2 MIMO array (MIMO1) exhibited high mutual coupling (-13 dB). To mitigate this, metallic vias were introduced, reducing surface wave coupling and improving isolation to -22 dB. Further enhancement was achieved by integrating a metasurface

above the MIMO2 array, which suppressed near-field interactions and reduced coupling to below -30 dB across both operating bands. Fabricated prototypes were evaluated in an anechoic chamber, with measured results aligning closely with simulations. The final design demonstrated significant improvements, including isolation below -30 dB, ECC less than 0.04, TARC below -10 dB, and diversity gain exceeding 9.91 dB. It is noteworthy that this technique of combining metallic vias and metasurface in compact spacing has not been previously reported, and to the best of authors' knowledge, it represents the first implementation of such a technique.

In conclusion, compact and highly isolated MIMO antenna systems at the mmWave band are achievable through the implementation of these techniques without increasing the dimensions of antenna designs. Furthermore, the findings contribute significantly to the advancement of MIMO designs suitable for mmWave band WBAN, IoT, and 5G communication systems.

6.2 Future work directions

The advancement of mutual coupling reduction techniques in MIMO antennas offers various research opportunities for improving isolation performance. Below is a detailed explanation of four such potential future directions:

1. **Reconfigurable FSS designs:**
   The increasing demands in communication systems necessitate antennas that operate at multiple frequency bands. However, designing FSS for mutual coupling reduction that operate at multiple frequencies presents significant challenges. This highlights limitations that can be addressed through reconfigurable FSS designs. These surfaces function by selectively reflecting or transmitting certain frequencies, which aids in blocking unwanted signals between closely spaced antennas. By incorporating tunable components, such as varactor, the FSS can modify its behaviour in real time. Varactors are electronic components that adjust their capacitance based on the applied voltage. This will make the FSS to shift its operating frequency as required and are particularly advantageous for multi-band systems, such as 5G MIMO antennas, where multiple frequencies are utilized simultaneously. Furthermore, reconfigurable FSS can respond to changes in the surface current.

2. **AI-Driven optimization:**
   Machine learning (ML) and artificial intelligence (AI) can optimize antenna configurations by analyzing critical design parameters and predicting the most efficient layouts. In MIMO antennas, where mutual coupling between closely placed elements degrades performance, ML models can learn from simulations

and experiments to identify configurations that enhance isolation. This approach will significantly accelerates the design process time and results.

3. **New materials:**
   More metamaterials, such as high-impedance surfaces (HIS), can be embedded into substrates to minimize surface wave propagation, which is a major cause of mutual coupling. Additionally, substrate flexibility in wearable antennas can be explored to understand its impact on reducing coupling in WBAN applications.

4. **Hybrid isolation approaches:**
   Combining multiple isolation techniques, including metallic vias, DGS, and neutralization lines, offers a more comprehensive solution for mutual coupling mitigation. Hybrid methods utilize the unique strengths of each approach which will result in enhanced isolation and less mutual coupling.

Bibliography

[1] L. Kong, M. K. Khan, F. Wu, G. Chen, and P. Zeng, "Millimeter-wave wireless communications for iot-cloud supported autonomous vehicles: Overview, design, and challenges," *IEEE Communications Magazine*, vol. 55, no. 1, pp. 62–68, 2017.

[2] O. Semiari, W. Saad, M. Bennis, and M. Debbah, "Integrated millimeter wave and sub-6 ghz wireless networks: A roadmap for joint mobile broadband and ultra-reliable low-latency communications," *IEEE Wireless Communications*, vol. 26, no. 2, pp. 109–115, 2019.

[3] V. Begishev, E. Sopin, D. Moltchanov, R. Pirmagomedov, A. Samuylov, S. Andreev, Y. Koucheryavy, and K. Samouylov, "Performance analysis of multi-band microwave and millimeter-wave operation in 5g nr systems," *IEEE Transactions on Wireless Communications*, vol. 20, no. 6, pp. 3475–3490, 2021.

[4] B. T. Jijo, S. R. Zeebaree, R. R. Zebari, M. A. Sadeeq, A. B. Sallow, S. Mohsin, and Z. S. Ageed, "A comprehensive survey of 5g mm-wave technology design challenges," *Asian Journal of Research in Computer Science*, vol. 8, no. 1, pp. 1–20, 2021.

[5] S. Juneja, R. Pratap, and R. Sharma, "Design considerations for implementation of planar antennas for millimeter wave (mmw) 5g network: a review," *Circuit World*, vol. 50, no. 2/3, pp. 247–256, 2024.

[6] M. Drissi, N. Benjelloun, P. Descamps, and A. Gharsallah, "Analysis & implementation of siso, simo, miso and mimo in 5g communication systems based on sdr," *International Journal of Computer Science & Network Security*, vol. 23, no. 2, pp. 140–146, 2023.

[7] Y. Yang, C.-X. Wang, J. Huang, and J. Thompson, "Characteristics and channel capacity studies of a novel 6g non-stationary massive mimo channel model considering mutual coupling," *IEEE Journal on Selected Areas in Communications*, 2024.

[8] A. Patel, A. Vala, A. Desai, I. Elfergani, H. Mewada, K. Mahant, C. Zebiri, D. Chauhan, and J. Rodriguez, "Inverted-l shaped wideband mimo antenna for millimeter-wave 5g applications," *Electronics*, vol. 11, no. 9, p. 1387, 2022.

[9] S. A. Ali, M. Wajid, A. Kumar, and M. S. Alam, "Design challenges and possible solutions for 5g siw mimo and phased array antennas: A review," *IEEE Access*, vol. 10, pp. 88567–88594, 2022.

[10] A. D. Tadesse, O. P. Acharya, and S. Sahu, "Wideband mimo antenna mutual coupling reduction with electromagnetic band-gap structure," *IETE Journal of Research*, vol. 69, no. 9, pp. 6014–6021, 2023.

[11] T. Pei, L. Zhu, J. Wang, and W. Wu, "A low-profile decoupling structure for mutual coupling suppression in mimo patch antenna," *IEEE Transactions on Antennas and Propagation*, vol. 69, no. 10, pp. 6145–6153, 2021.

[12] A. D. Tadesse, O. P. Acharya, and S. Sahu, "Wideband mimo antenna mutual coupling reduction with electromagnetic band-gap structure," *IETE Journal of Research*, vol. 69, no. 9, pp. 6014–6021, 2023.

[13] M. N. Mohanty, S. Satrusallya, and T. Al Smadi, "Antenna selection criteria and parameters for iot application," in *Printed Antennas*, pp. 283–295, CRC Press, 2022.

[14] N. Kishore and A. Senapati, "5g smart antenna for iot application: A review," *International Journal of Communication Systems*, vol. 35, no. 13, p. e5241, 2022.

[15] A. G. Alharbi, H. A. Rahman, M. M. Khan, M. I. Abbasi, A. A. Albraikan, and F. A. Almalki, "Design and study of a miniaturized millimeter wave array antenna for wireless body area network," *International Journal of Antennas and Propagation*, vol. 2022, no. 1, p. 1736377, 2022.

[16] M. Bilal, S. Shahid, Y. Khan, Z. Rauf, R. A. Wagan, M. A. Butt, S. N. Khonina, and N. L. Kazanskiy, "A miniaturized fss-based eight-element mimo antenna array for off/on-body wban telemetry applications," *Electronics*, vol. 11, no. 4, p. 522, 2022.

[17] H. Yon, N. H. A. Rahman, M. A. Aris, M. H. Jamaluddin, I. Kong Cheh Lin, H. Jumaat, F. N. Mohd Redzwan, and Y. Yamada, "Development of c-shaped parasitic mimo antennas for mutual coupling reduction," *Electronics*, vol. 10, no. 19, p. 2431, 2021.

[18] M. A. Sufian, N. Hussain, A. Abbas, J. Lee, S. G. Park, and N. Kim, "Mutual coupling reduction of a circularly polarized mimo antenna using parasitic elements and dgs for v2x communications," *IEEE Access*, vol. 10, pp. 56388–56400, 2022.

[19] R. C. Godi, R. R. Patil, and R. S. Kinagi, "Parasitic isolation structure for mutual coupling reduction in a multiple input multiple output antenna," *Bulletin of Electrical Engineering and Informatics*, vol. 13, no. 6, pp. 4430–4438, 2024.

[20] F. Amillia, E. Setijadi, and G. Hendrantoro, "The effect of parasitic patches addition on bandwidth enhancement and mutual coupling in 2× 2 sub-arrays," *IEEE Access*, vol. 10, pp. 72057–72064, 2022.

[21] M. R. Jadhav and U. L. Bombale, "Design of f-shaped parasitic mimo antenna with dgs for vehicle-to-everything communication.," *Progress in Electromagnetics Research B*, vol. 109, 2024.

[22] A. Khabba, J. Amadid, S. Mohapatra, Z. El Ouadi, S. Ahmad, S. Ibnyaich, and A. Zeroual, "Uwb dual-port self-decoupled o-shaped monopole mimo antenna with small-size easily extendable design and high diversity performance for millimeter-wave 5g applications," *Applied Physics A*, vol. 128, no. 8, p. 725, 2022.

[23] Z. Wang, W. Mu, M. Yang, and C. Li, "Design of compact multiband mimo antenna based on ground neutralization line decoupling," *The Applied Computational Electromagnetics Society Journal (ACES)*, pp. 702–715, 2022.

[24] X.-J. Zou, G.-M. Wang, G.-Q. Kang, W. Song, M. Tan, X.-G. Xu, and H. Zhu, "Wideband coupling suppression with neutralization-line-incorporated decoupling network in mimo arrays," *AEU-International Journal of Electronics and Communications*, vol. 167, p. 154688, 2023.

[25] R. H. Elabd and H. H. Abdullah, "A high isolation uwb mimo vivaldi antenna based on csrr-nl for contemporary 5g millimeter-wave applications," *Journal of Infrared, Millimeter, and Terahertz Waves*, vol. 43, no. 11, pp. 920–941, 2022.

[26] N. R. Palepu and J. Kumar, "Neutralized meander line patch antipodal vivaldi defected ground millimeter-wave (mm-wave) antenna array," *AEU-International Journal of Electronics and Communications*, vol. 166, p. 154663, 2023.

[27] M. K. Khan, S. Liu, and M. I. Khan, "A wideband eight-port mimo antenna with reduced mutual coupling for future 5g mm-wave applications," *Sensors*, vol. 25, no. 2, p. 484, 2025.

[28] A. A. Khan, Z. Wang, D. Li, and A. Ahmed, "A compact c-band multiple-input multiple-output circular microstrip patch antenna array with octagonal slotted ground plane and neutralization line for improved port isolation in 5g handheld devices," *Electronics*, vol. 13, no. 11, p. 2196, 2024.

[29] R. H. Elabd and A. J. A. Al-Gburi, "Low mutual coupling miniaturized dual-band quad-port mimo antenna array using decoupling structure for 5g smartphones," *Discover Applied Sciences*, vol. 6, no. 4, p. 189, 2024.

[30] G. Zhao, L. Zhao, M. Xi, Y. Guo, G.-L. Huang, Y. Li, X. Wang, and W. Lin, "A three-port coupled resonator decoupling network for mutual coupling reduction of three-element antenna arrays," *IEEE Transactions on Microwave Theory and Techniques*, 2024.

[31] M. Elahi, A. Altaf, E. Almajali, and J. Yousaf, "Mutual coupling reduction in closely spaced mimo dielectric resonator antenna in h-plane using closed metallic loop," *IEEE Access*, vol. 10, pp. 71576–71583, 2022.

[32] N. P. Lawrence, B. W.-H. Ng, H. J. Hansen, and D. Abbott, "5g terrestrial networks: Mobility and coverage—solution in three dimensions," *IEEE Access*, vol. 5, pp. 8064–8093, 2017.

[33] A. K. Singh, S. K. Mahto, P. Kumar, and R. Sinha, "Analysis of path loss and channel capacity in quad element mimo antenna for terahertz communication systems," *International Journal of Circuit Theory and Applications*, vol. 51, no. 3, pp. 1460–1475, 2023.

[34] S. S. Shekhawat, D. Lodhi, and S. Singhal, "Dual band notched superwideband mimo antenna for 5g and 6g applications," *AEU-International Journal of Electronics and Communications*, vol. 184, p. 155419, 2024.

[35] Y. Meng, A. Ren, C. Wang, G. Xu, L. Zhao, Y. Li, L. Yang, and Z.-X. Huang, "Sub-6 ghz and mm-wave dual-band aperture-shared phone mimo antenna for 5g/6g applications," *IEEE Antennas and Wireless Propagation Letters*, 2024.

[36] R. T. Schwarz, T. Delamotte, K.-U. Storek, and A. Knopp, "Mimo applications for multibeam satellites," *IEEE Transactions on Broadcasting*, vol. 65, no. 4, pp. 664–681, 2019.

[37] J.-K. Che, C.-C. Chen, and J. F. Locke, "A compact four-channel mimo 5g sub-6 ghz/lte/wlan/v2x antenna design for modern vehicles," *IEEE Transactions on Antennas and Propagation*, vol. 69, no. 11, pp. 7290–7297, 2021.

[38] Shailesh, G. Srivastava, S. Kumar, S. Aldosary, W. El-Shafai, B. Goyal, and S. K. Palaniswamy, "A flexible reconfigurable mimo antenna for iot-enabled smart systems," *International Journal of Antennas and Propagation*, vol. 2024, no. 1, p. 7557178, 2024.

[39] S. Kumar, K. Srivastava, S. Kumar, D. Sharma, R. N. Tiwari, A. Kandwal, M. K. Singh, and B. Goyal, "Design and implementation of high isolation textile mimo antenna for wearable applications," *International Journal of Communication Systems*, vol. 38, no. 4, p. e70010, 2025.

[40] L. Zhong, S. He, J. Lin, J. Wu, X. Li, Y. Pang, and Z. Li, "Technological requirements and challenges in wireless body area networks for health monitoring: A comprehensive survey," *Sensors*, vol. 22, no. 9, p. 3539, 2022.

[41] Y. Kim, S. Lee, and S. Lee, "Coexistence of zigbee-based wban and wifi for health telemonitoring systems," *IEEE journal of biomedical and health informatics*, vol. 20, no. 1, pp. 222–230, 2015.

[42] T. Saeidi, S. Saleh, N. Timmons, S. Karamzadeh, A. J. A. Al-Gburi, and F. Razzaz, "Enhancing connectivity/mobility in wban applications through detachable wearable multi-band mimo antenna," *Physica Scripta*, vol. 99, no. 7, p. 075315, 2024.

[43] D. A. Sehrai, M. E. Munir, S. H. Kiani, N. Shoaib, A. D. Algarni, H. Elmannai, M. M. Nasralla, and T. Ali, "A high gain array based millimeter wave mimo antenna with improved isolation and decorrelated fields," *IEEE Access*, vol. 12, pp. 89794–89803, 2024.

[44] X.-C. Wang, Y.-J. Xia, J.-H. Yang, and W.-Z. Lu, "Wideband high-gain circularly polarized substrate integrated cavity antenna array for millimeter-wave applications," *IEEE Transactions on Antennas and Propagation*, vol. 71, no. 1, pp. 1041–1046, 2023.

[45] M. Aboualalaa and I. Mansour, "Dual-band end-fire four-element mimo antenna array using split-ring structure for mm-wave 5g applications," *IEEE Access*, vol. 11, pp. 57383–57390, 2023.

[46] A. A. Althuwayb, N. Rashid, K. Kaaniche, A. B. Atitallah, O. I. Elhamrawy, V. Sorathiya, and S. Lavadiya, "Broadband, high gain 2× 2 spiral shaped resonator based and graphene assisted terahertz mimo antenna for biomedical and wban communication," *Wireless Networks*, vol. 30, no. 1, pp. 495–515, 2024.

[47] A. Aidakhmetov, A. Karimov, K. Dautov, and M. Hashmi, "Design of millimeter wave array-based antenna for wban applications," in *2023 IEEE International Symposium On Antennas And Propagation (ISAP)*, pp. 1–2, IEEE, 2023.

[48] R. N. Tiwari, O. S. Sai, D. Sharma, M. S. Kumar, P. Singh, P. Kumar, C. Sreemanya, and S. Rajasekaran, "A low-profile dual-band millimeter wave

patch antenna for high-speed wearable and biomedical applications," *Results in Engineering*, vol. 24, p. 103212, 2024.

[49] U. Farooq and G. Rather, "A miniaturised ka/v dual band millimeter wave antenna for 5g body centric network applications," *Alexandria Engineering Journal*, vol. 61, no. 10, pp. 8089–8096, 2022.

[50] I. C. on Non-Ionizing Radiation Protection *et al.*, "Guidelines for limiting exposure to electromagnetic fields (100 khz to 300 ghz)," *Health physics*, vol. 118, no. 5, pp. 483–524, 2020.

[51] R. H. Elabd and A. J. A. Al-Gburi, "Ultra-compact 4-port mimo antenna with defected ground structure and sar analysis for 28/38 ghz 5g mobile devices," *Journal of Electromagnetic Waves and Applications*, pp. 1–26, 2024.

[52] K. R. Foster, M. C. Ziskin, Q. Balzano, and A. Hirata, "Transient thermal responses of skin to pulsed millimeter waves," *IEEE Access*, vol. 8, pp. 130239–130251, 2020.

[53] M. Hussain, W. A. Awan, S. M. Abbas, and Y. Zhu, "Design and development of low-profile polymer based broadband antenna for on-body applications," *Results in Engineering*, vol. 25, p. 103818, 2025.

[54] S. Douhi, A. Eddiai, M. Idiri, O. Cherkaoui, and M. Mazroui, "Investigation of sar reduction and gain enhancement using an all-textile antenna with metamaterial structure for wireless body area network applications," *Materials Today: Proceedings*, 2023.

[55] P. K. Sharma, N. Gupta, and P. I. Dankov, "Analysis of dielectric properties of polydimethylsiloxane (pdms) as a flexible substrate for sensors and antenna applications," *IEEE Sensors Journal*, vol. 21, no. 17, pp. 19492–19504, 2021.

[56] B. Almohammed, A. Ismail, and A. Sali, "Electro-textile wearable antennas in wireless body area networks: Materials, antenna design, manufacturing techniques, and human body consideration—a review," *Textile Research Journal*, vol. 91, no. 5-6, pp. 646–663, 2021.

[57] P. Kumar, T. Ali, and M. M. M. Pai, "Electromagnetic metamaterials: A new paradigm of antenna design," *IEEE Access*, vol. 9, pp. 18722–18751, 2021.

[58] S. Abdullah, G. Xiao, and R. E. Amaya, "A review on the history and current literature of metamaterials and its applications to antennas and radio frequency identification (rfid) devices," *IEEE Journal of Radio Frequency Identification*, vol. 5, no. 4, pp. 427–445, 2021.

[59] W. Adepoju, I. Bhattacharya, M. Sanyaolu, M. E. Bima, T. Banik, E. N. Esfahani, and O. Abiodun, "Critical review of recent advancement in metamaterial design for wireless power transfer," *IEEE Access*, vol. 10, pp. 42699–42726, 2022.

[60] M. S. Khan, R. Shakoor, O. Fayyaz, and E. M. Ahmed, "A focused review on techniques for achieving cloaking effects with metamaterials," *Optik*, vol. 297, p. 171575, 2024.

[61] Y. Roh, S.-H. Lee, J. Kwak, H. S. Song, S. Shin, Y. K. Kim, J. W. Wu, B.-K. Ju, B. Kang, and M. Seo, "Terahertz imaging with metamaterials for biological applications," *Sensors and Actuators B: Chemical*, vol. 352, p. 130993, 2022.

[62] N. Alrayes and M. I. Hussein, "Metamaterial-based sensor design using split ring resonator and hilbert fractal for biomedical application," *Sensing and Bio-Sensing Research*, vol. 31, p. 100395, 2021.

[63] X. Huang, C. Zhang, L. Cong, R. Cai, F. Yang, and C. Lu, "Development and prospects of metamaterial in wireless power transfer," *IET Power Electronics*, vol. 14, no. 15, pp. 2423–2440, 2021.

[64] E. Cusworth, S. Ho, V. G. Kravets, B. L. Ong, A. Rusydi, K. S. Novoselov, and A. N. Grigorenko, "Highly oriented single-crystalline gold quantum-dot metamaterials as prospective materials for photonics," *Optics Express*, vol. 32, no. 10, pp. 17922–17931, 2024.

[65] C. Milias, R. B. Andersen, P. I. Lazaridis, Z. D. Zaharis, B. Muhammad, J. T. Kristensen, A. Mihovska, and D. D. Hermansen, "Metamaterial-inspired antennas: A review of the state of the art and future design challenges," *IEEE Access*, vol. 9, pp. 89846–89865, 2021.

[66] A. A. Ibrahim and W. A. Ali, "High gain, wideband and low mutual coupling amc-based millimeter wave mimo antenna for 5g nr networks," *AEU-International Journal of Electronics and Communications*, vol. 142, p. 153990, 2021.

[67] C. Du, L.-R. Pei, J. Zhang, and C.-X. Shi, "A gain enhanced dual-band low sar amc-based mimo antenna for wban and wlan applications," *Progress In Electromagnetics Research M*, vol. 115, pp. 21–34, 2023.

[68] J. Ahmad, M. Hashmi, and G. Nauryzbayev, "Fabry–perot cavity based decagonal shape patch antenna for millimeter-wave band applications," in *2023 International Symposium on Networks, Computers and Communications (ISNCC)*, pp. 1–4, 2023.

[69] J. Ahmad and M. Hashmi, "A compact mimo antenna for wban applications at millimeter-wave frequencies," in *2023 31st Telecommunications Forum (TELFOR)*, pp. 1–4, 2023.

[70] J. Zafar, H. Z. Khan, A. Jabbar, J. u. R. Kazim, M. U. Rehman, A. M. Siddiqui, Q. H. Abbasi, and M. A. Imran, "Asymmetric multi-band reflective metasurface for linear and circular polarizations conversion in ku, k, ka, and u bands," *Scientific Reports*, vol. 15, no. 1, p. 4977, 2025.

[71] I. Hossain, M. T. Islam, N. M. Sahar, A. A. Maash, H. Alsaif, M. S. Soliman, and M. Samsuzzaman, "Flexible substrate based wideband polarization converter with extremely high polarization conversion ratio," *Alexandria Engineering Journal*, vol. 111, pp. 259–269, 2025.

[72] T. Sanislav, G. D. Mois, S. Zeadally, and S. C. Folea, "Energy harvesting techniques for internet of things (iot)," *IEEE access*, vol. 9, pp. 39530–39549, 2021.

[73] J. Ahmad, M. Hashmi, G. Nauryzbayev, and F. Falcone, "A multi-band efficient metamaterial absorber for millimeter-wave band wban applications," in *2024 IEEE International Symposium on Antennas and Propagation and INC/USNC-URSI Radio Science Meeting (AP-S/INC-USNC-URSI)*, pp. 1777–1778, IEEE, 2024.

[74] M. Edries, H. A. Mohamed, and A. A. Ibrahim, "A dual band 28/38 ghz metamaterial absorber for 5g applications," *Journal of Infrared, Millimeter, and Terahertz Waves*, vol. 44, no. 11, pp. 898–911, 2023.

[75] H. Yon, N. H. A. Rahman, M. A. Aris, M. H. Jamaluddin, I. Kong Cheh Lin, H. Jumaat, F. N. Mohd Redzwan, and Y. Yamada, "Development of c-shaped parasitic mimo antennas for mutual coupling reduction," *Electronics*, vol. 10, no. 19, p. 2431, 2021.

[76] M. Alibakhshikenari, F. Babaeian, B. S. Virdee, S. Aïssa, L. Azpilicueta, C. H. See, A. A. Althuwayb, I. Huynen, R. A. Abd-Alhameed, F. Falcone, and E. Limiti, "A comprehensive survey on "various decoupling mechanisms with focus on metamaterial and metasurface principles applicable to sar and mimo antenna systems"," *IEEE Access*, vol. 8, pp. 192965–193004, 2020.

[77] K. Da Xu, J. Zhu, S. Liao, and Q. Xue, "Wideband patch antenna using multiple parasitic patches and its array application with mutual coupling reduction," *IEEE Access*, vol. 6, pp. 42497–42506, 2018.

[78] R. Zaker, "Design of a very closely-spaced antenna array with a high reduction of mutual coupling using novel parasitic l-shaped strips," *International Journal of RF and Microwave Computer-Aided Engineering*, vol. 28, no. 9, p. e21422, 2018.

[79] F. Amillia, E. Setijadi, and G. Hendrantoro, "The effect of parasitic patches addition on bandwidth enhancement and mutual coupling in 2× 2 sub-arrays," *IEEE Access*, vol. 10, pp. 72057–72064, 2022.

[80] N. O. Parchin, Y. I. Al-Yasir, H. J. Basherlou, and R. A. Abd-Alhameed, "A closely spaced dual-band mimo patch antenna with reduced mutual coupling for 4g/5g applications," *Progress In Electromagnetics Research C*, vol. 101, pp. 71–80, 2020.

[81] E. Fritz-Andrade, H. Jardon-Aguilar, and J. A. TIRADO-MENDEZ, "Mutual coupling reduction of two 2x1 triangular-patch antenna array using a single neutralization line for mimo applications.," *Radioengineering*, vol. 27, no. 4, 2018.

[82] X.-J. Zou, G.-M. Wang, G.-Q. Kang, W. Song, M. Tan, X.-G. Xu, and H. Zhu, "Wideband coupling suppression with neutralization-line-incorporated decoupling network in mimo arrays," *AEU-International Journal of Electronics and Communications*, vol. 167, p. 154688, 2023.

[83] C.-Z. Han, L. Xiao, Z. Chen, and T. Yuan, "Co-located self-neutralized handset antenna pairs with complementary radiation patterns for 5g mimo applications," *IEEE Access*, vol. 8, pp. 73151–73163, 2020.

[84] M. K. Khan, S. Liu, and M. I. Khan, "A wideband eight-port mimo antenna with reduced mutual coupling for future 5g mm-wave applications," *Sensors*, vol. 25, no. 2, p. 484, 2025.

[85] M. Li, Y. Zhang, D. Wu, K. L. Yeung, L. Jiang, and R. Murch, "Decoupling and matching network for dual-band mimo antennas," *IEEE Transactions on Antennas and Propagation*, vol. 70, no. 3, pp. 1764–1775, 2021.

[86] R. H. Elabd and A. J. A. Al-Gburi, "Low mutual coupling miniaturized dual-band quad-port mimo antenna array using decoupling structure for 5g smartphones," *Discover Applied Sciences*, vol. 6, no. 4, p. 189, 2024.

[87] T. Pei, L. Zhu, J. Wang, and W. Wu, "A low-profile decoupling structure for mutual coupling suppression in mimo patch antenna," *IEEE Transactions on Antennas and Propagation*, vol. 69, no. 10, pp. 6145–6153, 2021.

[88] J. Li, Y. Zhu, H. Liu, and W. Hong, "Low-profile uwb millimeter-wave antenna array under triple resonant modes based on pcb technology," *IEEE Transactions on Components, Packaging and Manufacturing Technology*, 2024.

[89] Y. Tang, T. Wang, J. Zheng, Z. Lyu, X. Tian, and J. Mou, "Mutual coupling suppression of mimo array with non-uniform curved-strip ebg structure via shape and layout co-optimization," *AEU-International Journal of Electronics and Communications*, vol. 178, p. 155306, 2024.

[90] A. K. Oladeinde, E. Aryafar, and B. Pejcinovic, "Mmwave tx-rx self-interference suppression through a high impedance surface stacked ebg," *Electronics*, vol. 13, no. 15, p. 3067, 2024.

[91] T. Hemalatha and B. Roy, "Low-profile co-csrr and ebg loaded tri-quarter circular patch ewb mimo antenna with multiple notch bands," *IEEE Open Journal of Antennas and Propagation*, 2024.

[92] P. Mondal, D. Dhara, and A. Harish, "Partially reflective fss-based superstrate as a decoupling structure for reducing the mutual coupling of circularly polarized antennas," *IEEE Transactions on Antennas and Propagation*, 2024.

[93] R. K. Mistri, A. K. Singh, S. K. Mahto, R. Sinha, K. Alhassoon, A. J. A. Al-Gburi, and M. M. Ismail, "An eight-element mimo antenna system supporting dual bands for 5g mobile, fss, and dbs communication," *Progress in Electromagnetics Research B*, vol. 107, pp. 125–137, 2024.

[94] M. K. Sharma, A. Sharma, and R. Kumari, "A cpw thz-mimo antenna with reduced mutual coupling using frequency selective surface for future wireless applications," *Optical Materials*, vol. 148, p. 114929, 2024.

[95] L. Malviya, R. K. Panigrahi, and M. V. Kartikeyan, "Mimo antennas with diversity and mutual coupling reduction techniques: a review," *International Journal of Microwave and Wireless Technologies*, vol. 9, no. 8, pp. 1763–1780, 2017.

[96] J. Zhang, M. O. Akinsolu, B. Liu, and G. A. Vandenbosch, "Automatic ai-driven design of mutual coupling reducing topologies for frequency reconfigurable antenna arrays," *IEEE Transactions on Antennas and Propagation*, vol. 69, no. 3, pp. 1831–1836, 2020.

[97] C. A. Balanis, *Antenna theory: analysis and design*. John wiley & sons, 2015.

[98] M. S. Sharawi, "Current misuses and future prospects for printed multiple-input, multiple-output antenna systems [wireless corner]," *IEEE Antennas and Propagation Magazine*, vol. 59, no. 2, pp. 162–170, 2017.

[99] J. Medbo, K. Börner, K. Haneda, V. Hovinen, T. Imai, J. Järvelainen, T. Jämsä, A. Karttunen, K. Kusume, J. Kyröläinen, *et al.*, "Channel modelling for the fifth generation mobile communications," in *The 8th European Conference on Antennas and Propagation (EuCAP 2014)*, pp. 219–223, IEEE, 2014.

[100] G. Saxena, P. Jain, and Y. K. Awasthi, "High diversity gain mimo-antenna for uwb application with wlan notch band characteristic including human interface devices," *Wireless Personal Communications*, vol. 112, pp. 105–121, 2020.

[101] G.-P. Gao, J.-M. Bai, L.-J. Jin, W.-D. Guo, G. Ma, and B. Hu, "A compact dual port circularly polarized mimo antenna for on-/off-body wban applications," *IEEE Antennas and Wireless Propagation Letters*, 2025.

[102] J. Ahmad, G. Nauryzbayev, and M. Hashmi, "Design of a compact millimeter wave band antenna for smartwatch wban applications," in *2024 IEEE Asia-Pacific Microwave Conference (APMC)*, pp. 1111–1113, 2024.

[103] P. K. Sharma, N. Gupta, and P. I. Dankov, "Characterization of polydimethylsiloxane (pdms) as a wearable antenna substrate using resonance and planar structure methods," *AEU-International Journal of Electronics and Communications*, vol. 127, p. 153455, 2020.

[104] R. B. Simorangkir, Y. Yang, K. P. Esselle, and B. A. Zeb, "A method to realize robust flexible electronically tunable antennas using polymer-embedded conductive fabric," *IEEE Transactions on Antennas and Propagation*, vol. 66, no. 1, pp. 50–58, 2017.

[105] A. Arif, M. Zubair, M. Ali, M. U. Khan, and M. Q. Mehmood, "A compact, low-profile fractal antenna for wearable on-body wban applications," *IEEE Antennas and Wireless Propagation Letters*, vol. 18, no. 5, pp. 981–985, 2019.

[106] H. Li, J. Du, X.-X. Yang, and S. Gao, "Low-profile all-textile multiband microstrip circular patch antenna for wban applications," *IEEE Antennas and Wireless Propagation Letters*, vol. 21, no. 4, pp. 779–783, 2022.

[107] V. Kumar and B. Gupta, "On-body measurements of ss-uwb patch antenna for wban applications," *AEU-International Journal of Electronics and Communications*, vol. 70, no. 5, pp. 668–675, 2016.

[108] Y. Li, L. Yang, M. Gao, X. Zhao, and X. Zhang, "A study of a one-turn circular patch antenna array and the influence of the human body on the characteristics of the antenna," *Ad Hoc Networks*, vol. 99, p. 102059, 2020.

[109] R. Zhang, J. Liu, Y. Wang, Z. Luo, B. Zhang, and J. Duan, "Flexible wearable composite antennas for global wireless communication systems," *Sensors*, vol. 21, no. 18, p. 6083, 2021.

[110] M. El Atrash, M. A. Abdalla, and H. M. Elhennawy, "A wearable dual-band low profile high gain low sar antenna amc-backed for wban applications," *IEEE Transactions on Antennas and Propagation*, vol. 67, no. 10, pp. 6378–6388, 2019.

[111] R. Joshi, E. F. N. M. Hussin, P. J. Soh, M. F. Jamlos, H. Lago, A. A. Al-Hadi, and S. K. Podilchak, "Dual-band, dual-sense textile antenna with amc backing for localization using gps and wban/wlan," *IEEE Access*, vol. 8, pp. 89468–89478, 2020.

[112] Y. B. Chaouche, M. Nedil, I. B. Mabrouk, and O. M. Ramahi, "A wearable circularly polarized antenna backed by amc reflector for wban communications," *IEEE Access*, vol. 10, pp. 12838–12852, 2022.

[113] U. Ali, S. Ullah, A. Basir, B. Kamal, L. Matekovits, and H. Yoo, "Design and sar analysis of amc-based fabric antenna for body-centric communication," *IEEE Access*, 2023.

[114] M. Bose, A. Kundu, A. Sarkhel, and U. Chakraborty, "A review of design challenges of metamaterial-inspired body-worn antennas," *Advances in Microwave Engineering*, pp. 115–144, 2023.

[115] C. Constantinescu, C. Pacurar, A. Giurgiuman, C. Munteanu, S. Andreica, and M. Gliga, "High gain improved planar yagi uda antenna for 2.4 ghz applications and its influence on human tissues," *Applied Sciences*, vol. 13, no. 11, p. 6678, 2023.

[116] A. Kafizov, M. Hashmi, D. Rano, and D. Kupreyev, "End-fire yagi antenna with dgs for wban applications," in *2019 8th Asia-Pacific Conference on Antennas and Propagation (APCAP)*, pp. 426–427, IEEE, 2019.

[117] Z. Iman, A. Shungeyev, D. Rano, and M. Hashmi, "A planar end-fire antenna for wireless body area network," in *2020 International Workshop on Antenna Technology (iWAT)*, pp. 1–3, IEEE, 2020.

[118] X. Shi, Y. Cao, Y. Hu, X. Luo, H. Yang, and L. H. Ye, "A high-gain antipodal vivaldi antenna with director and metamaterial at 1–28 ghz," *IEEE Antennas and Wireless Propagation Letters*, vol. 20, no. 12, pp. 2432–2436, 2021.

[119] B. A. Munk, *Frequency selective surfaces: theory and design*. John Wiley & Sons, 2005.

[120] Z. Wang, C. Li, and Y. Yin, "A meta-surface antenna array decoupling (maad) design to improve the isolation performance in a mimo system," *IEEE Access*, vol. 8, pp. 61797–61805, 2020.

[121] S. Harmer, N. Rezgui, N. Bowring, Z. Luklinska, and G. Ren, "Determination of the complex permittivity of textiles and leather in the 14–40 ghz millimetre-wave band using a free-wave transmittance only method," *IET Microwaves, Antennas & Propagation*, vol. 2, no. 6, pp. 606–614, 2008.

[122] A. R. Guraliuc, N. Chahat, C. Leduc, M. Zhadobov, and R. Sauleau, "End-fire antenna for ban at 60 ghz: Impact of bending, on-body performances, and study of an on to off-body scenario," *electronics*, vol. 3, no. 2, pp. 221–233, 2014.

[123] A. Iqbal, A. Basir, A. Smida, N. K. Mallat, I. Elfergani, J. Rodriguez, and S. Kim, "Electromagnetic bandgap backed millimeter-wave mimo antenna for wearable applications," *IEEE Access*, vol. 7, pp. 111135–111144, 2019.

[124] P. Njogu, B. Sanz-Izquierdo, A. Elibiary, S. Y. Jun, Z. Chen, and D. Bird, "3d printed fingernail antennas for 5g applications," *IEEE Access*, vol. 8, pp. 228711–228719, 2020.

[125] D. Wen, Y. Hao, M. O. Munoz, H. Wang, and H. Zhou, "A compact and low-profile mimo antenna using a miniature circular high-impedance surface for wearable applications," *IEEE Transactions on Antennas and Propagation*, vol. 66, no. 1, pp. 96–104, 2017.

[126] M. J. Shehab, I. Kassem, A. A. Kutty, M. Kucukvar, N. Onat, and T. Khattab, "5g networks towards smart and sustainable cities: A review of recent developments, applications and future perspectives," *IEEE Access*, vol. 10, pp. 2987–3006, 2021.

[127] D. G. Arnaoutoglou, T. M. Empliouk, T. N. Kaifas, M. T. Chryssomallis, and G. Kyriacou, "A review of multifunctional antenna designs for internet of things," *Electronics*, vol. 13, no. 16, p. 3200, 2024.

[128] P. K. Malik, A. Naim, and R. Singh, *Printed Antennas: Design and Challenges*. CRC Press, 2022.

[129] N. Kumprasert, "Theoretical study of dual-resonant frequency and circular polarization of elliptical microstrip antennas," in *IEEE Antennas and Propagation Society International Symposium. Transmitting Waves of Progress to the Next Millennium. 2000 Digest. Held in conjunction with: USNC/URSI National Radio Science Meeting (C*, vol. 2, pp. 1015–1020 vol.2, 2000.

[130] B. P. Shariff, S. Pathan, P. R. Mane, and T. Ali, "Characteristic mode analysis based highly flexible antenna for millimeter wave wireless applications," *Journal of Infrared, Millimeter, and Terahertz Waves*, vol. 45, no. 1, pp. 1–26, 2024.

[131] B. P. Shariff, S. Pathan, P. R. Mane, and T. Ali, "Characteristic mode analysis based highly flexible antenna for millimeter wave wireless applications," *Journal of Infrared, Millimeter, and Terahertz Waves*, vol. 45, no. 1, pp. 1–26, 2024.

[132] Z. Szabó, G.-H. Park, R. Hedge, and E.-P. Li, "A unique extraction of metamaterial parameters based on kramers–kronig relationship," *IEEE Transactions on Microwave Theory and Techniques*, vol. 58, no. 10, pp. 2646–2653, 2010.

[133] M. Manteghi and Y. Rahmat-Samii, "Multiport characteristics of a wide-band cavity backed annular patch antenna for multipolarization operations," *IEEE Transactions on Antennas and Propagation*, vol. 53, no. 1, pp. 466–474, 2005.

[134] M. K. Elmezughi and T. J. Afullo, "An efficient approach of improving path loss models for future mobile networks in enclosed indoor environments," *IEEE Access*, vol. 9, pp. 110332–110345, 2021.

[135] R. N. Tiwari, K. G. Malya, G. Nandini, P. Nikhitha, D. Sharma, P. Singh, and P. Kumar, "Quad-band $1\times$ 4 linear mimo antenna for millimeter-wave, wearable and biomedical telemetry applications," *Sensors*, vol. 24, no. 14, p. 4427, 2024.

[136] A. Ahmad, D.-y. Choi, and S. Ullah, "A compact two elements mimo antenna for 5g communication," *Scientific Reports*, vol. 12, no. 1, p. 3608, 2022.

[137] D. A. Sehrai, M. Asif, N. Shoaib, M. Ibrar, S. Jan, M. Alibakhshikenari, A. Lalbakhsh, and E. Limiti, "Compact quad-element high-isolation wideband mimo antenna for mm-wave applications," *Electronics*, vol. 10, no. 11, p. 1300, 2021.

[138] Z. Chen, Y.-X. Wang, K.-D. Hong, and T. Yuan, "A multiantenna system with high isolations for millimeter-wave sensing," *IEEE Antennas and Wireless Propagation Letters*, vol. 21, no. 12, pp. 2482–2486, 2022.

[139] N. Sghaier, A. Belkadi, I. B. Hassine, L. Latrach, and A. Gharsallah, "Millimeter-wave dual-band mimo antennas for 5g wireless applications," *Journal of Infrared, Millimeter, and Terahertz Waves*, vol. 44, no. 3, pp. 297–312, 2023.

[140] R. N. Tiwari, D. Sharma, P. Singh, and P. Kumar, "Design of dual-band 4-port flexible mimo antenna for mm-wave technologies and wearable electronics," *IEEE Access*, 2024.

[141] M. Ikram, N. Nguyen-Trong, and A. Abbosh, "Multiband mimo microwave and millimeter antenna system employing dual-function tapered slot structure," *IEEE Transactions on Antennas and Propagation*, vol. 67, no. 8, pp. 5705–5710, 2019.

[142] J. Ahmad and M. Hashmi, "A compact mimo antenna for wban applications at millimeter-wave frequencies," in *2023 31st Telecommunications Forum (TELFOR)*, pp. 1–4, IEEE, 2023.

[143] M. I. Khan, S. Liu, M. K. Khan, and S. U. Rahman, "Eight elements mm-wave mimo antenna for anti-collision radar sensing application with novel hybrid techniques," *AEU-International Journal of Electronics and Communications*, vol. 167, p. 154687, 2023.

[144] S. Nej, A. Ghosh, S. Ahmad, J. Kumar, A. Ghaffar, and M. I. Hussein, "Design and characterization of 10-elements mimo antenna with improved isolation and radiation characteristics for mm-wave 5g applications," *IEEE Access*, vol. 10, pp. 125086–125101, 2022.

[145] A. Khan, Y. He, and Z. N. Chen, "An eight-port circularly polarized wideband mimo antenna based on a metamaterial-inspired element for 5g mmwave applications," *IEEE Antennas and Wireless Propagation Letters*, vol. 22, no. 7, pp. 1572–1576, 2023.

[146] S. Roy, J. J. Tiang, M. B. Roslee, M. T. Ahmed, A. Z. Kouzani, and M. P. Mahmud, "Quad-band rectenna for ambient radio frequency (rf) energy harvesting," *Sensors*, vol. 21, no. 23, p. 7838, 2021.

[147] D.-A. Nguyen, G. T. Bui, H. Nam, and C. Seo, "Extended dynamic-range and high-efficiency rectifier based on adaptive power distribution and synthesized low-pass matching network," *IEEE Access*, 2023.

[148] D. Sarkar, S. M. Mikki, and Y. M. Antar, "Poynting localized energy: Method and applications to gain enhancement in coupled antenna systems," *IEEE Transactions on Antennas and Propagation*, vol. 68, no. 5, pp. 3978–3988, 2020.

[149] Y. Zhang, J.-Y. Deng, M.-J. Li, D. Sun, and L.-X. Guo, "A mimo dielectric resonator antenna with improved isolation for 5g mm-wave applications," *IEEE Antennas and Wireless Propagation Letters*, vol. 18, no. 4, pp. 747–751, 2019.

[150] I. Ud Din, M. Alibakhshikenari, B. S. Virdee, R. K. R. Jayanthi, S. Ullah, S. Khan, C. H. See, L. Golunski, and S. Koziel, "Frequency-selective surface-based mimo antenna array for 5g millimeter-wave applications," *Sensors*, vol. 23, no. 15, p. 7009, 2023.

[151] W. Song, X.-W. Zhu, L. Wang, and W. Hong, "Simple structure e-plane decoupled millimeter wave antenna based on current cancellation model," *IEEE Transactions on Antennas and Propagation*, vol. 70, no. 10, pp. 9871–9876, 2022.

[152] S. Gupta, Z. Briqech, A. R. Sebak, and T. A. Denidni, "Mutual-coupling reduction using metasurface corrugations for 28 ghz mimo applications," *IEEE Antennas and Wireless Propagation Letters*, vol. 16, pp. 2763–2766, 2017.

[153] R. Selvaraju, M. H. Jamaluddin, M. R. Kamarudin, J. Nasir, and M. H. Dahri, "Mutual coupling reduction and pattern error correction in a 5g beamforming linear array using csrr," *IEEE Access*, vol. 6, pp. 65922–65934, 2018.